Effect of the TiO$_2$-modifications anatase and rutile on the solid-state synthesis of (Ba,Ca)TiO$_3$ and the electrical characteristics of (Ba,Ca)TiO$_3$-based ceramics with PTCR

Kathleen Kirstein

August 2011

A thesis submitted in partial fulfilment of the requirements of the

Graz University of Technology

(Institute for Chemistry and Technology of Materials)

for the degree of Doctor technicæ (Dr.techn.)

In cooperation with

EPCOS OHG Deutschlandsberg (Austria)

A Member of TDK-EPC Corporation

Deutsche Fassung:
Beschluss der Curricula-Kommission für Bachelor-, Master- und Diplomstudien vom 10.11.2008
Genehmigung des Senates am 1.12.2008

EIDESSTATTLICHE ERKLÄRUNG

Ich erkläre an Eides statt, dass ich die vorliegende Arbeit selbstständig verfasst, andere als die angegebenen Quellen/Hilfsmittel nicht benutzt, und die den benutzten Quellen wörtlich und inhaltlich entnommene Stellen als solche kenntlich gemacht habe.

Graz, am ……………………………   ………………………………………..
(Unterschrift)

Englische Fassung:

STATUTORY DECLARATION

I declare that I have authored this thesis independently, that I have not used other than the declared sources / resources, and that I have explicitly marked all material, which has been quoted either literally or by content from the used sources.

……………………………   ………………………………………..
(date)   (signature)

Abstract

In this thesis the cause and effect of commercially available anatase-TiO_2 on the positive temperature coefficient of resistivity (PTCR) characteristics of donor- and acceptor-codoped $(Ba,Ca)TiO_3$-ceramics have been investigated.

Compositions containing several anatase and rutile raw materials have been prepared with help of the commonly used fabrication process, which includes the solid-state synthesis of n-conducting barium titanate, powder refinement and device shaping as well as the sintering process.

Thermally untreated material compositions have been analysed by using simultaneous thermal analyzing techniques (STA), especially thermal gravimetry and differential scanning calorimetry (TG/DSC). Furthermore, the calcined powders have been characterised using X-ray diffraction (XRD).

Sintered parts have been studied electrically by commonly used measuring techniques e.g. resistivity and capacity measurements as a function of temperature or impedance spectroscopy. In addition microstructure and chemical composition have been determined by means of scanning and transmission electron microscopy (SEM and TEM), in particular energy and wavelength dispersive X-ray spectroscopy (EDXS and WDXS) electron backscattering diffraction (EBSD) and electron probe microanalysis (EPMA).

It has been clearly shown that the crystallographic modifications rutile and anatase are replaceable without any significant effect on the PTCR-characteristics, in case of similar physical and chemical properties such as grain size, specific surface area and impurity content. Further, it has been demonstrated that the impurities of commercial anatase powders, which are a result of the preparation conditions, strongly affect the PTCR-characteristics by influencing the calcination as well as the sintering mechanism.

By use of impedance analysis and electron backscattering diffraction (EBSD) and electron probe microanalysis (EPMA), it has been concluded for compositions having minor Ti-excess that the differences in PTCR-characteristics can be attributed to changes in dopants distribution together with segregative additive effects and not to microstructural modifications. On the contrary, for compositions prepared with increased Ti-excess it has been demonstrated that the change in PTCR-performance mainly results from microstructure variations likewise induced by the impurities detected in anatase-based TiO_2.

With respect to the results gained during solid-state synthesis a modified calcination mechanism for the anatase-based materials has been presented that enables an explanation of the differences in calcine properties. Finally, a modified sintering mechanism has been proposed based on the observations obtained from the sintered parts.

Kurzbeschreibung

In dieser Arbeit wurde der Einfluss von handelsüblichen Anatas-Rohstoffen auf den positiven Wiederstands-Temperaturkoeffizienten ([PTC](#)-Effekt) in Donor- und Akzeptor-codotiertem $(Ba,Ca)TiO_3$ untersucht.

Es wurden Mischungen mit verschiedenen Anatas- und Rutil-Rohstoffen hergestellt, wobei ein vom industriellen Fertigungsprozess abgeleitetes Herstellverfahren zum Einsatz kam. Die Probenherstellung umfasste die Festphasensynthese von n-leitendem Bariumtitanat, die Pulveraufbereitung, den Formgebunsprozess und den abschliessenden Sinterprozess.

Die thermisch unbehandelten Materialmischungen wurden mittels Simultan-Thermoanalyse ([STA](#)) untersucht, einer Kombination von Thermogravimetrie und Differential-Kalorimetrie ([TG](#)/[DSC](#)). Weiter wurden die kalzinierten Pulver mittels Röntgenbeugung ([XRD](#)) charakterisiert. Die gesinterten Probekörper wurden elektrische analysiert mit Hilfe von Wiederstands- und Kapazitätsmessungen als Funktion der Temperatur sowie Impedanz-spektroskopische Aufnahmen. Weiters wurden für die Gefüge-untersuchungen und chemischen Analysen sowohl die Rasterelektronen-mikroskopie ([SEM](#), [EBSD](#)) als auch die Transmissionselektronenmikroskopie ([TEM](#)) verwendet. Zur chemischen Bereichsanalyse wurden insbesondere Energie- und Wellenlängen-dispersive Röntgenverfahren wie [EDX](#) und [WDX](#) sowie die enegiedispersive Röntgenmikrobereichanalyse ([EPMA](#)) verwendet.

Im Rahmen der vorliegenden Arbeit konnte eindeutige gezeigt werden, dass die kristallografischen Modifikation Rutil und Anatas austauschbar sind und keinen signifikanten Einfluss auf den [PTC](#)-Effekt zeigen. Voraussetzung hierfür ist, dass die physikalischen und chemischen Eigenschaften wie z.B. die Korngröße, die spezifische Oberfläche und der Verunreinigungsgrad der Rohstoffe vergleichbar sind. Des Weiteren konnte nachgewiesen werden, dass die Verunreinigungen in handelsüblichen Anatas-Rohstoffen die [PTC](#)-Charakteristik stark beeinflussen, indem sie auf den Kalzinations- sowie den Sinter-Mechanismus wirken.

Mit Hilfe von Impedanz-Spektroskopie, Rücksstreu-Elektronenbeugung ([EBSD](#)) und Röntgenmikrobereichanalyse ([EPMA](#)) konnte für diejenigen Materialzusammensetzungen mit geringem Titanüberschuss gefolgert werden, dass die Unterschiede in den [PTC](#)-Charakteristiken einerseits auf eine Änderung in der Dotierstoffverteilung und andererseits auf die Wirkung von segregierenden Additiven zurückzuführen ist und nicht durch eine Modifikation der Mikrostruktur bewirkt wird. Im Gegensatz dazu konnte für solche Zusammensetzungen mit erhöhtem Titanüberschuss aufgezeigt werden, dass die Änderung der [PTC](#)-Performance im Wesentlichen durch eine Variation der Mikrostruktur verursacht wird, welche wiederum von den Verunreinigungen in den Anatas-Rohstoffen beeinflusst wird.

Gestützt auf die Analysenergebnisse bei der Festphasensynthese, wurde ein modifizierter Kalzinationsmechanismus für Anatas-basierte Materialien beschrieben, welcher die Unterschiede in den Eigenschaften der kalzinierten Pulver zu deuten vermag. Abschließend wurde basierend auf den Beobachtungen gesinterten Probekörpern ein abgewandelter Sintermechanismus vorgeschlagen.

Content

1. Introduction and motivation

Titanates are of great importance in the field of functional ceramics especially in electronic ceramics. Electronic ceramics can be divided into three material groups [Sal-07]. Firstly, the dielectric materials, which are for example used to produce capacitors, microwave components or substrates. Secondly, ferroelectric ceramics that are employed e.g. to manufacture piezoelectric sensors and actuators, ferroelectric memories, pyroelectric infrared detectors or fast eletrooptical switches. Finally, the group of ionic and electronic conductors of which for instance fuel cells, varistors, superconductors and thermistors are fabricated. The latter group is further divided into thermistors having negative temperature coefficient of resitivity (NTCR) and materials that show positive temperature coefficient of resistivity (PTCR) [Sal-07]. PTC thermistors for example are applied to fuses for overcurrent protection, switches for motor starting, heater elements and level or temperature sensors [EPC-08]. For PTC thermistor applications, titanates of barium, calcium, strontium and lead are used as well as a wide range of their solid solutions. Since the PTCR-effect is a grain boundary phenomenon, it only occurs in semiconducting donor-doped (n-conducting) ceramics with polycrystalline microstructure. Semiconductivity in $BaTiO_3$-based ceramics is achieved by doping the material with kations of higher valency such as lanthanum or niobium, which substitute for barium and titanium respectively [Huy-95, EPC-08]. This thesis focuses on donor- and acceptor-codoped $(Ba,Ca)TiO_3$ for PTCR application prepared from different titanium dioxide raw materials.

Commonly, $BaTiO_3$-based PTCR-materials are produced on a large scale via a modified solid-state-synthesis route that is well investigated since the 1960s [Ueo-74/1, Huy-95, Lee-09]. Increasing application requirements e.g. due to advancing miniaturisation of electronic components account for high performance starting materials with regard to purity, reactivity, sintering properties and applicability in barium titanate synthesis process [Aue-01]. Several scientists carried out kinetic studies on the solid-state synthesis using the titania modifications anatase and rutile. These researchers revealed that the reactivity of the titania material during $BaTiO_3$ formation is determined by the raw material properties, especially the grain size, specific surface area, pre-treatment of the raw material as well as type and quantity of impurities. The latter primarily affecting the secondary phase formation during synthesis [Spi-61, Kub-67, Suy-75/1, Suy-75/2, Suy-77, Ami-83, Bea-83/1, Bea-83/2, Fer-91/1, Fer-91/2, Tsu-01, Brz-02, Ryu-07].

Empirical observations have shown that the use of anatase for PTCR-production is not possible, although no satisfying scientific explanation has been available yet. Rather some authors suppose that the anatase modification is kinetically preferable in PTCR-production [Sau-60, Hey-65, Kul-81]. This discrepancy can be attributed to the differing properties of the investigated raw materials, which result from the preparation conditions. However, the use of commercial anatase TiO_2 was discussed within the framework of this thesis because this modification is a cheap mass product, which is found in paints and fillers. Consequently, great advantage results from the possibility to reduce raw material costs by using cheaper anatase materials in PTCR-production. The main impurities of this type of material are potassium and phosphorus in the range of several hundred ppm.

1. Introduction and motivation

Due to the insufficient understanding about the effects of anatase-TiO_2 on the electrical characteristics of PTCR-components, the aim of this work is to clarify the role of anatase raw materials on the electrical properties of donor-and acceptor-codoped $(Ba,Ca)TiO_3$.

In this context, some essential questions need to be examined in the framework of this thesis. Firstly, which titania raw material properties affect the $(Ba,Ca)TiO_3$-formation. Furthermore, in what manner is the solid-state synthesis process governed by the titania modification.

Secondly, is there any influence of the titania modification on the sintering process, which ultimately affects the PTCR-properties of the material. Moreover, assuming there is an influence on the sintering process, how does this mechanism proceed and in which way does it modify the PTCR-characteristics.

Finally, is anatase-TiO_2 in principle applicable in the manufacturing of PTCR-components?

2. Theoretical background

This section deals with the state of the art of science and technology in relation to the commercial synthesis processes of titanium dioxide and semiconducting barium titanate with positive temperature coefficient of resistivity (PTCR). Additionally the theoretical foundations in this field of application are presented. The intention is to give the reader an appropriate background to understand and follow the lines of argument.

2.1. Titanium dioxide raw materials

Titanium dioxide (TiO_2) is a nontoxic chemically very stable oxide with excellent optical properties e.g. its high index of refraction, its very good reflectivity and its absorbing capacity of ultraviolet radiation. These properties make it one of the most famous white pigments not only for the colour and paint industry but also for the plastic, the ceramic and enamel as well as the food industry. Additionally titanium dioxide comes with respectable dielectric and interesting semiconducting properties for which reason it is used in capacitor and catalytic materials.
Due to the manifold application possibilities, the worldwide annual requirement of titanium dioxide amounts to several million tons whereas for electroceramic applications the global consumption exceeds 10kt per year [Aue-01, EIP-07/1, UWi-01].
Commercial titanium dioxide raw materials are produced by two preparation routes: the sulphate and the chloride process. Both methods were already established in the 1940´s and were described in detail and published by Barksdale [Bar-49]. In this section, the processes are introduced and their discrepancies with respect to the raw material qualities are characterized.

2.1.1. Commercial TiO$_2$ synthesis

During the sulphate process titanium containing materials such as the mineral Ilmenit ($FeTiO_3$) are primarily solubilised with concentrated, hot sulphuric acid corresponding to Equation 2.1-I [Aue-01, Bar-49, Ges-01, EIP-07/1, UWi-01].

$$FeTiO_3 + 3H_2SO_4 \xrightarrow{130-220°C} FeSO_4 + Ti(SO_4)_2 + 3H_2O$$
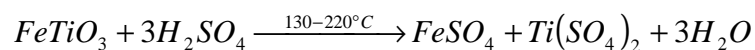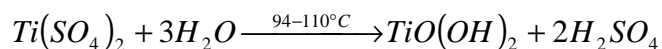
Equation 2.1-I

By adding water to the solution and cooling it down to 10°C the iron sulphate crystallizes to iron (II) sulphate heptahydrate (green vitriol; Equation 2.1-II). The iron sulphate crystallites can be separated from the solubilised titanium sulphate by centrifugation.

$$FeSO_4 + 7H_2O \xrightarrow{5-15°C} FeSO_4 \cdot 7H_2O$$
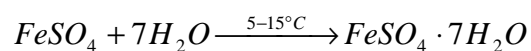
Equation 2.1-II

2. Theoretical background

Further, the titanium sulphate is transformed into the slightly soluble metatitanic acid (see Equation 2.1-III) by again adding water and heating the solution [Bar-49, Ges-01]. This step creates a huge amount of dilute acid (acid solution with low H_2SO_4 concentration) which has to be recycled [EIP-07/1, UWi-01].

$$Ti(SO_4)_2 + 3H_2O \xrightarrow{94-110°C} TiO(OH)_2 + 2H_2SO_4$$

Equation 2.1-III

Depending on the composition of the starting ore and the quality demands of the product, several refinement steps are performed before calcination e.g. the elution of adsorbed sulphate or reductive removal of transition metal ions [Bar-49, Ges-01].

At that point of the titanium dioxide preparation, it is worth mentioning that the metatitanic acid frequently is processed with phosphoric acid and alkaline compounds to promote the crystallization during calcination. The amount of such mineralisers accounts up to one percent. For the synthesis of anatase pigments, higher contents of mineralisers are required compared to rutile synthesis [Aue-01, Ges-01].
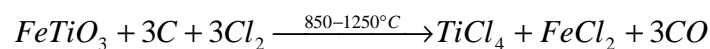
Finally, the metatitanic acid is calcined in a rotary furnace at temperatures between 800 and 1000°C. Within this step the amorphous $TiO(OH)_2$ is crystallized to titanium dioxide (Equation 2.1-IV).

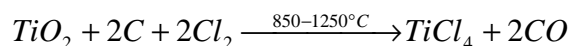$$TiO(OH)_2 \xrightarrow{800-1000°C} TiO_2 + H_2O$$
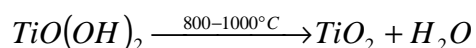
Equation 2.1-IV

Without any additives, the metastable anatase modification is formed from metatitanic acid whereas the thermodynamic stable rutile modification is formed when adding rutile crystal seeds during calcination [Aue-01, Bar-49, Ges-01, UWi-01].

For the chloride process titanium containing raw materials e.g. ilmenit or titanium dioxide are used [Bar-49, EIP-07/1, UWi-01]. In the presence of carbon and chlorine gas at temperatures between 850°C and 1250°C gaseous titanium tetrachloride is formed (Equation 2.1-V and Equation 2.1-VI).

$$FeTiO_3 + 3C + 3Cl_2 \xrightarrow{850-1250°C} TiCl_4 + FeCl_2 + 3CO$$

Equation 2.1-V

$$TiO_2 + 2C + 2Cl_2 \xrightarrow{850-1250°C} TiCl_4 + 2CO$$

Equation 2.1-VI

The gaseous titanium chloride can now easily be cleaned by separating solid compounds such as iron (II) chloride. After that, the condensed $TiCl_4$ is further cleaned via distillation. At this juncture several additives are added which are able to chemically bind present impurities such as vanadium [EIP-07/1, UWi-01]. Finally, the refined $TiCl_4$ is reoxidized in a reactor at temperatures between 900°C and 1400°C as depicted in Equation 2.1-VII.

2. Theoretical background

$$TiCl_4 + O_2 \xrightarrow{900-1400°C} TiO_2 + 2Cl_2$$
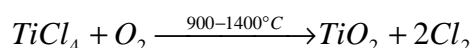
Equation 2.1-VII

This reoxidation process has to be well defined due to its great effect on the titanium dioxide pigment quality. Among others, parameters such as the reaction temperature and atmosphere as well as the kind and amount of additives influence the particle size and distribution of the pigment powder [Aue-01].

From Equation 2.1-VII the main advantage of the chloride process compared to the sulphate process can easily be seen. The reformed chlorine gas can directly be returned to the preparation process (Equation 2.1-V). In this manner considerable lower amounts of polluting residues such as dilute acid are formed. On the contrary, a great disadvantage of the chloride process is that by reason of the higher process temperatures usually the thermodynamic stable rutile modification is obtained [EIP-07/1, UWi-01].

Comparing both synthesis processes TiO_2 pigments obtained by the chloride process generally show better optical and physicochemical properties such as brightness and durability. On the contrary, for challenging applications such as catalysts or electroceramics mainly sulphate processed TiO_2 is used [Aue-01].

Beside these two commercial preparation methods, several alternative methods for titanium dioxide preparation on the laboratory scale are known. For example Barksdale [Bar-49] already reported in 1949 on the fluorine and the chlorine-acetate process for the preparation of rutile raw materials. Later on e.g. Czanderna [Cza-57], Suzuki [Suz-62] or Yoganarasimhan [Yog-62] elucidated other methods for the preparation of the anatase modification.

2.1.2. Properties of anatase and rutile TiO_2

Titanium dioxide naturally appears in three rock-forming, crystallographic modifications: rutile, anatase and brookite. In this case, the rutile modification represents the thermodynamically stable material, which irreversible forms from anatase and brookite at elevated temperatures [Mur-87]. Due to its difficult preparation conditions, brookite more or less is irrelevant in large-scale production [Aue-01]. Relevant crystallographic and physical properties of the two TiO_2 minerals anatase and rutile are summarised in Table 2.1-I. Crystal structures are depicted in Figure 2.1-I and Figure 2.1-II both displayed by using the Diamond program version 3.1f.

Table 2.1-I: Crystal data and physical properties of the TiO_2 modifications rutile and anatase (data collected from [Aue-01])

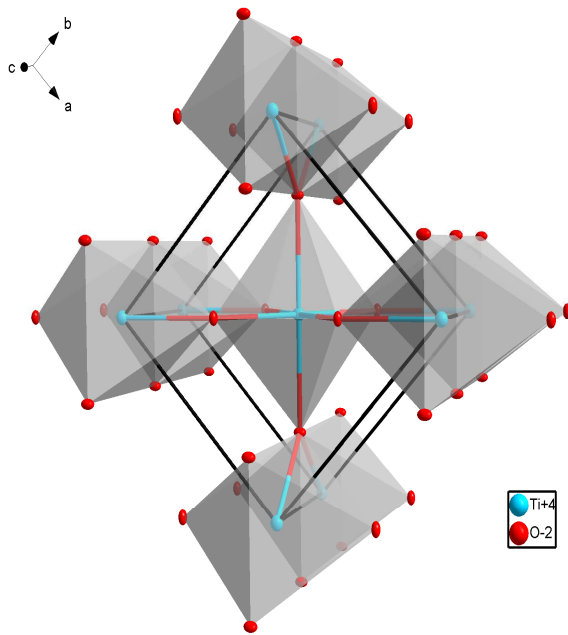| Mineral	Rutile	Anatase
Crystal system	tetragonal	tetragonal
Space group	P4$_2$/mnm	I4$_1$/amd
Point group	4/m2/m2/m	4/m2/m2/m
Unit cell [Á]	C = 2.9587	C = 9.5143
	A = 4.5937	A = 3.7845
twinning {hkl}	often in {011}; bend shaped or netlike in {031}	rare in {112}
Density [g/cm³]	4.25	3.89
Mohs hardness	6-6.5	5.5-6
Refractive index (632nm)	2.80	2.55
Band gap [eV]	3.03	3.15

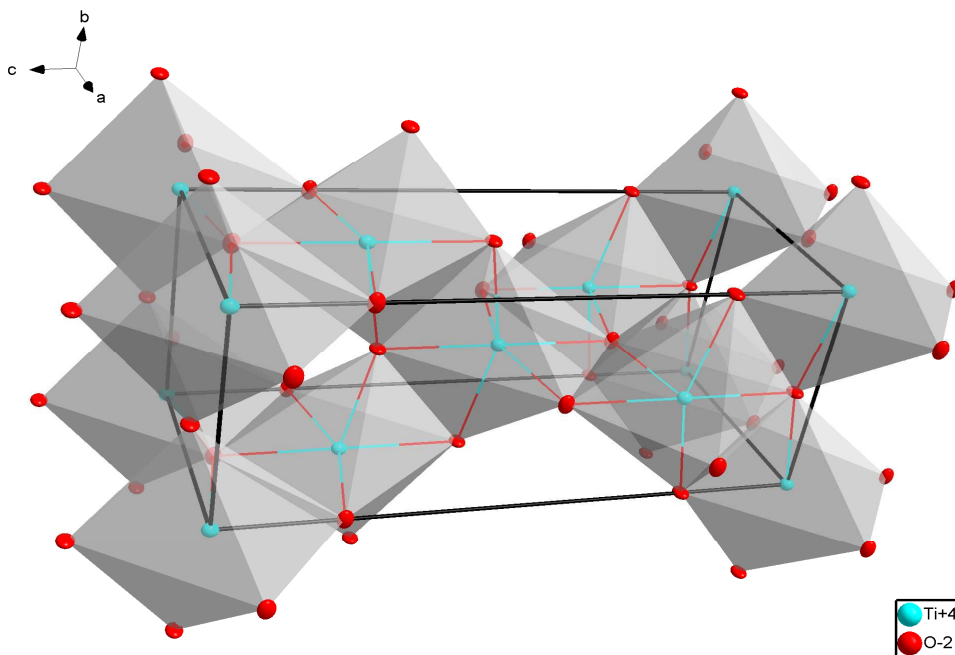**Figure 2.1-I:** Crystal structure of rutile based on ICSD no.63710.

Figure 2.1-II: Crystal structure of anatase based on ICSD no. 63711.

In order to analyze and interpret the differences between the anatase and rutile modification in terms of the synthesis of barium titanate based PTCR-materials the thermo-physical properties of the anatase material itself are of basic interest. In general, titanium dioxide catalyzes the barium carbonate decomposition during

solid-state synthesis (see section 2.2.1). Thus, various thermal and physical properties of the titania raw materials may on the one hand influence the synthesis process (calcination). On the other hand, they may also affect the sintering activity of the calcined powder hence affecting the PTCR-characteristics. For this reason, some basic knowledge of the phase transformation and phase stability of anatase is essential.

Anatase is the kinetically preferred TiO_2 modification, which is generated by low temperature synthesis methods. At elevated temperatures, metastable anatase is irreversible transformed into the thermodynamically stable rutile modification [Cza-57]. Due to the growing market for titania application since the 1950th a notable number of scientists have intensively studied the anatase-rutile phase transition. In this context, the reaction kinetics as well as influencing parameters on the phase transition have been investigated.

Already Barksdale [Bar-49] reported on the effect of small impurity concentrations on the anatase-rutile phase transition. The working group around Czanderna thus prepared spectroscopically pure anatase by oxidation of metallic titanium [Cza-57, Cza-58]. Later on for example Rao [Rao-60] or Yoganarasimhan [Yog-62] systematically investigated the effect of impurities respectively additives e.g. alumina and sulphate on the phase stability of anatase. Both authors revealed that anatase is stabilized in the presence of impurity ions i.e. additional activation energy is needed to initiate the phase transition.

Nowadays in line with pigment or catalytic applications, the influence of more complex additives on the thermo-physical properties of anatase is analyzed [Oli-93, Grz-07, Rao-61, Hea-72, Amo-95, Cri-83, Sha-65, Ges-97, Grz-04, Had-89, Bar-04, Bar-05]. Table 8.2-I (see appendix) summarizes the relevant literature and the main results obtained by these researchers. Appropriate findings for this work are the following. Anatase is in most instances stabilized by impurity ions such as Cl^- or SO_4^{2-} etc., which result from the process conditions during TiO_2 preparation. Several researchers on the one hand concluded that impurity ions such as Li^+ or Cu^{2+}, which are incorporated into the TiO_2 lattice by substituting for Ti^{4+} and generating oxygen vacancies, promote the anatase-rutile phase transition. On the other hand, it is deduced that impurities, which are adsorbed at the anatase surface such as phosphates and sulphates strongly inhibit the anatase-rutile transition owing to a reduction of ion mobility at the anatase particle surfaces [Cri-83, Sha-65].

If the thermo-physical properties of the anatase titanium raw material influence the phase transition and the sintering behaviour, it can be assumed that these properties may affect the PTCR-characteristic as well due to modifications in the barium titanate formation mechanism and the sintering behaviour of the PTCR-material.

2.2. Barium titanate based PTCR-ceramics

Oxide semiconductors exhibiting a positive temperature coefficient of resistance (PTCR) are mainly based on modified barium titanate compositions. Such materials were primarily investigated in the 1950´s [Kul-81, Huy-95]. Today they are mass products counted in several thousand tons per year [Hey-71, Kul-81, Was-94, Huy-95]. The commercial fabrication strategy and technology is

reviewed in section 2.2.1 followed by a detailed discussion on the research activities related to the solid-state synthesis of barium titanate (section 2.2.2).

Barium titanate based PTCR-ceramics enable various applications for example in overload protection, as heating elements, temperature sensors or simple thermostatic switches [Feu-82]. In section 2.2.3 the theoretical basics of the PTCR-effect are discussed followed by a defect chemical interpretation of the theory (section 2.2.4). Finally, relevant process related parameters and their effects on the PTCR-characteristic are reviewed in section 2.2.5.

2.2.1. PTC thermistor fabrication

Commonly $BaTiO_3$ based PTCR-materials are produced on large scale using a modified solid-state synthesis route [Mou-03, Feu-82, Was-94]. This synthesis strategy has well been investigated since the 1960´s [Sau-60, Hey-65, Ueo-74/1, Kul-81, Bla-93/1, Lac-95, Huy-95] and is still the most cost effective large-scale process although new chemical synthesis strategies have been investigated such as hydrothermal synthesis or oxalate route [Mou-03, Pit-05].

The PTC thermistor manufacturing process contains the following main steps [Ueo-74/1, Feu-82, Bla-93/1, Was-94].

- Material synthesis
- Refining
- Shaping
- Sintering
- Metallization

In the production of PTC thermistors material synthesis starts with weighing in of the raw materials according to the composition by using an electronic balance followed by intensive wet homogenization e.g. in an agitator ball mill. Typical raw materials are Ba-, Ca-, Sr- and/or Pb-carbonates and high purity rutile TiO_2 as well as doping additives such as La, Dy and Nb added as solution of e.g. chlorides or acetates in concentrations between 0.1 and 1.0at.-%. Frequently a few mol-% of a glass forming sintering aid is added to the compositions to improve liquid phase sintering. [Ueo-74/1, Feu-82, Was-94]. Subsequently the homogenized mixture is dried either by predrying the slurry in a filter press and final drying the filter cake in a continuous drier or alternatively by spray drying the slurry [Phe-05, EIP-07/2]. The latter offers the advantage that the dried mixture can directly be placed in a calcination sagger without previously crushing the dried filter cake. Finally, material synthesis, mostly performed in a continuous electrical kiln, is finished by means of a calcination step at temperatures above 1000°C in air [Phe-05, EIP-07/3]. During this step, the semiconducting barium titanate is formed (see section 2.2.2).

After calcination, the barium titanate powder is refined in order to prepare the material for shaping. At this juncture the calcined powder is again dispersed in deionised water and wet milled in an agitator ball mill to grain sizes around a few micron. Subsequently the slurry is typically granulated by spray drying [Ueo-74/1, Feu-82, Was-94, EIP-07/2].

Commonly the shaping process is performed using an axial moulding press to compact disc-shaped green parts in various dimensions (dry pressing). Alternatively e.g. for PTCR exhibiting surface mounted devices (SMD), which
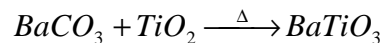
were prepared in multilayer technology, a tape casting process is used [Phe-05, EIP-07/2].

No doubt sintering of the green parts is the key process, which has to be accurately controlled. Sintering usually takes place at temperatures between 1200°C and 1400°C in air. The green parts are stacked, assembled in a sagger and sintered in batch furnaces or continuous kilns. Depending on the material composition and the application requirements the sintering regime has to be adjusted, i.e. the requirements have to comply with debindering period, sintering temperature and dwell time as well as the cooling rate [Ueo-74/1, Lac-95, EIP-07/2].
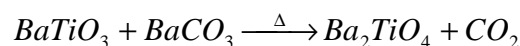
Finally, the sintered parts are metalised e.g. by applying a chromium-nickel sputter layer and screen printing silver electrodes. Then electrodes are soldered on the metalised parts [Was-94, Mou-03, Phe-05, Gre-05]. Some applications require an additional encapsulation with epoxy resins [Was-94].

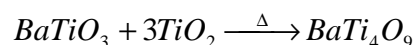## 2.2.2. The solid-state synthesis of barium titanate

As introduced above the solid-state synthesis process is commonly used for the production of PTCR-ceramics [Mou-03, Feu-82, Was-94]. Since PTC-devices have become a mass product extensive research on the synthesis processes of $BaTiO_3$ especially the solid-state route has been performed for the last 60 years [Spi-61, Kub-67, Suy-75/1, Suy-75/2, Yam-76, Suy-77, Nom-78, Bea-83/1, Bea-83/2, Mut-84, Nie-90, Tsu-01, Hen-01/1, Bus-05, Ryu-07, Sim-07, Kob-08]. The first systematic investigation on this subject was published by Spieß [Spi-61]. He studied the effects of grain size, molar composition and crystallographic modification on the solid-state formation of barium metatitanate by analyzing the CO_2 evolution as a function of temperature and time. Spieß concluded that the reaction rate is influenced by increasing the specific surface area of the raw materials. Moreover he discovered that depending on the molar composition of the initial mixtures besides $BaTiO_3$ (Equation 2.2-I) titanium- and barium-rich secondary phases are formed in variable concentrations (Equation 2.2-II and Equation 2.2-III). Concerning the TiO_2 modifications, he observed that when using anatase the reaction rate is slowed down and shifted to higher temperatures and also the secondary phase formation is enhanced. In addition, this author firstly described the reaction mechanism in the following way. The solid-state reaction between $BaCO_3$ and TiO_2 proceeds in two main steps. Initially barium titanate is formed in a contact reaction catalyzed by the titanium dioxide i.e. depending on the TiO_2 reactivity (Equation 2.2-I) followed by a diffusion reaction through the initially formed $BaTiO_3$ [Spi-61].

$$BaCO_3 + TiO_2 \xrightarrow{\Delta} BaTiO_3$$

Equation 2.2-I

$$BaTiO_3 + BaCO_3 \xrightarrow{\Delta} Ba_2TiO_4 + CO_2$$

Equation 2.2-II

$$BaTiO_3 + 3TiO_2 \xrightarrow{\Delta} BaTi_4O_9$$

Equation 2.2-III

2. Theoretical background

In relation to this early work, it must be critically noted that the used titanium dioxide raw materials showed significant differences in grain size distribution (GSD) ranging between 0.5 and 20µm for anatase and 0.3 to 2µm for the rutile material respectively. However, this discrepancy is not discussed by the author [Spi-61].

Kubo et al. [Kub-67] modelled the solid-state mechanism between $BaCO_3$ and rutile TiO_2 (average grain size ~2µm) in more detail by using high temperature X-ray diffraction. These authors agree to a large extend with the mechanism described by Spieß but contrary to the latter this group detected the secondary phase Ba_2TiO_4 despite using the rutile modification. Kubo et al. attributed this observation to the formation mechanism, which they depicted in the following manner. Initially a thin layer of $BaTiO_3$ is formed at the TiO_2 grain surfaces (Equation 2.2-I). Depending on the grain size of TiO_2 this layer is not detectable due to its very low volume concentration compared to the residual mixture. Further, a noticeable amount Ba_2TiO_4 is formed at the $BaCO_3$-$BaTiO_3$ interfaces due to the relatively slower diffusion of barium through the $BaTiO_3$-layer (Equation 2.2-II). Simultaneously at the TiO_2 interface inside the grains, $BaTiO_3$ is formed following Equation 2.2-IV.

$$Ba_2TiO_4 + TiO_2 \xrightarrow{\Delta} 2BaTiO_3$$
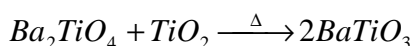
Equation 2.2-IV

Owing to the chemical equilibrium of reactions Equation 2.2-II and Equation 2.2-IV, the amount of barium metatitanate remains constant until the adjacent $BaCO_3$ is completely consumed. Subsequently all Ba_2TiO_4 decomposes into $BaTiO_3$ following Equation 2.2-IV. Additionally Kubo et al. expected that other titanium rich compositions e.g. barium tetratitanate only emerge if an adequate titanium dioxide excess is added [Kub-67].

Suyama and Kato [Suy-75/1, Suy-75/2, Suy-77] intensively studied the effect of TiO_2 grain size on the solid-state reaction with $BaCO_3$. These authors exclusively used TiO_2 raw materials (anatase and rutile, particle size <2µm) prepared from chloride process which they assumed to be more reactive compared to sulphate processed raw materials. Moreover, they concluded on the one hand that the particle size of the TiO_2 determines the reactivity of the material especially when it is smaller than 0.2µm. On the other hand, they observed no significant difference in reactivity and activation energy between the anatase and rutile TiO_2 modification [Suy-75/1, Suy-75/2, Suy-77].

Simultaneously Yamaguchi and co-workers [Yam-76, Nom-78] evaluated the effects of rutile TiO_2 powder properties (GSD <1µm, aggregates up to 100µm) on the solid-state synthesis of $BaTiO_3$. These researchers confirmed the proposed reaction mechanism published by Kubo et al. [Kub-67] and reviewed above. Additionally they ascribe the magnitude of secondary phase formation to the titanium dioxide degree of aggregation [Yam-76, Nom-78].

Around 1983 Beauger et al. [Bea-83/1, Bea-83/2, Mut-84] reinvestigated the solid-state synthesis of barium metatitanat in various atmospheres (air, CO_2 and vacuum). These authors used anatase TiO_2 with grain size of <0.4µm (BET 8-10m²/g). Generally, their results concerning the formation mechanism of $BaTiO_3$ in air were in conformity with the results presented by Kubo et al. [Kub-67] or Yamaguchi and co-workers [Yam-76]. Beauger et al. refined the mentioned

mechanism with their work by examining macroscopic reaction couples of the involved phase interfaces $BaCO_3$-TiO_2, $BaCO_3$-$BaTiO_3$ and Ba_2TiO_4-$BaTiO_3$ [Bea-83/2]. Their experiments confirmed that $BaTiO_3$ is formed at the expense of TiO_2 by diffusion of barium into the titanium dioxide. Additionally they supported the assumption that Ba_2TiO_4 is formed by a similar mechanism at the $BaCO_3$-$BaTiO_3$ interface. Lastly, these authors clarified the decomposition mechanism of Ba_2TiO_4 into $BaTiO_3$ and a barium-rich species, which finally reacts with the residual TiO_2 (Equation 2.2-IV) [Bea-83/2]. Niepce and Thomas [Nie-90] complemented these results by defect chemical aspects.

Tsutai and co workers [Tsu-01] further improved this mechanism by elucidating the expansion phenomenon during $BaTiO_3$ formation. They attributed this volume expansion to a modified formation mechanism due to a few coarse-grained $BaCO_3$ particles (grain sizes: $BaCO_3$ 0.3 to 31µm, TiO_2 <11µm). These $BaCO_3$ particles in contact with $BaTiO_3$ and Ba_2TiO_4 form a $BaCO_3$-BaO liquid phase around 950°C. Since this liquid phase does not completely wet the TiO_2 grains, it acts as barium source hence enhancing the $BaTiO_3$ formation in this temperature range. Consequently, the space wherein the coarse-grained $BaCO_3$ particles had been finally remained as free air space (pores). Simultaneously, the rearrangement of TiO_2 i.e. the $BaTiO_3$ formation owing to unidirectional diffusion of barium, resulted in the volume expansion [Tsu-01].

At the same time Hennings et al. [Hen-01/1] analyzed the effects of submicrometer ($d_{50} \sim 0.2$µm) raw materials on the solid-state synthesis. This group concluded that the grain size of the calcined powder is determined by the size of the TiO_2 starting powder and that by using fine grained $BaCO_3$ the secondary phase formation (Ba_2TiO_4) is suppressed [Hen-01/1]. Later Buscaglia [Bus-05, Bus-08] or Ryu [Ryu-07] verified these results by using nanocrystalline $BaCO_3$ and TiO_2 powders. In addition, the mechanical activation of the solid raw materials has intensively been studied for the last decade. Several researchers figured out that by mechanical activation of the raw material mixture the reaction rate of the synthesis can be increased and the reaction temperature can be decreased [Brz-00, Gom-00, Ber-01, Kon-02, Brz-03, Pav-08].

Contemporaneous to the fundamental investigations on the synthesis process and the reaction mechanism reviewed above, numerous kinetic studies on the solid-state synthesis using both anatase and rutile have been carried out [Car-61, Cou-79/1, Cou-79/2, Val-96/1, Val-96/2]. For example Cournil [Cou-79/1, Cou-79/2] and Valdevieso [Val-96/1, Val-96/2] described the kinetic effects of the gaseous atmosphere on the solid-state synthesis of $BaTiO_3$ revealing on the one hand that increasing carbon dioxide or nitrogen gas pressure decreases the reaction rate of the $BaTiO_3$ formation. On the other hand, they indicated that an elevated oxygen gas pressure enhances the reaction rate [Cou-79/1, Cou-79/2, Val-96/1, Val-96/2].

Summarizing the above mentioned studies it is evident that the reactivity of the TiO_2 material during $BaTiO_3$ formation is determined by the raw material properties, namely grain size distribution, specific surface area, pre-treatment of the raw material and the type and quantity of impurities, the latter primarily affecting the secondary phase formation during synthesis. Additionally the properties of $BaCO_3$ likewise seem to influence the reaction rate and further affect the secondary phase formation.

2. Theoretical background

Although such intensive work has been carried out on the solid-state synthesis using different TiO_2 raw materials, the effect of the crystallographic modification anatase and rutile is still not completely understood.

2.2.3. The PTCR-effect

Typical resistivity-temperature characteristics of donor doped $BaTiO_3$ ceramics are shaped as depicted schematically in Figure 2.2-I. Such graphs are sectioned into three temperature regions. First below the temperature at the minimum resistivity (ρmin), second the temperature range between minimum and maximum resistivity and third above the temperature of the maximum resistivity (ρmax). The former and the latter region show negative temperature coefficient of resistivity (NTCR) i.e. decreasing resistivity with increasing temperature, which is the natural progress of semiconducting ceramic materials. In between this temperature range, the material is characterised by a steep rise of the resistivity of several orders of magnitude [Huy-95, Was-94, Feu-82, Mou-03].
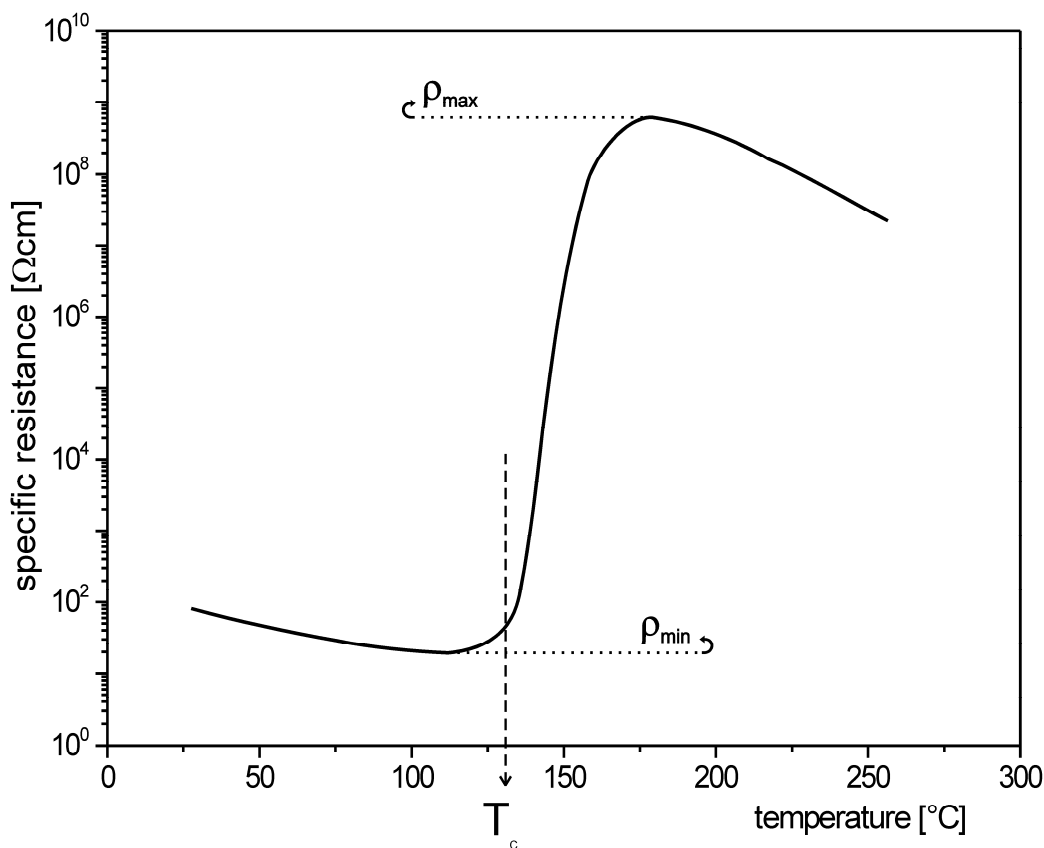

Figure 2.2-I: Schematically depicted resistivity-temperature characteristic of a PTC material

To comprehend the basics of the PTCR-effect the crystallographic configuration of the material has to be taken into account. Barium titanate at room temperature crystallises in tetragonal symmetry. Above approximately 120°C or rather above the Curie temperature (T_C) the material transforms to the cubic structure (Figure 2.2-II) [Hey-71, Dan-79, Huy-95, Mou-03]. Below T_C a spontaneous polarization is induced by the symmetry of the tetragonal crystal structure resulting in the formation of randomly oriented domains, which compensate the overall electric

dipole moment i.e. the material becomes ferroelectric. Above T_C the domain structure is broken up due to the higher symmetry of the cubic structure resulting in paraelectric behavior [Dan-79, Mou-03].
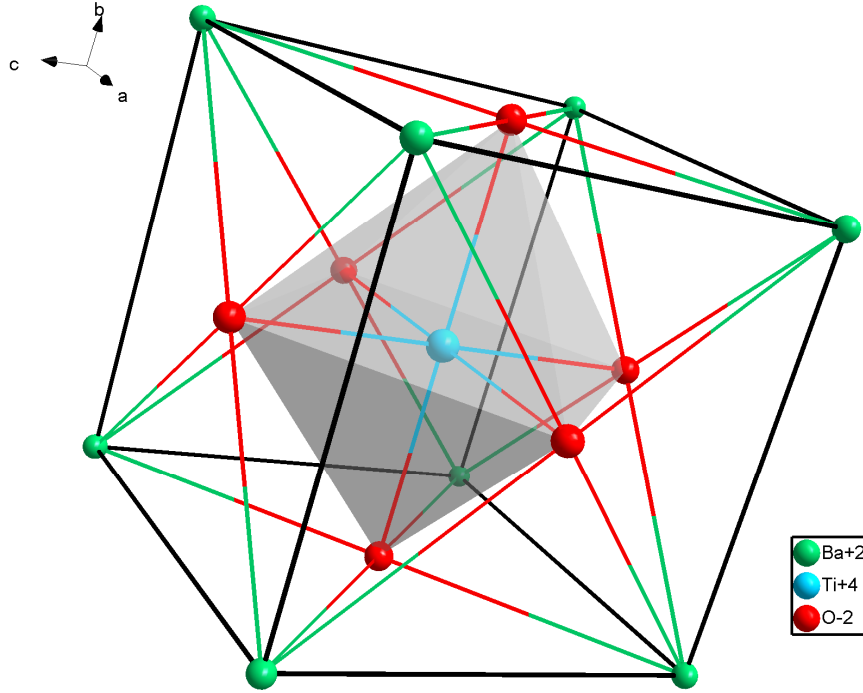

Figure 2.2-II: Crystal structure of cubic BaTiO$_3$ based on ICSD no.67518.

Early experimental observations showed that the PTCR only occurs in polycrystalline n-BaTiO$_3$ and depicted that the starting temperature of the resistivity jump correlates to the phase transition temperature T_C. Based on these observations Heywang [Hey-61] and Jonker [Jon-64] developed a widely accepted model to explain the resistivity temperature characteristic in n-BaTiO$_3$. While the Heywang model is suitable to describe the R-T behaviour above the Curie temperature (T_C), the Jonker model fits below T_C [Huy-95].

Heywang explained the PTCR-effect by assuming a two-dimensional layer of acceptor states at the grain boundaries (see Figure 2.2-III). Such acceptor states trap electrons from the n-conducting bulk generating a thin depletion layer w (Equation 2.2-V) which results in a potential barrier height Φ_w at the grain boundary (Equation 2.2-VI).

$$w = \frac{N_s}{2N_d}$$

Equation 2.2-V

$$\Phi_w = \frac{e^2 N_s^2}{8\varepsilon_0 \varepsilon_{gb} N_d}$$

Equation 2.2-VI

Where N_s represents the occupied acceptor state density, N_d the donor concentration in the bulk, e the electron charge, ε_0 and ε_{gb} the permittivity of

2. Theoretical background

vacuum and the grain boundary layer respectively [Hey-61, Jon-64, Huy-95, Wan-90]. Finally, the relation between the resistivity R and the potential barrier can be expressed by Equation 2.2-VII.

$$R = R_0 \exp\left(\frac{\Phi_w}{kT}\right)$$

<div align="right">**Equation 2.2-VII**</div>

In which k is the Boltzmann constant and R_0 denotes a constant, which is mainly temperature independent and includes some bulk properties [Hey-61, Jon-64, Huy-95, Wan-90]. From above equations and Figure 2.2-III the PTC-jump above the Curie point can easily be explained. According to Equation 2.2-VI the potential barrier height is inversely proportional to the permittivity. Above T_C the permittivity rapidly decreases with ascending temperature following the Curie-Weiss law and consequently the potential barrier increases. For that reason the resistivity raises dramatically due to the exponential relation with the potential barrier (Equation 2.2-VII) [Dan-79, Huy-95].
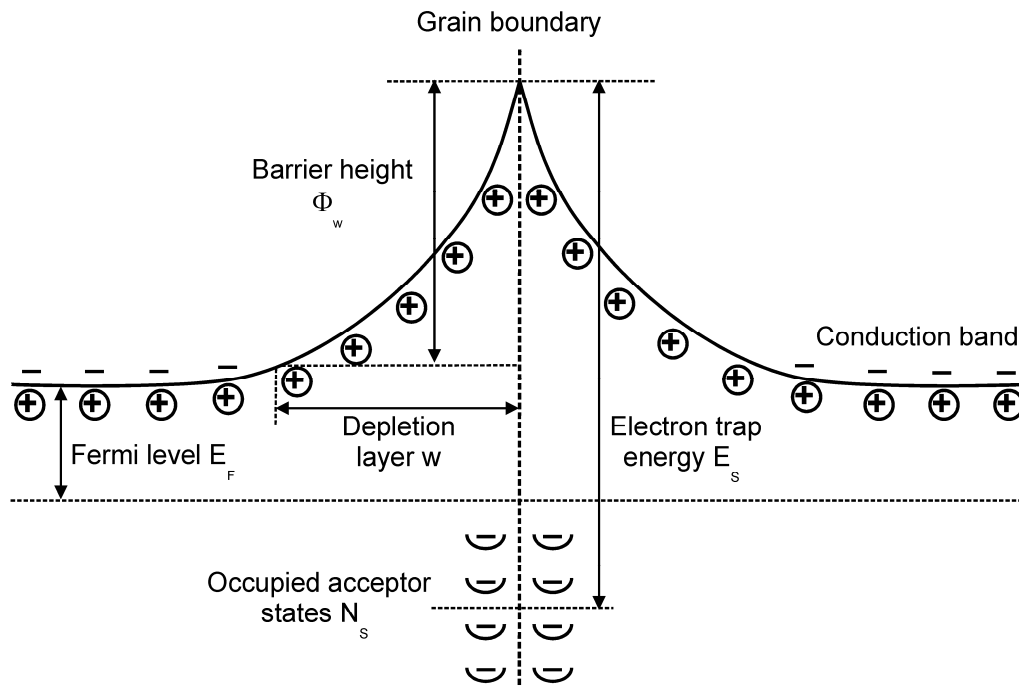

Figure 2.2-III: Schematically drawn potential barrier at a grain boundary representing the conditions at Curie temperature (redrawn after [Jon-64, Mou-03]).

Later Jonker [Jon-64] modelled the R-T characteristic below T_C since the Heywang model is not able to interpret the low resistivity values in this region. Jonker attributed this behaviour to the ferroelectric properties of $BaTiO_3$. As already mentioned, spontaneous polarization occurs below the cubic to tetragonal transition temperature thereby generating randomly oriented domains. Due to the different orientations a net surface charge at each grain surface is generated which accounts for the compensation of the depletion layer and gives rise to the disappearance of the grain boundary resistance [Jon-64, Huy-95, Mou-03].

Although alternative theories to explain the PTCR-effect have been reported for example by Lewis et al. [Lew-85, Lew-86] or Kutty and co-workers [Kut-85, Kut-

86], these models were less able to elucidate the origin of the PTCR entirely. Already Daniels et al. [Dan-79] discovered some open questions concerning the model proposed by Heywang and Jonker. These researchers firstly attributed the PTCR-effect to the defect chemistry in BaTiO$_3$, which is discussed in the following section.

2.2.4. Relation between defect chemistry and PTCR-characteristics

The defect chemistry in barium titanate seems to be a suitable extension to interpret the PTCR in BaTiO$_3$. Daniels and co-workers [Dan-76, Dan-76/2, Hen-76, Wer-76, Dan-76/3, Dan-79] studied the electrical conductivity of doped barium titanate as a function of the oxygen partial pressure at temperatures above 1000°C. Consequently, they investigated the defect chemistry at elevated temperatures and the kinetics of the equilibration during cooling. As a result Daniels et al. were able to answer the remaining questions concerning the nature of the acceptor states proposed by Heywang`s model and the effect of process conditions on the PTCR. Based on their investigations they detected the following mechanism [Dan-76/3, Dan-79]. Firstly, they suggested that the relevant defects in n-BaTiO$_3$ are barium and oxygen vacancies according to the simplified equilibrium conditions presented in Equation 2.2-VIII [Dan-76].

$$n + [V_{Ba}^{'}] + 2 \cdot [V_{Ba}^{''}] = p + [V_{O}^{\bullet}] + 2 \cdot [V_{O}^{\bullet\bullet}] + [D^{\bullet}]$$

<div align="right">**Equation 2.2-VIII**</div>

With n and p representing the electron and hole concentration respectively. The concentration terms illustrate the vacancy (V) defects inside the kation sublattice (X) and the anion sublattice (Y) having negative (') and positive ($^\bullet$) charge respectively [Krö-56]. Finally, D denotes the donor dopant concentration (e.g. lanthanum or niobium) added to the material.

At elevated temperatures during sintering (>1220°C in air) equilibration is adjusted between the material and the surrounding atmosphere. When cooled down the barium vacancy concentration at the grain boundaries is raised giving rise to a diffusion of barium vacancies from the grain boundaries into the bulk due to equilibration [Dan-76]. Chemically this leads to the disappearance of secondary phase and the formation of BaTiO$_3$. Owing to the decelerating diffusion rate with decreasing temperature the barium vacancy diffusion is frozen in at a defined temperature (<1220°C in air), which depends on the oxygen partial pressure. At this point it should be noted that in addition to the barium vacancies, available oxygen vacancies are assumed to remain highly mobile below temperatures at which barium vacancy diffusion has already stopped [Dan-76/3, Dan-79]. Thus, at room temperature, the material divides into a thin grain boundary layer (GBL) containing a high barium vacancy concentration, which generates low conductivity and the residual bulk is remaining highly conductive due to the lower barium vacancy concentration (Figure 2.2-IV). Accordingly, the barium vacancies act as electron traps compensating for the donors hence creating the potential barrier at the grain boundaries [Dan-76/3, Dan-79, Huy-95].
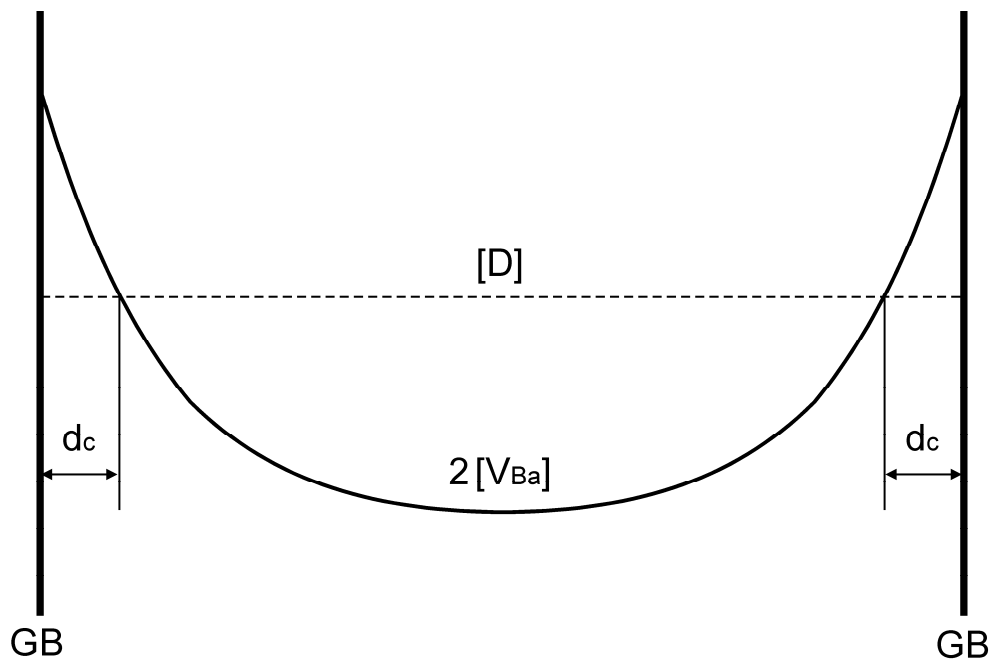
2. Theoretical background

Figure 2.2-IV: barium vacancy and donor concentration profile inside a donor doped BaTiO$_3$ bulk grain (redrawn after [Dan-79])

Daniels et al. claimed that the barium vacancy diffusion is very slow and therefore can be neglected at lower temperatures [Dan-76/3]. Several authors e.g. Igarashi et al. [Iga-81] or Kuwabara [Kuw-84] investigated the PTCR-characteristic by annealing the material in reducing atmospheres (e.g. vacuum, CH$_4$ or CO) at moderate temperatures and short times to prove the thesis made by Daniels et al. Other experiments for example carried out by Jonker [Jon-67] attempted to illustrate that adsorbed oxygen or rather adsorbed gases give rise to the dependence of the PTCR-effect on the atmosphere. All mentioned researchers yielded the result that applying heat treatments in reducing atmospheres significantly decreases the PTCR-jump. Additionally Alles [All-89] and Takahashi [Tak-90] performed experiments using undoped, oxygen-deficient BaTiO$_3$. Annealing in an appropriate atmosphere such as fluorine or oxygen resulted in barium titanate materials showing PTCR-jumps of up to six orders of magnitude. According to the mentioned results and the low mobility of barium vacancies as characterized by Daniels at al. it is concluded that barium vacancies as well as adsorbed gases can act as acceptor states (electron traps) in n-BaTiO$_3$ [Dan-76/3, Jon-67, Iga-81, Kuw-84, All-89, Tak-90]. Simultaneously Koschek and co-workers [Kos-85, Kos-89] experimentally investigated the grain boundary characteristic by applying cathode luminescence (CL). According to the measurements, Koschek correlated the CL-properties of the GBL to doubly ionized barium vacancies (V$_{Ba}^{''}$) which were predicted to emerge during cooling and represent the compensating defects in PTCR-BaTiO$_3$ at room temperature. With their CL-measurements, these researchers were also able to verify that the GBL width varies significantly with sintering time and cooling rate [Kos-85, Kos-89].

Contrarily Lewis and co-workers [Lew-85, Lew-86] proposed another mechanism to explain the nature of acceptor states in PTCR-BaTiO$_3$ by defect chemical calculations. Due to energetic disadvantages induced by immobile titanium vacancies, which they revealed to be the major compensating defects in donor-doped BaTiO$_3$, these authors predicted acceptor segregation (impurity and/or

doped) at the grain boundaries for low charge states. Such acceptors are compensated by highly mobile oxygen vacancies at low oxygen partial pressures or higher temperatures respectively. During oxidative cooling or with increasing oxygen partial pressure the oxygen vacancies are filled up and compensation of the acceptor states is achieved by holes. Hence, an insulating space charge layer is formed around the donor grains resulting in the barrier layer responsible for the PTCR-effect [Lew-85, Lew-86]. Later Chan et al. [Cha-86] as well as Makovec and co-workers [Mak-00] verified the defect model proposed by Lewis experimentally.

Miki et al. [Mik-98] related their Electron Paramagnetic Resonance (EPR) measurements to the PTCR-effect in donor and acceptor codoped samples by assuming associated defect centers of manganese with oxygen vacancies as well as cation-oxygen vacancy centers. According to their observations, these authors explained the relation between the steep PTCR-effect observed in Mn-codoped n-$BaTiO_3$ and the EPR-data in terms of a trap activation of Mn-V_O defect centers due to the tetragonal to cubic phase transition. Consequently, Miki et al. concluded that the strongly increased PTCR-effect in acceptor-codoped n-$BaTiO_3$ could not only be attributed to the spontaneous polarization mechanism proposed by Jonker [Jon-64] but also to the trap activation generated by the phase transition [Mik-98]. However based on EPR measurements these researchers concluded that most probably barium vacancies or rather V_{Ba}-V_O defect centers represent the main defects in n-$BaTiO_3$ [Jid-96].

The defect chemistry of oxides under equilibrium and frozen-in conditions are universally calculated by Sasaki and Maier [Sas-99, Sas-99/2] for undoped and doped materials respectively. With their systematical calculations, they were able to predict defect concentrations in equilibrium and the major defects present at temperatures below equilibration as well as the dominating trapping mechanisms as a function of temperature and oxygen partial pressure. Relevant findings applicable for donor and acceptor codoped $BaTiO_3$ are in the first place that at high temperatures i.e. in complete equilibrium only the major dopant dominates the defect concentration and minor dopants are negligible. Secondly at temperatures below equilibration that is to say at partially frozen-in states, redox-active (deep level) acceptor dopants strongly affect the defect concentration although they are present in minor concentration. Both dopant effects finally give rise to the p_{O2} dependence in partially frozen-in state, which is shifted to higher values and increased in range [Sas-99]. Since the PTCR-effect is explained by means of the defect chemistry, which is frozen-in during cooling as published by Daniels et al. [Dan-79], the findings of Sasaki and Maier are helpful to understand and interpret the results obtained in this work. Therefore the calculated defect concentrations of a major donor and minor acceptor codoped material are depicted in Figure 2.2-V and Figure 2.2-VI, which also represent the PTCR-materials investigated in this work consisting of Y-donor and Mn-acceptor codoped $(Ba,Ca)TiO_3$.
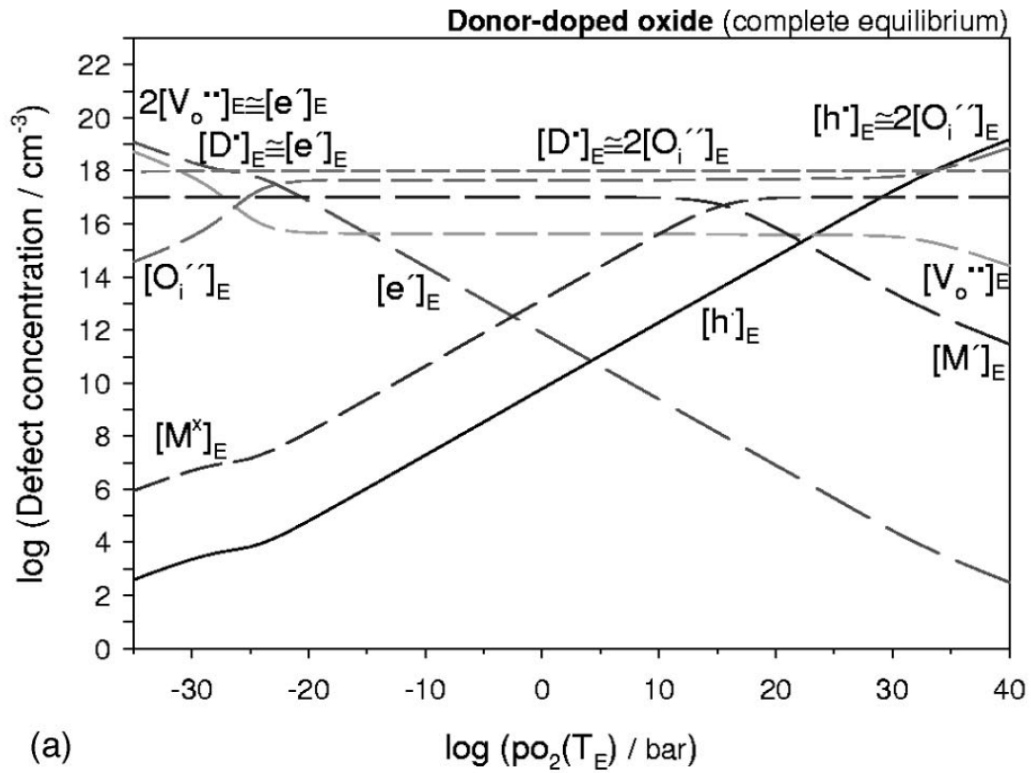
2. Theoretical background

Figure 2.2-V: Brouwer or Kröger-Vink diagram showing the calculated defect concentrations of a major donor and minor acceptor codoped oxide at equilibrium temperature (800°C) [Sas-99].
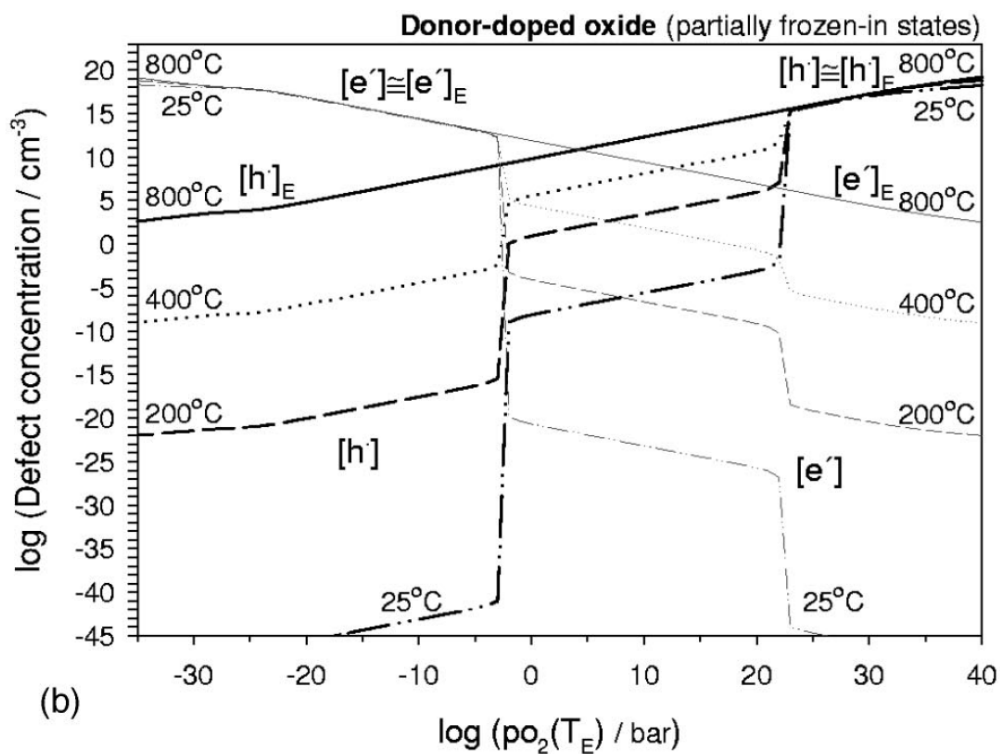

Figure 2.2-VI: Brouwer or Kröger-Vink diagram showing the calculated defect concentrations of a major donor and minor acceptor codoped oxide at partially frozen-in temperatures (<800°C) [Sas-99].

2. Theoretical background

The general calculations by Sasaki and Maier [Sas-99, Sas-99/2] support the work made by Kim et al. [Kim-92]. These authors calculated the inversion temperature, which was firstly defined by Daniels et al. [Dan-76/3, Dan-79], of antimony doped PTCR-BaTiO$_3$ by the Finite Difference Method (FDM). They depicted the strong dependence of the width of the grain boundary layer (GBL) on the cooling rate and finally discovered that the inversion temperature depends on the donor dopant concentration. Their material showed an inversion temperature of 1160°C, which is 60°C below the one published by Daniels et al. [Kim-92].

As a final statement and reminder, it should be noted that it is still ambiguous whether barium or titanium vacancies are the main compensating defects in donor doped barium titanate. Furthermore, cation vacancies do not appear to be the exclusive compensating defects rather adsorbed gases or defect complexes can act as electron traps as well. Additionally it is worth noting that compositional effects regarding the A/B-ratio of the ceramic material must be taken into account when the defect chemistry is discussed.

2.2.5. Factors influencing the PTCR-characteristic

As already mentioned the PTCR is known to occur in n-conducting BaTiO$_3$ that can be obtained by doping the isolating BaTiO$_3$ with tri- or pentavalent ions, which substitute for barium and titanium respectively [Huy-95, Was-94, Feu-82, Mou-03]. According to this observation, intensive research was performed to elucidate the effects of rare earth doping on the PTCR in BaTiO$_3$. Such compositions always show a maximum conductivity and a minimum resistivity at characteristic doping concentrations, which is illustrated schematically in Figure 2.2-VII [Fuk-79, Pen-88, Ill-90, Bla-92, Hur-98, Qi-02]. This effect is commonly known as the anomaly of conductivity [Huy-95].
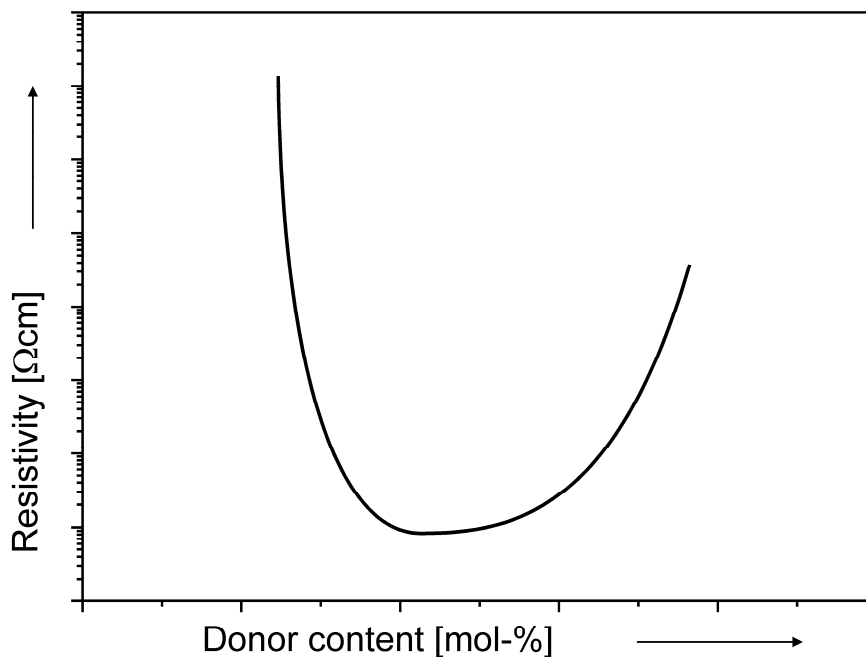

Figure 2.2-VII: Schematic diagram of the resistivity as a function of donor dopant content

2. Theoretical background

For example, Fukami et al. [Fuk-79], Blanchard and co-workers [Bla-92] as well as Hur et al. [Hur-98] investigated the effect of yttrium doping. All three observed the minimum resistivity for samples sintered at 1350°C in air between 0.2mol-% and 0.8mol-% yttrium doping content. An additional dependence on the sintering additive content is observed that resultes in a broadening of the yttrium content range in which the ceramic shows low resistivity [Fuk-79, Bla-92]. Other scientists such as Peng et al. [Pen-88], Urek [Ure-99] or Morrison [Mor-01] focussed on lanthanum doped BaTiO$_3$ ceramics and again others concentrated on niobium, antimony or holmium doping etc. [Ala-88, Ala-88/2, Ill-90, Gli-00, Qi-02, Par-09]. All mentioned researchers observed not only the dopant effect on the resistance characteristic but also an effect of dopant nature and concentration on the microstructure namely the anomaly of grain size. Especially Peng et al. [Pen-88] and Al-Allak et al. [Ala-88] firstly published this correlation, which is illustrated in Figure 2.2-VIII.
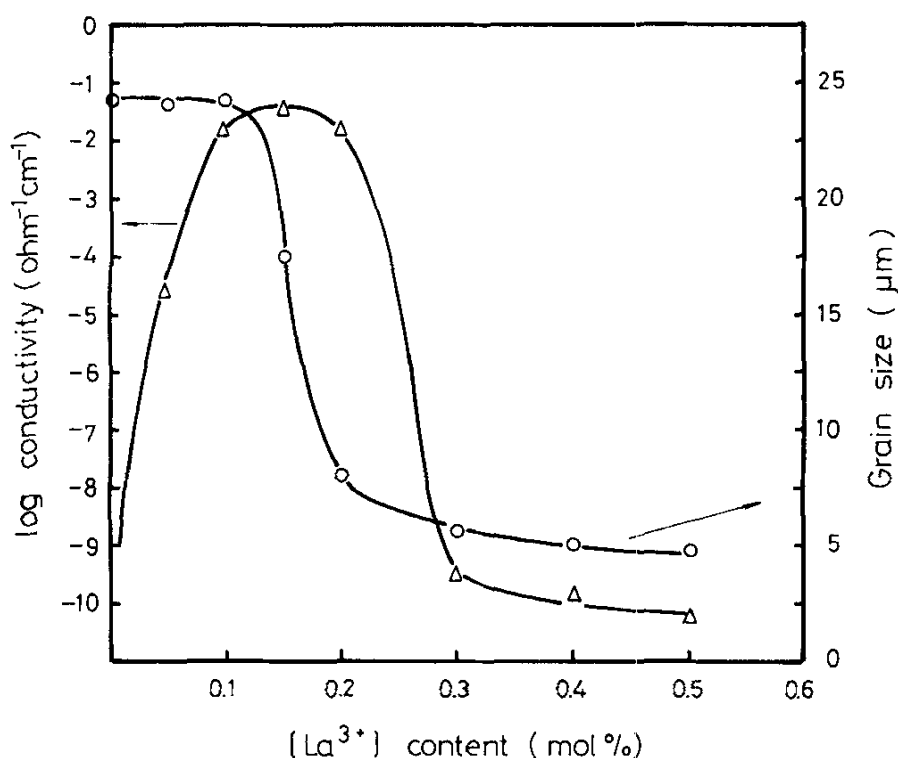
Figure 2.2-VIII: Correlation of the resistivity and the grain diameter as functions of the donor dopant content [Pen-88]

Additionally Drofenik et al. [Dro-82, Dro-84, Dro-86] experimentally determined the maximum dopant amount above which grain growth is inhibited and demonstrated the dependence of the critical donor concentration on the oxygen partial pressure as depicted in Figure 2.2-IX. Furthermore they always detected an oxygen release in samples showing anomalous grain growth which depends on the donor dopant concentration. Consequently, Drofenik et al. developed a model, which explains the relation between the anomaly of grain size and conductivity [Dro-87, Dro-90, Dro-93, Dro-99, Dro-02].
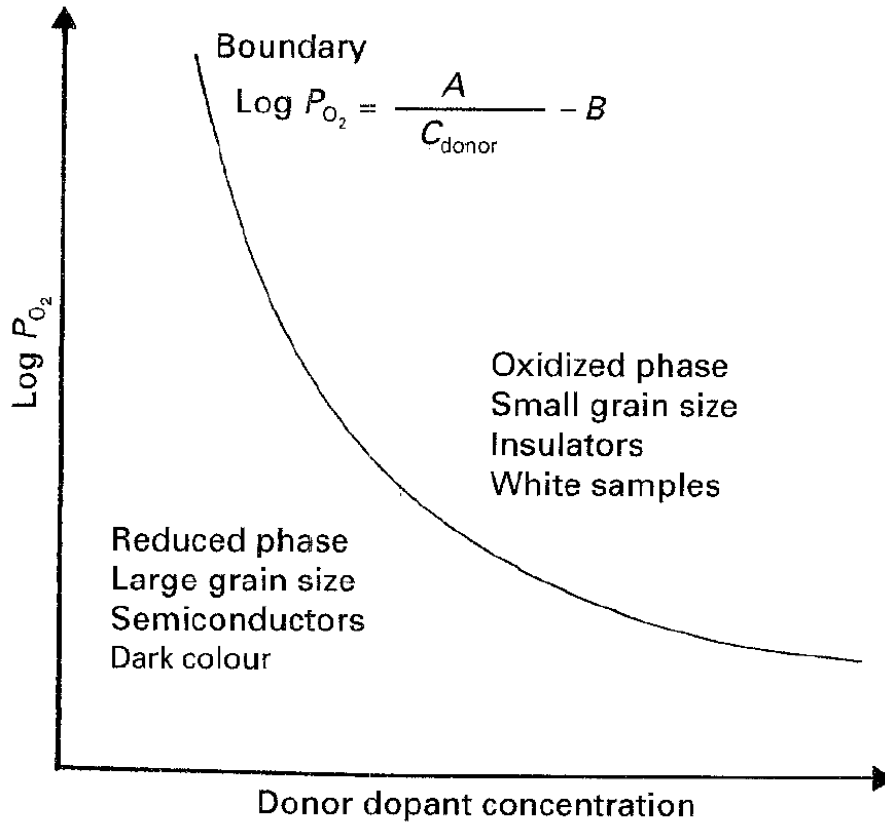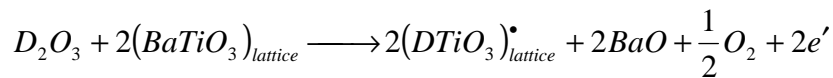
Figure 2.2-IX: The critical donor dopant level of the model proposed by Drofenik as a function of the oxygen partial pressure [Huy-95]

The thermodynamic model of Drofenik is based on the change in total free Gibbs energy (ΔG, see Equation 2.2-IX) needed for the incorporation of a donor ion (D) during grain growth process as exemplarily illustrated in Equation 2.2-X for barium substitution [Dro-87].

$$\Delta G = \Delta G_S + \Delta G_{SS} + \Delta G_{OX}$$

Equation 2.2-IX

$$D_2O_3 + 2(BaTiO_3)_{lattice} \longrightarrow 2(DTiO_3)^{\bullet}_{lattice} + 2BaO + \frac{1}{2}O_2 + 2e'$$

Equation 2.2-X

Where ΔG_S is the free surface energy change, ΔG_{SS} represents the energy change during solid solution formation between $BaTiO_3$ and a donor dopant. ΔG_{OX} illustrates the energy change induced by an oxygen release of the donor dopant.
In this context, it is worth to note a consequence of this model. In a composition that contains a compensating acceptor ion and a donor dopant, both substituting for the same lattice site, the grain growth process is independent from the donor concentration due to the disappearance of the oxygen release [Dro-86].
However, for the aim of this work the Drofenik model must be kept in mind especially when the microstructure or rather grain size is varied within equally composed samples.

2. Theoretical background

Another enhancing effect on the PTCR-jump is obtained by adding 3d-elements such as cobalt, iron or manganese [Huy-95]. With such elements the slope and height of the PTCR-jump is strongly improved [Ueo-74/1, Ueo-74/2, Kna-79, Ihr-81, Tin-90, Jia-02, Din-08/2, Xia-08]. Following Ueoka [Ueo-74/1, Ueo-74/2] who explained the effectiveness of manganese doping on the PTCR-jump, the effect of 3d acceptor dopants in general can be attributed to their behaviour during cooling. In the course of sintering the manganese ion is incorporated at titanium lattice sites and is compensated by oxygen vacancies. During cooling, the grain boundaries are oxidized and the oxygen vacancies diminish resulting in a change of the manganese oxidation state (Mn^{2+} to Mn^{3+} or Mn^{4+}). Consequently, these higher oxidation states react as electron traps as described in section 2.2.4 [Ueo-74/2]. Later Ting et al. [Tin-90] systematically investigated the improving effect of manganese on lanthanum doped barium titanate. These authors observed the minimum resistivity at net donor concentrations following Equation 2.2-XI and related it to the development of the microstructure (see Figure 2.2-X and Figure 2.2-XI). Accordingly, they verified the assumptions made by Ueoka [Ueo-74/2] in relation to the incorporation site and oxidation state as well as to the compensation mode during cooling [Tin-90].

$$\left[La^{3+}\right] - 2\left[Mn^{2+}\right] \sim 0.15 mol - \%$$
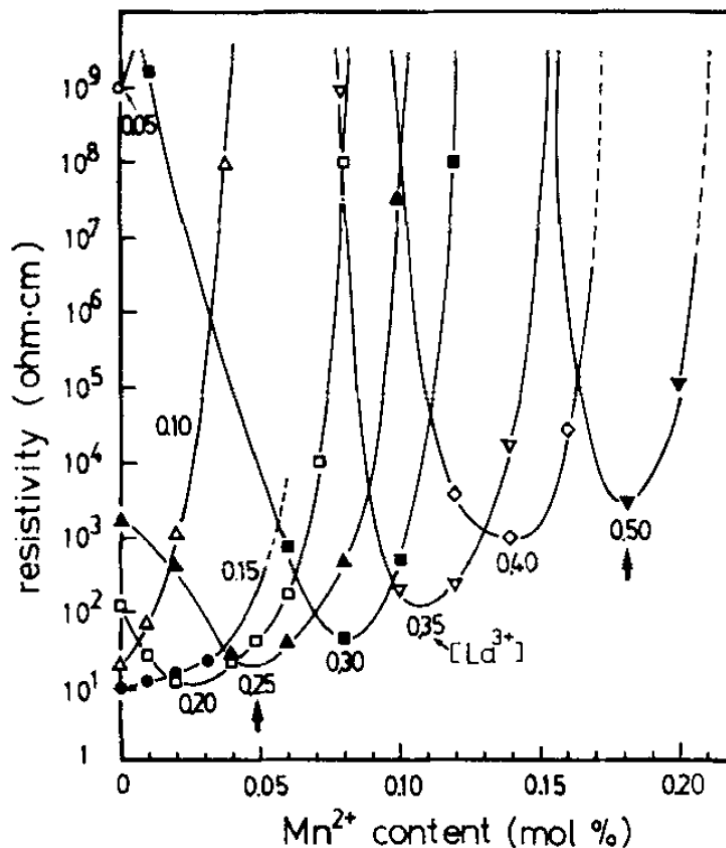
Equation 2.2-XI

Figure 2.2-X: Compensating effect of manganese doping on the room temperature resistivity [Tin-90]
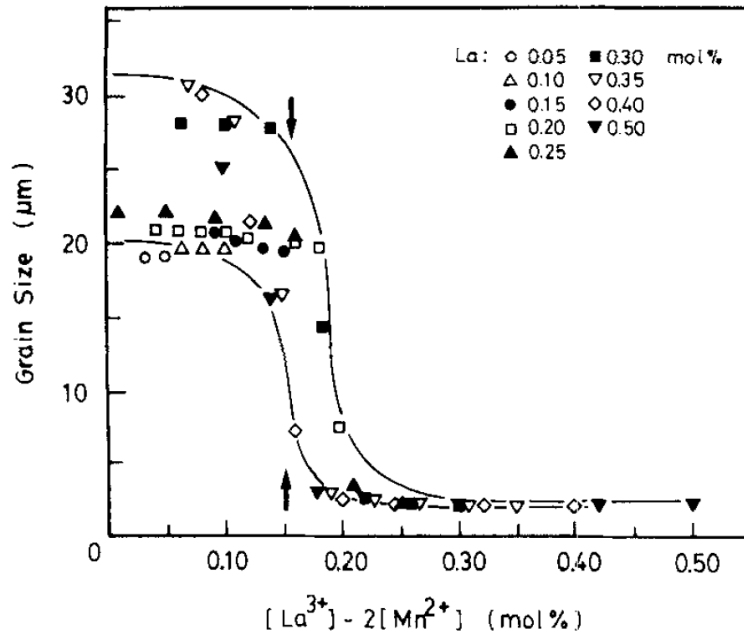
2. Theoretical background

Figure 2.2-XI: Microstructure evolution in La-Mn codoped BaTiO3 [Tin-90]

Furthermore sintering aids such as SiO_2, B_2O_3 or excess TiO_2, which simultaneously support liquid phase generation and influence dopant distribution, show an increasing effect on the PTCR-characteristic when added in suitable amounts [Fuk-79, Abi-91, Bla-92, Rav-92, Ho-94, Kut-98, Yoo-03, Jay-06, Erk-06, Zub-08/1, Zub-08/2]. As already mentioned in the beginning of this section, the addition of sintering aids cause a broadening of the low resistivity range that is generated by donor doping [Fuk-79, Bla-92]. In general, it can be summarized that sintering aids give rise to lower resistivity values at room temperature and vary the steepness of the PTCR-jump by shifting the temperature at which the maximum resistivity occurs. This effect can be attributed to secondary phase formation, which is provoked due to the chemical interaction between the bulk material composition i.e. the doped $BaTiO_3$ and the sintering aid [Kut-98, Yoo-03, Jay-06, Erk-06, Zub-08/1, Zub-08/2].

It has already been mentioned that Ti-excess i.e. an A/B-ratio <1 supports liquid phase sintering due to the formation of an eutectic melt, indicating that the A/B-ratio possibly affects the PTCR-characteristic too [Han-87, Lin-90, Bus-01, Jay-04, Sak-04, Nii-07, Lee-07/1]. Especially Lin et al. [Lin-90] and Jayanthi et al. [Jay-04] investigated the A/B-ratio effect on the PTCR characteristic. These researchers found that Ba-excess results in slightly reduced ρ_{min} (about $10^5 \Omega$cm) and enhanced ρ_{max} compared to the stoichiometric composition, which showed resistivity values about $10^6 \Omega$cm. Contrary Ti-excess strongly reduces the resistivity to values below $10^3 \Omega$cm [Lin-90].

As mentioned in section 2.2.3 the ferroelectric-paraelectric phase transition at TC in pure $BaTiO_3$ occurs around 120°C. This characteristic temperature can be shifted towards lower or higher temperatures by solid solution formation of barium titanate with strontium- or lead-titanate respectively. Whereas the formation of $(Ba,Ca)TiO_3$ solid solution is not accompanied by a shift in the Currie-temperature (T_C). Accordingly the PTCR-jump of $(Ba,Pb)TiO_3$ or $(Ba,Sr)TiO_3$ solid solutions varies between room temperature and 300°C [Hey-61, Hey-71, Feu-82, Was-94, Jo-09].

2. Theoretical background

In this context, it seems useful to complete this section regarding the compositional influences by presenting the relevant phase diagrams of the system investigated in this work. Based on the early investigations of Rase and Roy [Ras-55] the equilibrium phase relations in the BaO-TiO_2 system have been adapted by several authors [Obr-74, Neg-74, Kir-91, Lee-07/2, Zhu-10]. Lee et al. [Lee-07/2] published the latest modifications around $BaTiO_3$ depicted in Figure 2.2-XII. In contrast, Zhu et al. [Zhu-10] focussed on the TiO_2-rich region of the system and published latest results concerning the stability of $BaTi_2O_5$.

According to the compositions investigated in this work, the phase relations in the ternary system BaO-CaO-TiO_2 are of great interest too. The pseudo-binary system $BaTiO_3$-$CaTiO_3$ was investigated by DeVries and Roy [Dev-55] and is illustrated in Figure 2.2-XV. Moreover, Kwestroo and Paping [Kwe-59] determined the ternary system BaO-CaO-TiO_2, which is displayed in Figure 2.2-XIV.

However, phase diagrams, although they exclusively represent equilibrium states, are helpful on the one hand for the phase identification e.g. for the interpretation of X-ray diffraction data. On the other hand, they provide a useful basis for the interpretation of formation or sintering mechanisms (see section 4.2).
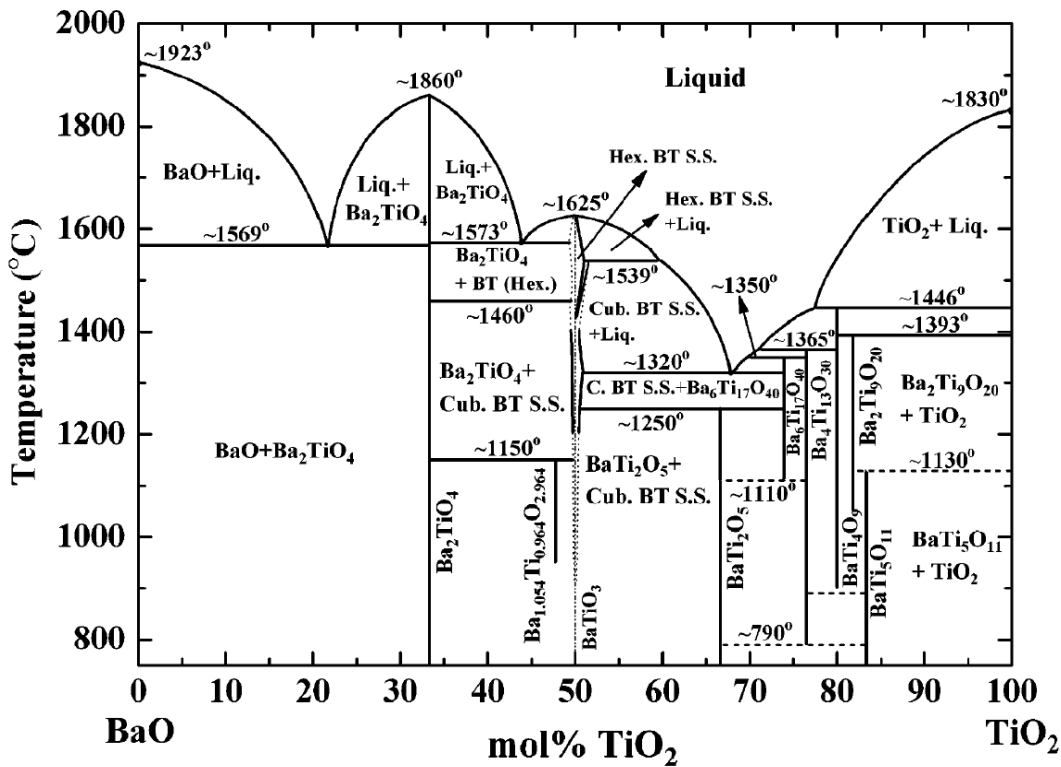
Figure 2.2-XII: Pseudo-binary phase diagram of the system BaO-TiO_2 [Lee-07/2]
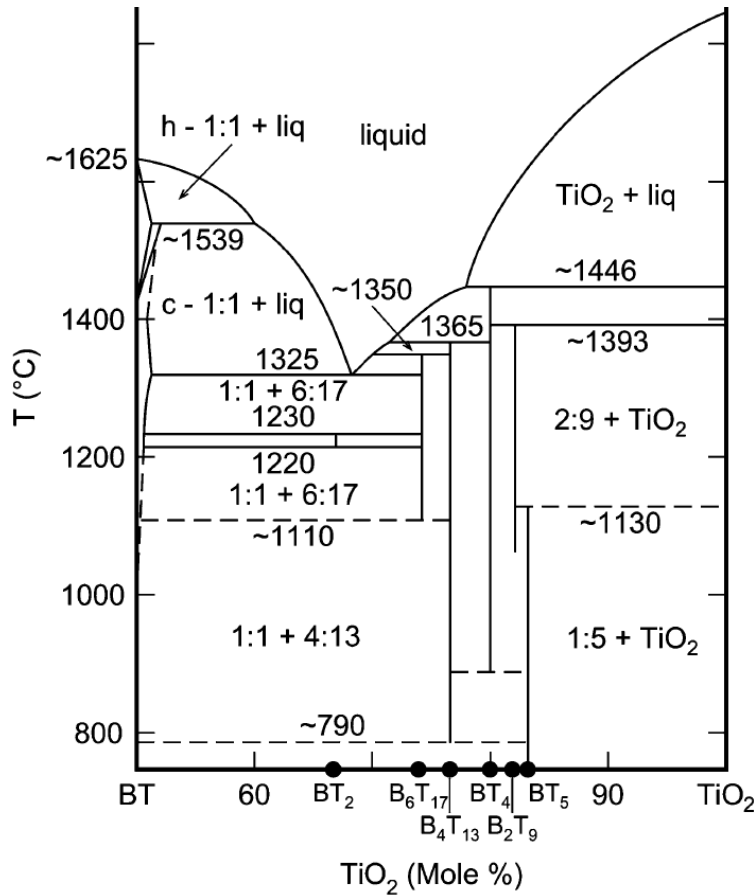
Figure 2.2-XIII: Phase relation in the TiO$_2$-rich region of the BaO-TiO$_2$ pseudo-binary system [Zhu-10]; composition abbreviations are summarised in appendix **Table 8.2-II**
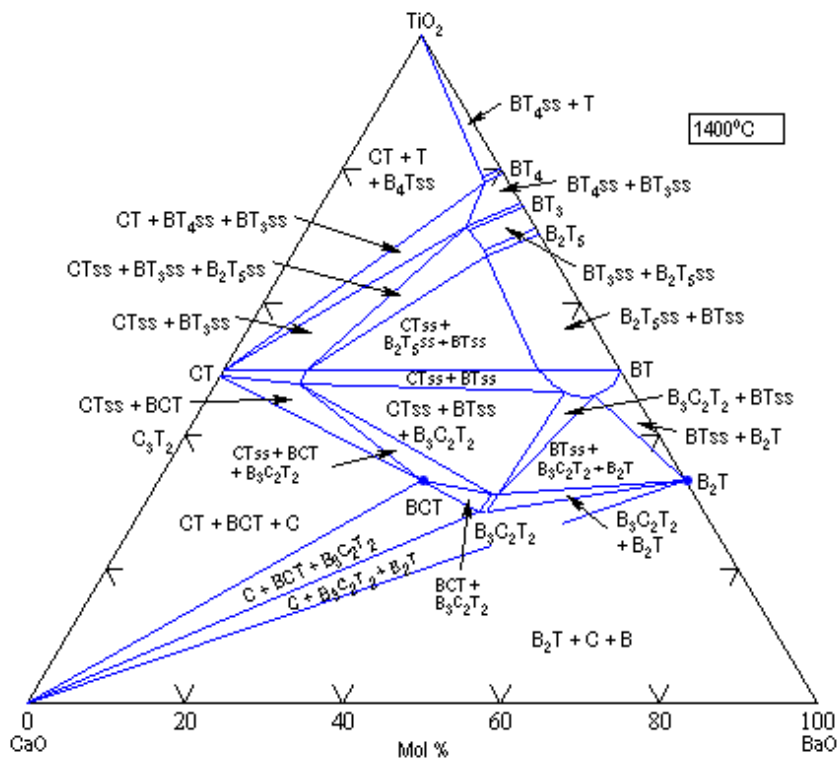

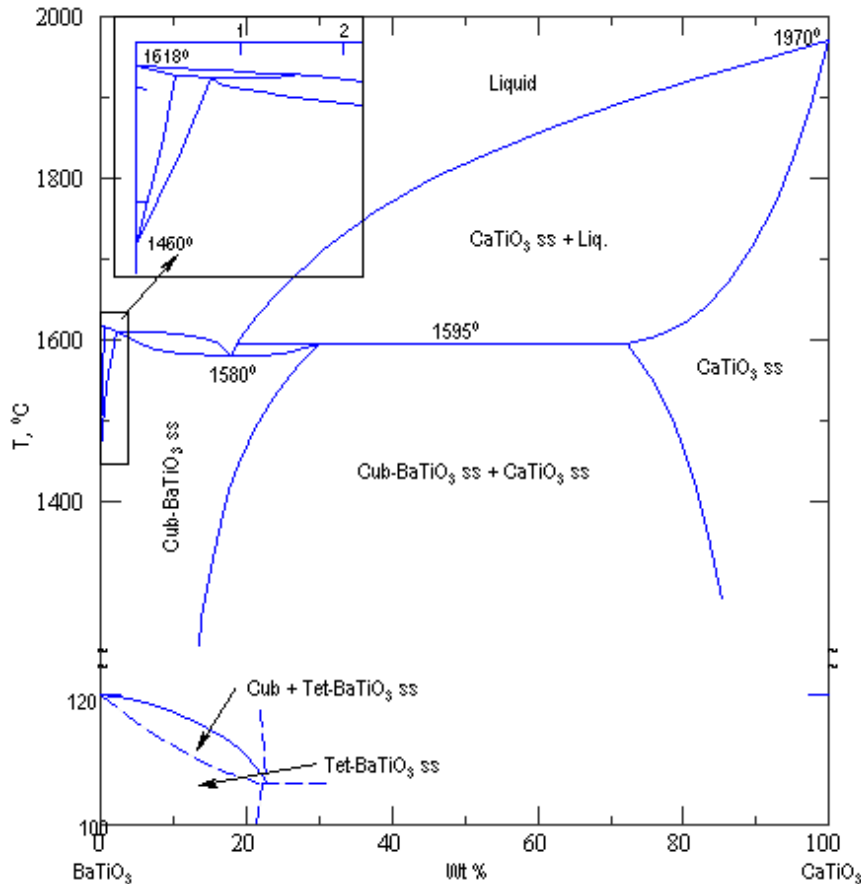**Figure 2.2-XIV:** Phase diagram of the ternary system BaO-CaO-TiO$_2$ at 1400°C [Kwe-59]

Figure 2.2-XV: Phase diagram of the pseudo-binary system $BaTiO_3$-$CaTiO_3$ [Dev-55]

Finally, process parameters such as sintering temperature, sintering atmosphere and cooling conditions have to be taken into account. Each influencing the formation of the potential barrier, which is located at the grain boundaries and originates the PTCR as discussed in detail in section 2.2.3. Therefore process conditions have to be carefully selected and controlled [Sau-60; Ueo-74/1, Bla-93/1, Bla-93/2, Kim-92, Huy-95, Lac-95, Bom-05]. Because of the process influences the sample preparation (section 3.3) is kept constant and followed by means of control measurements (section 3.4.1).

3. Experimental design and methods

This section deals with the experimental approach and the measurement methods used for this investigation. First, the experimental design and the material synthesis on laboratory scale are described and discrepancies between industrial scale and laboratory scale synthesis are identified. Starting with the raw material selection and characterization, continuing with the material synthesis and sample preparation process to the point of sintering and metallisation, the entire preparation process is specified. Further, the techniques for material characterisation are depicted and finally the measurement techniques for material and electrical characterisation are presented.

3.1. Raw material selection and characterisation

The carbonate raw materials used for material synthesis were high purity barium carbonate with an average grain size of 1.5µm and specific surface area of 1.8m²/g as well as calcium carbonate with an average grain size of 3.5µm and specific surface area of 2.5m²/g (SOLVAY BARIO E DERIVATI SpA). The main impurities in both carbonates are $SrCO_3$ with a maximum content of 0.17wt.-% and Na_2CO_3 with a maximum content of 0.03wt.-%. As donor dopant, yttrium was added (Treibacher Auermet Produktions GmbH) and manganese was selected as acceptor dopant (LACTAN Chemikalien und Laborgeräte Vertriebsgesellschaft m.b.H. & Co. KG). Both dopant materials were processed as acetate solutions.

As titanium source four different types of TiO_2 raw materials were used to study the effect of anatase in PTCR-materials: anatase no.1 (A-1), a commercially available material with specific surface area (BET) of 10.3m²/g, anatase no.2 (A-2) with specific surface area of 9.4m²/g, anatase-rutile mixture no.1 (A/R-1) containing about 89wt.-% anatase and 11wt.-% rutile and having a specific surface area of 14.3m²/g, and contrarily anatase-rutile mixture no.2 (A/R-2) containing about 9wt.-% anatase and 91wt.-% rutile with specific surface area of 10.2m²/g. Both anatase materials (A-1 and A-2) were manufactured by the sulphate process. The materials A/R-1 and A/R-2 were produced from chloride process. Finally, as a reference material, commercially available rutile (R-1) produced from sulphate process with a specific surface area of 6.1m²/g was used. Table 3.1-I summarises relevant properties and parameters of the TiO_2 raw materials mentioned.

Table 3.1-I: Properties of the titanium dioxide raw materials

	Labelling	A-1	A-2	R-1	A/R-1	A/R-2
General Information	Producer	Cerac Inc.	Kronos Intern. Inc.	Tronox Inc.	Tronox Inc.	Tronox Inc.
	Modification	Anatase	Anatase	Rutile	Anatase/ Rutile mixture	Rutile/ Anatase mixture
BET [m²/g]		9.38	10.31	6.06	14.25	10.17

3. Experimental design and methods

	Na	45.1	44.8	14.89	2.92	1.7
	Mg	14.22	3.8	2.86	n.d.	n.d.
	Al	53.05	18.56	12.38	0.27	0
Impurity content [ppm]♣	*P*	863.58	1019.16	42.37	35.02	30.3
	K	1261.2	1716.9	21.86	0	0
	Cl♦	n.d.	n.d.	n.d.	227	255
	Fe	6.14	4.58	6.22	7.52	4.5
	Zr	98.96	26.87	123.82	n.d.	n.d.
	Nb	111.59	101.08	79.47	2.22	3.11
Total [wt.-%]		0.245	0.294	0.03	0.027	0.029

It is evident from Table 3.1-I that both anatase materials prepared from sulphate process (A-1 and A-2) contain a higher amount of total impurities compared to the rutile reference (R-1). The main impurities in A-1 and A-2 are phosphor and potassium with an amount of approximately 0.3wt.-% in A-2 and 0.2wt.-% in A-1. In contrast, phosphor and potassium amounts less than 0.01wt.-% in both the rutile reference and the rutile-anatase mixture materials.

Figure 3.1-I to Figure 3.1-IV show the SEM micrographs of the raw material powders as received (untreated). It is obvious that the titanium powders independent of their crystallographic modification have spherical grain morphology whereas the carbonates show rather elongate grains. Additionally it can be seen that contrary to the rutile reference the anatase powders show increasing aggregation, which is consistent with the increased BET values shown in Table 3.1-I.
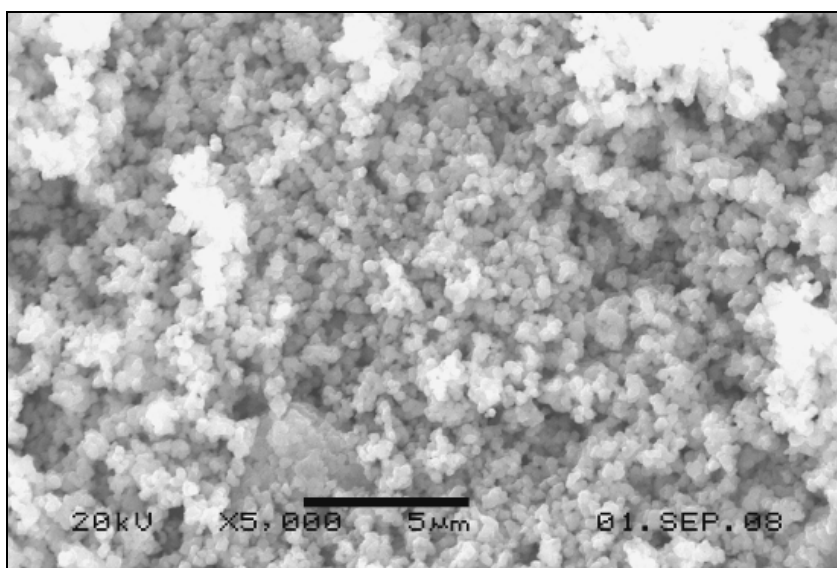
Figure 3.1-I: SEM micrograph of rutile TiO$_2$ R-1 (scale bar 5µm)

♣ Values measured using ICP-OES; see section 3.4.4
♦ Value measured by volumetric analysis (titration)

3. Experimental design and methods
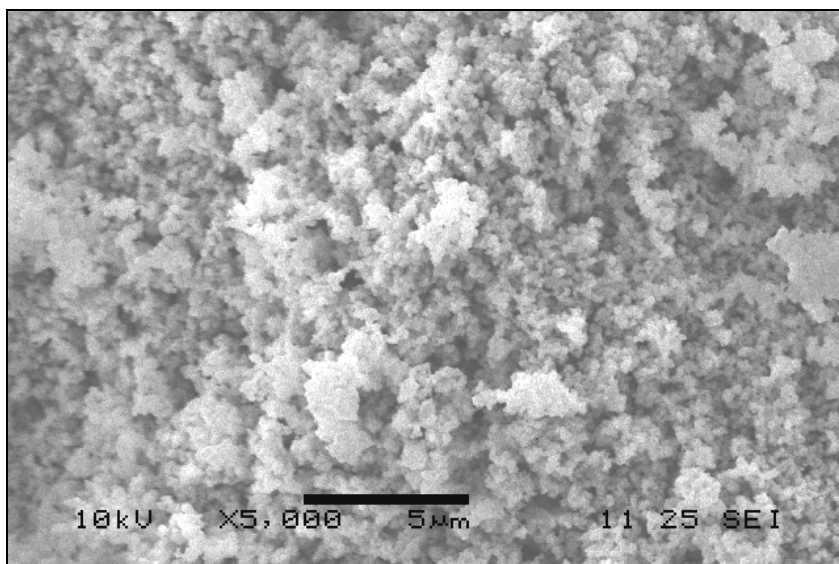
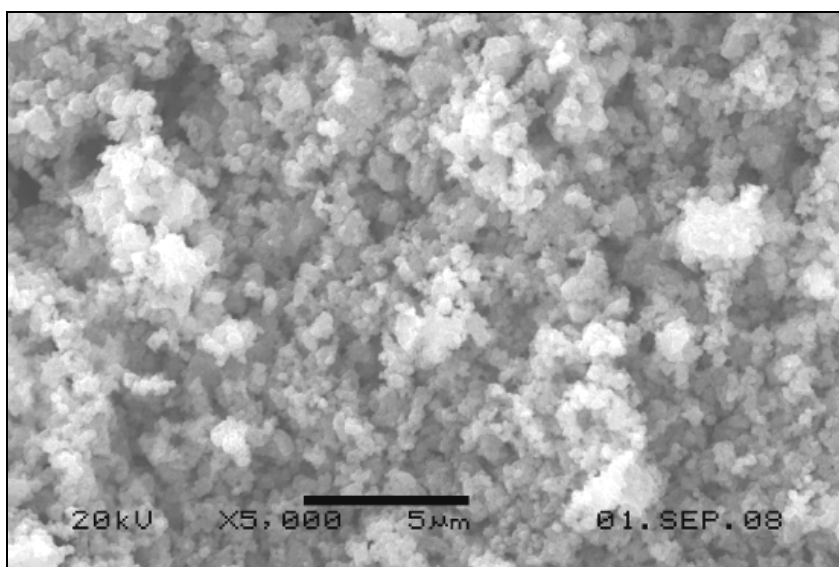**Figure 3.1-II:** SEM micrograph of anatase TiO_2 A-1 (scale bar 5µm)

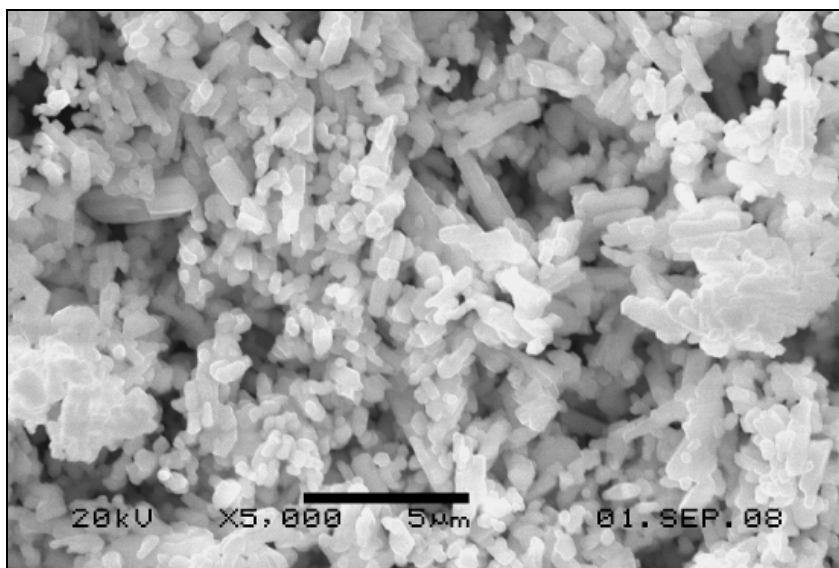**Figure 3.1-III:** SEM micrograph of anatase TiO_2 A-2 (scale bar 5µm)

Figure 3.1-IV: SEM of the $BaCO_3$ powder used (scale bar 5µm)

3.2. Experimental design

Two series of basic compositions (a and b) with varying titanium excess ranging from 0.002mol-% for series a to 0.015mol-% for series b were prepared from above listed raw materials. The amounts of dopants are set to a level of 0.25mol-% yttrium and 0.05mol-% manganese with respect to the barium content. In Table 3.2-I the compounds of series a and b are listed by molar compositions. Herein the A/B ratio denotes the theoretical relation between the A-side ions (Ba, Ca, Y) and the B-side ions (Ti, Mn) inside the $BaTiO_3$ (=ABO_3) lattice.
Furthermore, Table 3.2-II summarizes the molar compositions of the basic anatase experiments, which were performed to clarify the roles of the main impurities present in commercial anatase. The yttrium content was reduced in A-2c and enhanced in A-2d to 0.15 and 0.35mol-% respectively. In compositions A-2e and A-2f the silica amount has stepwise been decreased from 0.98mol-% to 0.74mol-%. The results of the experiments are described in section 4.

Table 3.2-I: Molar compositions of the basic experiment batches

Batch no.	TiO_2 labelling	Composition [mol-%]			Dopant		Additive	A/B ratio
		Ba	Ca	Ti	Y	Mn	SiO_2	
A-1a	A-1	41.79	7.43	49.49	0.25	0.05	0.99	0.998
A-2a	A-2	41.79	7.43	49.49	0.25	0.05	0.99	0.998
R-1a	R-1	41.79	7.43	49.49	0.25	0.05	0.99	0.998
A/R-1a	A/R-1	41.79	7.43	49.49	0.25	0.05	0.99	0.998
A/R-2a	A/R-2	41.79	7.43	49.49	0.25	0.05	0.99	0.998
A-1b	A-1	41.51	7.38	49.82	0.25	0.05	0.98	0.985
A-2b	A-2	41.51	7.38	49.82	0.25	0.05	0.98	0.985
R-1b	R-1	41.51	7.38	49.82	0.25	0.05	0.98	0.985
A/R-1b	A/R-1	41.51	7.38	49.82	0.25	0.05	0.98	0.985
A/R-2b	A/R-2	41.51	7.38	49.82	0.25	0.05	0.98	0.985

Table 3.2-II: Molar compositions of the anatase experiment batches

Batch no.	TiO_2 labelling	Composition [mol-%]			Dopant		Additive	A/B ratio
		Ba	Ca	Ti	Y	Mn	SiO_2	
A-2b	A-2	41.51	7.38	49.82	0.25	0.05	0.98	0.985
A-2c	A-2	41.56	7.39	49.87	0.15	0.05	0.98	0.983
A-2d	A-2	41.47	7.37	49.77	0.34	0.05	0.98	0.987
A-2e	A-2	41.57	7.39	49.88	0.25	0.05	0.86	0.985
A-2f	A-2	41.62	7.40	49.95	0.25	0.05	0.74	0.985

3.3. Sample preparation

The common industrial synthesis process has already been described in section 2.2.1. In order to prevent inaccurate interpretation, the laboratory-scale material synthesis of this work has been based on the industrial synthesis strategy. The batch size for basic compositions is set up to an amount of 5kg with respect to the

dried mixture. In this case, the raw materials are homogenized in deionised water using a ball mill with yttria-stabilized zirconia (YSZ) spheres of 3.0mm in diameter followed by drying at 90°C in a drying chamber for at least 48h. In this case the drying step somewhat differs from the industrial process where the homogenized mixture is spray dried, which is much more cost-effective on the large scale. In contrast, for much smaller batch sizes of 5kg prepared in laboratory-scale, spray drying becomes highly inaccurate due to material losses during the process owing to the dust, which is collected inside the cyclone. Supplementary a significant amount of metallic abrasion particles is generated resulting from the facing tile inside the spray dryer. Such impurities can act as additional doping elements.

After drying, the homogenized mixture is calcined in a batch furnace in air at a temperature of 1190°C. The calcined powder is then milled in deionised water, again by using a ball mill with YSZ spheres of 3.0mm, until a final grain size of 2.5 to 2.8µm (d_{50}) is obtained. The refined powder then is mixed with 3wt.-% of a cellulose binder mixture for spray drying. Subsequently the granulated material is compacted by means of an axial moulding press (DORST TPA-4) to pellets with a shape of 14.4mm in diameter and 3.15mm in height. The resulting green density of the compressed pellets amounts to 3.15g/cm³.Green parts finally are sintered in a batch furnace (CM Furnace Inc. Bloomfield N.J.) with inert zirconia sintering aids at a temperature of 1350°C, dwell time of 30min and a cooling rate of 5K/min.

For electrical characterisation, the sintered parts are metallized by first applying a chromium/nickel sputter layer and finally screen printing the sputtered parts with silver electrodes to prevent oxidation. The sputtering process has been done in the pilot sputter station Leibold-Heraeus Z400.

3.4. Material characterization

3.4.1. Process Control Parameter

Figure 3.4-I illustrates the preparation process and summarizes the recorded process control parameter during material synthesis and sample preparation. The most important process control tools and their mode of operation are briefly described in this section.

GSD of the dispersed powder was recorded by the laser diffraction method using a particle size analyser Mastersizer Hydro 2000G (Malvern Instruments Ltd., UK).
The moisture of the dried mixture was detected with the Halogen Moisture Analyzer HG53 (Mettler-Toledo International Inc.).
Specific surface area of the powders was measured by means of the gas adsorption method after Brunauer, Emmitt and Teller (BET) using the areameter Nova 4000e (Quantachrome GmbH & Co.KG).
The loss on ignition (LOI) that occurs during calcination due to carbon dioxide release was determined by dint of an electronic balance with measuring accuracy of 10^{-4}g.
The density of the calcined powder was measured using the pycnometer AccuPyc 1330 (Micromeritics Instrument Corporation).

3. Experimental design and methods

Properties of the granules such as compressibility or granule density were determined via the powder-testing centre PTC-03DT (KZK Powder Tech Corp., USA).

GSD of the granules was measured by incoherent light diffraction method (laser optic system by Jenoptik, Germany) using the dry dispersing module Crystalsizer DR100 (Retsch Technology GmbH).

Geometric green and sintering density (ρ_{geo}) of the samples as well as the linear sintering shrinkage (S_{lin}) of the pellets were calculated by using the following equations.

$$\rho_{geo} = \frac{w}{(1/4 \, \pi d^2 h)}$$

Equation 3.4-I

$$S_{lin} = 100 - \left(\frac{100 \cdot d_{\sin ter}}{d_{green}} \right)$$

Equation 3.4-II

Where w represent the weight, d the diameter and h the height of the pellets. The corresponding weights and dimensions were registered by means of an electronic balance, a digital measuring slide and a digital micrometer gauge. Additionally the density and open porosity of the sintered parts was measured using the Archimedes principle (hydrostatic weighting) with the aid of an electronic balance (Sartorius AG). Density (ρ_w) and open porosity (P) was calculated by Equation 3.4-III and Equation 3.4-IV respectively.

$$\rho_w = \rho_{water} \left(\frac{m_1}{m_3 - m_2} \right)$$

Equation 3.4-III

$$P = \frac{m_3 - m_1}{m_3 - m_2} \cdot 100$$

Equation 3.4-IV

With ρ_{water} being the density of water depending on the temperature, m_1 the weight of the dried sample, m_2 the sample weighed in water and m_3 the sample weight with penetrated water.

The A/B ratio was measured by means of X-ray fluorescence analysis (XRF). It denotes the measured relation of the A-side ions (Ba, Ca, Y) and the B-side ions (Ti, Mn) inside the $BaTiO_3$ (=ABO_3) lattice. Measuring device was the wavelength dispersive X-ray fluorescence (WDXRF) spectrometer S4 Pioneer (Bruker AXS). Calibration was performed with internal standards.

3. Experimental design and methods

<div align="center">Process step   Process control</div>

```
┌─────────────────────────────┐        ┌──────────────────────────────┐
│   Compound preparation via  │   ⇒    │  o  GSD                      │
│   mixed oxide method and    │        │  o  moisture content of the  │
│          drying             │        │     dried mixture            │
└─────────────────────────────┘        └──────────────────────────────┘
              ⇓
┌─────────────────────────────┐        ┌──────────────────────────────┐
│   Calcination at 1192°C     │   ⇒    │  o  LOI                      │
│                             │        │  o  GSD and BET              │
│                             │        │  o  Powder density           │
│                             │        │  o  Powder morphology        │
└─────────────────────────────┘        └──────────────────────────────┘
              ⇓
┌─────────────────────────────┐        ┌──────────────────────────────┐
│   Grinding and spray drying │   ⇒    │  o  GSD                      │
│                             │        │  o  Properties of the        │
│                             │        │     granules                 │
│                             │        │  o  A/B cation ratio         │
└─────────────────────────────┘        └──────────────────────────────┘
              ⇓
┌─────────────────────────────┐        ┌──────────────────────────────┐
│   Sample compression        │   ⇒    │  o  Green density            │
│          moulding           │        │                              │
└─────────────────────────────┘        └──────────────────────────────┘
              ⇓
┌─────────────────────────────┐        ┌──────────────────────────────┐
│   Sintering at 1350°C       │   ⇒    │  o  Sintering density        │
│                             │        │  o  Ceramic characteristic   │
│                             │        │     values                   │
└─────────────────────────────┘        └──────────────────────────────┘
              ⇓
┌─────────────────────────────┐        ┌──────────────────────────────┐
│   Metallisation             │   ⇒    │  o  Electrical characteristics│
└─────────────────────────────┘        └──────────────────────────────┘
```

Figure 3.4-I: Process flow chart: preparation process on laboratory-scale

3.4.2. Thermal analysis

Differential scanning calorimetry (DSC) and thermal gravimetry (TG) have been performed to investigate the calcination process. For that purpose, the simultaneous DSC/TG unit Netzsch STA 409 C/C3/F with electrical SiC-furnace for temperature profiles ranging between 25 and 1550°C was used. Measurements were performed in nitrogen/oxygen atmosphere (80vol.-%N_2:20vol.-%O_2) with gas flow of 50 ml/min. Samples of approximately 35mg were placed in a Pt-crucible and heated from room temperature to 1250°C. The heating rate has been set to 10°C/min. For gas analysis, a capillary linked quadrupole mass spectrometer QMS 403 C (Balzers) has been used. Using this device preselected

mass fragments between 12 and 74g/mol have been recorded (MID-mode). This range includes the emerging mass fragments of water, carbon dioxide and short-chained organic compounds.

3.4.3. X-ray diffraction

Calcined powders and sintered samples were examined by x-ray diffraction (XRD) using the Panalytical X´Pert PRO powder diffractometer with Co-Kα-radiation and the solid-state detector X´Celerator, which operates at real-time multiple strip technology (RTMS). Typical measurement parameter used are a source voltage of 45kV, measurement current of 40mA and a 2Θ-range between 15° and 100° with step size of 0.004°.
The measured spectra were analyzed using the Bruker XRD evaluation software programs Diffrac Plus EVA (version 12.0) and TOPAS (version 3.0). PDF files used for phase identification and quantification are listed in appendix (Table 8.2-II). The phase composition was quantified using the Rietveld refinement method [Din-08/1].

3.4.4. Chemical trace analysis

The analysis of trace elements has been realized using the Inductive Coupled Plasma - Optical Emission Spectrometer (ICP-OES) Spectro Arcos (Spectro Analytical Instruments GmbH). Element concentrations were determined using the method of standard addition. Included relevant elements are Na, Mg, Al, P, K, Fe, Zr and Nb. Due to the digestion method used for sample preparation the chloride concentration was separately measured using volumetric analysis (titration). Quantification of the detected elements was done by the Smart Analyzer Vision software (Spectro GmbH). Sample preparation has been carried out by the following procedure: 0.1g of the powder sample was weighed and dissolved by microwave assistance in a mixture of 5ml deionised H_2O, 10ml HCl and 2ml HBF_4. Finally, the sample solution was filled up with deionised water until a volume of 100ml was reached.

3.4.5. Scanning electron microscopy

Scanning electron microscopy (SEM) has been applied to investigate the microstructure and microchemistry of the sintered parts. Cross sections of the sintered pellets were embedded in epoxy resin and ground and polished. Finally, the specimens were polished with an alkaline colloidal silica solution (OP-U suspension from Struers, 0.04µm granularity) for 60 minutes. This preparation procedure was necessary in order to perform electron backscatter diffraction (EBSD). Additionally, these specimens were used for wavelength and energy dispersive x-ray spectrometry (WDXS and EDXS). The EDXS, WDXS and EBSD analyses were accomplished on a Zeiss Ultra 55 FESEM equipped with a Trident system from the EDAX Company. The Trident system comprises a Sapphire Si(Li) EDX detector and a TEXS WDX spectrometer for element analyses and a CCD-Digiview-camera for EBSD. The EDXS and WDXS data

were recorded and evaluated with the Genesis software V6.1, the EBSD data with OIM 5.3 software. The operation conditions (high voltage and beam current) for EDXS were 15kV and 1.5nA, for WDXS 20 kV and 30nA. During EBSD characterisation the microscope was operated at 20kV and 1.8nA and an area of 100x100µm was scanned with a step size of 100nm (hexagonal pixels). Grain boundaries were characterized by a misorientation larger than 5° between neighbouring measurement points. To reduce the influence of noise in the results, a grain must comprise at least six pixels which results in a minimum grain diameter of around 0.4 µm.

3.4.6. Electron probe microanalysis

In order to perform quantitative elemental analysis the Electron Probe Microanalyzer (EPMA) Jeol JXA 8200 SuperProbe has been used. This device, which works in principle like a SEM optimised for quantitative analysis, consists of five WDX spectrometers in combination with one EDX spectrometer. Analysis crystals incorporated in the equipment are TAP (thallium acid pthalate), LIF (lithium fluoride), LIFH (high-resolution LIF), PETJ (high-reflectivity PET) and PETH (high-resolution PET). Using EPMA a simultaneous detection of up to 5 elements can be achieved. Compared to SEM-EDX the spectral resolution is considerably increased and the elemental detection is ranging from boron to uranium. The device is equipped with a W-filament electron source, a high-precision sample stage and a vacuum-pump unit. The configuration for quantitative elemental analysis has been set up by firstly selecting an appropriate analyser crystal for each element, secondly calibrating the measurement for each element by using mineral standards (SPI Supplies / Structure Probe, Inc; 53 standards set). The elements included in the measurement file for quantification were Ba (Lβ), Ca (Kα), Ti (Kα), O (Kα), Si (Kα), Y (Lα), Mn (Kα), P (Kα), K (Kα) and S (Kα). Quantitative (point) analysis was performed using the line analysis operation mode, which includes 20 separated reading points. The measurement conditions used are an accelerating voltage of 15kV with probe current of $1*10^{-8}$A, the testing times amount to 20sec for peak and 10sec for background measurement. For matrix correction the phi-rho-zet (PRZ) method was used. In contrast, the elemental maps are recorded using the map analysis program, i.e. only peak measurement is employed. The measured area for elemental mapping amounts to 40x40µm with spatial resolution of 1024x1024 reading points. Typical measurement conditions were an accelerating voltage of 15kV, a probe current of $3*10^{-8}$A and a step size of 0.04µm. Measurements were performed on the samples prepared for SEM/EBSD (see section 3.4.5).

3.4.7. Transmission electron microscopy

For high-resolution imaging and chemical analysis, the Tecnai F20 Transmission Electron Microscope (TEM) manufactured by FEI Eindhoven has been used. Due to the high-resolution imaging filter and monochromator assembled, this device is optimized for nanoanalytical tasks such as Electron Energy-Loss Spectrometry (EELS), Energy-Filtering TEM (EFTEM) and EDXS. The used microscope is equipped with a Schottky field emitter, an S-TWIN objective lens (FEI Company)

and a Gatan Imaging Filter (GIF) Quantum (GATAN Inc.). X-ray spectra are recorded using the Sapphire Si(Li) EDX detector from the EDAX Company (STEM-mode). The EELS-spectra are collected in STEM mode using the GIF Quantum manufactured by GATAN Inc. Company. Measurements are performed using an acceleration voltage of 200kV. Sample preparation has been carried out using the following procedure. Firstly the sintered parts are cut. Further the pieces are embedded in an alumina tube (internal diameter 1.8mm) followed by a grinding and polishing step until a thickness of 100µm is reached. Then the thinned samples are dimpled (30µm) and finally ion beam thinned until electron transparency is reached (approximately at 100nm thickness). For ion beam thinning the equipment PIPS (Precision Ion Polishing System) of GATAN Inc. Company is used.

3.5. *Electrical characterisation*

3.5.1. Room temperature resistivity and ρ-T-characteristic

The electrical resistivity at 25°C (ρ_{25}) was measured using a digital multimeter Keithley 199 (Keithley Instruments Inc.) with a working range of up to 300MΩ (measurement current 1.7mA to 0.5µA).

The R-T characteristic was recorded between 30°C and 280°C in air by means of a test assembly containing the source measure unit Keithley 237, the switch system Keithley 7001 (Keithley Instruments Inc.) and the air convection oven Memmert UFE 400 (Memmert GmbH & Co.KG). A measurement voltage between 1V and 400V was applied to estimate the voltage dependence as exemplarily depicted in Figure 3.5-I.
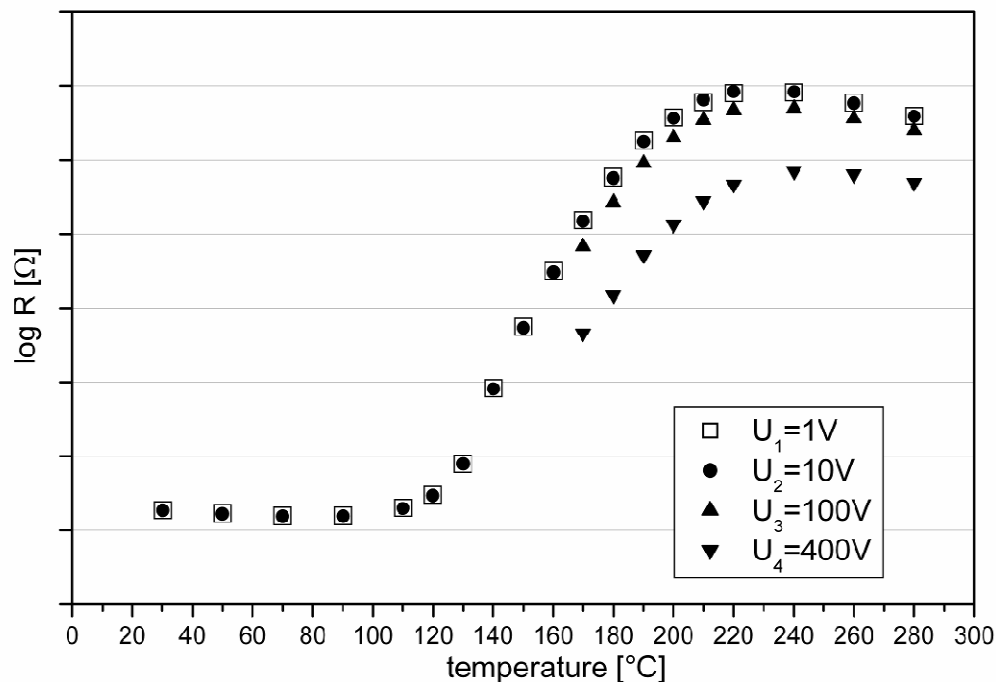
Figure 3.5-I: Schematically depicted monitoring program for the detection of the R-T-characteristic

3.5.2. Impedance analysis

Impedance measurements were performed on disc-shaped samples (diameter: 12mm, thickness: 2.5mm) in air at temperatures between room temperature and 110°C by employing a high-precision impedance analyzer (Novocontrol Alpha-A). The effective ac voltage amounted to 1.0V and the frequency range was from 10MHz to 100mHz. The specimens were placed in the sample holder between two gold foils by light spring action. The stray inductance of the leads of the measurement jig was determined on the empty short-circuited sample holder. The ac measurements have been carried out in a tube furnace equipped with a temperature controller (Eurotherm 2416) and the temperature was recorded in the vicinity of the sample by type-K thermocouples.

3.5.3. ε-T-characteristic

The relative permittivity (ε_r) as a function of temperature was calculated based on capacitance (C) measurements in the temperature range of -55 to 155°C (Vötsch VTM7004 temperature test chamber). The C-T-characteristic was detected using the Precision LCR Bridge HP4284A. Standard measurement parameters are a voltage of 1V and frequency of 1kHz. The relative permittivity then was calculated considering the geometry of the sample parts (Equation 3.5-I).

$$\varepsilon_r = C \cdot \frac{1}{\varepsilon_0} \cdot \frac{d}{A}$$

Equation 3.5-I

Where ε_0 denotes the permittivity of vacuum, d is the thickness of the sample and A the effective electrode area which equates to the surface area of the samples.

4.   Results and discussion

This section includes the results and discussion of the experiments described in section 3.2. Commencing with the measured electrical properties a detailed analysis of the synthesis process is subsequently given. Finally, the results are discussed in terms of microstructural and chemical evolution of the sintered parts and their consequences on the electrical characteristic.

4.1.   Electrical characteristic

4.1.1.   Room temperature resistivity and ρ-T-characteristics

Figure 4.1-I depicts the measured resistivity (ρ_{25}) values of all compositions at room temperature.
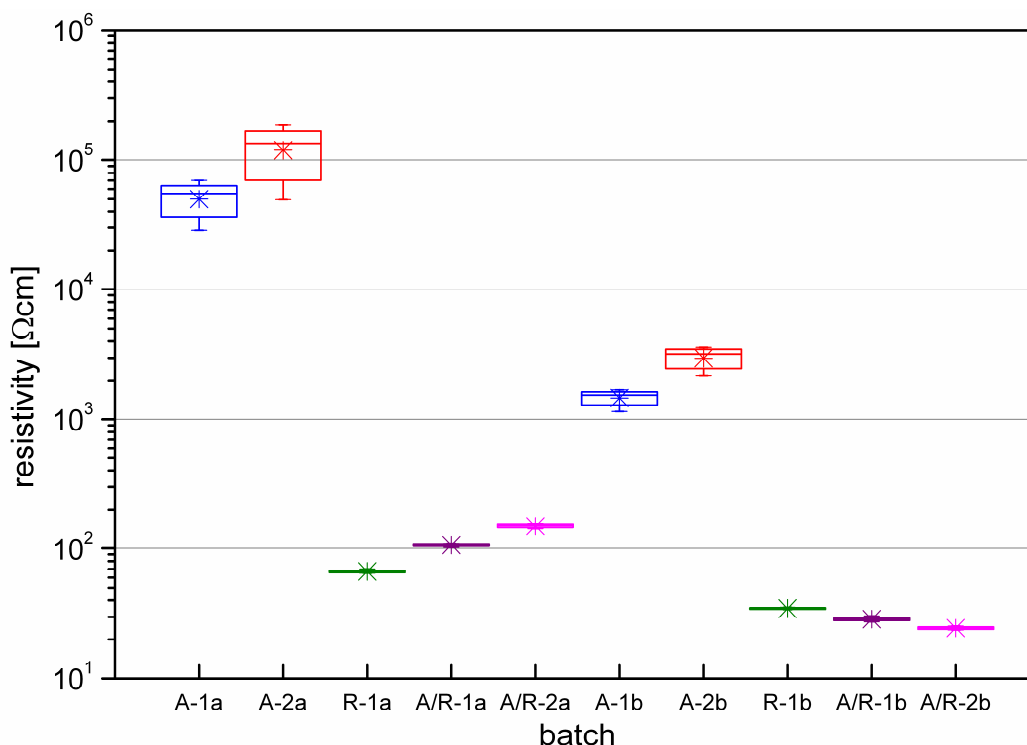
Figure 4.1-I: Box plot of the resistivity at room temperature of series a- and b- compositions

It can be seen from Figure 4.1-I that compounds containing anatase TiO_2 prepared from the sulphate process exhibit much higher resistivity. The values ranging from 5.0×10^4 to $1.2 \times 10^5 \Omega$cm for compositions A-1a and A-2a (A/B-ratio 0.998) and 1.4×10^3 to $3.0 \times 10^3 \Omega$cm for compositions A-1b and A-2b (A/B-ratio 0.985) which are 2 to 4 orders of magnitude higher than the rutile references R-1a and R-1b showing resistivity values of about 66.9Ωcm and 34.7Ωcm respectively. In contrast the anatase-rutile mixture materials A/R-1 and A/R-2 (a and b series) do not show any significant changes in room temperature resistance compared to the

4. Results and discussion

rutile reference R-1. The resistivity values obtained with these raw materials on the one hand range from 106.3Ωcm to149.2Ωcm for series "a" (A/B-ratio 0.998). On the other hand, the resistivity amounts to 28.8Ωcm and 24.6Ωcm for b series (A/B-ratio 0.985). These values are quite close to the reference values of 66.9Ωcm and 34.7Ωcm achieved for composition R-1a and R-1b respectively. Additionally it is evident from Figure 4.1-I that the use of anatase raw materials with higher impurity level significantly increases the standard deviation of the resistivity values.

The PTCR-characteristics of the compositions prepared are illustrated in Figure 4.1-II and Figure 4.1-III. It is obvious that commercial anatase-based materials show PTCR-characteristics as well, although the shape changes especially with regard to the slope and height of the PTCR-jump and the characteristic temperatures (temperature of minimum and maximum resistance, onset-temperature). Compared to the rutile reference the maximum resistivity (ρ_{max}) and the temperature at maximum resistivity (T_{max}) respectively are shifted towards lower temperatures when using sulphate-processed anatase as the TiO_2 source (compositions A-1a and A-2a compared to R-1a). This observation is also applicable for compositions A1b, A-2b and R-1b. Furthermore, the anatase-rutile mixture materials A/R-1a and A/R-2a (Figure 4.1-II) show slight increase in the resistivity values around T_{max} and a minor shift of ρ_{max} to lower temperatures when compared to the rutile reference R-1a. Opposed to that the PTCR-characteristic of the compositions A/R-1b and A/R-2b (Figure 4.1-III) do not show significant changes compared to R-1b. Moreover it is visible from Figure 4.1-II that changing the A/B-ratio towards higher Ti-excess leads to a shift of the room temperature resistivity respectively ρ_{min} towards lower values which is consistent with literature as described in section 2.2.5 [Lin-90, Sak-04, Jay-04, Nii-07].

For better comparison Table 4.1-I summarizes the characterizing parameters ρ_{min}, ρ_{max}, T_{max} and $\alpha_{(130-180°C)}$ of series a- and b-compositions. An entire overview of the characterizing parameters is given in appendix Table 8.2-V.

Table 4.1-I: Characteristic values of the ρ-T-graphs (measured at 10V)

Batch no.	ρ_{min} [Ωcm]	ρ_{max} [Ωcm]	T_{max} [°C]	$\alpha_{(130-180°C)}$ [%/°C]
A-1a	5.7E+04	2.9E+08	200	11.67
A-2a	1.6E+05	4.4E+08	209	10.49
R-1a	5.3E+01	2.1E+07	247	15.16
A/R-1a	8.6E+01	6.6E+07	224	17.23
A/R-2a	1.3E+02	9.8E+07	223	17.15
A-1b	1.1E+03	8.2E+07	240	14.56
A-2b	2.8E+03	7.4E+07	233	12.85
R-1b	2.9E+01	1.0E+07	252	15.45
A/R-1b	2.4E+01	1.0E+07	257	15.08
A/R-2b	2.0E+01	5.8E+06	253	14.59

4. Results and discussion
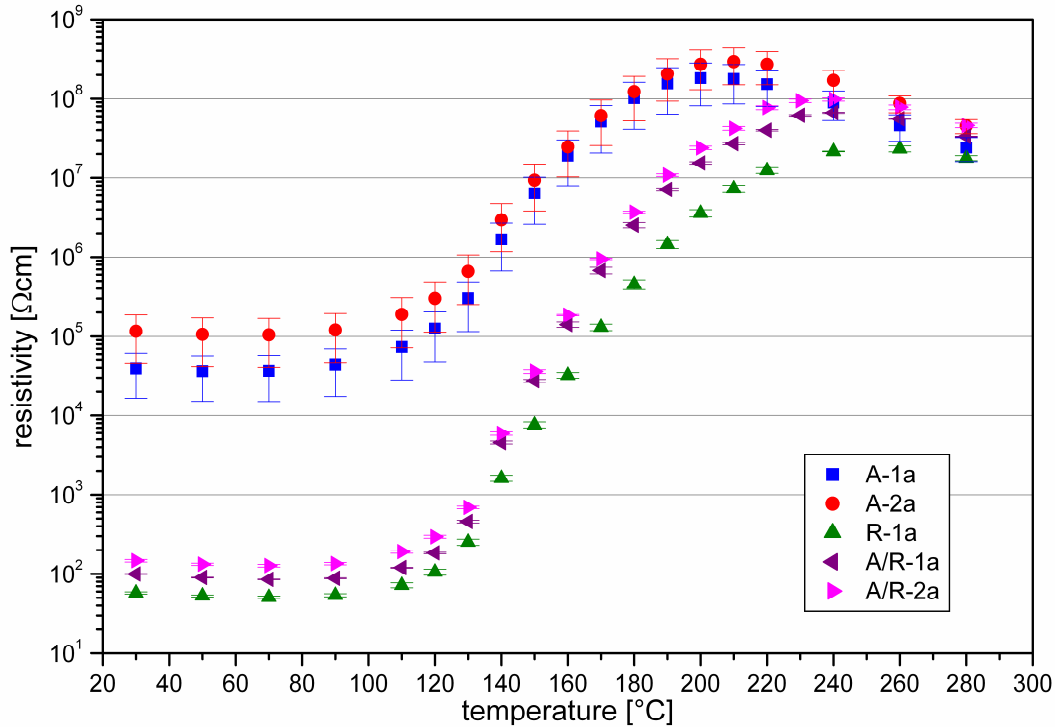
Figure 4.1-II: Resistivity as a function of temperature (ρ-T-characteristic) of series a-compositions at a measurement voltage of 10V.
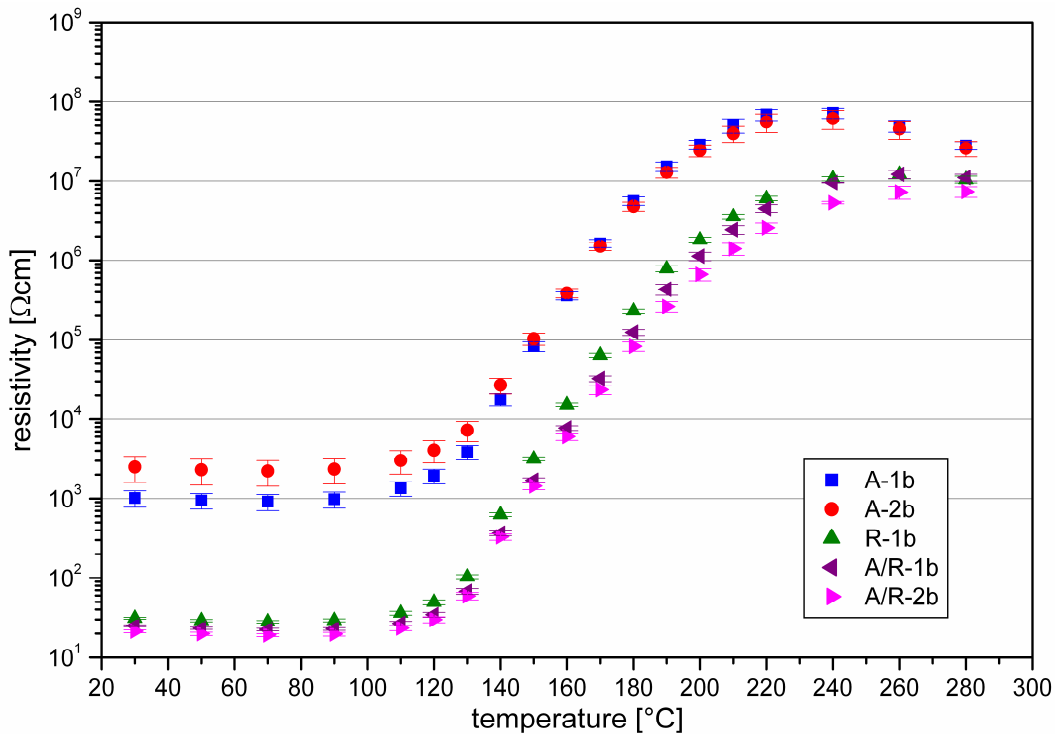
Figure 4.1-III: Resistivity as a function of temperature (ρ-T-characteristic) of series b-compositions at a measurement voltage of 10V.

Additionally Figure 4.1-IV and Figure 4.1-V represent the resulting values for $\Delta\rho/\Delta T$ i.e. the slopes of the PTCR-jump plotted against temperature. One characteristic point therein is the reversal from positive to negative alpha values representing T_{max}. It is apparent from Figure 4.1-IV and Figure 4.1-V (and Table 4.1-I) that the rutile reference composition (R-1) as well as the anatase-rutile

4. Results and discussion

mixture compositions (A/R-1, A/R-2) show flat $\Delta\rho/\Delta T$ vs. T curves resulting in higher T_{max}. Whereas the compositions prepared from anatase (A-1, A-2) show much steeper $\Delta\rho/\Delta T$ vs. T graphs and for this reason lower T_{max}. Moreover, it is obvious that higher Ti-excess results in flatter $\Delta\rho/\Delta T$ vs. T curves once again correlated with an increase in T_{max}.
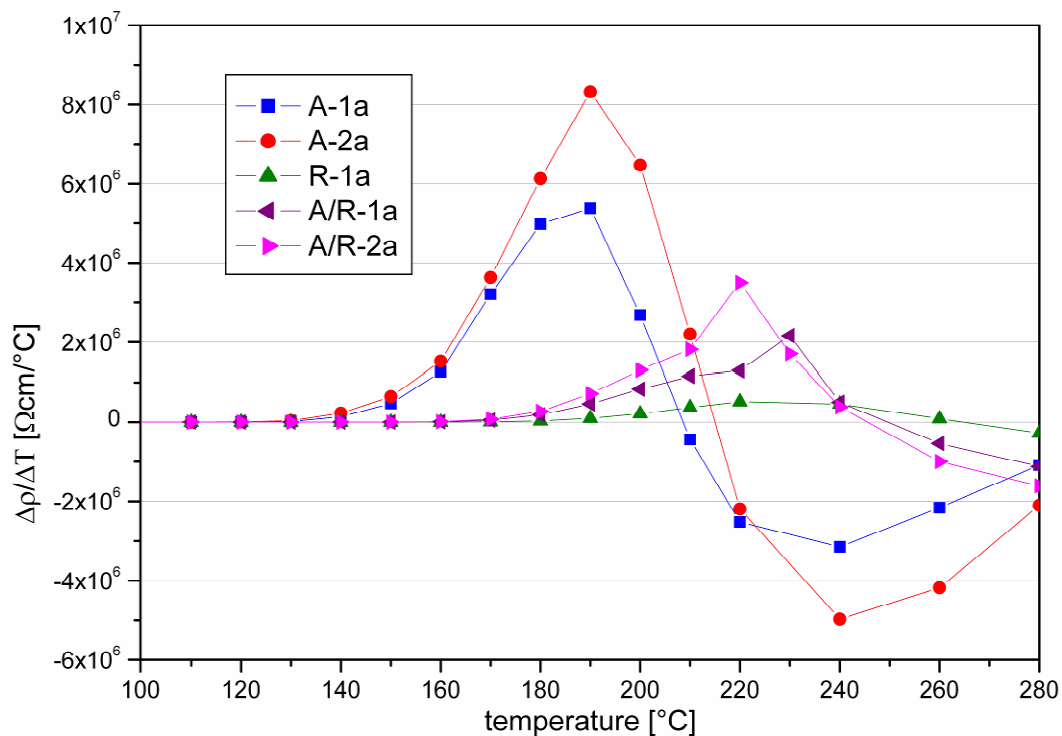
Figure 4.1-IV: Plot of $\Delta\rho/\Delta T$ as a function of temperature for a-compounds
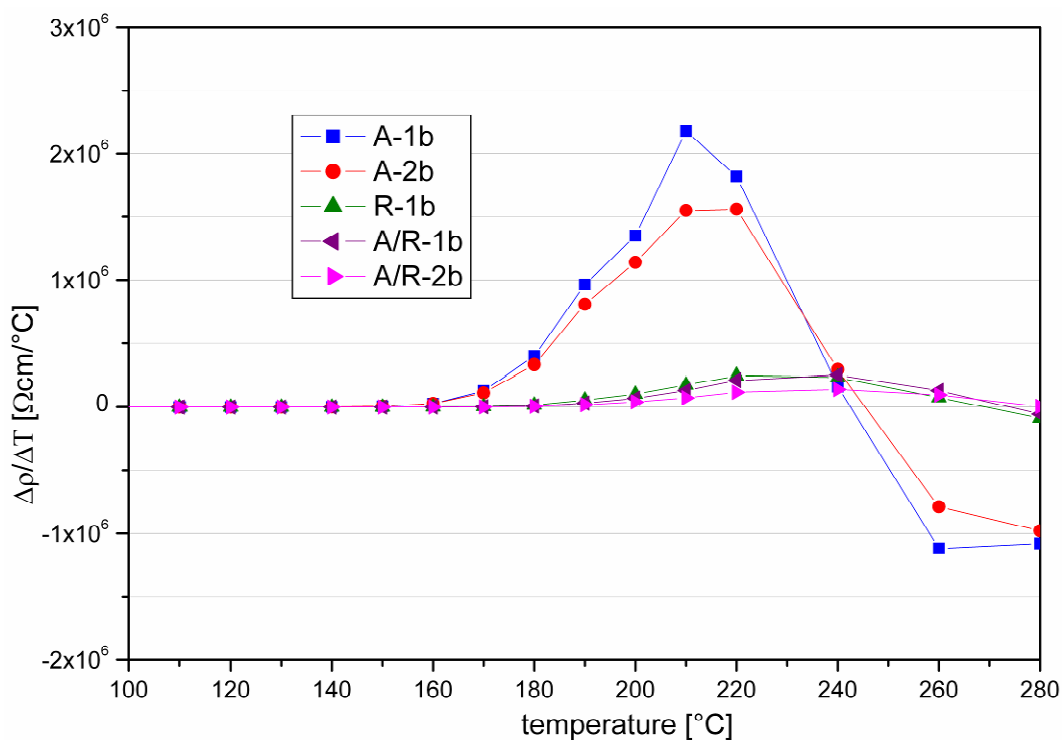
Figure 4.1-V: Plot of $\Delta\rho/\Delta T$ as a function of temperature for b-compounds

4. Results and discussion

Furthermore, in Figure 4.1-VI and Figure 4.1-VII the characteristic resistivity values and temperatures of all compositions are compared. The correlation of ρ_{min} and ρ_{max} with ρ/T-ratio (Figure 4.1-VI) directly visualizes that the change in slope and height represented by the the ρ/T-ratio mainly can be attributed to a change in low temperature resistivity (ρ_{min}), which decreases about 2 to 3 orders of magnitude (A-1 and A-2 compared to R-1). On the contrary, ρ_{max} only decreases about half of that. Finally, Figure 4.1-VI illustrates that the distingtions of resistivity between the commercial anatase compounds, the rutile reference and the anatase-rutile mixture materials in b-compositions is decreased especially in the low temperature area. This illustrates the homogenising (equilibration) effect of a liquid phase available during sintering. Similar observations can be made by analysing Figure 4.1-VII. The variation in characteristic temperatures for a-compositions exceeds the variation range for b-compositions. Besides T_{max} is much stronger affected than T_{min}.
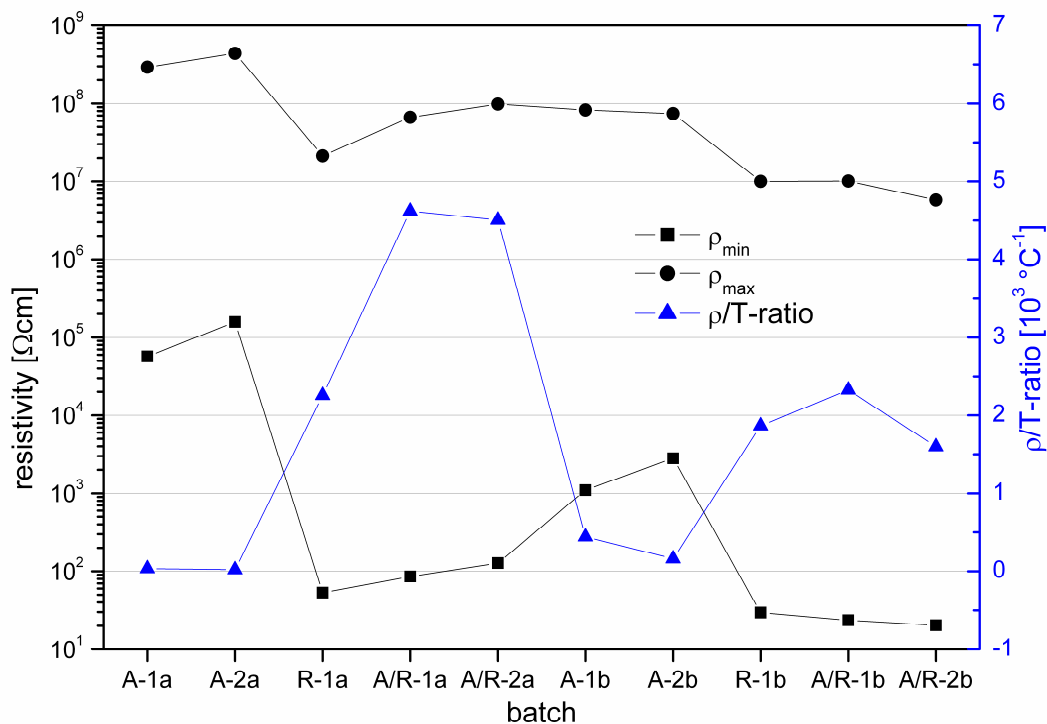
Figure 4.1-VI: Comparison of the characteristic values ρ_{min}, ρ_{max} and ρ-T-ratio of the compositions
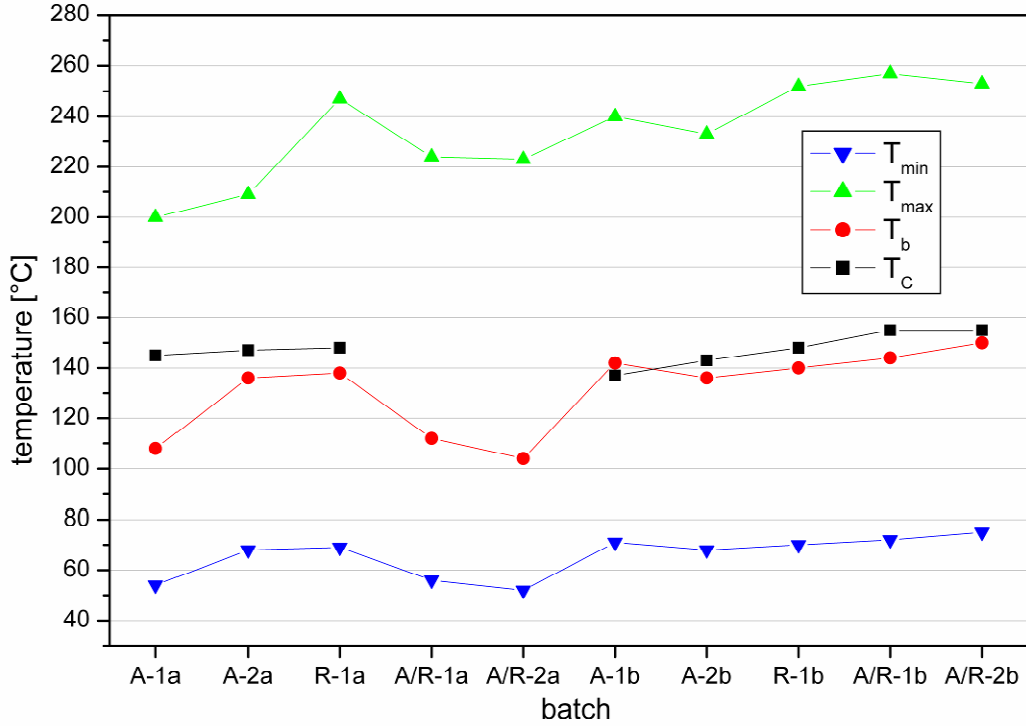
Figure 4.1-VII: Comparison of the characteristic temperatures T_{min}, T_{max}, T_b and T_C of basic compositions[*]

4.1.2. Complex impedance analysis

Impedance measurements, as described in section 3.5.2, were carried out for a- and b-compositions between room temperature and 110°C i.e. below the ferroelectric to paraelectric phase transition at Curie temperature (T_C). The complex plane plots of the impedance data typically consisted of one suppressed semicircle, which was somewhat shifted along the real axis. The impedance spectra were analyzed by means of complex non-linear least squares (CNLS) fitting of the equivalent circuit $L_sR_{bulk}(R_{gb}CPE_{gb})$ to the experimental data (WinFit), yielding values for the bulk (R_{bulk}) and grain boundary (R_{gb}) resistances as well as the grain boundary capacitances, extracted from the constant phase element CPE_{gb}, with typical values ranging from 1.9nF to 15.3nF. The inductance of the sample holder, $L_s = 0.5\mu H$, was held constant during the fitting procedure.

The following figures (Figure 4.1-VIII to Figure 4.1-XI) show the resulting complex plane impedance plots (Z´-Z´´-plots). Herein the visible shifts along the real axis (Z´) represent the bulk resistance whereas the semicircle corresponds to the response of the grain boundaries. The resistance vs. temperature plots for bulk and grain boundaries are depicted in Figure 4.1-XII and Figure 4.1-XIII. For comparison, the obtained bulk resistance ranges between 1Ω and 5Ω. On the contrary, the grain boundary resistance varies between 1Ω and 10^5Ω. Figure 4.1-XII and Figure 4.1-XIII clearly illustrate that the variation in total resistance i.e. $R_{gb} + R_b$, and for this reason the dc resistivity (see section 4.1.1) are only generated by differences in the grain boundary resistance (R_{gb}) and cannot be attributed to changes in bulk resistance (R_b).

---

[*] The ε-T-characteristics of batches A/R1-a and A/R-2a have not been determined

4. Results and discussion
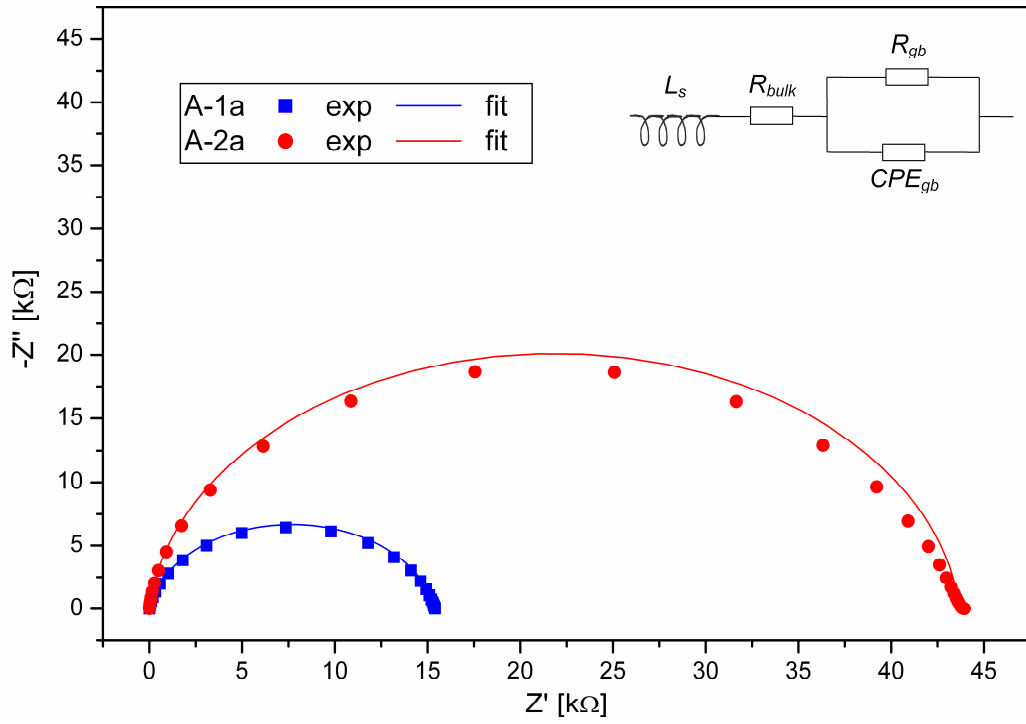
Figure 4.1-VIII: Complex plane impedance plot of a-compositions A-1a and A-2a
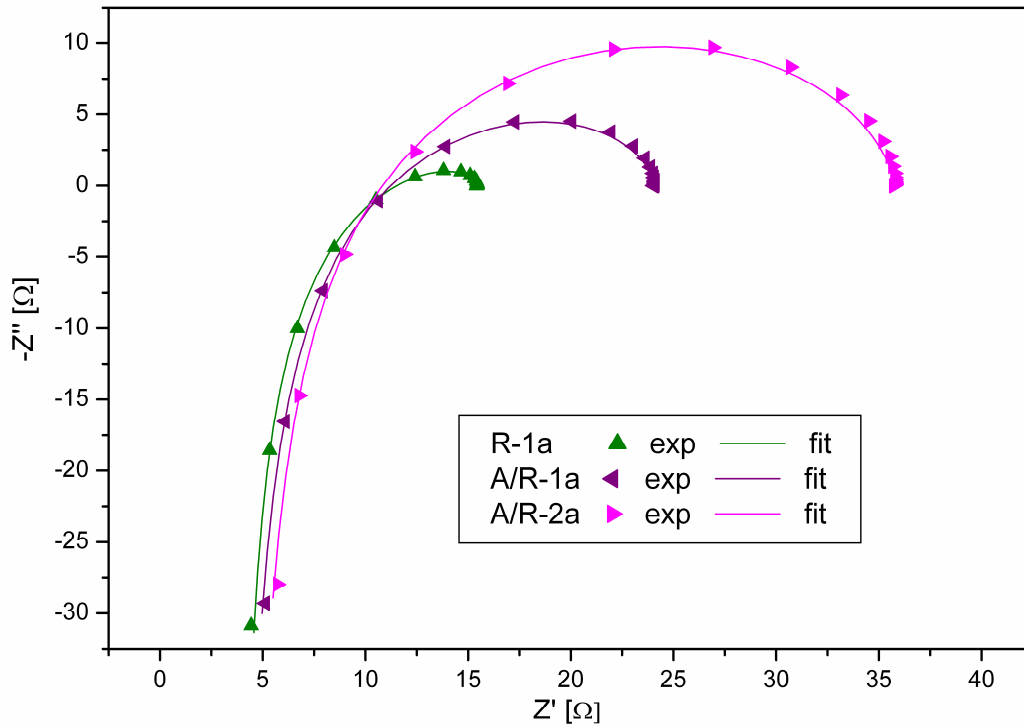
Figure 4.1-IX: Complex plane impedance plot of a-compositions R-1a, A/R-1a and A/R-2a

4. Results and discussion
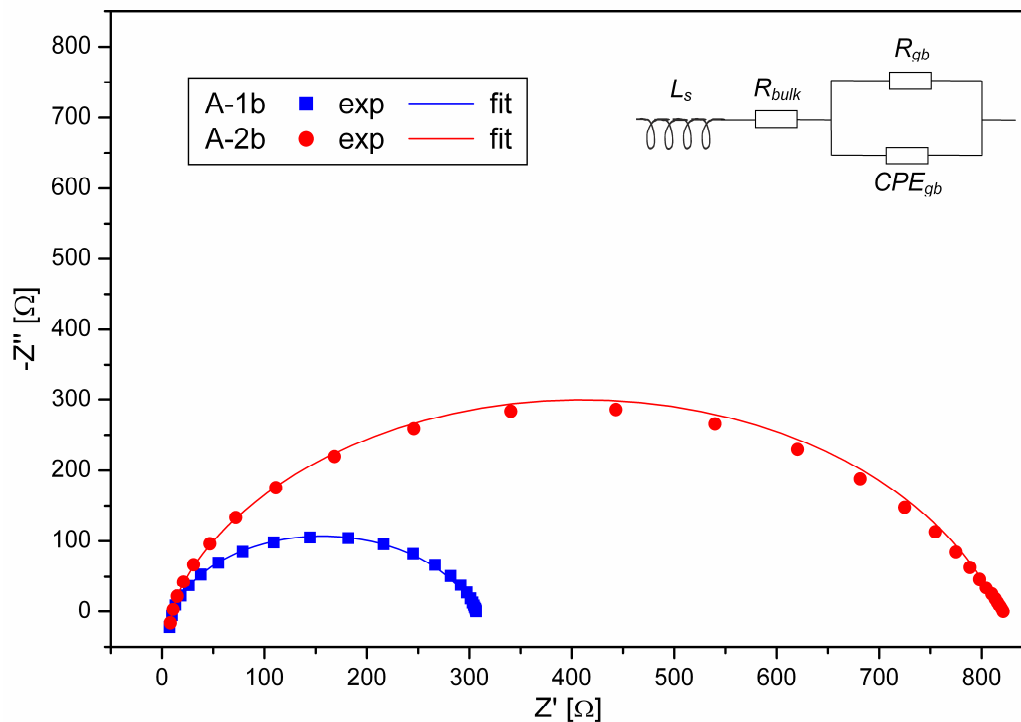
Figure 4.1-X: Complex plane impedance plot of b-compositions A-1b and A-2b
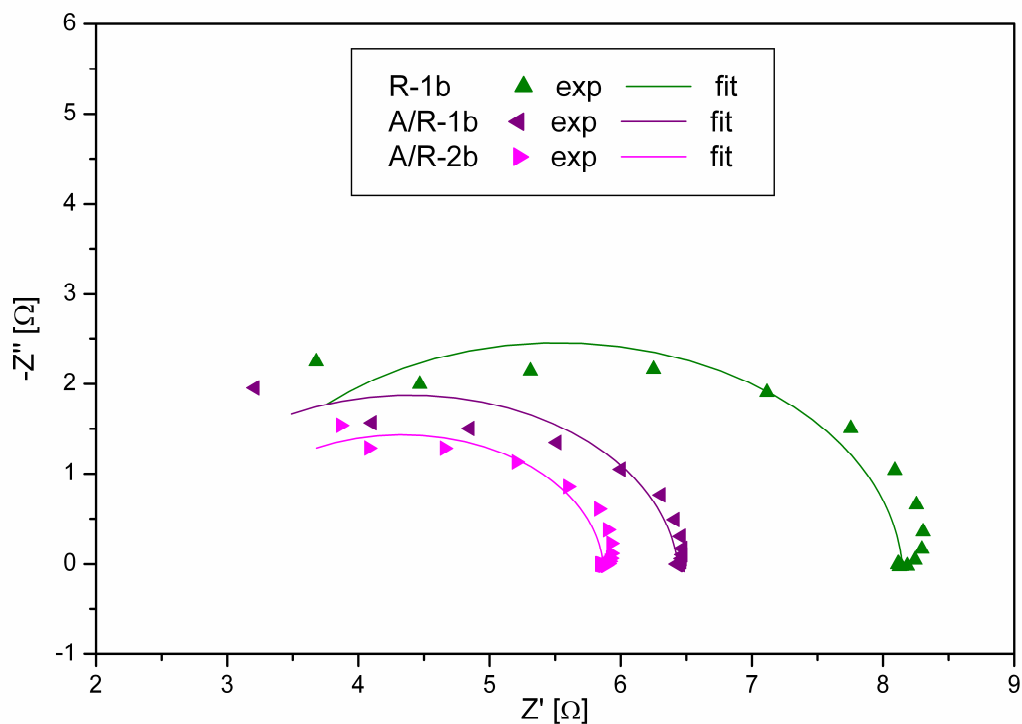
Figure 4.1-XI: Complex plane impedance plot of b-compositions R-1b, A/R-1b and A/R-2b
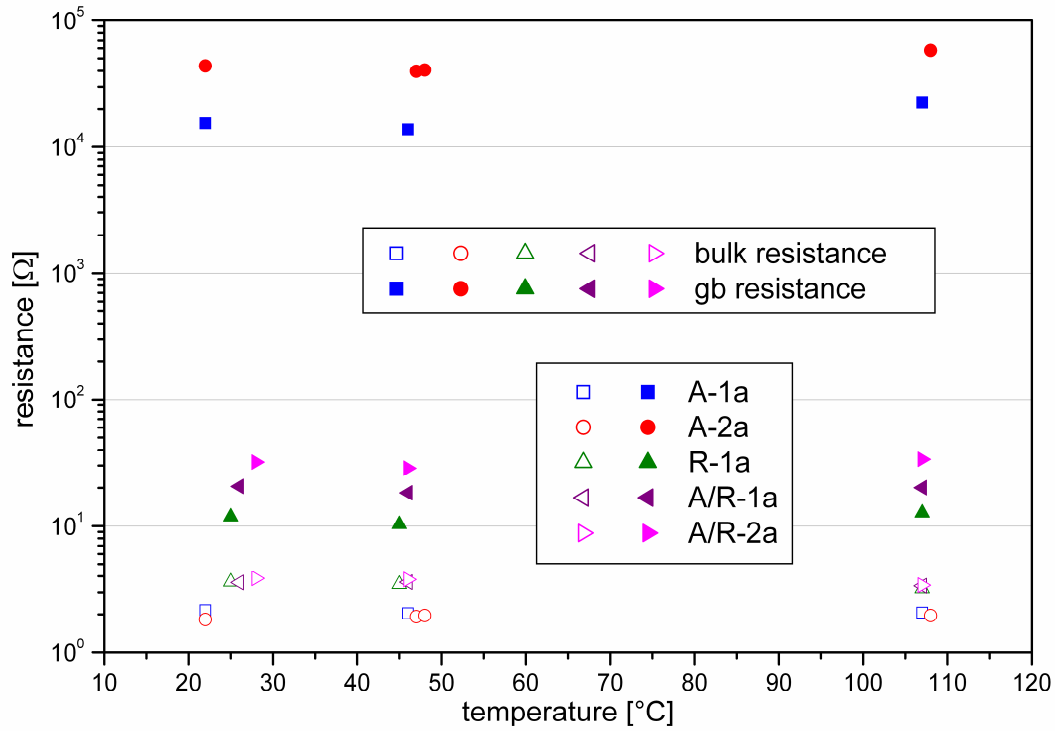
Figure 4.1-XII: Resistance vs. temperature plot of a-compositions
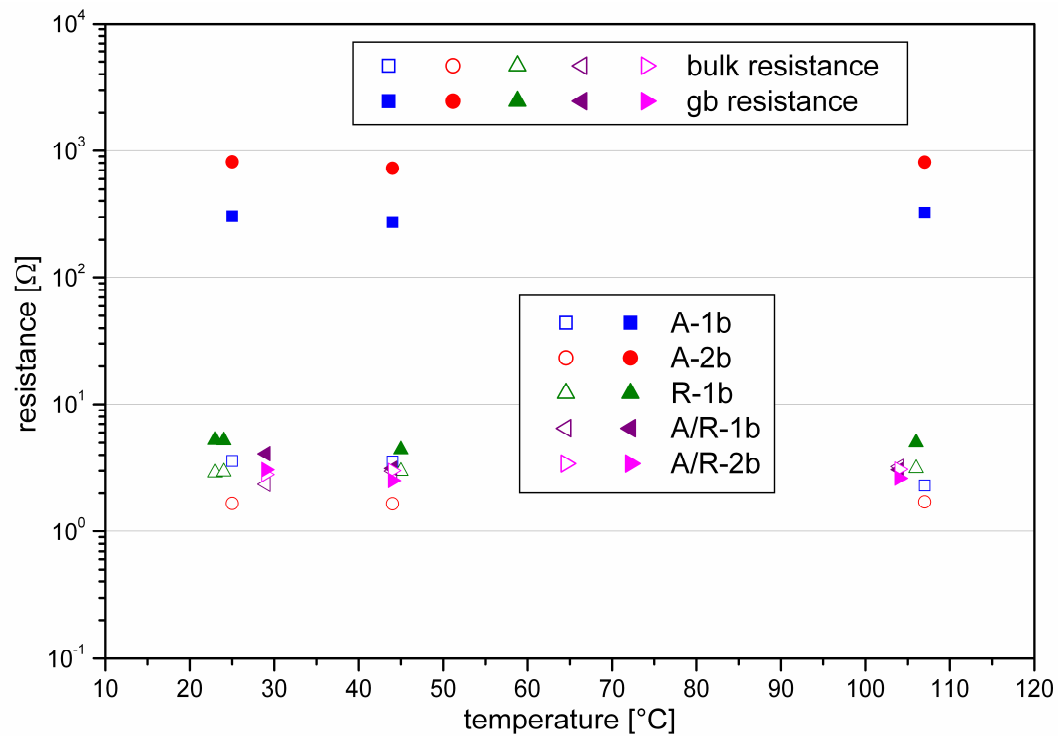
Figure 4.1-XIII: Resistance vs. temperature plot of b-compositions

4.1.3. ε-T-characteristic

The relative permittivity (ε_r) as a function of temperature is illustrated in Figure 4.1-XIV. Therein it can be seen that compositions having low resistivity values (R-1, A/R-1 and A/R-2) show negative permittivity values at low temperatures or

rather negative capacity values are recorded during measurement. Of course, this is impossible but can be explained considering the measuring apperatus. In this case, it has to be attributed to the measuring instrument and arrangement, i.e. as long as the wiring and testing bridge is not dimensioned for low-ohmic parts such an effect is always observed due to inductive effects. For this account the ε-T-characteristic has only been analysed to determine T_C, which is located at the temperature at which ε_r becomes maximum. The values determined for T_C are summarised in appendix Table 8.2-V. Figure 4.1-XIV and Table 8.2-V clearly illustrate that the permittivity maximum is flattened and T_C is shifted towards lower values in anatase-based compositions (A-1 and A-2) whereas the rutile reference and the anatase-rutile mixture materials (R-1, A/R-1 and A/R-2) show relatively sharp permittivty maxima and higher values for T_C.
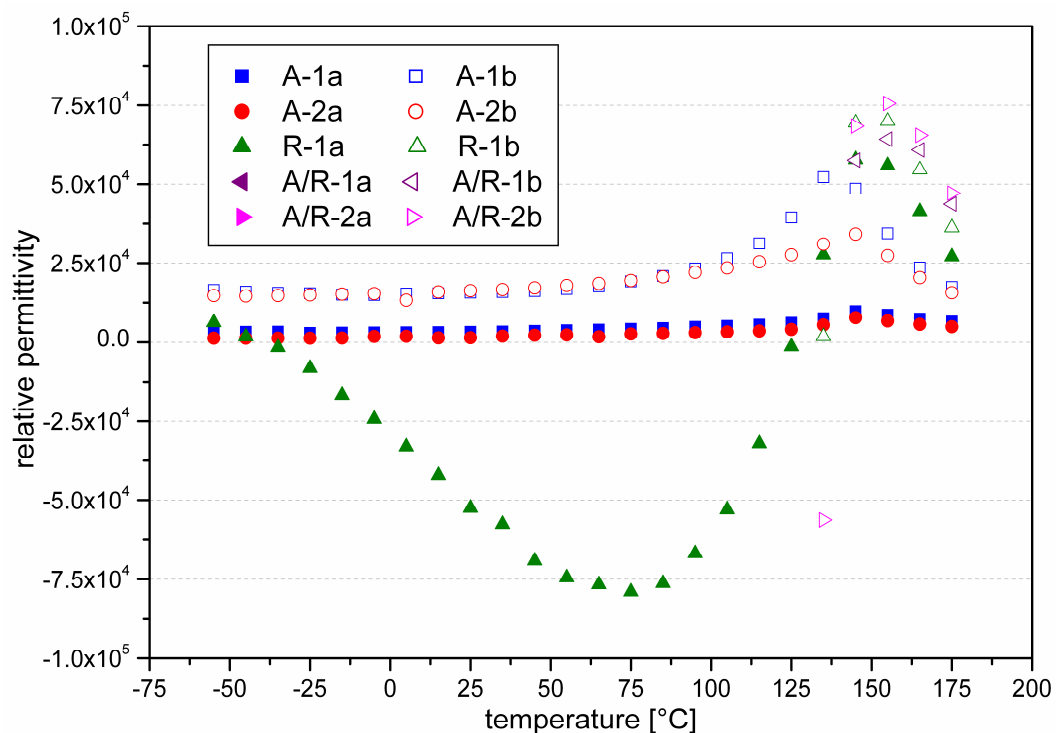
Figure 4.1-XIV: ε-T-characteristic of all compositions (averaged results)

4.2. Investigation of the synthesis process

This section firstly deals with the investigations carried out to analyse the material synthesis process namely the thermal analysis of the calcination process, the X-ray diffraction study of the calcined powders as well as the quality control measurements performed during synthesis process. Subsequently the results are interpreted with respect to the differences between the raw materials employed.

4.2.1. Results of the process analyses

The industrial and bench-scale processes of the material synthesis have been described in sections 2.2.1 and 3.3. Additionally a literature overview has been given in section 2.2.2 with respect to the solid-state synthesis of $BaTiO_3$. On the

4. Results and discussion

basis of this information the properties of the semi-finished goods have intensively been inspected during (Ba,Ca)TiO$_3$ solid-state formation (see section 3.4.1). In appendix Table 8.2-III, the relevant control measurements are summarised.

Special interest is attracted to the properties of the calcined powders e.g. the BET that in comparison to the properties of the titania raw materials gives rise to the reactivity. Figure 4.2-I illustrates the correlation of the specific surface of the TiO$_2$ raw materials to the relative specific surface of the calcined powders (specified in percentage of the TiO$_2$ powders). This diagram directly demonstrates the variation in reactivity during calcination which was expectable due to the differences in the titania BET values (see section 2.2.2) [Hen-01/1]. Other measured process data will be placed and discussed in relevant context.
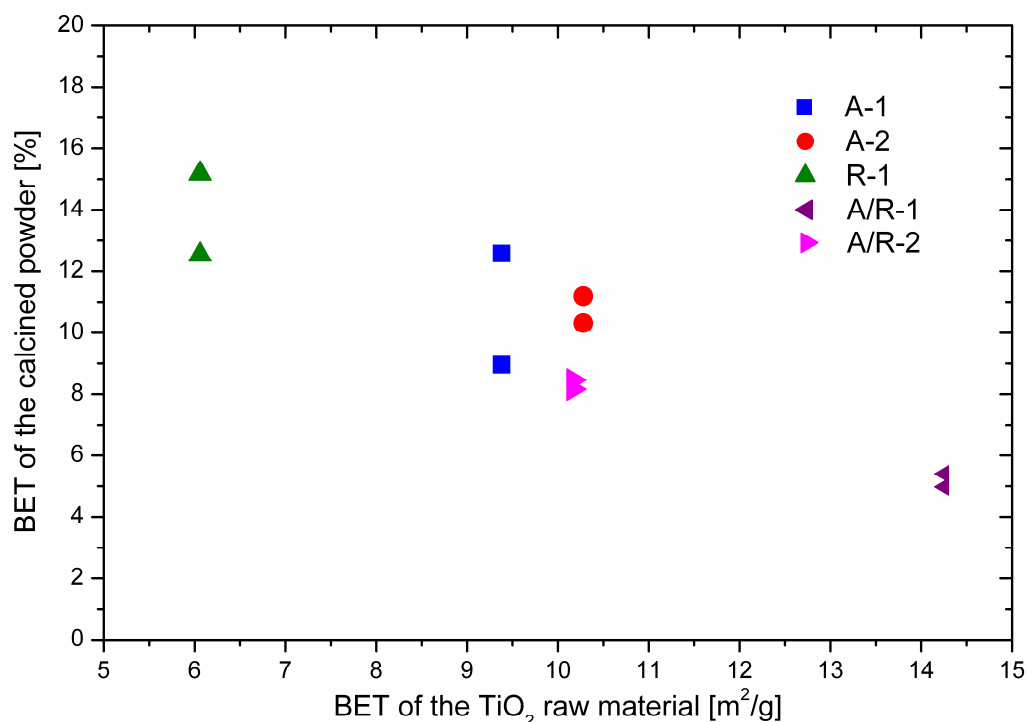
Figure 4.2-I: Correlation of the BET of the TiO$_2$ raw materials with the relative BET of the calcined powders calculated in percentage of the TiO$_2$ BET

4.2.2. Results of the thermal analyses

STA of the raw materials are depicted in Figure 4.2-II. Comparing the titania raw materials only minor differences are detected in the STA spectra. In principle the anatase raw materials (A-1 and A-2) should show a sharp exothermic DSC-peak at the temperature at which anatase-rutile transformation takes place but this is not clearly visible in the STA. Instead of that, all TiO$_2$ raw materials show a small and flat endothermal increase above 1000°C. For this reason it is supposed that the anatase-rutile transformation of the materials A-1 and A-2 takes places at temperatures above 1250°C and that the flat peaks above 1000°C most probably result from energy consumption due to sintering (surface free energy reduction) of the raw materials (see appendix Figure 8.1-I to Figure 8.1-IV) [Sal-07]. The overall energy consumption of the anatase materials between 100°C and 1200°C

4. Results and discussion

accounts for 2210µVs/mg for A-1 and 1666µVs/mg for A-2. Compared to the rutile reference value of 1564µVs/mg the anatase values are slightly increased. Additionally the position of this energy consumption peak (starting and maximum temperature) is shifted from 541°C for the reference rutile to approximately 35°C higher temperatures when using anatase TiO_2. This indicates the varying reactivity of the titania raw materials resulting from differences of the physical and chemical properties such as BET or impurity content [Rao-60, Rao-61, Sha-65, Cri-83, Amo-95, Grz-04, Grz-07, Sal-07].

The TG analysis of $BaCO_3$ pictures the decomposition of the material in the temperature range of 850-1200°C with a weight loss of 18.8wt.-%. The theoretical weight loss during decarbonation amounts to 22.30wt.-%. It is assumed that this discrepancy results from the formation of a eutectic melt between the formed BaO and the residual $BaCO_3$. This liquid phase forms during heat treatment above 950°C and is for example described by Tsutai et al. [Tsu-01] or Nakayama and Sasaki [Nak-63]. Simultaneous the DSC-curve shows a broad endothermic peak in the temperature region between 1000 and 1200°C with a peak maximum at approximately 1100°C, which can be attributed to the decarbonation. Additionally two sharp endothermal peaks at 826.5°C and 978°C are visible in the $BaCO_3$ DSC-curve, both representing the phase transitions presented in Equation 4.2-I from orthorhombic (γ) to hexagonal (β) modification and from hexagonal (β) to cubic (α) modification [Lan-49, Rao-79, Ant-07].

$$\gamma - BaCO_3 \xrightarrow{811°C} \beta - BaCO_3 \xrightarrow{982°C} \alpha - BaCO_3$$

Equation 4.2-I

For $CaCO_3$ the TG-graph shows a weight loss of 43.4wt.-% illustrating the decomposition of the powder in the temperature range of 500°C to 800°C. The theoretical weight loss in this case amounts to 43.97wt.-%, which is quite close to the measured value. The DSC-graph depicts a relatively broad endothermic peak between 600°C and 800°C with a peak maximum of about 775°C, which corresponds to the decarbonation. Contrary to $BaCO_3$, no phase transition peaks are visible for $CaCO_3$ [Smy-23, Lan-49, Sui-01].

Summarizing the results obtained by thermal analysis it can be assumed that the small differences in thermal properties of the titania raw materials probably affect the behaviour during calcination which is discussed below.

4. Results and discussion
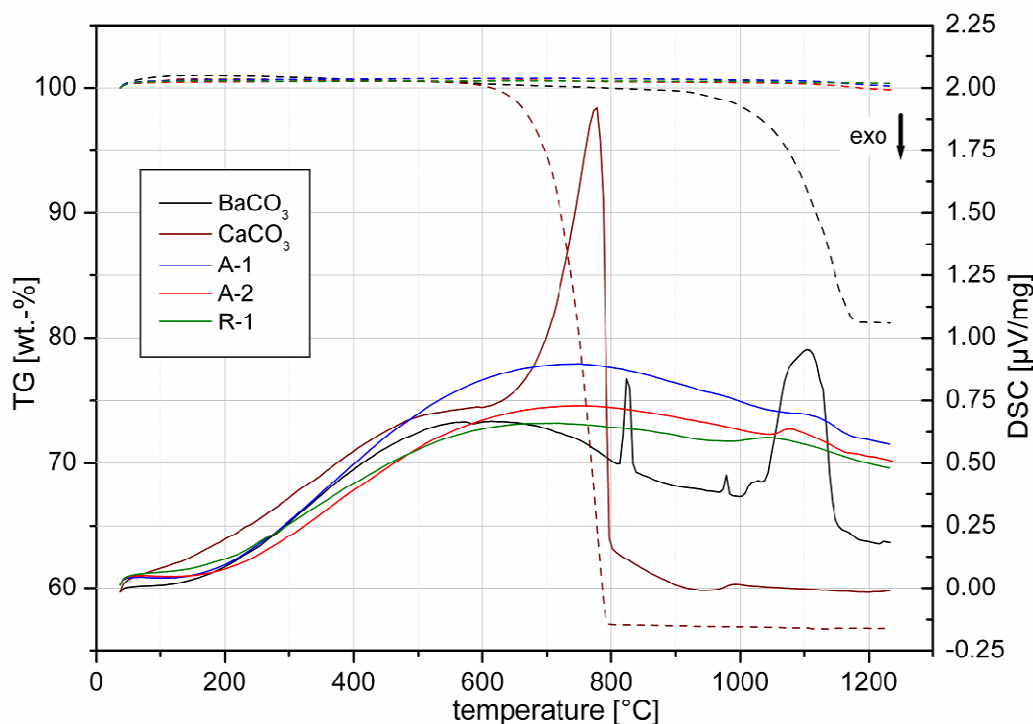
Figure 4.2-II: Simultaneous Thermal Analysis of the raw materials (DSC=solid lines, TG=dashed lines)

Thermal analysis as described in section 3.4.2 is employed to characterize differences between the used titania raw materials during calcination process. The simultaneous thermal analyses of composition A-1a, A-2a and R-1a are presented in Figure 4.2-III (A/B-ratio of 0.998). Moreover, Figure 4.2-IV illustrates the results obtained for b-compositions having an A/B-ratio of 0.985. It is visible from this figures that the TG- and DSC-characteristics show similar progresses for a- and b-compositions over the whole temperature range. The results obtained by analysing the STA-data are summeriszed in appendix Table 8.2-IV. The TG-curves clearly can be divided into three temperature intervals. The 1st ranging from room temperature (RT) to about 550°C, the 2nd between 550°C and 720°C and the 3rd ranging fom 720°C to 1050°C. The first temperature range is characterised by a minor weight loss of 0.6wt.-% to 1.6wt.-% in TG and an exothermic peak in the temperature range from 250°C to 400°C in the DSC-curves. Additionally the mass fragments for water, carbon dioxide and short-chained organic compounds are recorded by gas flow analyses in this temperature range (see for example appendix Figure 8.1-V and Figure 8.1-VI). Thus, the first temperature range includes binder burnout. In the second interval (550°C-720°C) a weight loss of approximately 2.5wt.-% is observed in the TG-curves and the DSC-graphs show an endothermal peak between 650°C and 720°C. The gas analysis in this temperature range clearly recorded carbon dioxide flow. Taking both curve progresses in account, this temperature interval can be attributed to the decomposition of $CaCO_3$ and simultaneous formation of $CaTiO_3$. The detected weight loss exactly represents the theoretical value calculated for $CaCO_3$ decomposition. The third temperature range (720°C-1050°C) denotes the largest weight loss in TG ranging from 13.1wt.-% to 14.0wt.-%. Again, the gas analysis clearly recorded carbon dioxide flow. The DSC-graphs in this temperature range show a sharp peak at about 840°C, which can be attributed to the $BaCO_3$ orthorhombic to tetragonal transformation described above. Furthermore, the

4. Results and discussion

shoulder around 906°C-934°C represents the temperature at which the CO_2-flow reaches its maximum. According to these results, the third temperature interval represents the $BaCO_3$ decomposition and simultaneous $BaTiO_3$ formation. The weight loss detected for $BaCO_3$ decomposition slightly differs from the theoretical value that amounts to 14.2wt.-%.
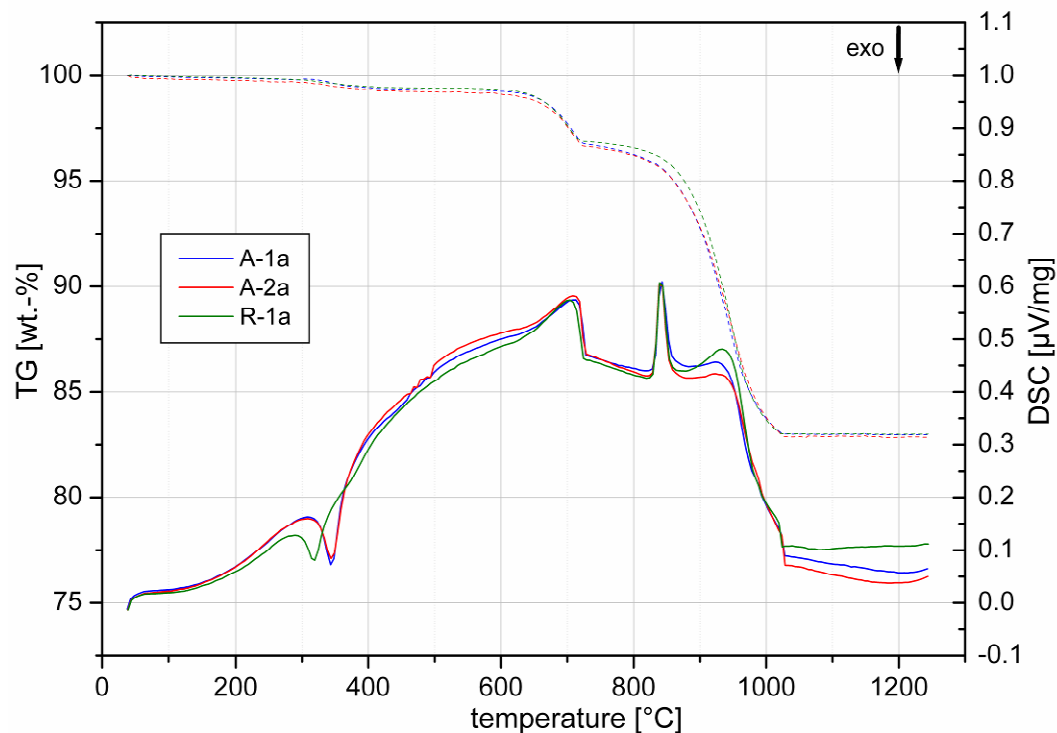
Figure 4.2-III: Simultaneous Thermal Analysis of a-batches A-1a, A-2a and R-1a (DSC=solid lines, TG=dashed lines)
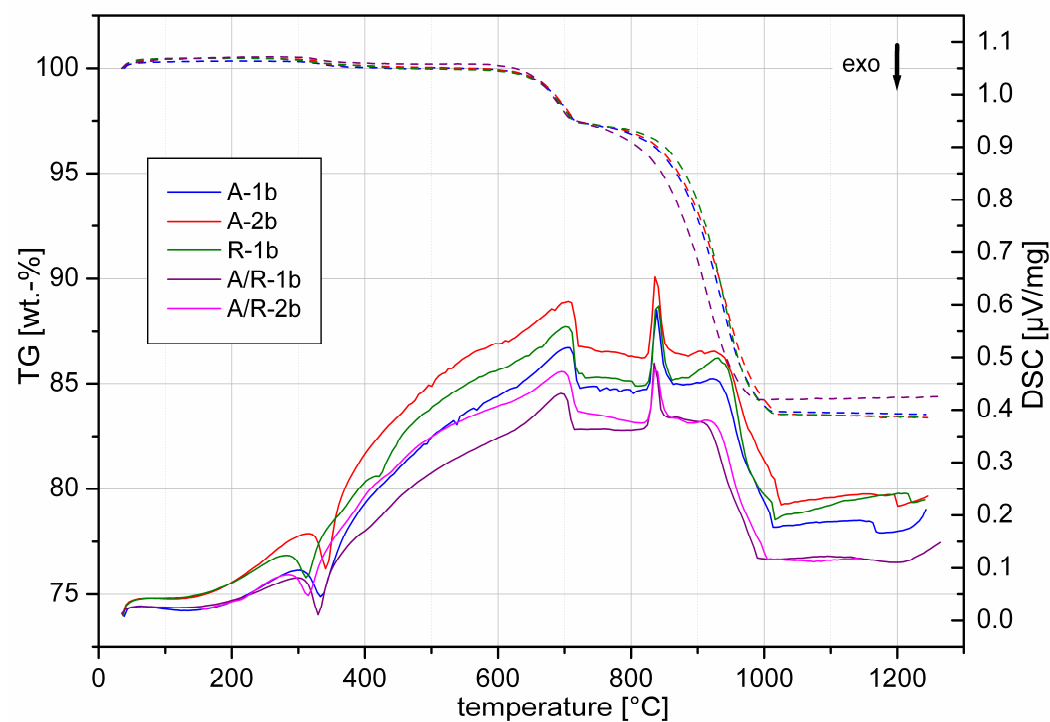
Figure 4.2-IV: Simultaneous Thermal Analysis of all b-batches (DSC=solid lines, TG=dashed lines)

4. Results and discussion

Analysing the differences resulting from the nature of the raw material, only two differences in the STA-progresses can be observed. Firstly, the maximum of the exothermal peak representing the binder burnout is shifted to about 25°C higher temperatures when using anatase TiO_2 (A-1, A-2 and A/R-1 compared to R-1 and A/R-2). This phenomenon most probably can be attributed to differences in the surface adsorption of water and/or binder compounds. Because anatase represents the metastable modification, surface adsorption increases the stability of the crystal particles as described in section 2.1.2 thus increasing the activation energy required for binder burnout. Another effect is visible (especially in Figure 4.2-III) at the shoulder around 920°C (DSC-curves) and in the TG-graphs between 800°C and 900°C. Using the rutile material R-1a results in slightly delayed $BaCO_3$ decomposition, i.e. the reaction rate of the $BaTiO_3$ formation below 850°C is lower when compared to the anatase materials but increases faster above 850°C. This effect can be ascribed to the differences in raw material BET (see Table 4.2-I). Similar observations have been made by Fernandez et al. [Fer-91/2] who investigated the the influence of the TiO_2 crystal structure and morphology on the solid-state synthesis of $BaTiO_3$.

Comparable to the thermal properties of the titania raw materials the calcination process is endothermal over a wide temperature range. The differences in calcination behaviour between the titania raw materials thus can be expressed by comparing the overall energy consumption during calcination between 100°C and 1025°C. These values are presented in Table 4.2-I. A correlation between the BET values of the titania raw material and the energy consumption during calcination is illustrated in Figure 4.2-V. On the one hand, this correlation does not show a direct dependence of the energy consumption on the raw material nature for a-compositions. On the other hand, such a correlation can be illustrated for the b-compositions. It is assumed that this observation can be attributed to the differences in titanium excess in b-compositions that will further be discussed in section 4.3.1 by considering the microstructure.

Table 4.2-I: Summary of the STA characteristic values compared to relevant correlating values

Batch	Weight loss (50-1050°C) [wt.-%]	Peak area (100-1025) [μVs/mg]	ρ [Ωcm]	BET calcined powder [m²/g]	BET calcined powder [%]	BET TiO₂ [m²/g]
A-1a	17.0	1468	3.19E+05	1.18	11.5	10.28
A-2a	17.0	1461	2.04E+06	1.15	12.3	9.38
R-1a	17.0	1463	1.23E+02	0.92	15.2	6.06
A-1b	17.1	1065	1.42E+03	0.84	8.2	10.28
A-2b	17.4	1301	2.75E+03	1.06	11.3	9.38
R-1b	17.1	1148	3.28E+01	0.76	12.6	6.06
A/R-1b	17.0	901	2.46E+01	0.77	5.4	14.25
A/R-2b	17.7	1095	2.27E+01	0.83	8.2	10.17
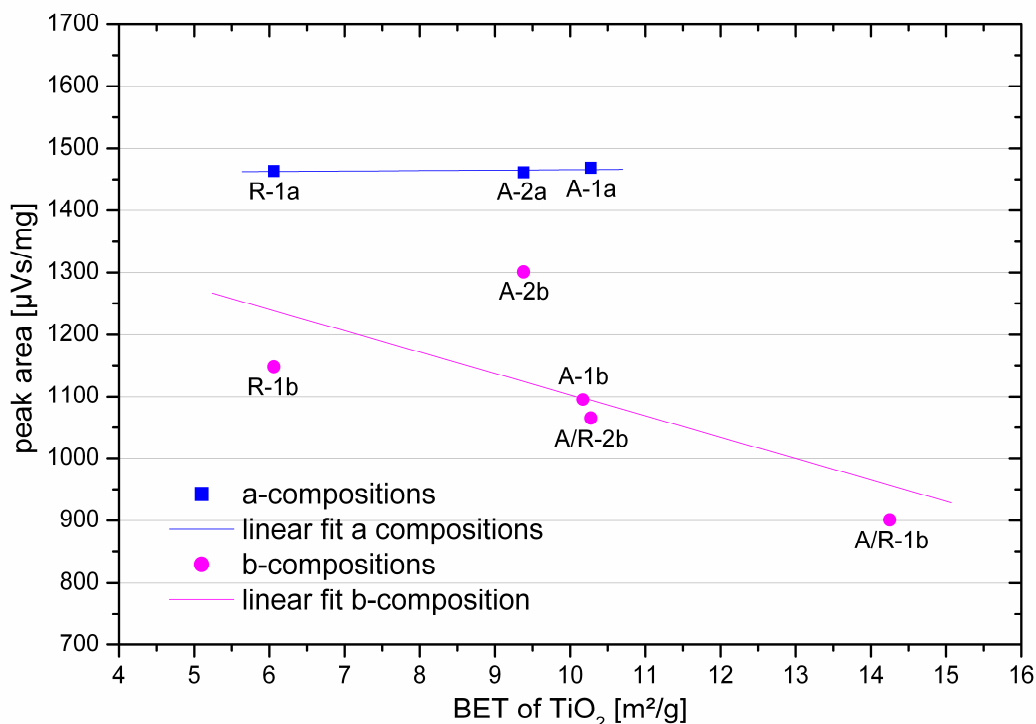
Figure 4.2-V: Correlation between the BET of the titania raw materials and the energy consumption (100-1025°C) of the compositions during calcination

4.2.3. Results of X-ray diffraction analyses

Table 4.2-II and Table 4.2-III summarize the quantified phase compositions analysed by Rietveld refinement. In addition, Figure 8.1-VII and Figure 8.1-VIII (appendix) show the zoomed section of the X-ray diffraction spectra between 20 and 50 degree 2Θ for the calcined powders. Spectra of the corresponding sintered parts are again depicted in appendix Figure 8.1-IX and Figure 8.1-X.

As a consequence of the two-stage $CaTiO_3$ and $BaTiO_3$ formation during calcination (see section 4.2.2) it is assumed that the formation of $(Ba,Ca)TiO_3$ solid solution proceeds only to some extend. This assumption is confirmed by the results obtained by XRD phase analysis. It can be seen from Table 4.2-II and Table 4.2-III that all calcined powders contain notable amounts of $CaTiO_3$. Generally, the a-batch powders are composed of barium-calcium titanate representing the main compound, calcium titanate, fresnoit ($Ba_2TiSi_2O_8$) that crystallises from the silicon liquid phase during cooling and $Ba_4Ti_{13}O_{30}$ a titanium-rich secondary phase. Additionally the b-batches contain of one further compound namely $Ba_6Ti_{17}O_{40}$ which forms due to the higher titanium excess (see phase diagrams in section 2.2.5). Comparing the a- and b-batches it is evident that the amount of secondary phases is about 5wt.-% higher in the Ti-rich b-batches. The TiO_2 modification in this context seems to be irrelevant. After sintering the $CaTiO_3$ secondary phase as well as the Ti-rich phase $Ba_4Ti_{13}O_{30}$ are disappeared and the parts only consist of $(Ba,Ca)TiO_3$, Fresnoite and the Ti-rich secondary phase $Ba_6Ti_{17}O_{40}$. Compared to the calcined powders the amount of secondary phases is decreased to approximately 4wt.-% for a-batches and 5wt.-% for b-batches. Furthermore an estimation about the dopant incorporation is attempted by comparing the lattice parameters of the $(Ba,Ca)TiO_3$ solid solution which are

represented by the c/a-ratio (see Table 4.2-II and Table 4.2-III). In the material system investigated here the c/a-ratio, which represents the tetragonality of the crystal, is decreased with enhanced donor dopant content due to an increase in the lattice parameter a [Tsu-00, Bus-01, Hen-01/2, Par-09]. The results illustrate that such a change in lattice parameter cannot be observed here because the c/a-ratio values amount to 1.010 and 1.011 for the calcined powder and to 1.011 and 1.012 for the sintered parts. With the results obtained by XRD, it can be concluded that the macroscopic phase composition for all batches is similar.

Table 4.2-II: Phase composition of the calcined powders detected by X-ray diffraction

calcined powder	c/a-ratio of (B,C)T	(B,C)T	CT	B_2TS_2	B_4T_{13}	B_6T_{17}
A-1a	1.010	93.8	2.7	0.7	2.8	n.d.
A-2a	1.010	94.5	2.6	n.d.	2.9	n.d.
R-1a	1.011	93.6	3.2	0.7	2.5	n.d.
A/R-1a	1.011	94.0	2.8	1.3	1.9	n.d.
A/R-2a	1.011	94.6	2.3	0.9	2.1	n.d.
A-1b	1.011	89.8	4.0	1.1	2.4	2.7
A-2b	1.010	89.6	2.9	0.8	3.5	3.2
R-1b	1.011	89.7	4.8	0.8	2.4	2.3
A/R-1b	1.011	89.2	5.0	1.2	1.9	2.6
A/R-2b	1.011	89.8	4.6	1.0	2.0	2.6

Table 4.2-III: Phase composition of the sintered parts detected by X-ray diffraction

sintered parts	c/a-ratio of (B,C)T	(B,C)T	B_2TS_2	B_6T_{17}
A-1a	1.011	96.6	1.3	2.1
A-2a	1.012	96.3	1.3	2.4
R-1a	1.011	96.4	1.1	2.5
A-1b	1.012	95.4	1.7	2.9
A-2b	1.012	95.3	1.7	3.0
R-1b	1.012	95.6	1.5	2.9
A/R-1b	1.012	95.0	1.8	3.2
A/R-2b	1.012	95.1	1.6	3.3

4.2.4. Interpretation of the synthesis process results

Since the thermal and process analysis showed differences in the calcination process between anatase and rutile based batches, it is assumed that the formation mechanism itself is affected by the raw material nature and properties. As already mentioned in section 4.2.1 the BET values of the calcined powders vary with respect to the BET of the TiO_2 powder. Micrographs of the calcined powders A-1a, A-2a and R-1a are depicted in Figure 4.2-VI to Figure 4.2-VIII. These pictures clearly demonstrate the differences in morphology of the calcines. The rutile reference R-1a (Figure 4.2-VI) shows relatively homogeneous round-grained aggregates with a BET of 0.92m²/g (see appendix Table 8.2-III). On the contrary, the anatase batches A-1a (Figure 4.2-VII) and A-2a (Figure 4.2-VIII), which have BET values of 1.18 and 1.15m²/g respectively, show inhomogeneous bimodal particle aggregates. These aggregates contain of larger round-grained particles and

4. Results and discussion

smaller irregular floret-shaped aggregates that adhere to the surfaces of the larger particles, the latter being responsible for the higher BET of the calcined powders.

The question to be discussed is how the calcination process or rather the $(Ba,Ca)TiO_3$ formation proceeds in anatase and rutile batches to produce the differences in calcine properties. Further questions will regard the relation between the properties of the calcine and their relevance for sintering.
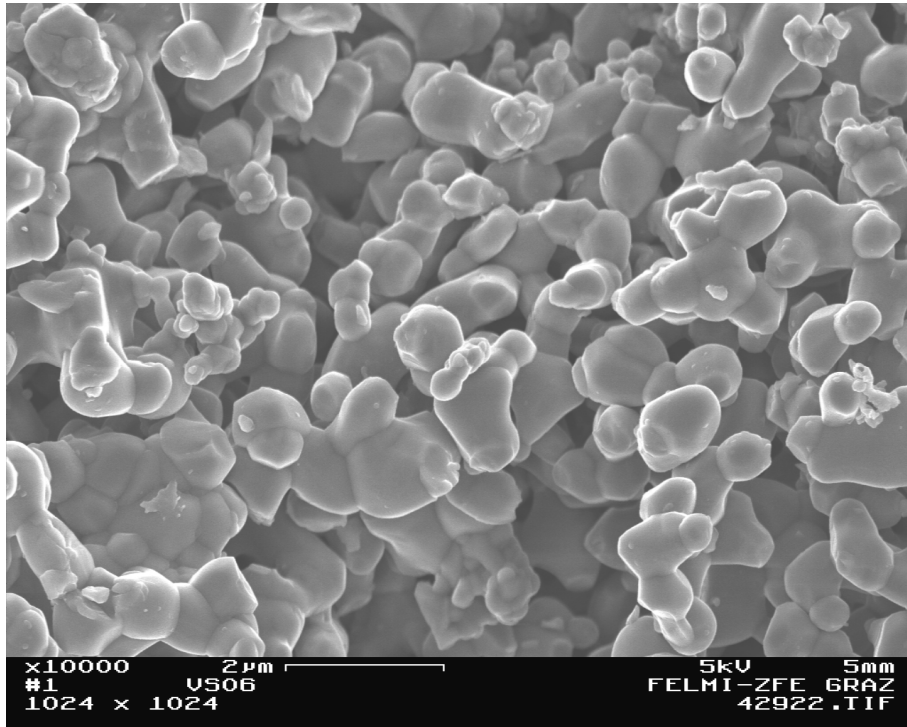
Figure 4.2-VI: SEM-micrograph of the calcined powder of composition R-1a; scale bar 2µm
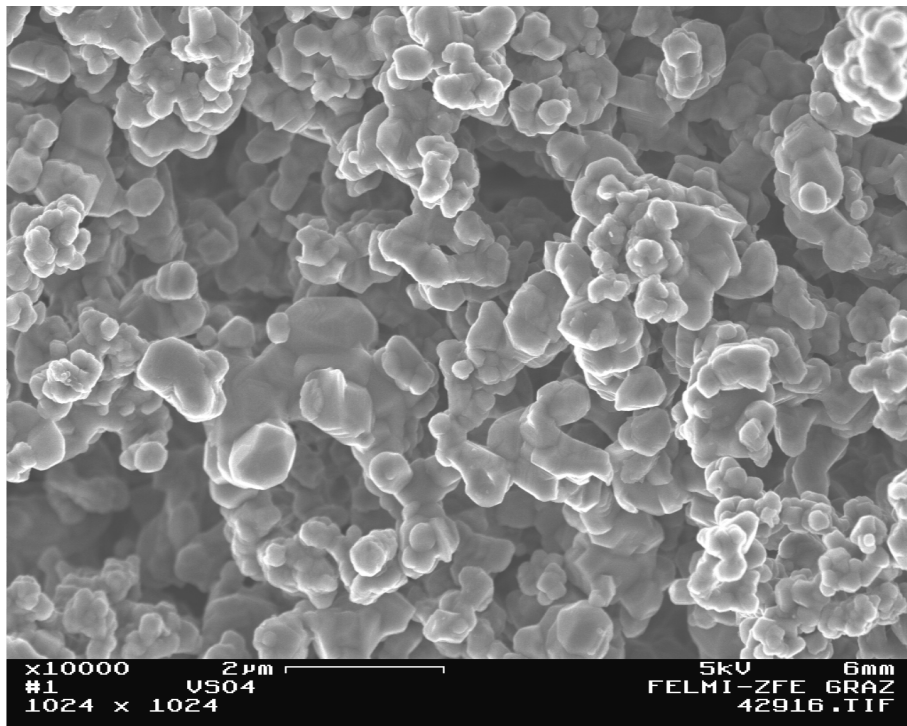
Figure 4.2-VII: SEM-micrograph of the calcined powder of composition A-1a; scale bar 2µm

4. Results and discussion
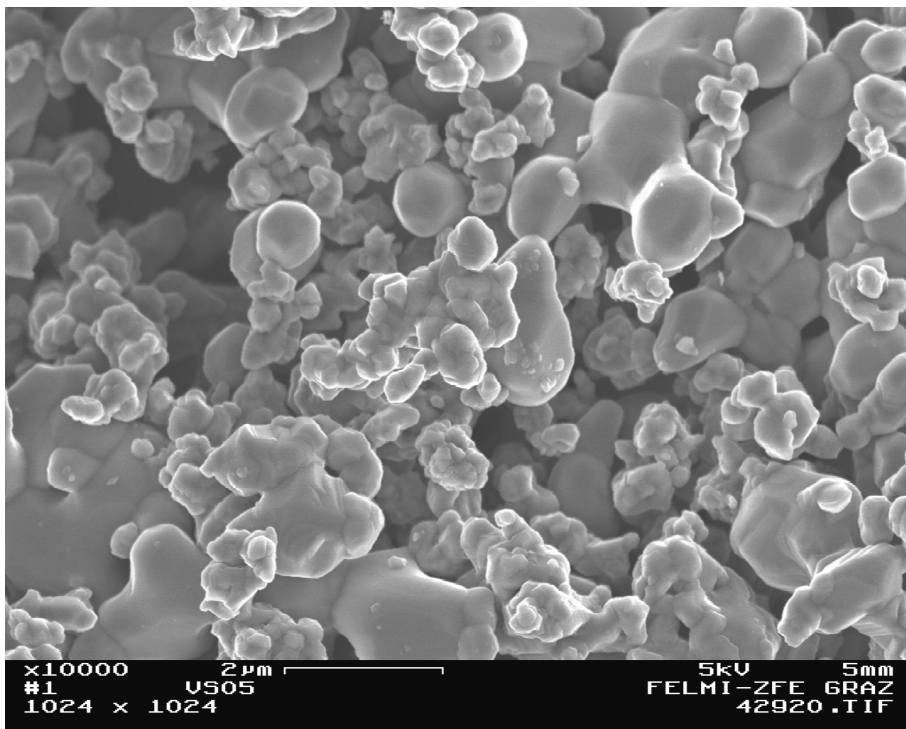
Figure 4.2-VIII: SEM-micrograph of the calcined powder of composition A-2a; scale bar 2µm

The widely accepted mechanism of $BaTiO_3$-formation using solid-state synthesis has been reviewed in section 2.2.2. This mechanism, which is schematically drawn in Figure 4.2-IX and had been described by Tsutai et al. [Tsu-01], is assumed to occur in compositions prepared from rutile-TiO_2 (R-1) and rutile-anatase mixture materials (A/R-1 and A/R-2). This mechanism leads to uniformly shaped calcined powders as presented in Figure 4.2-VI.

4. Results and discussion
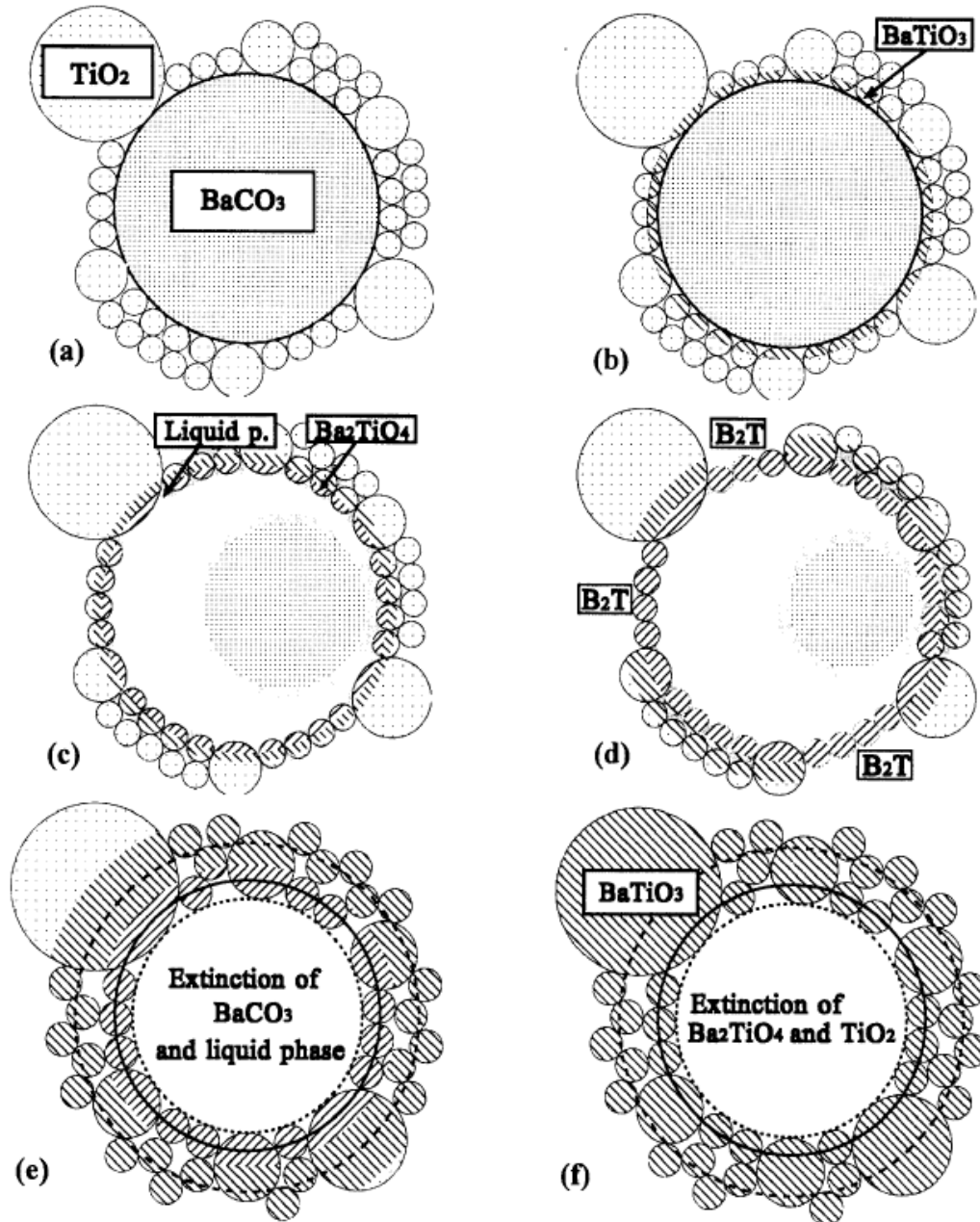
Figure 4.2-IX: Schematically drawn $BaTiO_3$ formation mechanism (after [Tsu-01])

On the contrary, a modified mechanism is proposed for the solid-state formation of the anatase compositions (A-1 and A-2). The proposed formation mechanism is based on the observations made by the group of Caballero and Fernandez [Fer-91/1, Fer-91/2, Cab-95] and Wang et al. [Wan-98]. These authors investigated the phase formation and dielectric properties in phosphorus doped $BaTiO_3$.

Based on their observations and the results obtained in this work, the modified solid-state formation mechanism of $(Ba,Ca)TiO_3$ prepared from phosphor-containing anatase TiO_2 can be described in the following manner. Resulting from the preparation conditions, phosphorus, which is added as mineraliser during TiO_2 calcination (see section 2.1.1), covers the anatase grains in order to stabilize the metastable modification at room temperature. During initial $BaCO_3$ and $CaCO_3$ decomposition at temperatures above 650°C the adsorbed phosphor-layer reacts

4. Results and discussion

with the diffusing Ba- and Ca-ions to form a low melting liquid phase with high P_2O_5 content. The corresponding phase diagram for the $BaO-P_2O_5$ system, which is depicted in Figure 4.2-X, has been described by McCauley and Hummel [McC-68]. It is assumed that the same is valid for the $CaO-P_2O_5$ system due to the glass forming tendency of the phosphor oxide especially in combination with alkaline or alkaline earth metals [Sch-90, Rao-02]. This phosphor-rich liquid phase, which consequently is located at the surface of the titania grains, further accelerates the Ba- and Ca-ion diffusion from the decomposing carbonate grains through the liquid phase into the titania particles hence accelerating the $BaTiO_3$ formation at the interface. Accordingly with increasing temperature the barium and calcium concentration within the liquid phase increases whereas the orthotitanate (B_2T) formation is reduced and finally $Ba_3(PO_4)_2$ and $Ca_3(PO_4)_2$ are formed. These compounds are high melting solids which cover the $BaTiO_3$ grains. As a consequence of the barium consumption the A/B-ratio in compositions containing anatase TiO_2 is shifted toward titanium excess at least in localized regions (local inhomogenities). Accordingly exaggerated grain growth can be observed in such compositions as illustrated for the calcined powders of A-1a and A-2a in Figure 4.2-VII and Figure 4.2-VIII [Mau-87, Fer-91/1, Cab-95, Lin-91]. Additionally the TiO_2 grain size similarly affects the decomposition rate of the carbonates because an increase in reactivity due to increased BET enhances the $(Ba,Ca)TiO_3$ formation [Spi-61, Suy-75/1, Suy-75/2, Suy-77]. The grain size effect thus enhances the phosphorus effect. This is at least valid for the b-compositions as has been demonstrated in Figure 4.2-V in section 4.2.2.
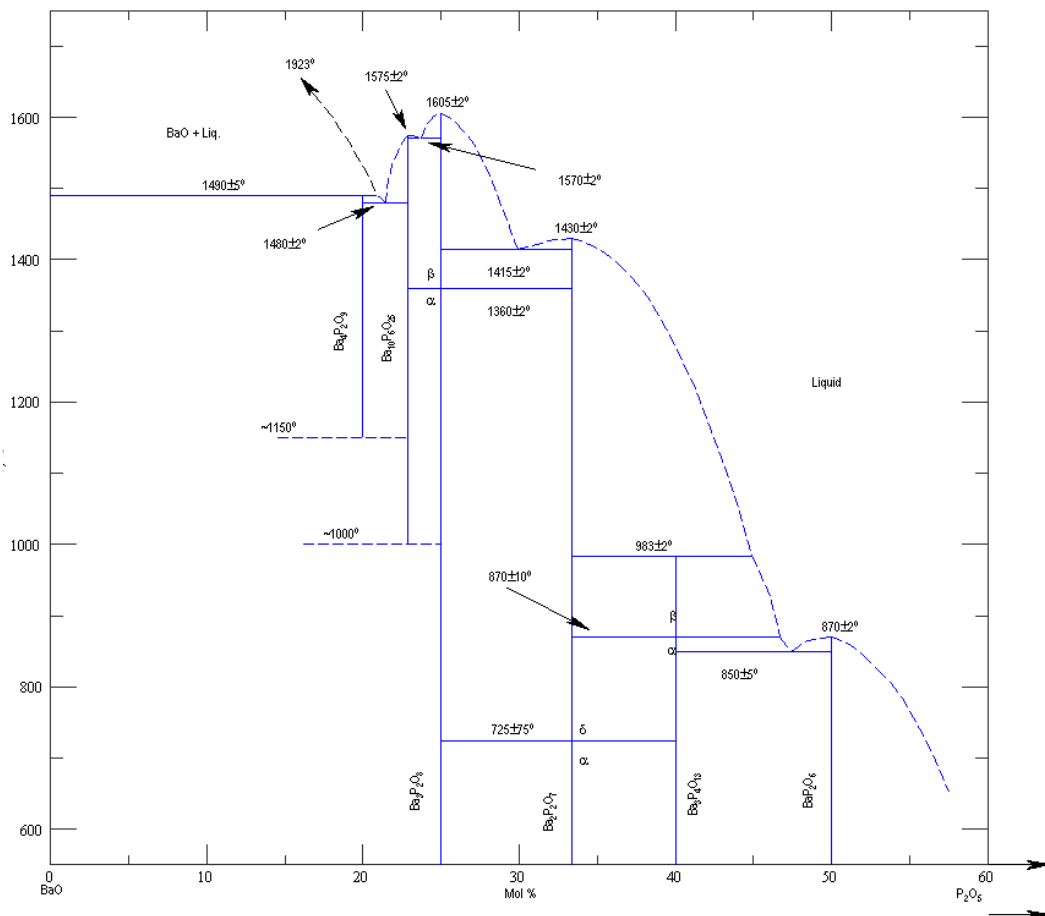
Figure 4.2-X: Phase diagram of the partial system $BaO-BaP_2O_6$ (after [McC-68])

4. Results and discussion

Additional verification for the proposed mechanism is given by the high-temperature XRD measurements depicted in Figure 4.2-XI and Figure 4.2-XII for compositions A-2a and R-1a respectively. These figures clearly demonstrate that the well known mechanism confirmed by Spieß, Kubo, Beauger and Tsutai [Spi-61, Kub-67, Bea-83/1, Tsu-01] cannot be applied to the phosphor containing anatase batches. In this case the anatase compositions would have shown lower decomposition rates and higher amounts of secondary phases compared to the rutile reference [Spi-61, Suy-75/1, Suy-75/2, Yam-76, Bea-83/1, Bea-83/2, Ish-87, Fer-91/2]. This is clearly not the case. Rather the anatase materials show lower secondary phase contents (see spectra at 900°C) and the $BaTiO_3$ formation is finished at somewhat lower temperatures (see spectra at 950°C). Additionally such a shift in decomposition temperature and rate is not observed in the thermal analyses which in fact support the high temperature XRD results especially for the a-compositions as described in section 4.2.2 (Figure 4.2-III).

Another question to be answered is why the phosphor containing secondary phases are not detectable in XRD. This effect can on the one hand be attributed to the uncertainties of the method as described elsewhere [Din-08/1] and on the other hand to the location of such secondary phases. The phosphor containing and barium enriched phases are always located at the grain surfaces of the TiO_2 grains and after calcination at the surfaces of the formed $BaTiO_3$ particles. The location together with the small concentrations of phosphor impurities thus result in very thin surface layers of less than 100nm thickness. On the contrary diffracted X-rays escape from an interaction volume of micrometer range depending on the accelerating voltage [Din-08/1]. Additionally such a thin surface layer may not be well crystallized, which is of fundamental importance for XRD measurements due to the fact that vitreous materials cannot diffract X-rays.

A similar explanation can be given for the XRF method. From XRF-measurements the A/B-ratio of the materials can directly be calculated. The results are shown in appendix Table 8.2-III. For anatase materials (a-compositions) the results clearly show Ba-excess in the calcined powder which is not detected in the rutile material. Or the other way around, in anatase compositions there seems to be titanium consumption during calcination. But this statement is not supportable because the applied sample preparation process gives no evidence for material losses (see section 3.3). Thus the measured Ba-excess most probably results from the sample properties and their relation with the method. Due to the proposed mechanism described above, Ba-rich secondary phases surround the $BaTiO_3$ grains. It is supposed that this layer at least partly absorbs the fluorescence radiation leading to a shift in the detected composition. Otherwise it makes no sense why during calcination titanium should be consumed and during sintering barium content should be reduced.

Additionally it is worth to note that the effect of titanium consumption during calcination to a lower extend also occurs in anatase based b-batches, which in contrast to the a-compositions do not result in Ba-excess. This is to be expected when taking into account the much higher titanium excess of 1.3mol-% in b-compositions.

4. Results and discussion
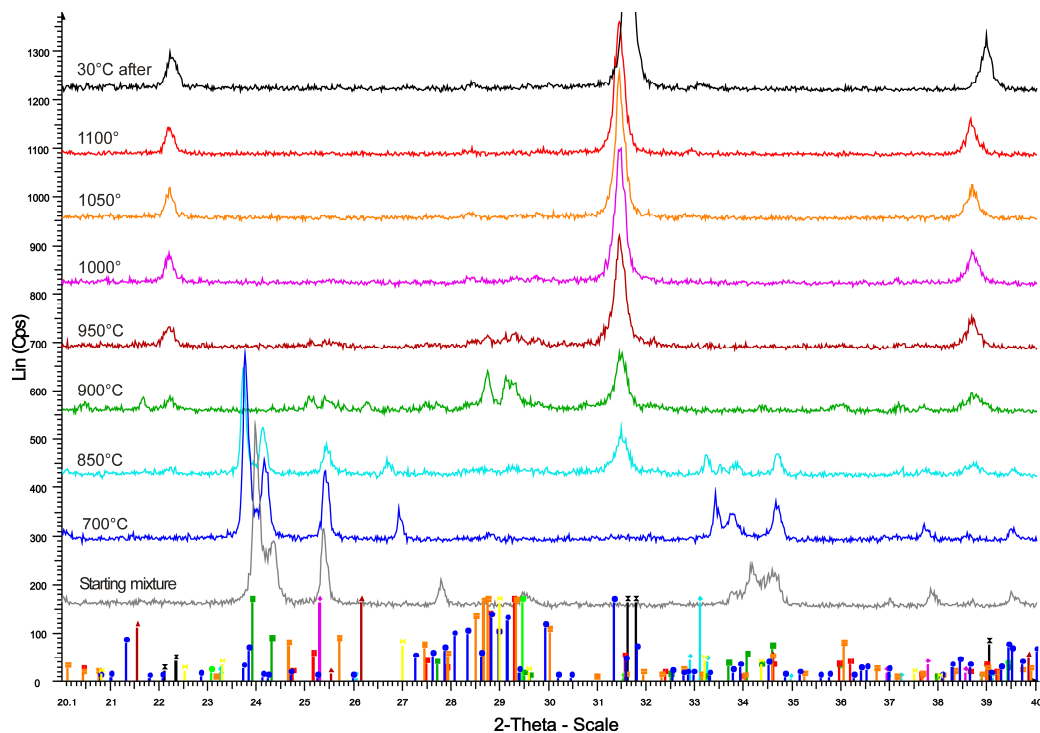
Figure 4.2-XI: high temperature XRD of composition A-2a
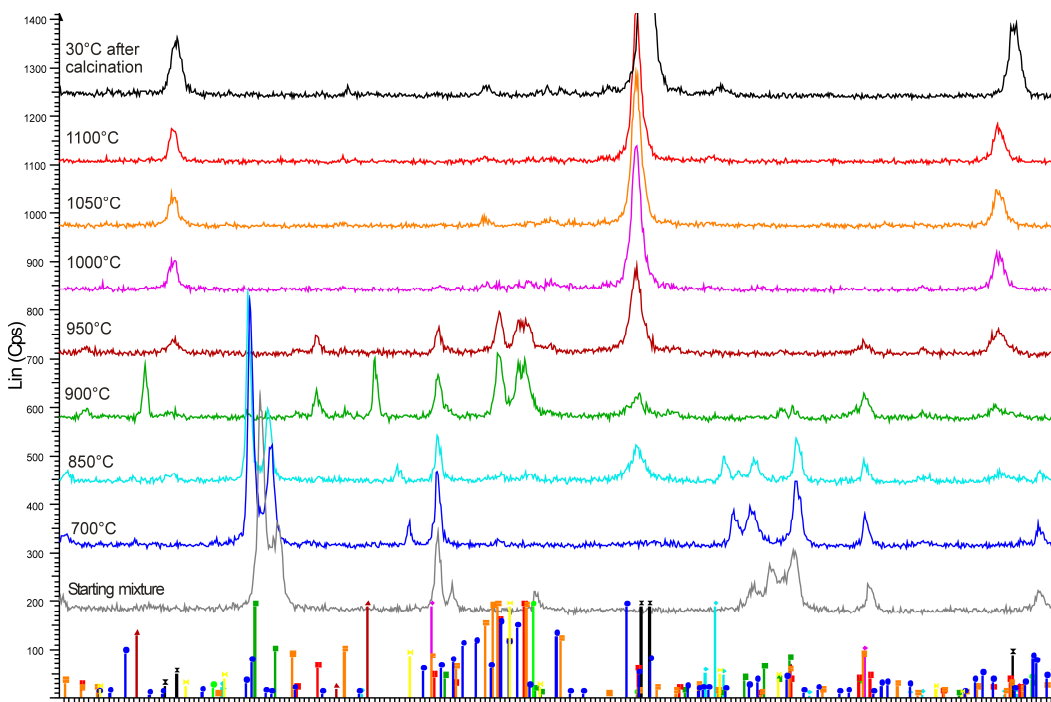
Figure 4.2-XII: high temperature XRD of composition R-1a

Finally, an assumption should be made regarding the effect of the differing calcination mechanism on the sintering behaviour of the materials. Starting with the calcined powder that contains $BaTiO_3$ and several barium- and titanium- rich secondary phases, the secondary phases act as barriers to volume diffusion during initial sintering [Sal-07]. At elevated temperatures titanium enrichment, which occurred during calcination, increases liquid phase formation thus accelerating the

formation of a homogeneous microstructure. This supposed effect and its consequences on the PTCR-characteristic are discussed in detail in section 4.3.6.

4.3. Investigation of the microstructure

The purpose of this section is firstly to illustrate and compare the obtained microstructures of compositions a and b (section 4.3.1 and 4.3.2). Secondly, the differences in microstructure chemistry are detected and analysed by the use of SEM, TEM and EPMA (section 4.3.3, 4.3.4 and 4.3.5). Finally, the results are discussed in relation to the PTCR performance (section 4.3.6).

4.3.1. SEM micrographs

Microscopic studies were performed in the manner described in section 3.4.5 to figure out the variation in microstructure with respect to the average grain size (section 4.3.1) and chemical composition (section 4.3.3).

Micrographs of the cross-sectioned and polished samples are depicted in Figure 4.3-I to Figure 4.3-X. Additionally the average grain-size values determined by linear analysis of the SEM micrographs are summarised in Table 4.3-I.

Table 4.3-I: Average grain sizes of the sintered parts

Batch	Average grain size [µm]	Batch	Average grain size [µm]
A-1a	5.23	A-1b	9.46
A-2a	4.73	A-2b	9.00
R-1a	4.53	R-1b	5.47
A/R-1a	4.63	A/R-1b	5.62
A/R-2a	4.05	A/R-2b	5.95

| WD = 3.8 mm | Width = 99.94 µm | 10 µm | | u35111.tif | |
| EHT = 15.00 kV | Detector = AsB | | 04A | FELMI-ZFE-GRAZ | |
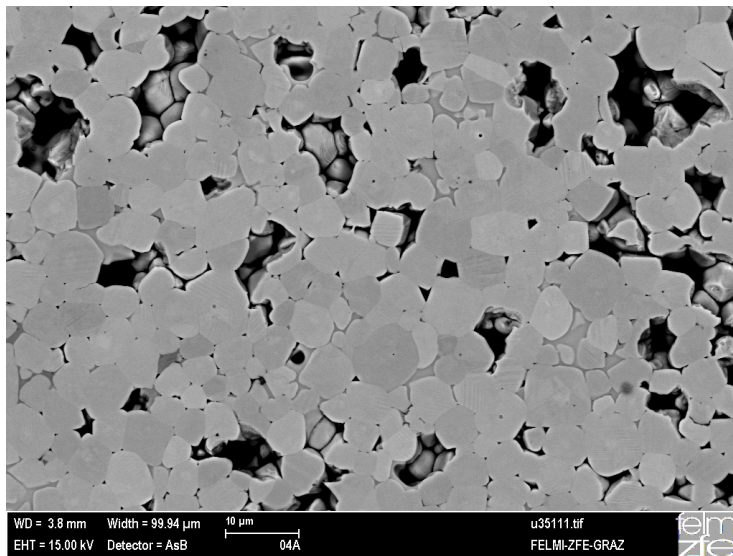
Figure 4.3-I: A-1a SEM micrograph; picture width 100µm

4. Results and discussion
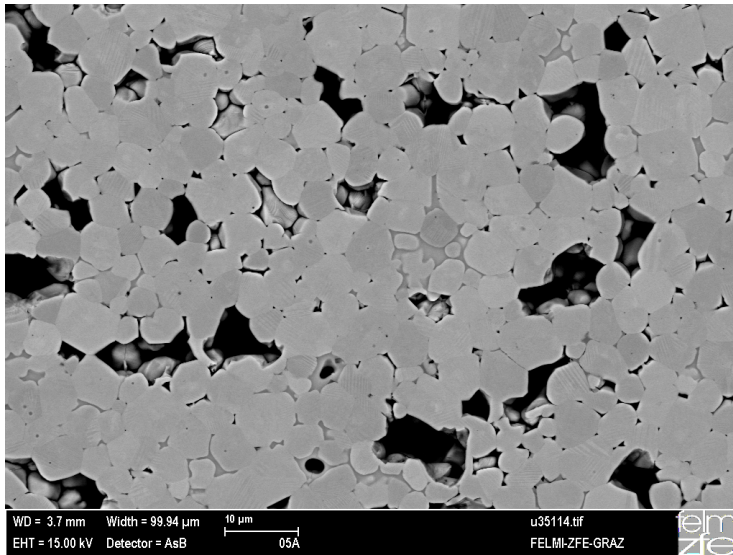
Figure 4.3-II: A-2a SEM micrograph; picture width 100µm
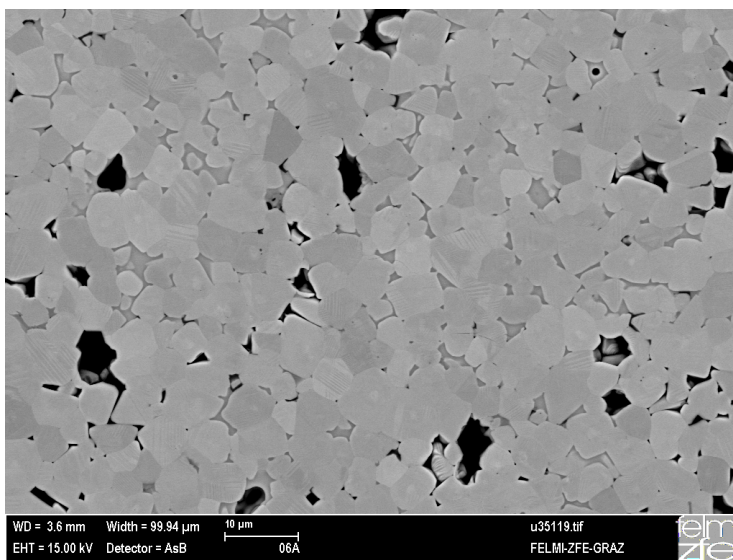
Figure 4.3-III: R-1a SEM micrograph; picture width 100µm
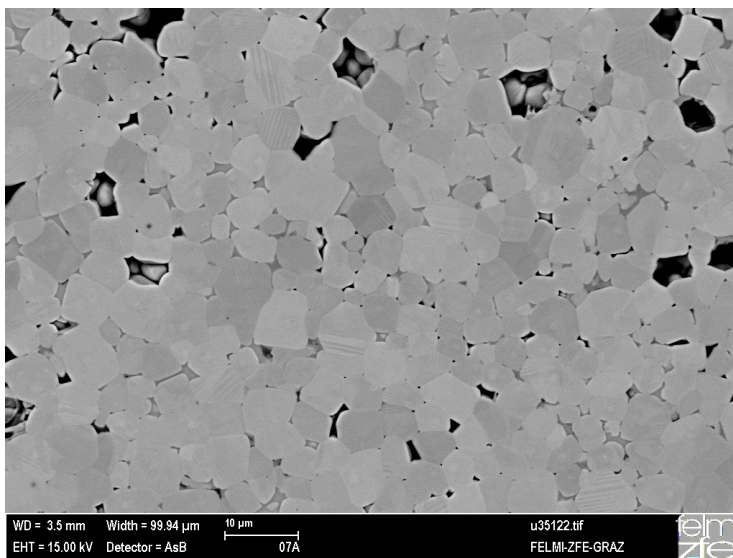
Figure 4.3-IV: A/R-1a SEM micrograph; picture width 100µm

4. Results and discussion
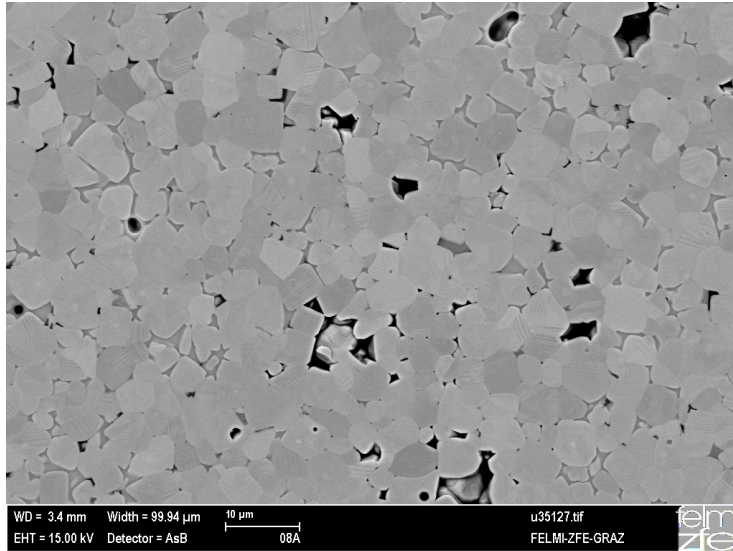
Figure 4.3-V: A/R-2a SEM micrograph; picture width 100µm

Comparing the microstructures of the a-batches (Figure 4.3-I to Figure 4.3-V), it is evident that the grain size in general is not affected by the raw material nature but the amount and size of pores varies significantly. For the anatase batches A-1a and A-2a the average grain size amounts to 5.2µm and 4.7µm respectively, whereas the rutile reference shows an average grain size of 4.5µm. The anatase-rutile mixture materials A/R-1a and A/R-2a again slightly differ from the rutile reference with values of 4.6µm and 4.1µm respectively. Furthermore, the micrographs of a-batches show that the pores in the anatase-based materials appear to be roughly doubled in size and quantity. Accordingly, the slightly increased average grain size of the anatase a-batches becomes comprehendible when considering the porosity. The differences in porosity can easily be illustrated by comparing the geometric densities of the sintered materials as shown in Table 4.3-II together with the hydrostatic weighing densities and the open porosities. For reference the theoretical density (TD) obtained from XRD-analyses is used which amounts to 5.87g/cm³ for the theoretical composition $(Ba_{0.85},Ca_{0.15})TiO_3$. This value for TD is valid for the sintered parts of a- and b-batches. The geometric densities clearly show differences between anatase- and rutile-based materials. The geometric densities of the anatase based batches A-1a and A-2a account for approximately 90% of the TD. Contrary the rutile reference and the anatase-rutile mixture materials show values of about 92% of the TD. Moreover, the hydrostatic densities do not show such dependence. This effect can be attributed to the type and quantity of porosity taken into account with the measurement i.e. the geometric density characterises the material including open and closed porosity whereas the hydrostatic density excludes the open porosity. In general the anatase based materials show lower open porosity values, which in the first instance seem to be contradictory to the geometrical density values. Taking both density measurements and the micrographs into account, it can be concluded that anatase based compositions contain a significantly higher quantity of closed porosity. This indicates that the sintering mechanism in anatase based materials differ from the behaviour of the rutile reference material as supposed above (section 4.2.4). This effect and its consequences on the PTCR-characteristic will be discussed in detail in section 4.3.6.

4. Results and discussion

Table 4.3-II: Comparison of densities obtained for basic batches

Batch	Geometric density	Geometric density	Hydrostatic sintering density	Hydrostatic sintering density	Open porosity
	[g/cm³]	[%TD]	[g/cm³]	[%TD]	[%]
A-1a	5.27	89.78	5.33	90.74	1.77
A-2a	5.28	89.95	5.42	92.38	0.99
R-1a	5.40	91.99	5.43	92.60	2.01
A/R-1a	5.42	92.33	5.47	93.27	2.07
A/R-2a	5.42	92.33	5.40	92.10	2.41
A-1b	5.23	89.10	5.35	91.22	2.31
A-2b	5.24	89.27	5.35	91.21	2.32
R-1b	5.26	89.61	5.32	90.78	2.43
A/R-1b	5.29	90.12	5.31	90.60	2.56
A/R-2b	5.28	89.95	5.32	90.69	2.67

The mentioned density dependence to a lower extend also is observed in b-compositions. In contrast to the a-batches, the grain size of the b-compositions strongly varies between anatase and rutile based compositions. On the one hand, the anatase-based materials A-1b and A-2b have average grain sizes of 9.5µm and 9.0µm respectively. Further, the rutile reference and the anatase-rutile mixture materials show average grain sizes between 5.5µm and 6.0µm. Indeed this discrepancy cannot be attributed to differences in porosity as can be seen from Table 4.3-II. Once more these results confirm the assumption that a modified sintering mechanism provokes the differences in microstructure and consequently in PTCR-characteristics (see section 4.3.6).
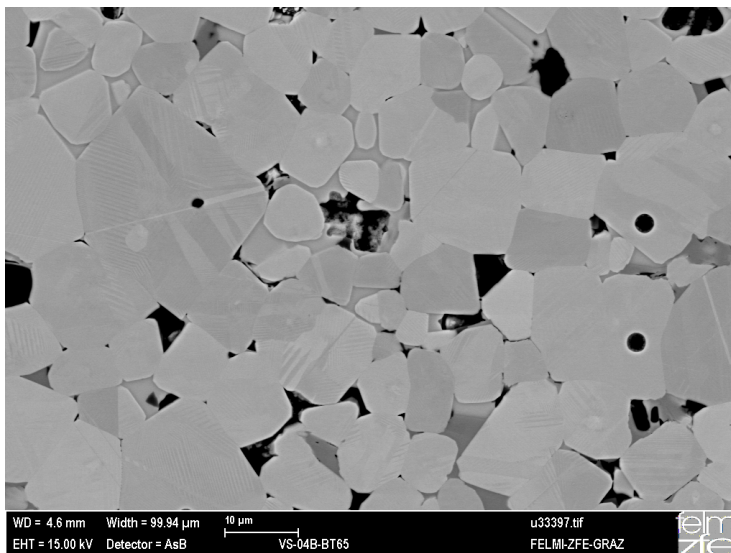
Figure 4.3-VI: A-1b SEM micrograph; picture width 100µm

4. Results and discussion
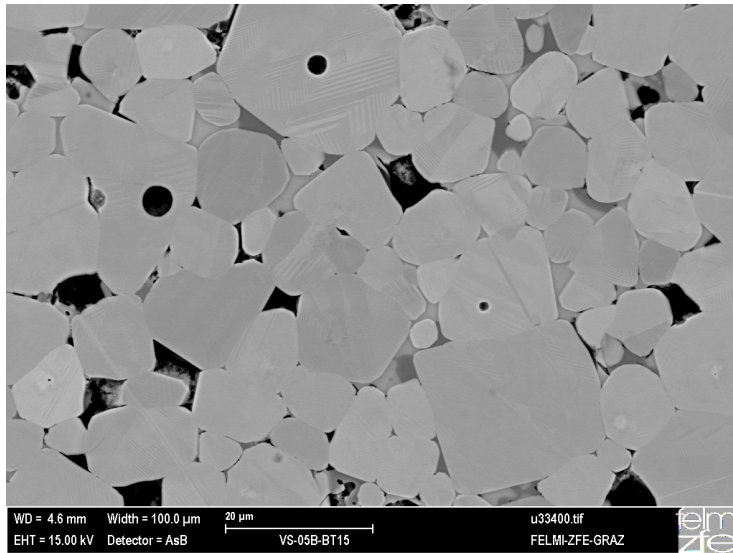
Figure 4.3-VII: A-2b SEM micrograph; picture width 100µm
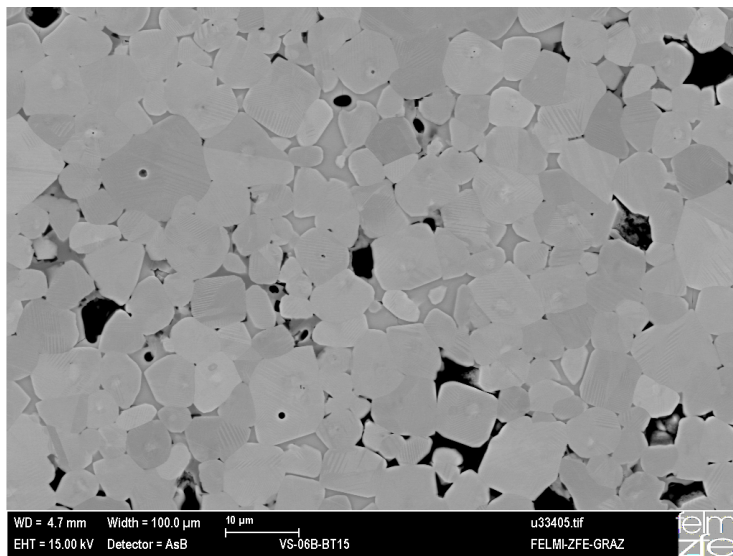
Figure 4.3-VIII: R-1b SEM micrograph; picture width 100µm
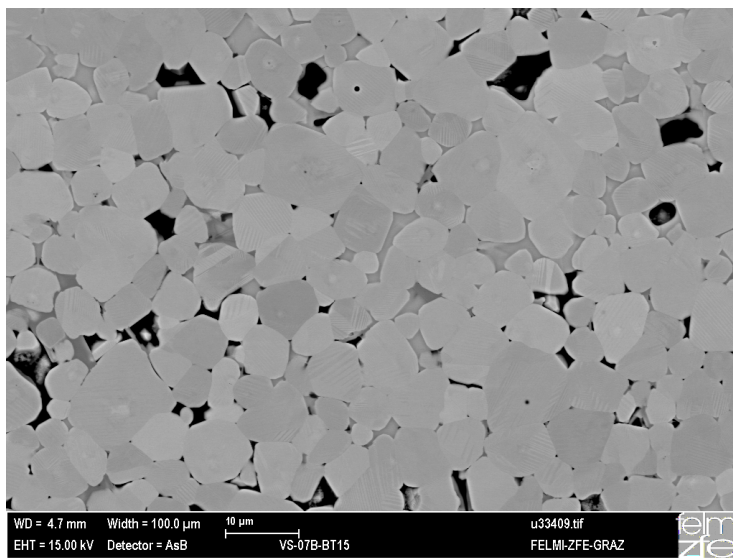
Figure 4.3-IX: A/R-1b SEM micrograph; picture width 100µm
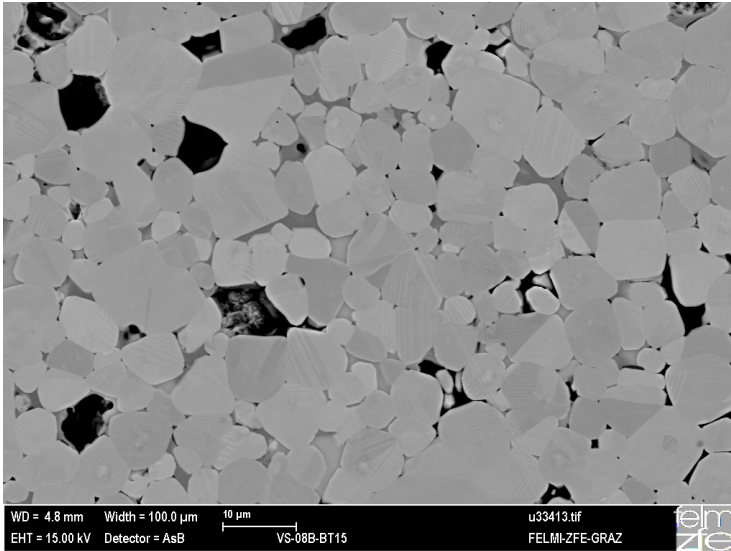
Figure 4.3-X: A/R-2b SEM micrograph; picture width 100µm

Finally a comprehensive view on the microstructures of the basic batches shows that the grains are not uniformly in size but rather exhibit a multimodal grain size distribution i.e. some grains are coarse and some remain fine. This is especially obvious in b-compositions. For example, in R-1b, A/R-1b and A/R-2b the coarse grains have sizes above 10µm and the fine grains range below 5µm. This observation is of fundamental interest because it can directly be related to the anomaly of grains size and conductivity as modelled by Drofenik [Dro-87, Dro-90, Dro-93, Dro-99, Dro-02] and reviewed in section 2.2.5. Ultimately, this means that for b-batches the observed differences in microstructure at least partially give rise to the variation in PTCR-characteristics (see section 4.3.6).

4.3.2. Electron backscattering diffraction

Besides grain size another microstructural feature is known, which influences the height and shape of the PTCR-jump, that is to say the number of electrical inactive low Σ grain boundaries [Nem-80, Oga-95, Kuw-96, Hay-96, Ger-01, Sea-05, Ran-05]. Fundamentally, low Σ grain boundaries originate from geometric relations between adjacent crystal grains i.e. such grains periodically share some of the crystal atoms. This relation is theoretically described by the coincident site lattice (CSL) theory for crystalline ensembles [Ger-01]. In short, this notation means the lower the Σ value the higher is the geometric relation between adjacent grains. The role of low Σ grain boundaries on the PTCR was investigated by several authors since the 1980´s e.g. by Kuwabara et al. [Kuw-96] or Seaton and Leach [Sea-05]. The latter found that low Σ grain boundaries, in particular Σ 3, 5 and 9 boundaries, are inactive with respect to the PTCR-effect hence influencing the steepness of the PTCR characteristics. Seaton and Leach explained this behavior by taking into account that the grain boundary oxidation during cooling from sintering temperature is diminished, which results in lower resistivity above the Curie-temperature i.e. decreased or suppressed PTCR-jumps or rather a flattened increase of resistivity [Sea-05].

Figure 4.3-XI to Figure 4.3-XIII compare the crystal orientation maps of compositions A-1a, A-2a and R-1a (A/B-ratio 0.998) obtained by EBSD. In these

4. Results and discussion

pictures, the low Σ grain boundaries are depicted as white lines between similarly oriented grains (the allowed angular deviation were calculated by the Brandon's criterion [Bra-65]). Moreover, Table 4.3-III summarizes the average grain size data and the percentage of low Σ grain boundaries both obviously ranging at similar values around 3.4µm and 6.6% respectively. It is evident from the orientation maps that no difference in amount of electrical inactive low sigma grain boundaries is observable (Σ 3, 5, 9) between anatase and rutile based batches, which was assumed to give reason for the shape of the PTCR characteristics in anatase compositions. Summarising the results it can be concluded that at least the microstructures of the a-compositions are comparable with respect to the average grain size and that the evolution of low Σ grain boundaries plays a minor role in the compositions investigated in this work.

Finally, the differences between the grain sizes obtained by SEM and EBSD measurements need to be argued. This discrepancy can be attributed to the detection method. On the one hand, SEM grain sizes are obtained by linear analysis including the pore volume. On the other hand, EBSD grain sizes are measured using a 2-dimensional software-assisted technique based on circular particles, which additionally excludes the pore volume. Considering this aspects it is evident why the grain size values obtained by SEM and EBSD differ from each other.

Table 4.3-III: Amount of low Σ grain boundaries and average grain-size values of composition A-1a, A-2a and R-1a

Batch no.	A-1a	A-2a	R-1a
Σ	Fraction [%]	Fraction [%]	Fraction [%]
3	3,5	3,6	3,8
5	1,2	2,2	1,7
9	1,7	1,1	1,1
Remain [%]	93,6	93,1	93,4
Grain Size [µm]	3,4	3,3	3,4
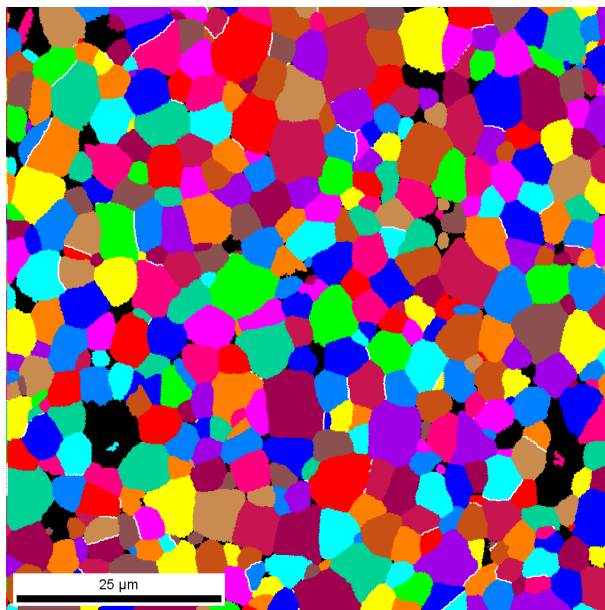
Figure 4.3-XI: Crystal orientation (EBSD) map of composition A-1a; picture width 75µm
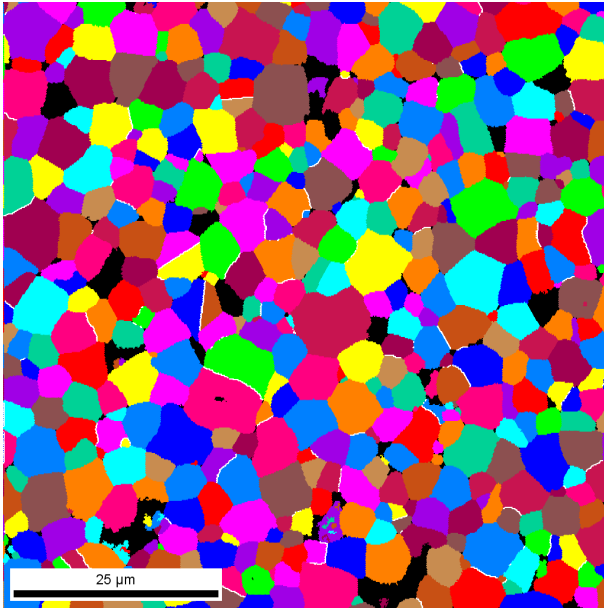
Figure 4.3-XII: Crystal orientation (EBSD) map of composition A-2a; picture width 75µm
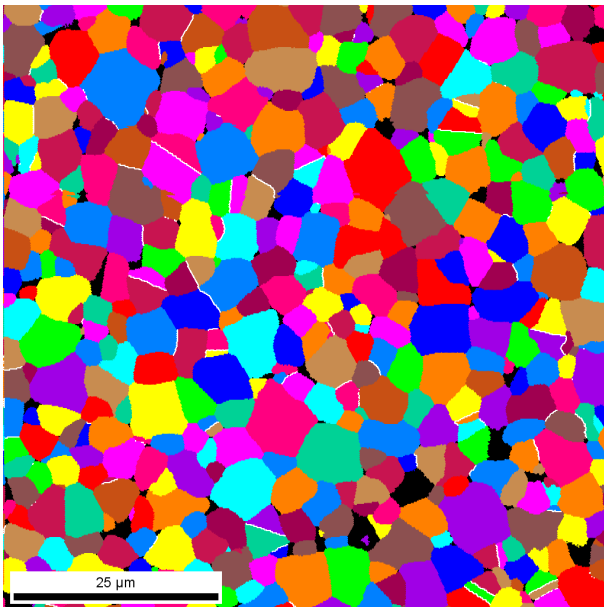
Figure 4.3-XIII: Crystal orientation (EBSD) map of composition R-1a; picture width 75µm

4.3.3. Chemical analysis using SEM-EDXS and -WDXS

To clarify the chemical phase composition, especially the locations where phosphorus and potassium are incorporated, microscopic investigations were performed by EDXS and WDXS, as described in section 3.4.5. Exemplary for both commercial anatase materials (A-1 and A-2), the EDX- and WDX-spectra of the anatase composition A-2a compared to the rutile composition R-1a and their location within the microstructure of the sintered parts are shown in Figure 4.3-XIV to Figure 4.3-XX. Expected main and minor phases which are typical for n-conducting $(Ba,Ca)TiO_3$ ceramics could clearly be detected. These are at first the main phase $(Ba,Ca)TiO_3$ representing the grain composition (area no.4, Figure 4.3-XVIII). Secondly, a titanium rich minor phase located in the grain interspaces

4. Results and discussion

representing the BaTiO$_3$-Ba$_6$Ti$_{17}$O$_{40}$ eutectic phase (area no.6, Figure 4.3-XX). Thirdly, silicon containing minor phase likewise located between the grains representing the liquid phase generated during sintering due to SiO$_2$ addition (area no.5, Figure 4.3-XIX). These results indicate that the chemical evolution of both compositions is similar with respect to the expected main and minor phases. Furthermore, the EDX-spectra of region no.3 (Figure 4.3-XVII) illustrate another minor phase, which was identified as CaTiO$_3$. This minor phase contains extraordinary high yttrium content in comparison to the grain composition. Finally, the spectra in Figure 4.3-XV and Figure 4.3-XVI (area no.1 and 2) show the location of a phosphor containing minor phase in composition A-2a whereas this phosphor content is not detectable in composition R-1a, which can clearly be seen in the overlaid spectra depicted in Figure 4.3-XXI. Even though the peak positions of phosphorus and yttrium are close to each other (phosphorus Kα at 2.014keV, yttrium Lα at 1.922keV) they can be easily distinguished by comparing the peak shapes i.e. if the yttrium peak contains a shoulder at slightly higher energy or the peak is shifted to slightly higher energy then the material truly contains phosphorus. It is important to note that neither manganese nor potassium is detectable at any of the observed main and minor phases.
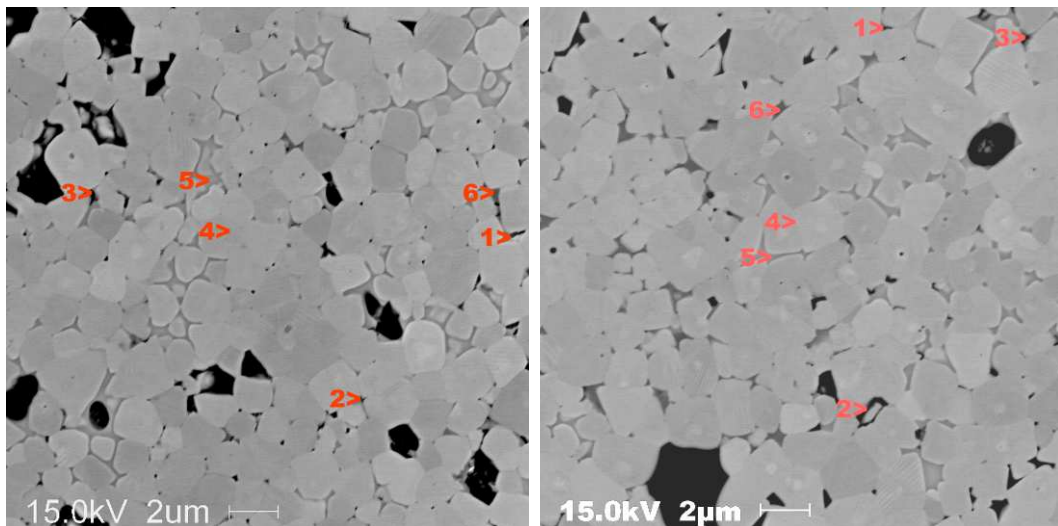
Figure 4.3-XIV: BSE micrographs of composition A-2a and R-1a (scale bar 2µm)
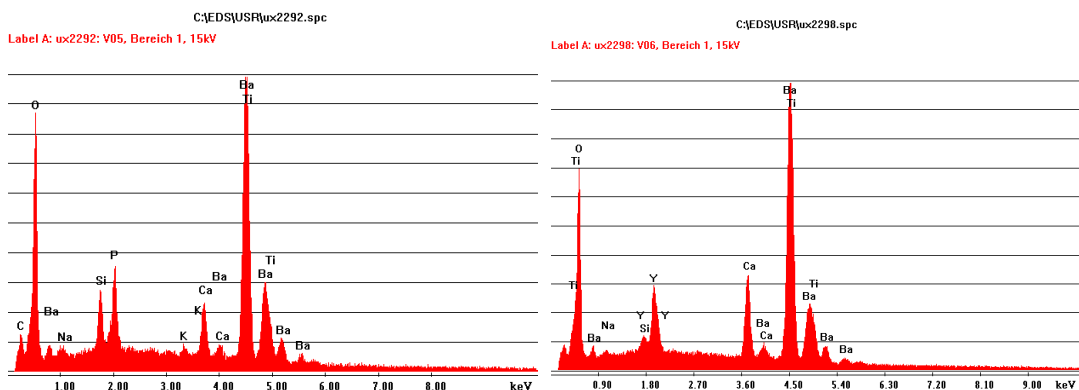
Figure 4.3-XV: EDX-spectra of area no.1; compositions A-2a (left hand) and R-1a (right hand)

4. Results and discussion
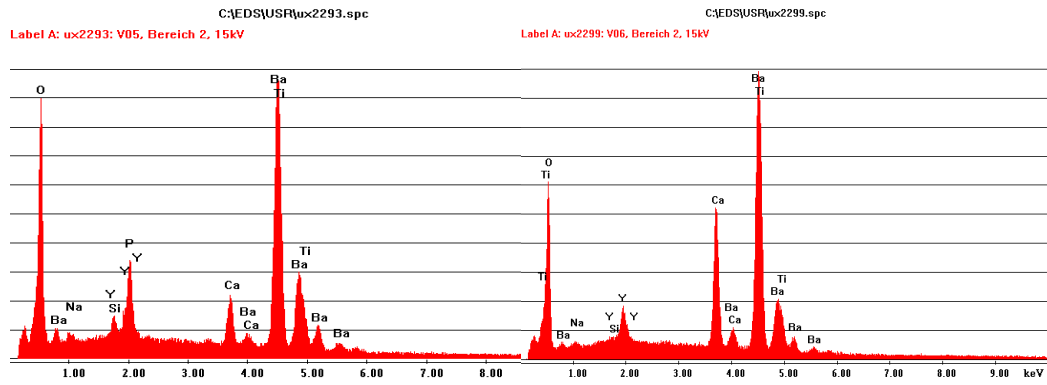
Figure 4.3-XVI: EDX-spectra of area no.2; compositions A-2a (left hand) and R-1a (right hand)
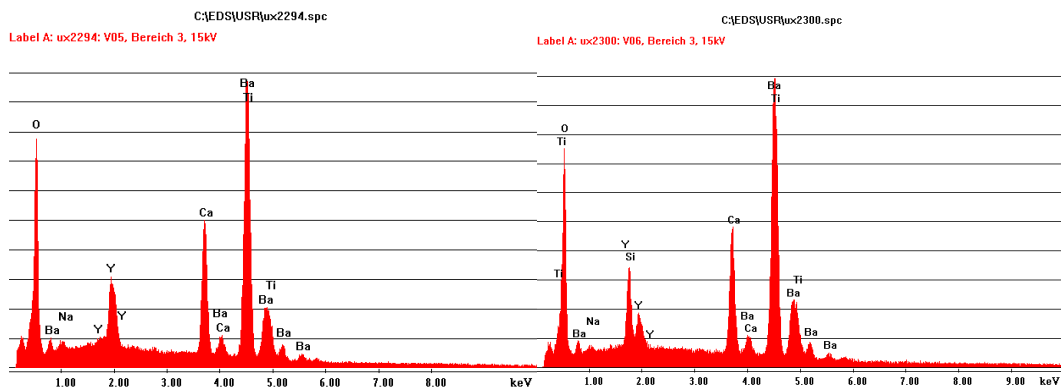
Figure 4.3-XVII: EDX-spectra of area no.3; compositions A-2a (left hand) and R-1a (right hand)
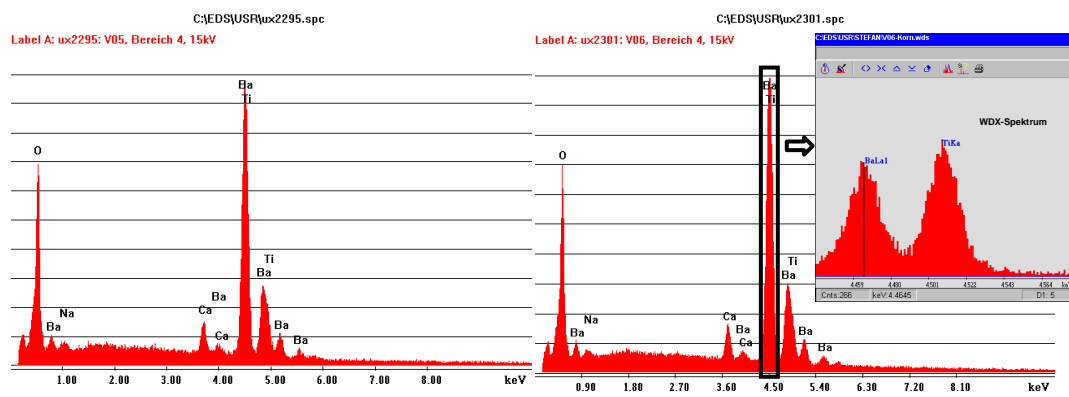
Figure 4.3-XVIII: EDX-spectra and partial WDX-spectrum of area no.4; compositions A-2a (left hand) and R-1a (right hand)

4. Results and discussion
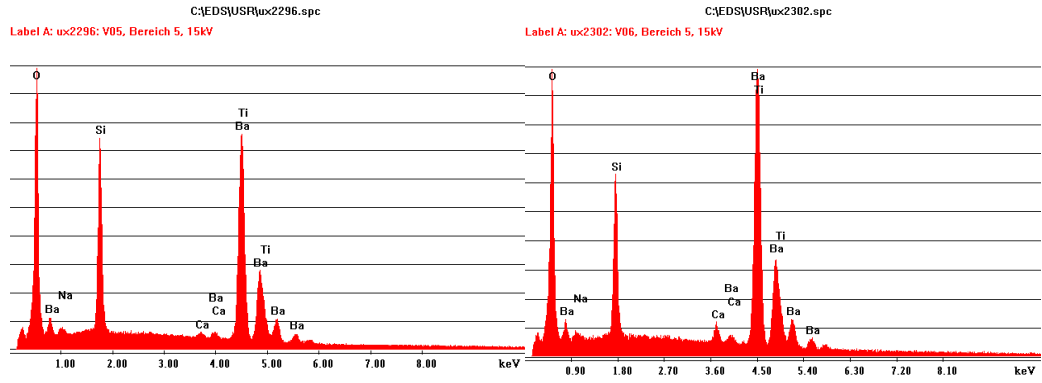
Figure 4.3-XIX: EDX-Spectra of area no.5; compositions A-2a (left hand) and R-1a (right hand)
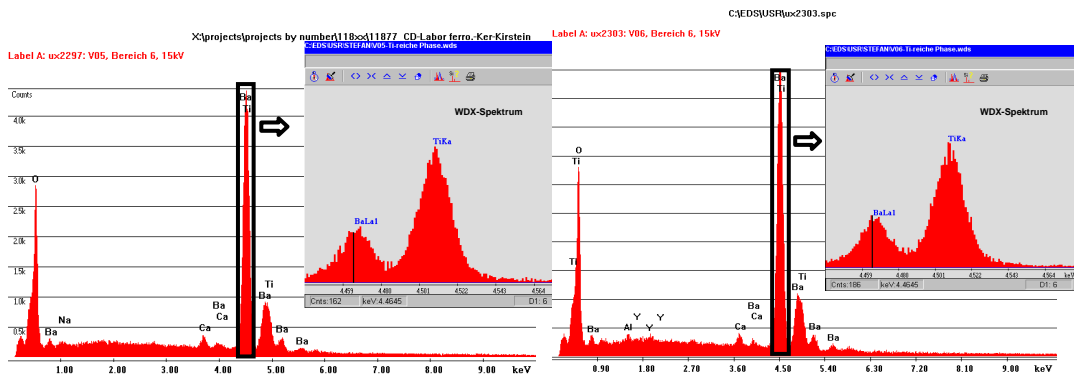
Figure 4.3-XX: EDX-spectra and partial WDX-spectra of area no.6; compositions A-2a (left hand) and R-1a (right hand)
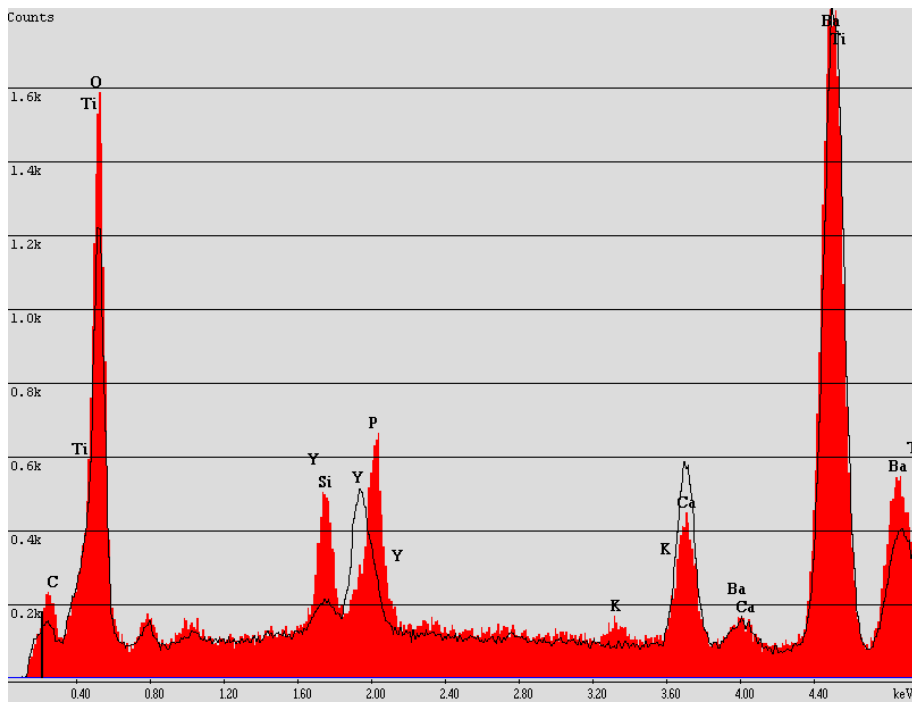
Figure 4.3-XXI: Overlay of spectra A-2a_section no.3 and R-1a_section no.2 showing phosphorus in batch A-2a (red solid spectrum) while no phosphorus is detectable in composition R-1a (black line spectrum)

4.3.4. Local chemical analysis using TEM-EDXS

TEM studies have been performed on composition A-2a and R-1a in the manner described in section 3.4.7. The purpose of this investigation on the one hand was to verify the results obtained by SEM-EDX. On the other hand, to discover the phase belonging and location of the dopants Y and Mn as well as of the impurities P and K in more detail. The detected TEM-EDX spectra have always been normalised on the highest peak (Ba/Ti-peak at 4.5keV) to enable a direct comparison of the relative amounts of the elemental compositions. Thus, the pictured EDX-spectra do not show the measured absolute values but the standardised values.

The overall spectra of both investigated materials (Figure 4.3-XXII and Figure 4.3-XXIII) show almost identical compositions containing barium, calcium, titanium, oxygen and a small amount of silicon. Small concentrations of iron and cobalt are also detected. These impurities do not result from the samples; rather they are fragments resulting from the detector positioning inside the equipment.
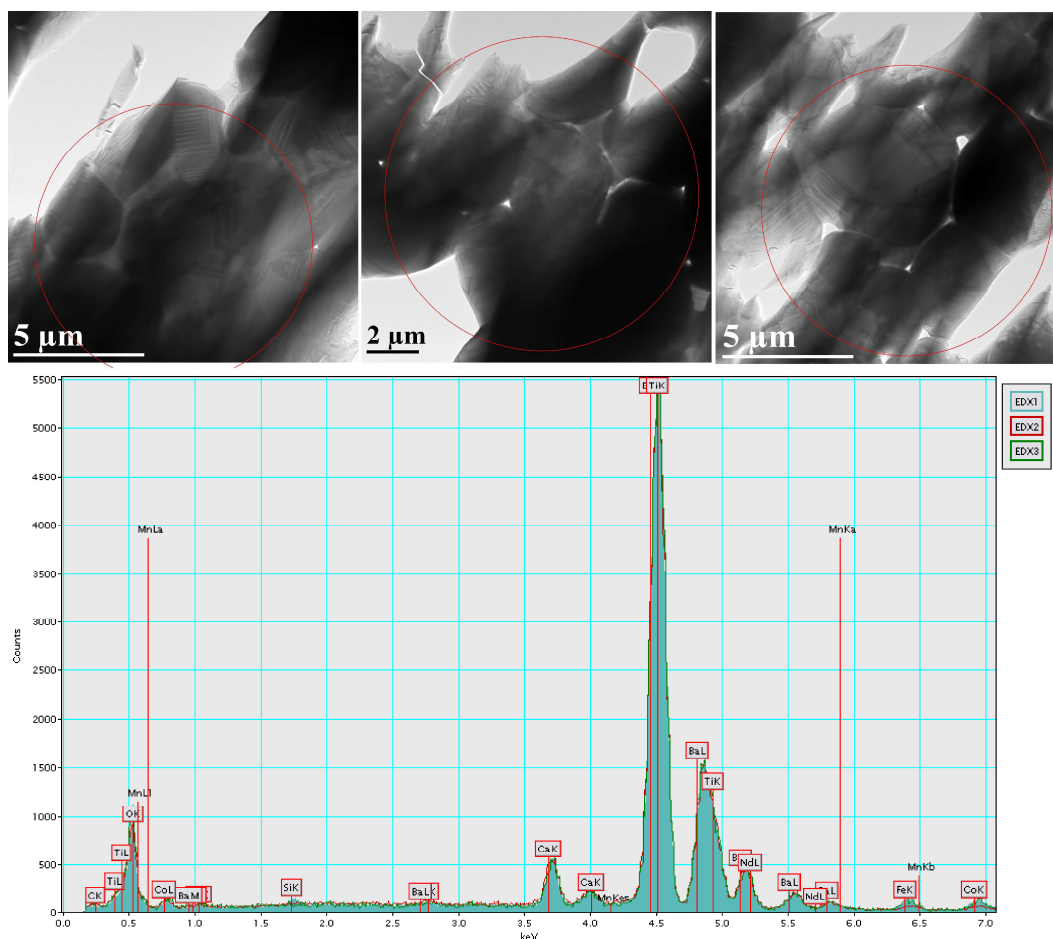
Figure 4.3-XXII: Composition overview spectra of batch A-2a

4. Results and discussion
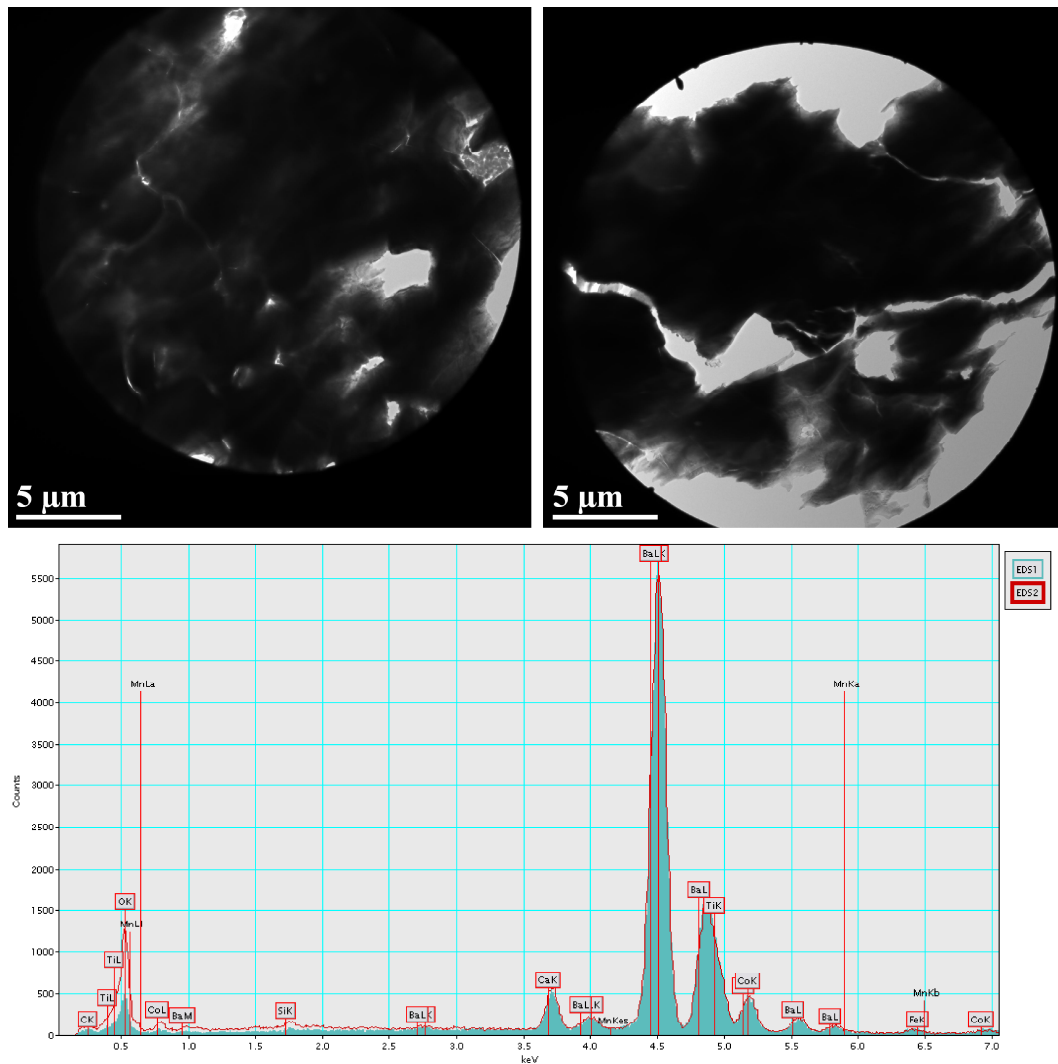
Figure 4.3-XXIII: Composition overview spectra of batch R-1a

Firstly, a selection of the EDX-measurements made on the anatase-based batch A-2a is presented, which is characteristic for the detected phases. Starting with the line-scan spectrum image illustrated in Figure 4.3-XXIV and Figure 4.3-XXV, which represent the compositional change at a triple junction filled with silicon containing secondary phase. The 3-D-graph clearly demonstrates the compositional changes that are the appearance of the silicon peak around 1.75keV, the disappearance of the calcium peaks at about 3.7keV and 4.0keV and the decreasing intensities of the Ba/Ti-peaks in the range of 4.25keV to 6.0keV. Additionally, Figure 4.3-XXVI shows the partial spectra in the range of 3.5keV to 7.0keV with the inlay representing the two main Ba/Ti-peaks (4.3keV to 5.0keV). When comparing the bulk composition (spectra no.1 and 5) with the silicon phase composition (spectrum no.3), it is evident that the calcium concentration is vanished and the barium concentration is increased or rather the Ba/Ti-ratio is shifted to higher barium content i.e. the Ba/Ti-peaks are shifted to lower electron volts (see inlay of Figure 4.3-XXVI). This verifies the XRD-results (section 4.2.3) where the silicon containing secondary phase could be detected as crystallised fresnoite ($Ba_2TiSi_2O_8$) i.e. a barium-rich secondary phase.

4. Results and discussion
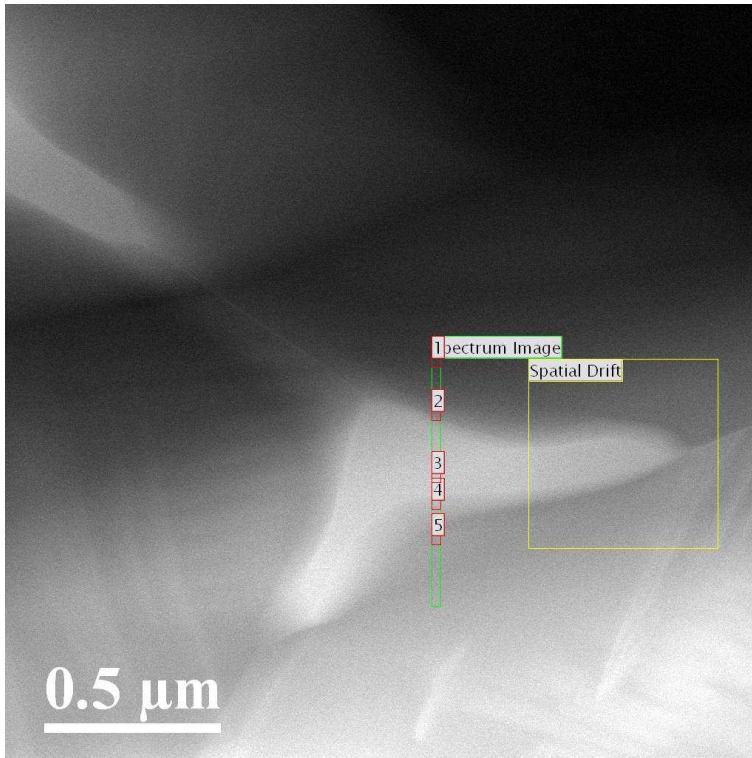
Figure 4.3-XXIV: Batch A-2a; TEM line scan of a triple junction containing silicon secondary phase
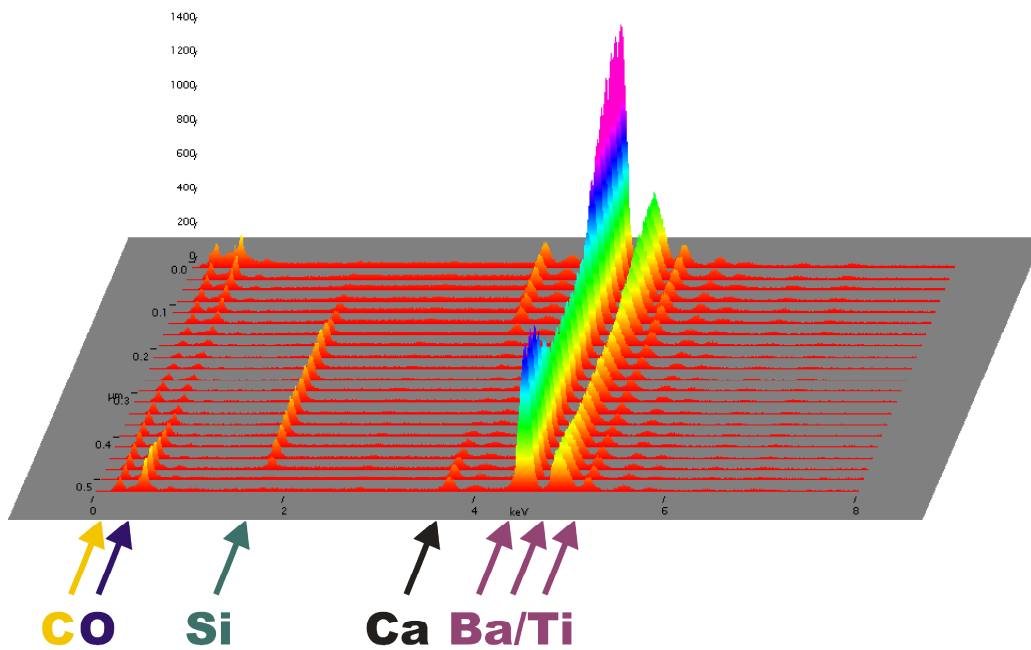
Figure 4.3-XXV: Batch A-2a; 3D-graph of the line scan spectra depicted in Figure 4.3-XXIV

4. Results and discussion
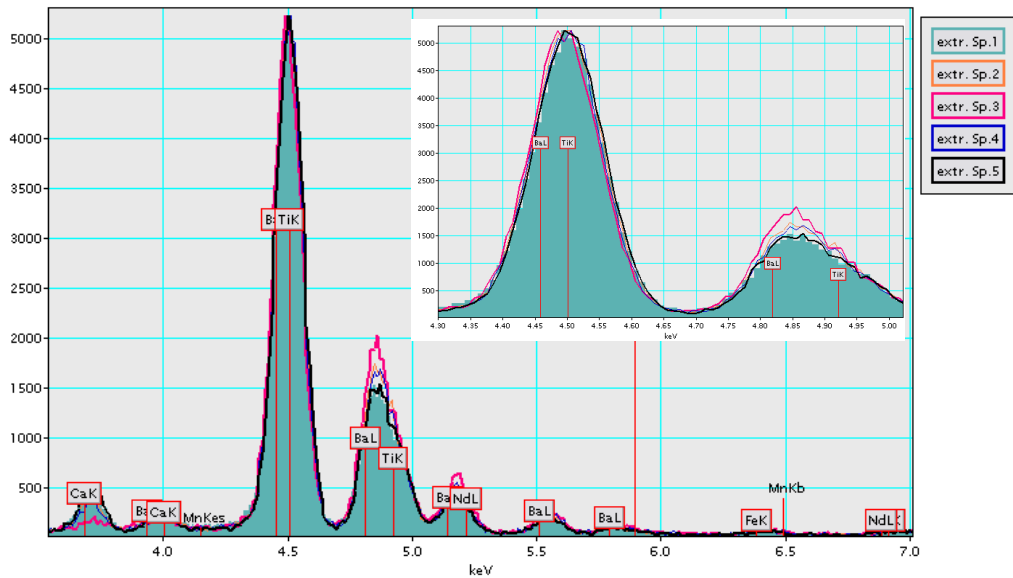
Figure 4.3-XXVI: Batch A-2a; partial spectra of the line scan depicted in Figure 4.3-XXIV; inlay: partial spectra around the Ba/Ti-peak

Figure 4.3-XXVII represents the 2-D scan array of another triple junction. The numbered spectra are depicted in Figure 4.3-XXVIII and the corresponding elemental maps of the spectrum array are pictured in Figure 4.3-XXIX. These figures illustrate the residual Y- $CaTiO_3$ phase that has already been detected by SEM-EDX (section 4.3.3). Additionally the 2-D scan results permit an estimation of the grain size for the residual Y-$CaTiO_3$ phase. For the illustrated measurement, the grain shows a size below 0.5µm. Since the residual Y-$CaTiO_3$ grains are always located at the triple junctions of the bulk phase, it can be assumed that this grain size is representative for the residual phase.
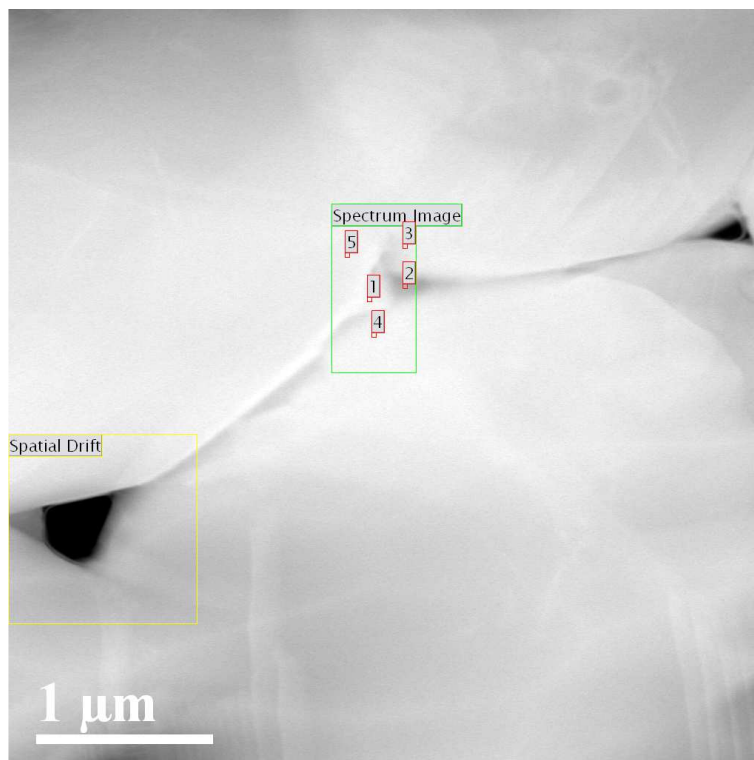
Figure 4.3-XXVII: Batch A-2a; 2D-scan survey no.1

4. Results and discussion
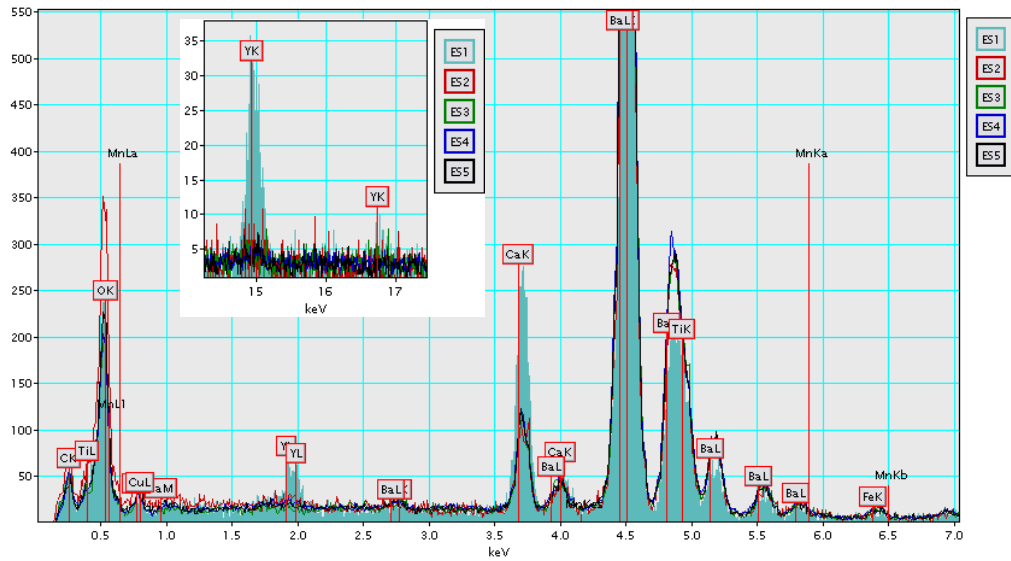
Figure 4.3-XXVIII: Batch A-2a; comparison of the spectra numbered in Figure 4.3-XXVII
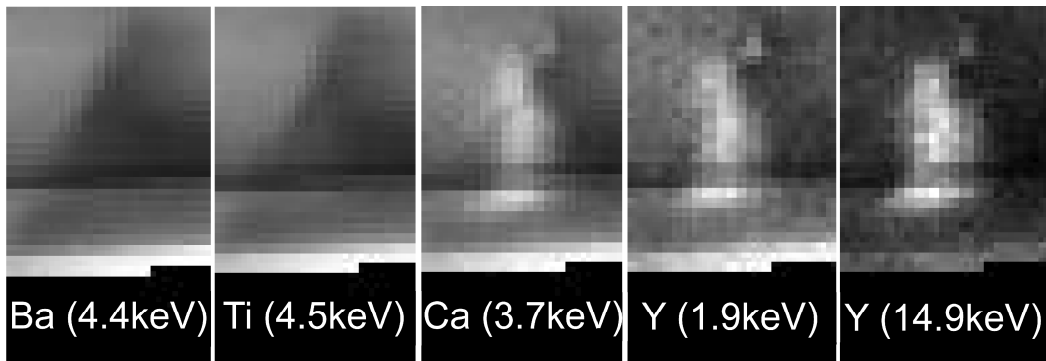
Figure 4.3-XXIX: Batch A-2a; elemental maps of the spectrum image in Figure 4.3-XXVII showing Y-rich $CaTiO_3$ phase

Another array scan is depicted in Figure 4.3-XXX that partly includes a triple junction and the grain boundary region of two adjacent grains.
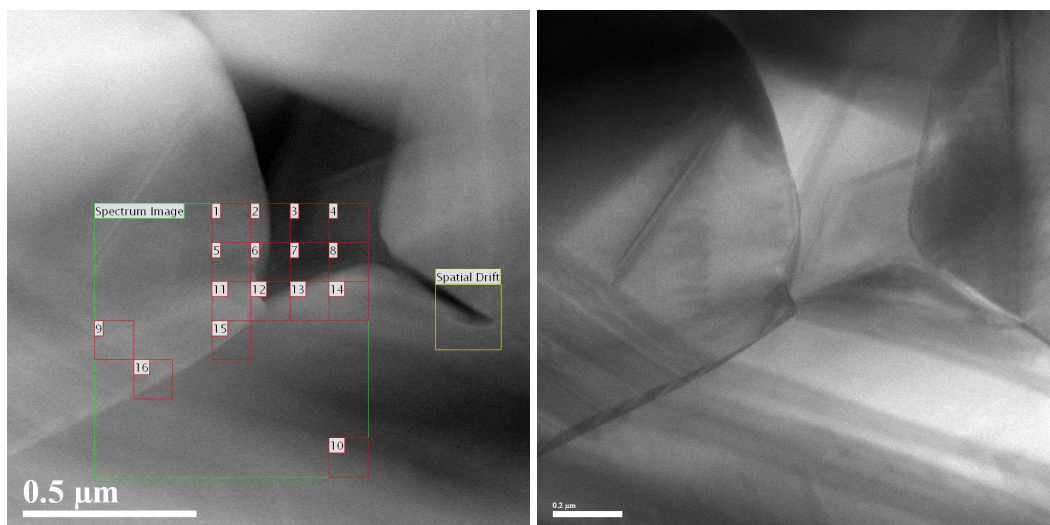
Figure 4.3-XXX: Batch A-2a; 2D-scan survey no.2 (left hand) and dark field image of the same region (right hand)

4. Results and discussion

Figure 4.3-XXXI compares the spectra of a phosphor containing secondary phase (spectra no.3 and 7) with the bulk composition (spectrum no.1). At first sight, this only confirms the results obtained by SEM-EDX (section 4.3.3). Looking in more detail it gets evident that the phase adjacent to the phosphorus phase is Ca- and Ba- depleted or rather Ti-enriched (spectrum no.8) compared to the bulk composition (spectrum no.1). The compositions of the Ti-rich phase in comparison to the bulk grain are illustrated in Figure 4.3-XXXII. This correlation between a phosphor-containing secondary phase and an adjacent titanium rich phase is observed for the first time. Moreover, spectra number 3 and 7 (Figure 4.3-XXXI) clarify the phase location of potassium, which could not be achieved by SEM-EDX. It is evident from spectra number 3 and 7 that on the one hand the potassium impurity mainly is present in the phosphorus secondary phase. On the other hand, this figure illustrates that the phosphor containing secondary phase is accompanied by a strong increase in Ba and Ca concentration compared to the bulk phase.

Another interesting effect can be observed in Figure 4.3-XXXIII and Figure 4.3-XXXIV, both showing a zoomed section of the Ti-rich spectra depicted in Figure 4.3-XXXII. These figures demonstrate that the acceptor ions manganese and aluminium, which both substitute for titanium, preferentially are incorporated in the titanium rich secondary phase i.e. acceptor segregation takes place at least in batch A-2a.

These observations verify the proposed calcination mechanism in anatase based compositions (see section 4.2.4) which gives rise to a higher amount of local inhomogeneities. Additionally the results indicate that the variation in sintering behaviour and the discrepancy between rutile and anatase based PTCR-characteristics in fact are provoked by the impurities incorporated by the titania raw materials. Finally, it can be assumed that the phosphor containing secondary phase together with potassium forms a low melting liquid phase that influences the sintering behaviour of the material. The mentioned results will be discussed in detail in section 4.3.6.
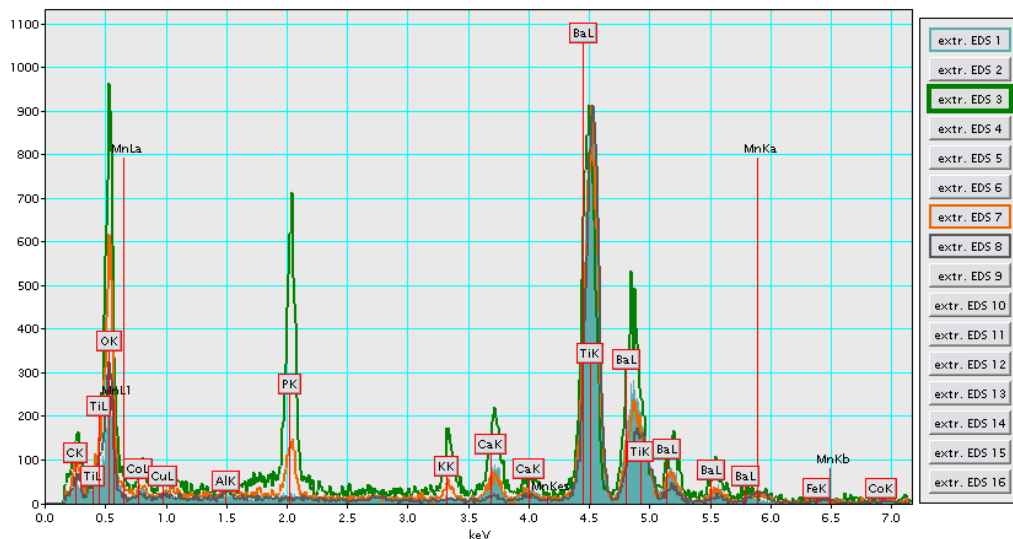
Figure 4.3-XXXI: Batch A-2a; phosphor containing and Ba/Ca-rich phase of spectra no.3 and 7 compared to the bulk spectrum no.1 and the Ti-rich spectrum no.8

4. Results and discussion
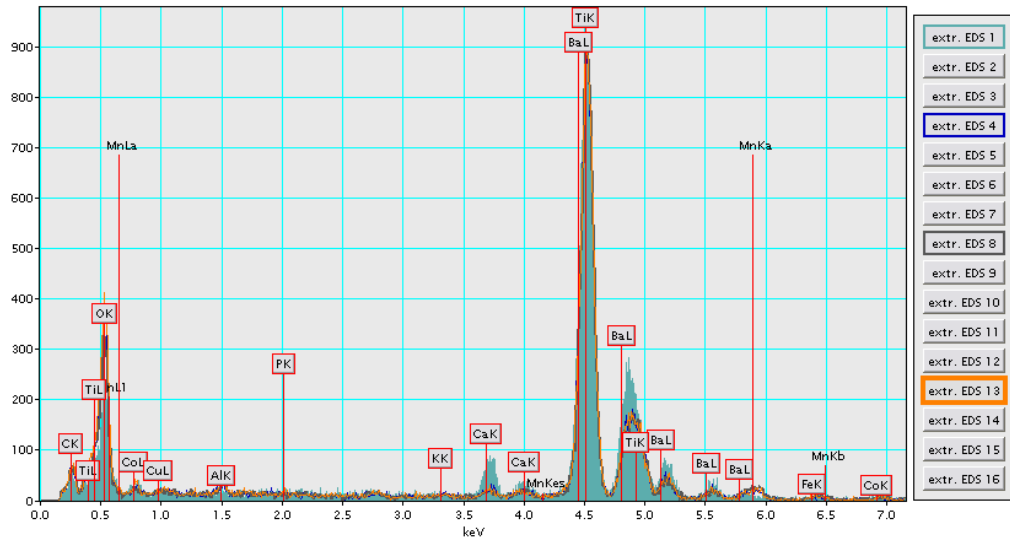
Figure 4.3-XXXII: Batch A-2a; Ti-rich secondary phase adjacent to the phosphor phase of spectra no.4, 8 and 13 compared to the bulk spectrum no.1
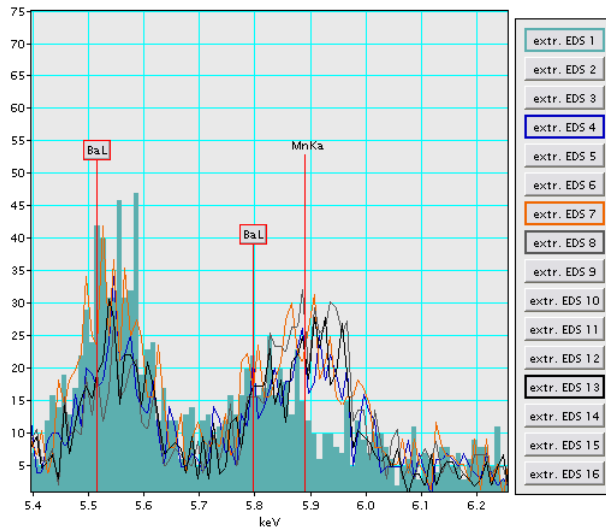
Figure 4.3-XXXIII: Batch A-2a; partial spectra no. 4, 7, 8 and 13 of the Ti-rich secondary phase showing manganese content compared to the bulk spectrum no.1
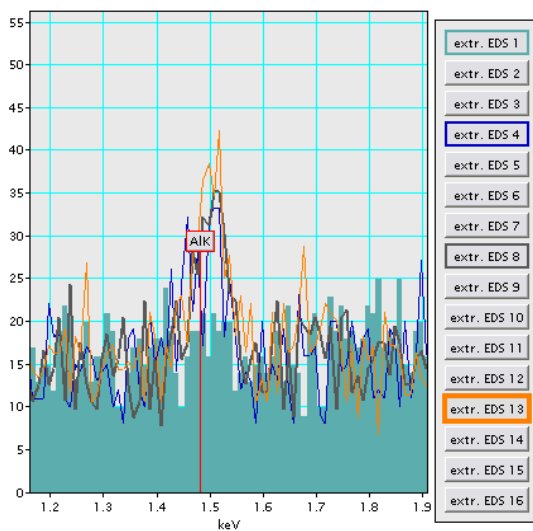
Figure 4.3-XXXIV: Batch A-2a; partial spectra no. 4, 8 and 13 of the Ti-rich secondary phase showing aluminium content compared to the bulk spectrum no.1

4. Results and discussion

Lastly, Figure 4.3-XXXV and Figure 4.3-XXXVI illustrate some point spectra and their location at a triple junction containing both, a silicon secondary phase (spectra no.3 and 4) and a phosphorus secondary phase (spectra no.1 and 2). The interesting point in this context is that both phases are strictly separated despite the vicinity of the two glass forming agents SiO_2 and P_2O_5, which in principle should be miscible.
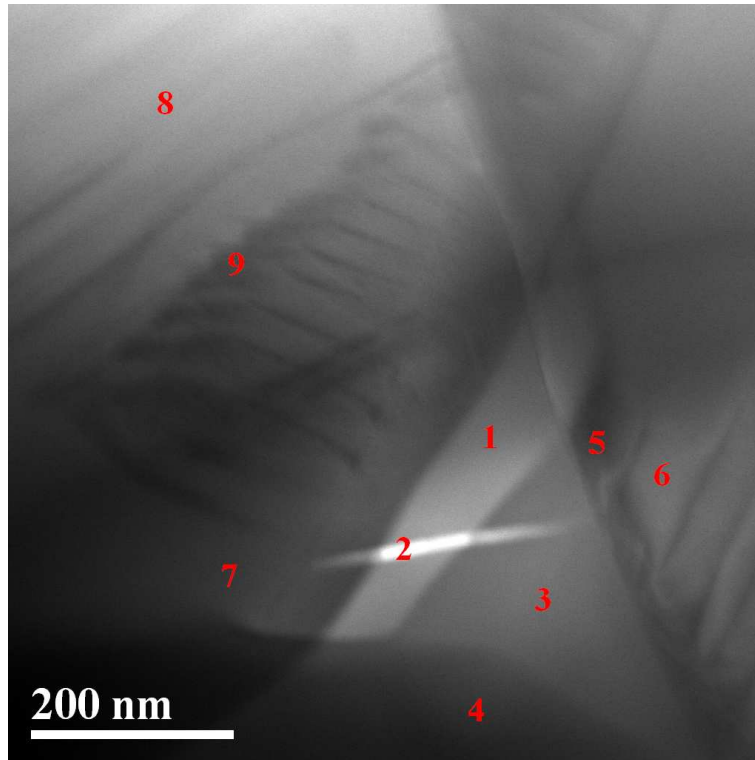
Figure 4.3-XXXV: Batch A-2a; point spectra positions at a triple junction
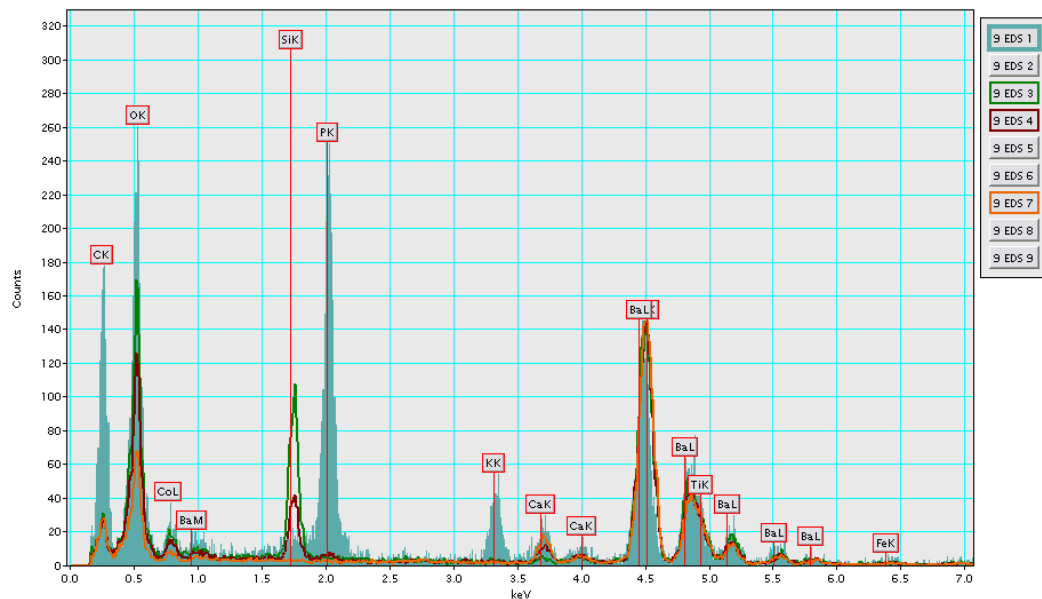
Figure 4.3-XXXVI: Batch A-2a; Comparison of the bulk composition (spectrum no.7) with the silicon containing secondary phase (spectra no.3 and 4) and the phosphorus containing secondary phase (spectrum no.1) detected at the triple junction in Figure 4.3-XXXV

4. Results and discussion

Further, some TEM analyses of the rutile-based batch R-1a are presented. First of all some point spectra taken around a thinned triple junction are shown in Figure 4.3-XXXVII. The detected EDX-spectra are compared in Figure 4.3-XXXVIII. The measurement identified three typical phases of the $(Ba,Ca)TiO_3$ ceramics investigated in this work. First, the bulk phase which is represented by spectra no. 2, 4, 5, 6 and 8. Second, the silicon containing secondary phase illustrated in spectra no. 1 and 7. Third, the Y-CaTiO$_3$ depicted in spectrum no.3. The compositional changes with respect to the (Ba+Ca)/Ti-ratio can be seen from the partial spectra (3.5keV to 5.0keV) pictured in Figure 4.3-XXXIX. The latter figure confirms the observations regarding barium enhancement within the silicon secondary phase made for the anatase based material (compare to Figure 4.3-XXVI) and measured by XRD (section 4.2.3).
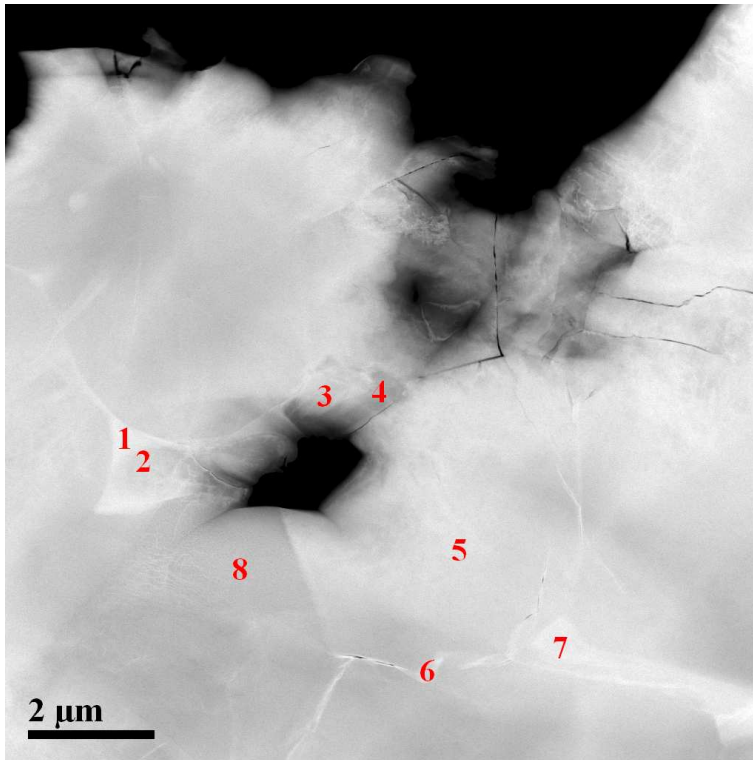
Figure 4.3-XXXVII: Batch R-1a; position of several point spectra around a triple junction

4. Results and discussion
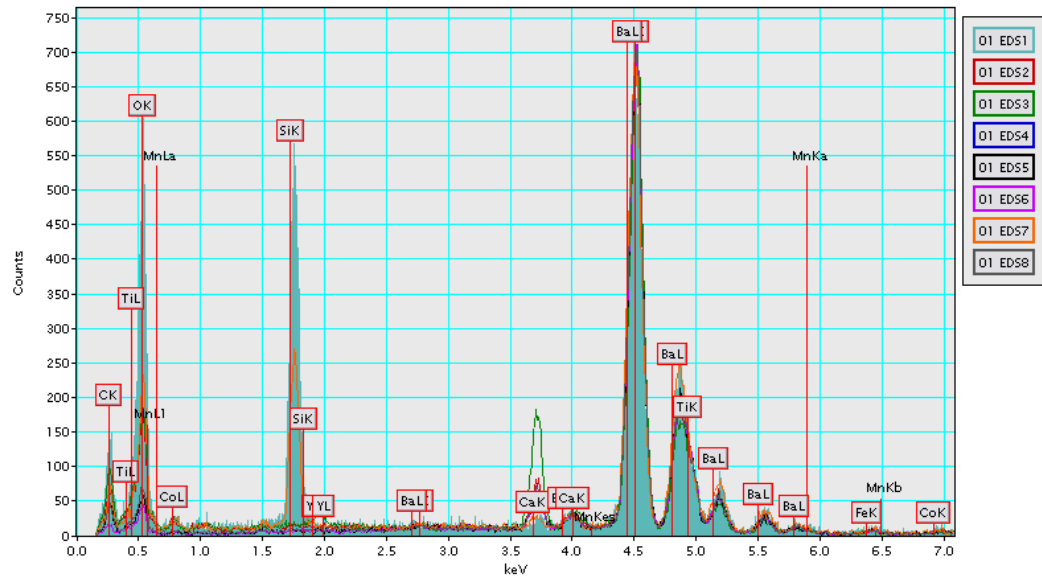
Figure 4.3-XXXVIII: Batch R-1a; comparison of the point spectra shown in Figure 4.3-XXXVII
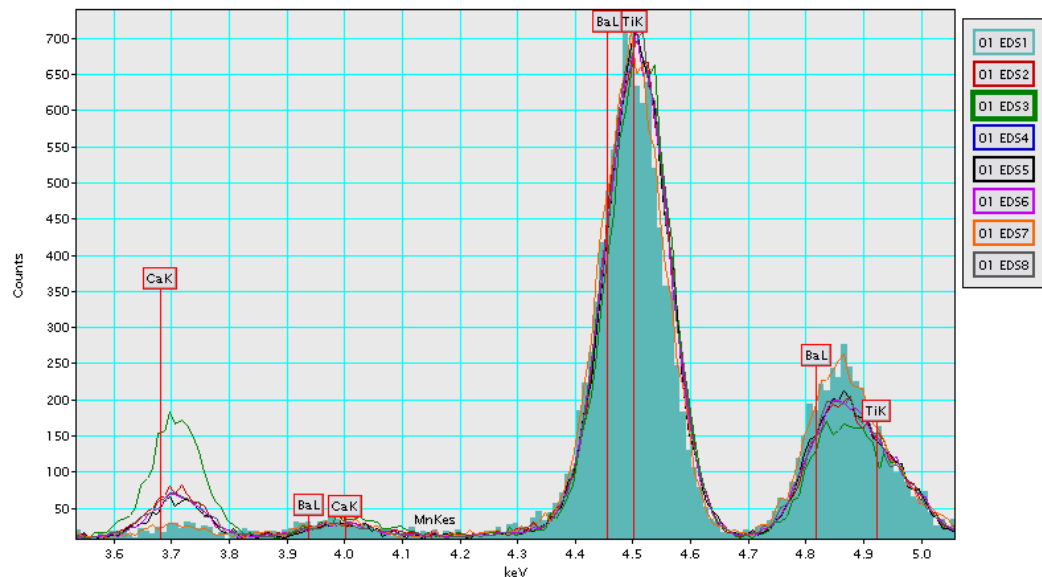
Figure 4.3-XXXIX: Batch R-1a; detailed picture of the spectra illustrated in Figure 4.3-XXXVII showing compositional variations

The line scan of a grain crossover is illustrated in Figure 4.3-XL and the 3D-graph of this scan is depicted in Figure 4.3-XLI. It can easily be seen from the figure that the scan starts at a residual yttrium containing $CaTiO_3$ grain and changes within the 50nm scan length to a composition closer to the bulk (q.v. Figure 4.3-XLII). It is also evident that the compositional change does not occur at a sharp line but rather proceeds continuously, which can be attributed to an overlap of the detected grains.

These results validate the observations made by SEM-EDX. Using SEM-EDX the residual yttrium containing $CaTiO_3$ phase was detected for the first time. In fact, the occurrence of the residual $CaTiO_3$ phase was independent of the raw material nature.
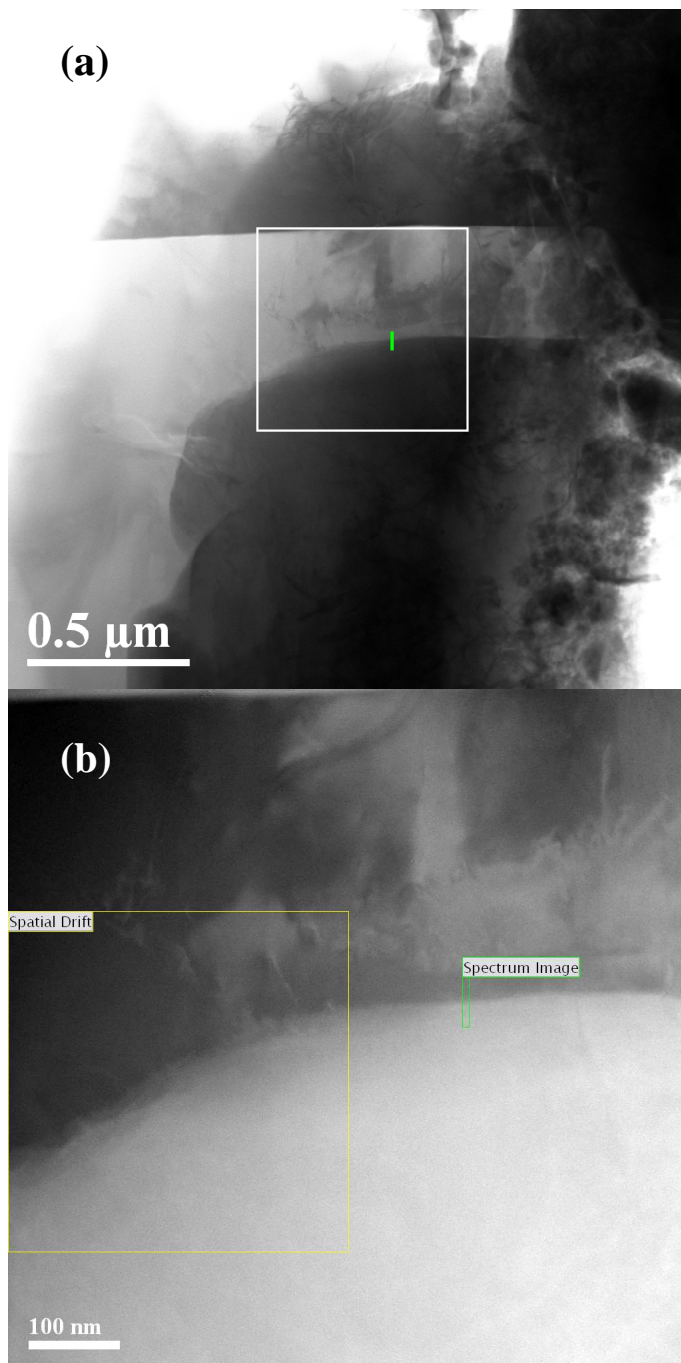
Figure 4.3-XL: Batch R-1a; (a) bright field image overview of the selected area and (b) dark field image of the line scan at the grain crossover

4. Results and discussion
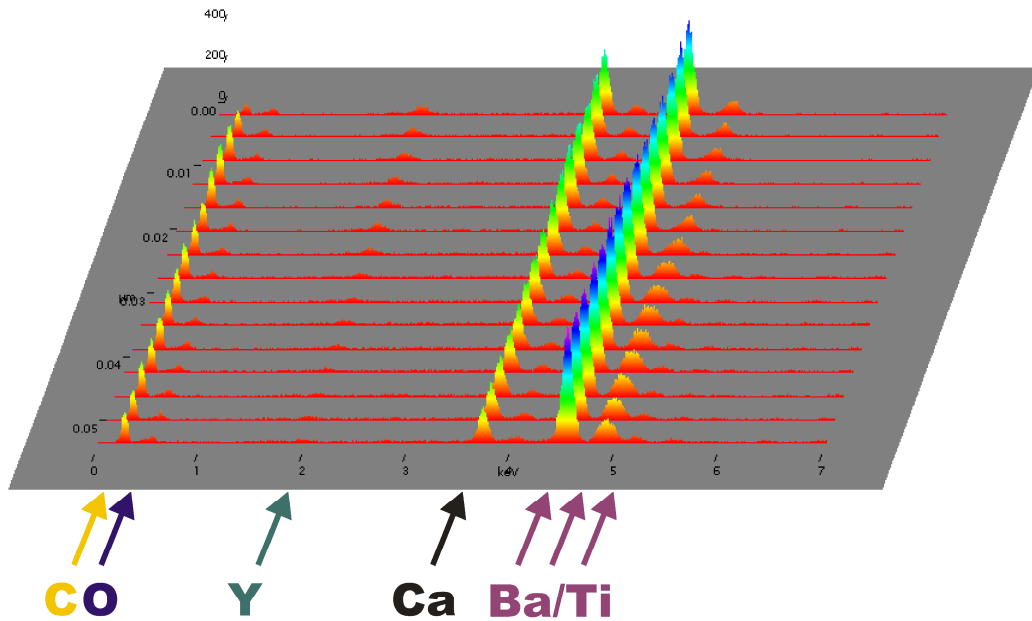
Figure 4.3-XLI: Batch R-1a; 3D-graph of the line scan spectra depicted in Figure 4.3-XL
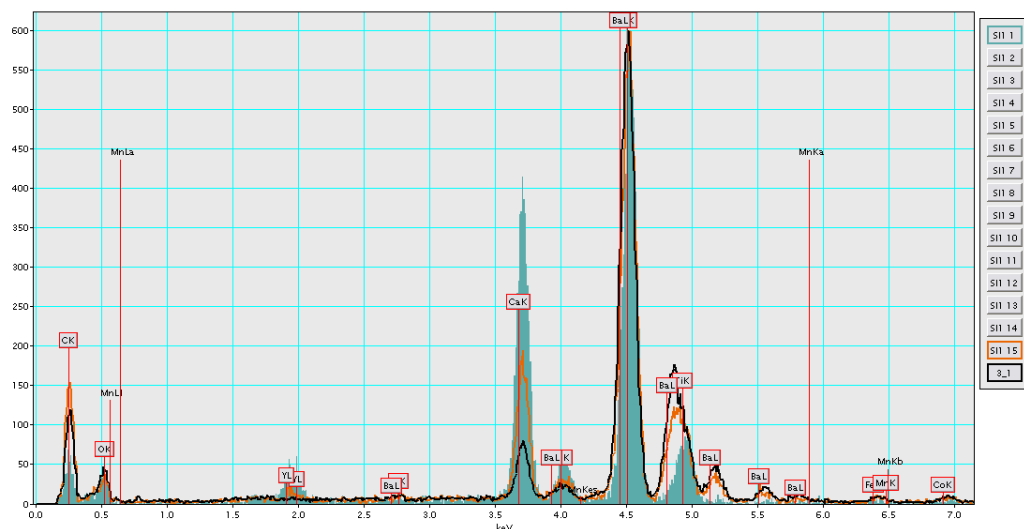
Figure 4.3-XLII: Batch R-1a; comparison of spectra no.1 and 15 depicted in Figure 4.3-XL with the bulk composition (spectrum 3_1)

Figure 4.3-XLIII shows another line scan that has been performed perpendicular to a grain boundary. The 3D-graph of the detected spectra is pictured in Figure 4.3-XLIV. This scan is presented because it demonstrates the grain boundary chemistry. On the one hand, it can clearly be observed that barium depletion or vice versa, titanium enrichment occurs along the grain boundary (Ba/Ti-peaks around 4.5keV and 4.8keV). On the other hand, this scan illustrates that the manganese acceptor ion in composition R-1a cannot be detected or rather does not segregate at the grain boundaries. Such scans have been performed in high quantity to answer the question of manganese segregation in rutile-based materials, which was found to be true for the anatase-based material A-2a (see Figure 4.3-XXXIII).

4. Results and discussion
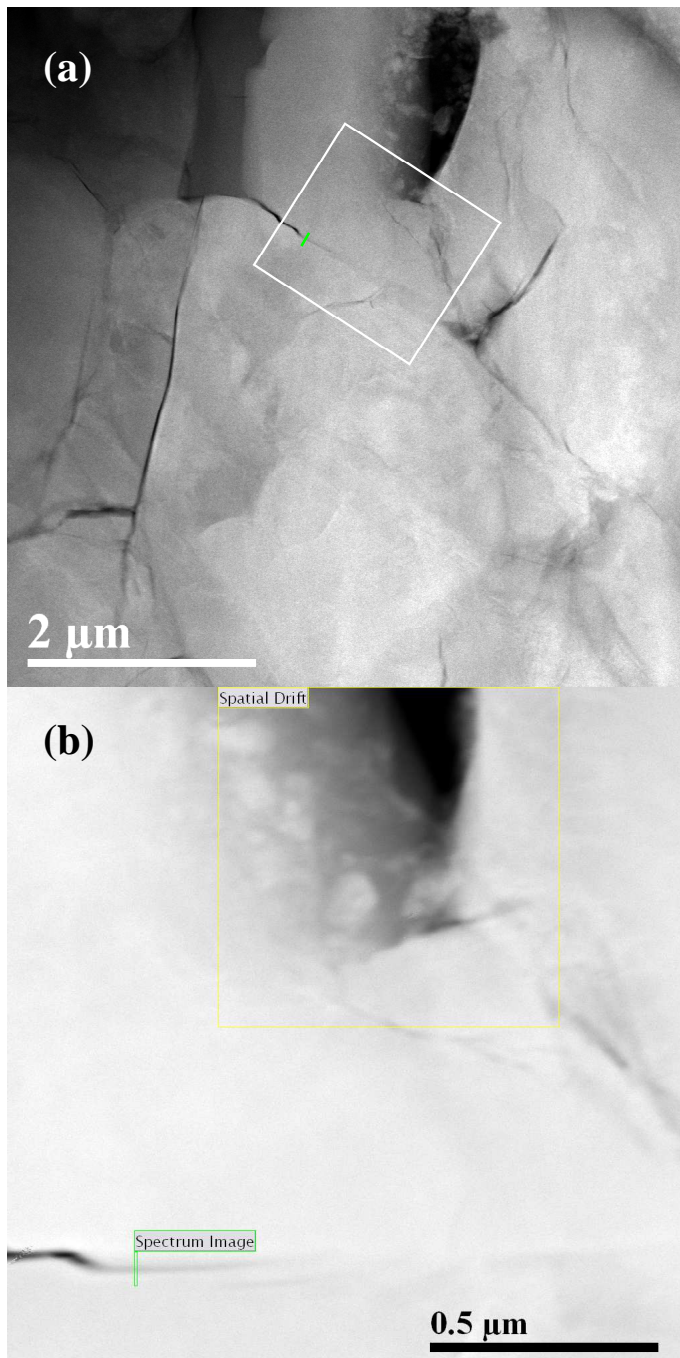
Figure 4.3-XLIII: Batch R-1a; (a) bright field image overview of the selected area and (b) bright field image of the line scan at a grain boundary
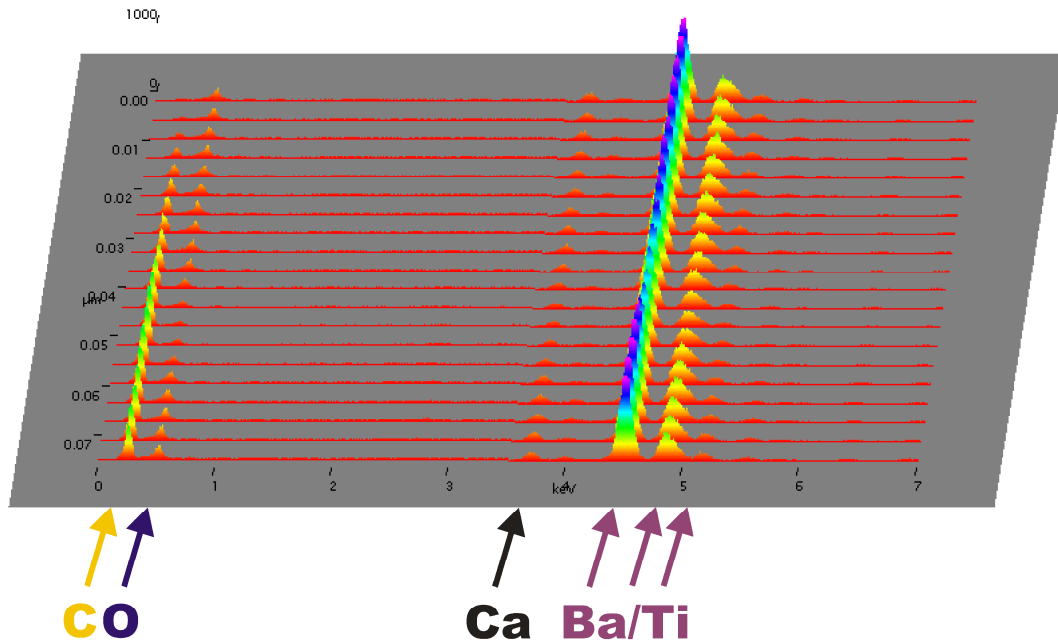
Figure 4.3-XLIV: Batch R-1a; 3D-graph of the line scan depicted in Figure 4.3-XLIII showing the crossover between two bulk grains

Additionally, Figure 4.3-XLV illustrates the positioning of seven point spectra measured across a grain boundary that is separated by a silicon containing secondary phase. The corresponding spectra are depicted in Figure 4.3-XLVI. The spectra clearly show that the calcium content decreases (Ca-peak at 3.7keV) when entering the silicon secondary phase. Simultaneously the barium content increases, which is obvious from the increasing Ba/Ti-peak at 4.5keV. Once again, this illustrates the chemical changes provoked by secondary phases or rather segregative additives as mentioned in section 2.2.5 and illustrated for the anatase material A-2a in Figure 4.3-XXXV and Figure 4.3-XXXVI. Such additives play an important role on the PTCR-characteristics, which will be discussed in section 4.3.6.

4. Results and discussion
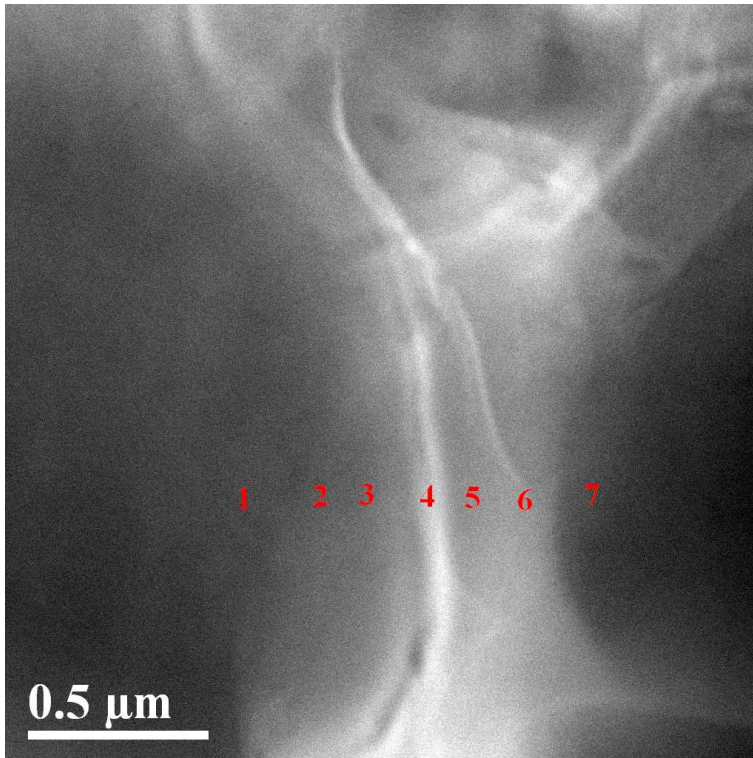
Figure 4.3-XLV: Batch R-1a; positions of point spectra at a grain boundary separated by a secondary phase
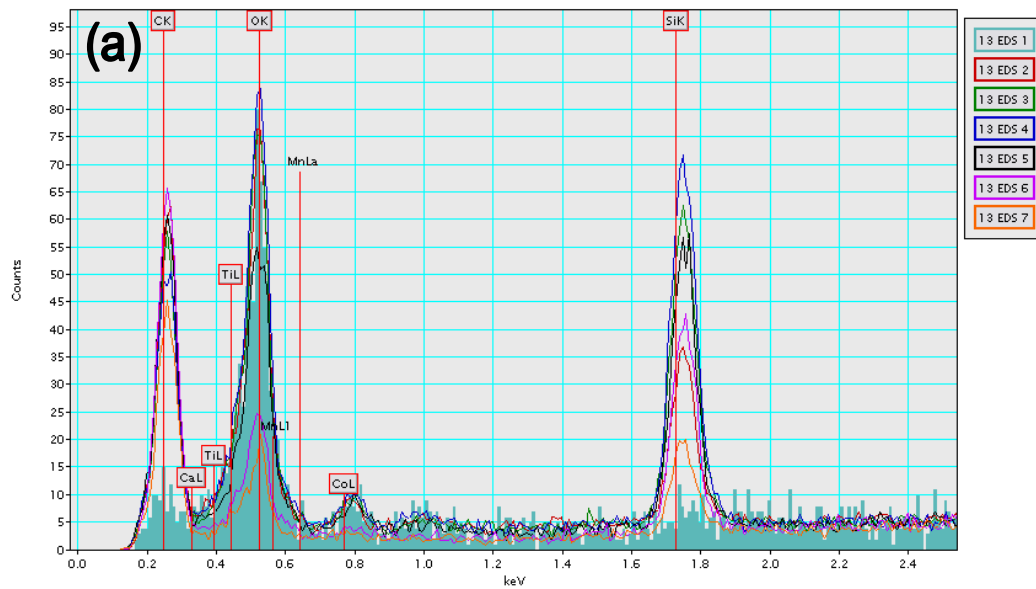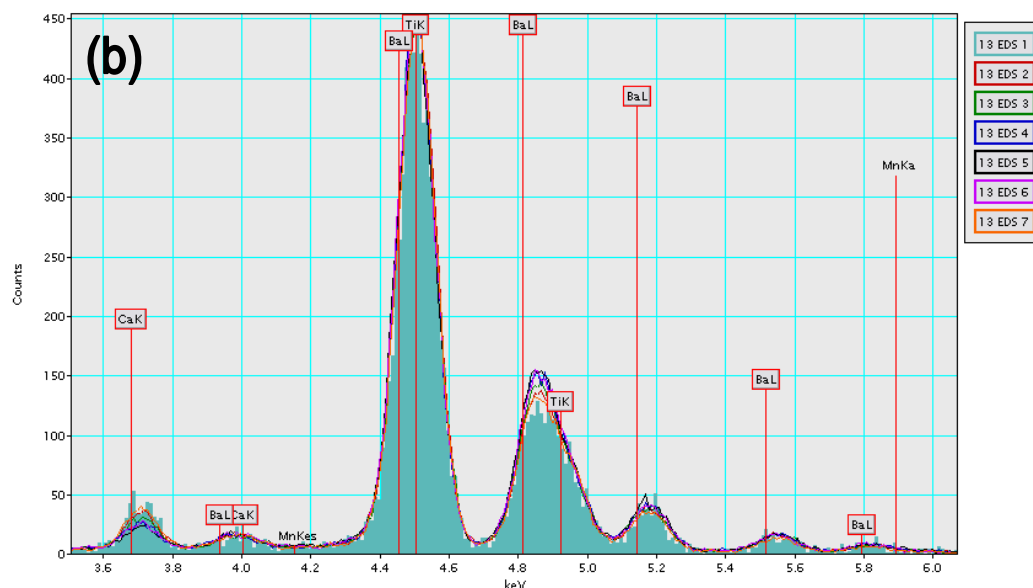
Figure 4.3-XLVI: Batch R-1a; comparison of the point spectra illustrated in Figure 4.3-XLV

Finally, the observations made by TEM-EDX can be summarised in the following manner. Both investigated samples A-2a and R-1a show comparable overall bulk compositions. Significant differences in local chemical composition between anatase and rutile based materials are detectable by detailed analysis of the secondary phases. Secondary phases that are detected in anatase and rutile based materials are on the one hand the silicate secondary phase that always contains higher barium amount than the bulk composition. This phase is in accordance with the fresnoite secondary phase detected by XRD. On the other hand, the existence of the residual Y-$CaTiO_3$ secondary phase as identified by SEM-EDX (section 4.3.3) is verified in both materials. Additionally a titanium-rich secondary phase is detected in both materials, which most likely corresponds to the $BaTiO_3$-$Ba_6Ti_{17}O_{40}$ eutectic melt (q.v. section 4.3.3). On the contrary, two other types of secondary phases could only be detected in anatase-based materials. Firstly the phosphor containing secondary phase, which results from the anatase impurities. This phase also contains the potassium impurity and shows barium enrichment in comparison to the bulk composition (q.v. section 4.3.3). Secondly a titanium rich secondary phase that contains a noticeable amount of acceptor elements especially manganese. The manganese enriched phase is only detectable directly adjacent to the phosphor phase (see Figure 4.3-XXX to Figure 4.3-XXXIV). Owing to the restricted location of the latter phase and the fact that manganese could not be identified in all other titanium rich secondary phases, it is concluded that the manganese containing titanium rich phase results from the local inhomogeneities provoked by the anatase impurity. Further, it is supposed that these local inhomogeneities finally give rise to the significant variations in PTCR-performance, which will be discussed in section 4.3.6.

4.3.5. Chemical composition determined by EPMA

EPMA measurements of composition A-2a and R-1a are performed in the manner described in section 3.4.6. Two line scans per batch have been carried out each

4. Results and discussion

containing of 20 separately measured points. The theoretical composition and the line scan results of the bulk composition are summarised in appendix

4. Results and discussion

Table 8.2-VI and Table 8.2-VII. Based on the assumption that all cations completely occupy the usually accepted lattice side, the resulting chemical formula of compositions A-2a and R-1a are noted below in Equation 4.3-I and Equation 4.3-II respectively.

$$(Ba_{0.8378}, Ca_{0.1508}, Y_{0.0044}, K_{0.0009})(Ti_{1.0008}, Mn_{0.0014})O_3$$

Equation 4.3-I

$$(Ba_{0.8435}, Ca_{0.1485}, Y_{0.0043}, K_{0.0001})(Ti_{0.9995}, Mn_{0.0014})O_3$$
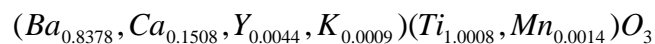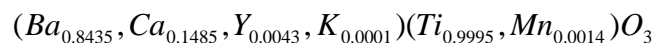
Equation 4.3-II

It is evident from the formulas above that the barium concentration in anatase-based compositions is reduced compared to the rutile composition. Consequently, this results in an increased calcium and titanium concentration. The corresponding A/B-ratios of both compositions, which amount to 0.992 for the anatase composition and 0.996 for the rutile batch, directly illustrate this effect. On the contrary, the yttrium and manganese dopant concentration seems to stay at a constant level. The observations indeed imply that the A/B-ratio or rather the (Ba+Ca)/Ti-ratio in anatase-based materials is shifted to higher titanium excess. Additionally the bulk formula illustrates that the potassium impurity dissolved in the grain bulk cannot be ignored in composition A-2a. The potassium concentration amounts to 0.023mol-% for the anatase based material A-2a whereas it only accounts for 0.002mol-% in the rutile reference (see Table 8.2-VII). This result indicates that in anatase-based materials the effective donor concentration at least is partly compensated by the potassium impurity.

The elemental maps obtained by EPMA confirm these observations. Figure 4.3-XLVII and Figure 4.3-XLVIII illustrate the scanned areas of composition A-2a and R-1a for elemental mapping. Moreover, Figure 4.3-XLIX indicates the colour code used to display the elemental concentrations. The elemental maps of the detected elements are depicted in Figure 4.3-L to Figure 4.3-LIX. Each figure represents the direct comparison of the anatase-based material (left hand) and the rutile reference (right hand). The maps of each element are normalised to the same counting range and smoothed to enhance colour contrast i.e. colour differences between the anatase and rutile based batch indicate real compositional changes. The main interesting points that can be observed from the elemental maps are the following. The barium concentration map (Figure 4.3-L) of batch A-2a shows a slightly decreased barium level compared to the rutile reference R-1a. The calcium content in the rutile-based material seems to be more homogeneously distributed i.e. the calcium content of several grains varies in a wider range in the anatase batch A-2a. This observation is in accordance with the concentration variations observable in the yttrium maps (Figure 4.3-LIII). Further, the titanium distribution (Figure 4.3-LII) shows significant variation in the anatase based material. Several dark red areas are visible in A-2a which are absent in the rutile reference R-1a where only a few light red areas are observable. Both compositions show a correlation between the titanium rich areas and the manganese (Figure 4.3-LIV) concentration especially at the light red areas. This indicates that the results obtained by TEM (q.v. section 4.3.4) regarding the titanium rich secondary phase, which contains an increased manganese concentration and only occurs in anatase based materials, at least are incomplete. The EPMA measurements

indicate that such a secondary phase exists in both materials. Lastly, the elemental maps of silicon (Figure 4.3-LV), phosphorus (Figure 4.3-LVI), potassium (Figure 4.3-LVII) and sulphur (Figure 4.3-LIX) need to be compared. It can be seen that the potassium content in A-2a mainly correlates with the secondary phase forming additive silicon as well as the impurity elements phosphorus and sulphur. The same is valid in R-1a apart from the phosphorus correlation. This supports the observation made by TEM that the potassium impurity preferentially is incorporated into a liquid forming secondary phase. However, in summary the mentioned results are generally in good agreement with the results obtained by SEM and TEM. Firstly, grain boundary segregation of the manganese acceptor could not be detected around the bulk grains. Secondly, barium and titanium rich secondary phases and local inhomogeneities (see section 4.3.4) provoked by the phosphor and potassium impurities most likely give rise to the compositional and electrical variations, which will further be discussed (section 4.3.6).
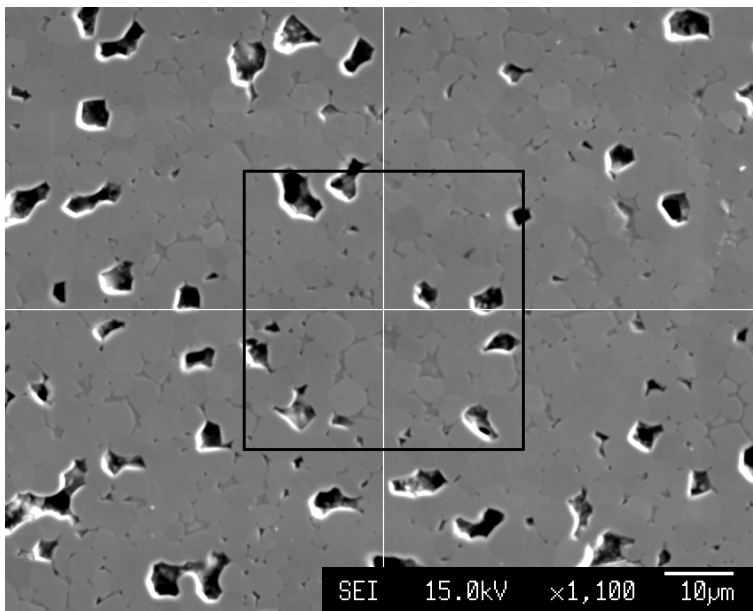
Figure 4.3-XLVII: SE-image of the spectrum area of composition A-1a determined for chemical mapping; scale bar 10µm

4. Results and discussion
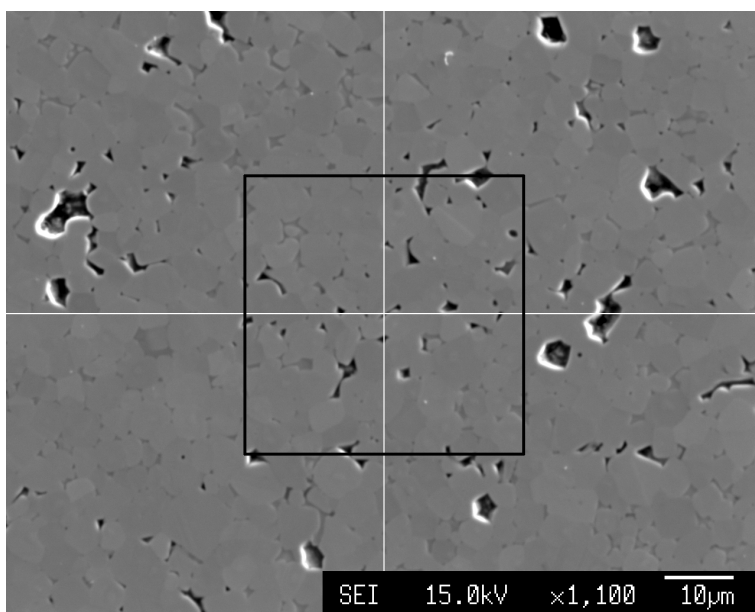
Figure 4.3-XLVIII: SE-image of the spectrum area of composition R-1a determined for chemical mapping; scale bar 10µm

Figure 4.3-XLIX: Colour coding used for all elemental maps; increasing concentrations are represented by the colour line starting from black illustrating no content over blue, green, yellow, red and violet up to white for the highest content
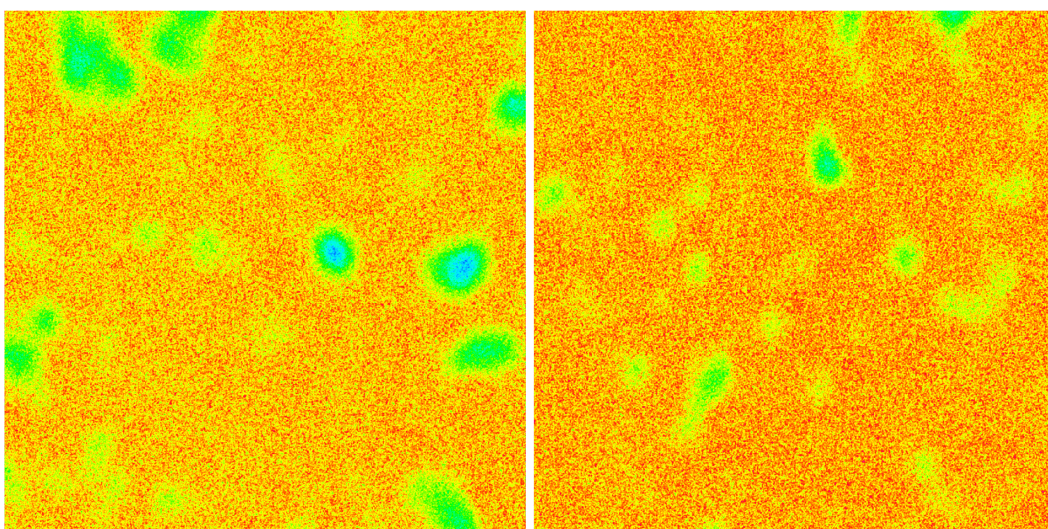
Figure 4.3-L: Barium elemental map of batches A-2a (left hand) and R-1a (right hand)

4. Results and discussion
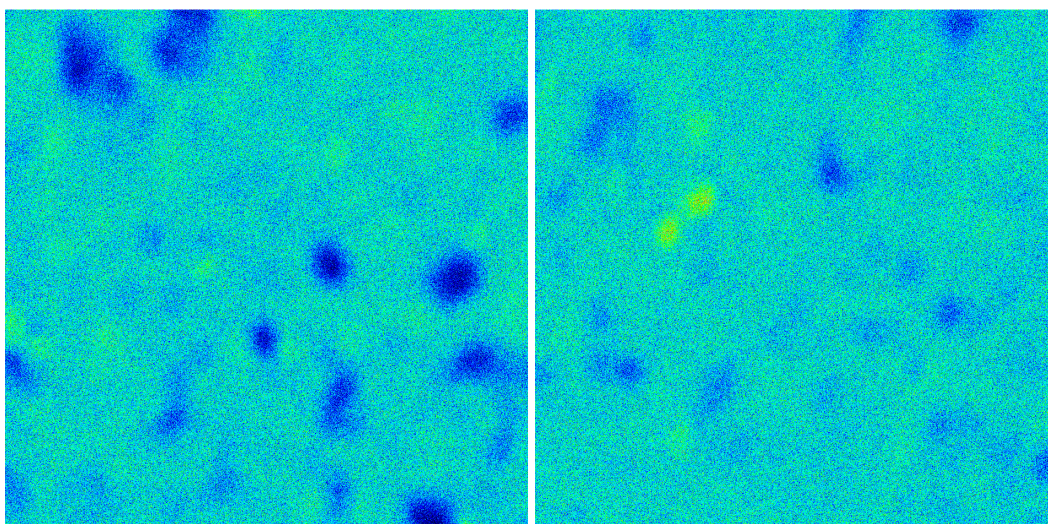
Figure 4.3-LI: Calcium elemental map of batches A-2a (left hand) and R-1a (right hand)
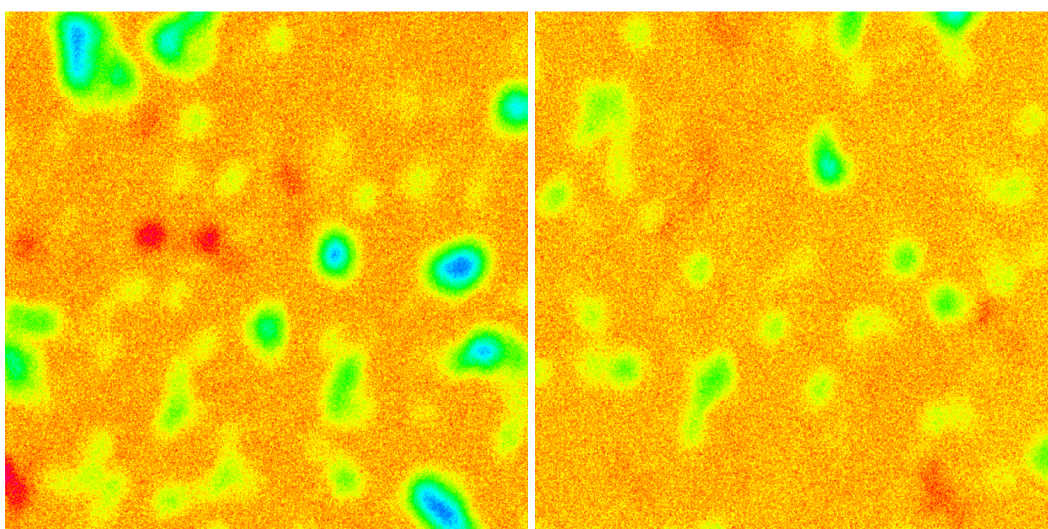
Figure 4.3-LII: Titanium elemental map of batches A-2a (left hand) and R-1a (right hand)
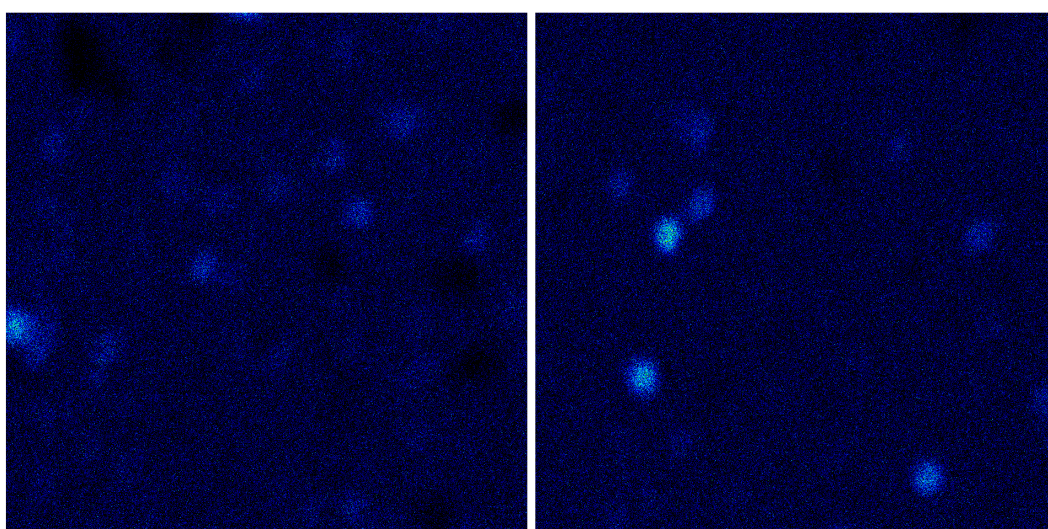
Figure 4.3-LIII: Yttrium elemental map of batches A-2a (left hand) and R-1a (right hand)
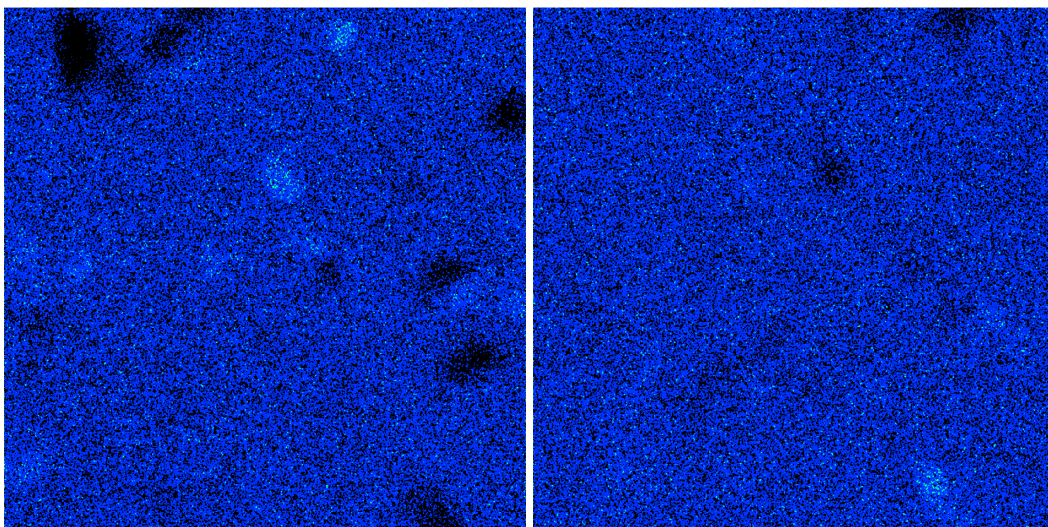
Figure 4.3-LIV: Manganese elemental map of batches A-2a (left hand) and R-1a (right hand)
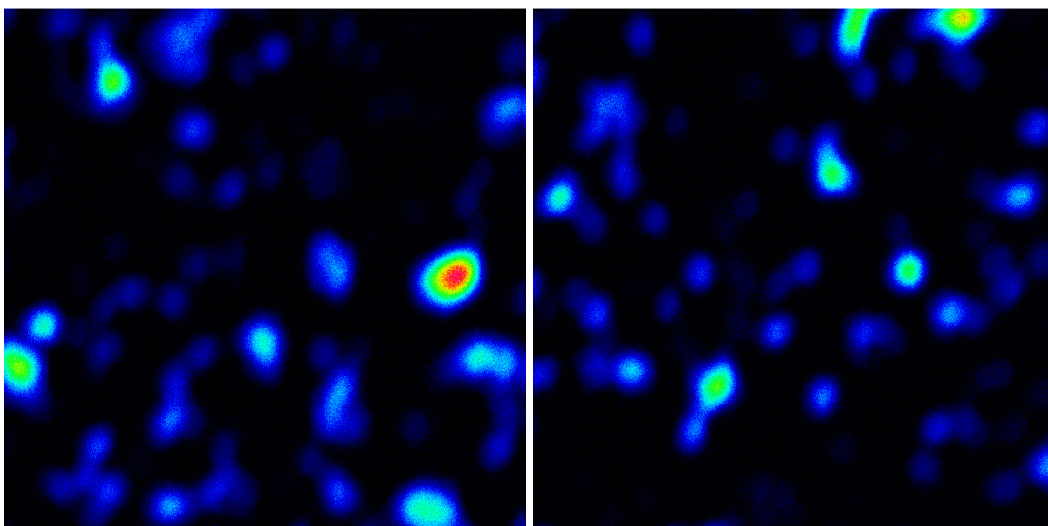
Figure 4.3-LV: Silicon elemental map of batches A-2a (left hand) and R-1a (right hand)
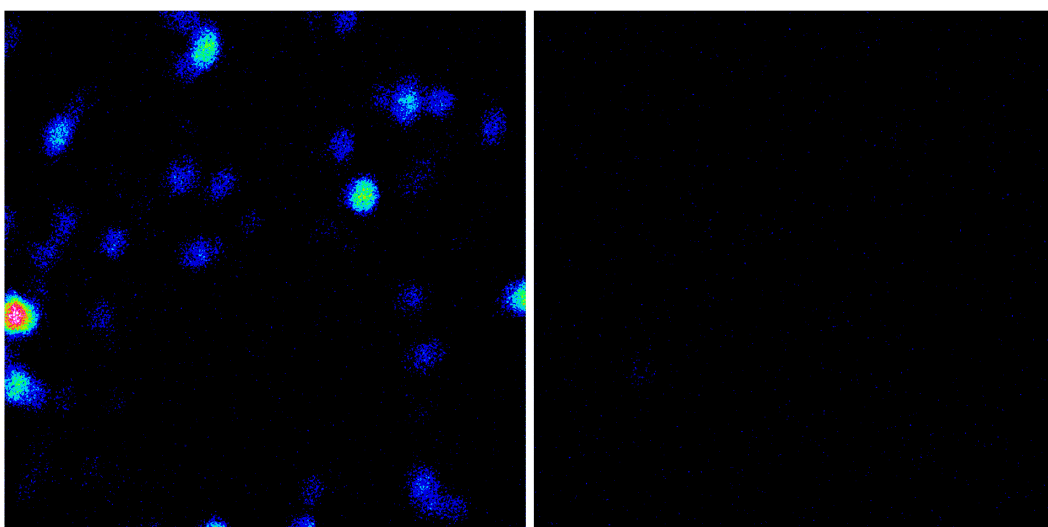
Figure 4.3-LVI: Phosphorus elemental map of batches A-2a (left hand) and R-1a (right hand)

4. Results and discussion
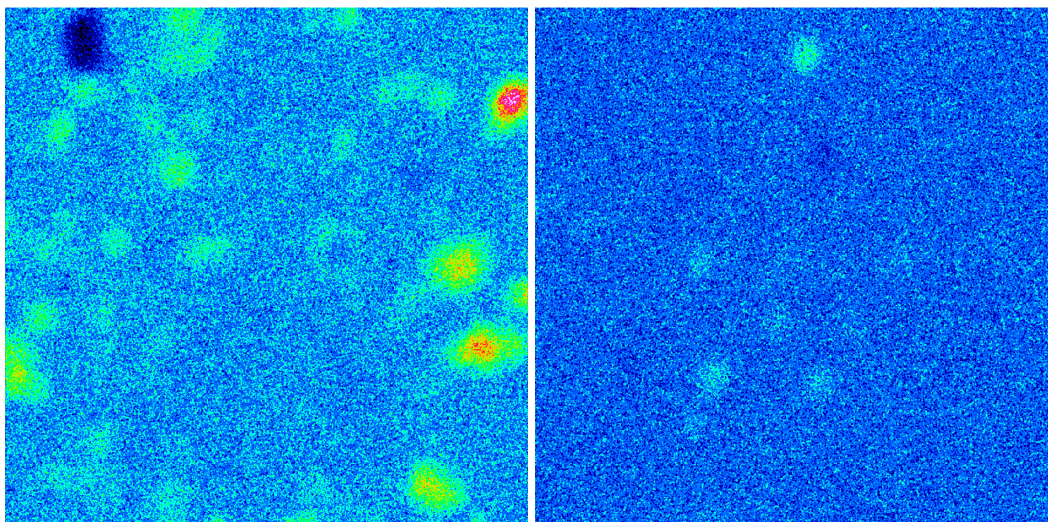
Figure 4.3-LVII: Potassium elemental map of batches A-2a (left hand) and R-1a (right hand)
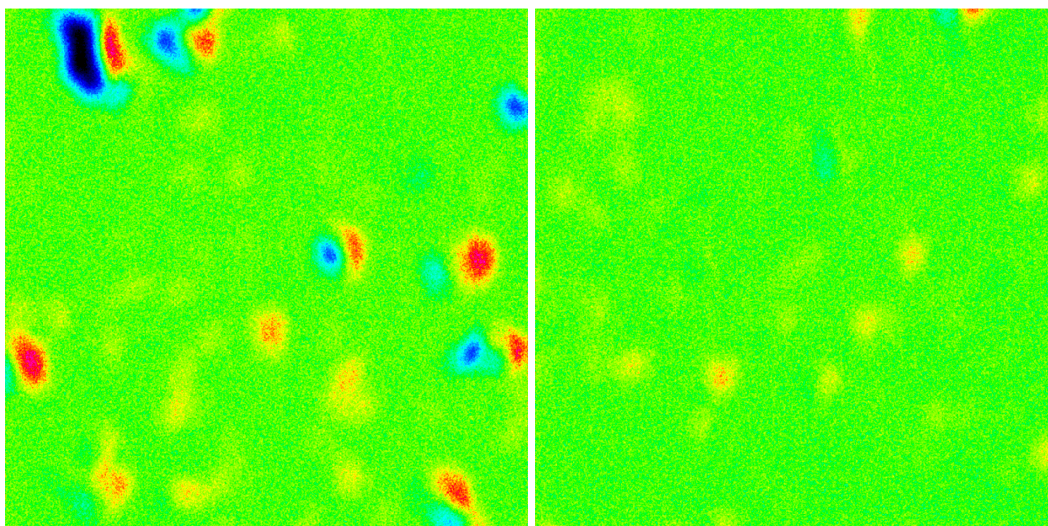
Figure 4.3-LVIII: Oxygen elemental map of batches A-2a (left hand) and R-1a (right hand)
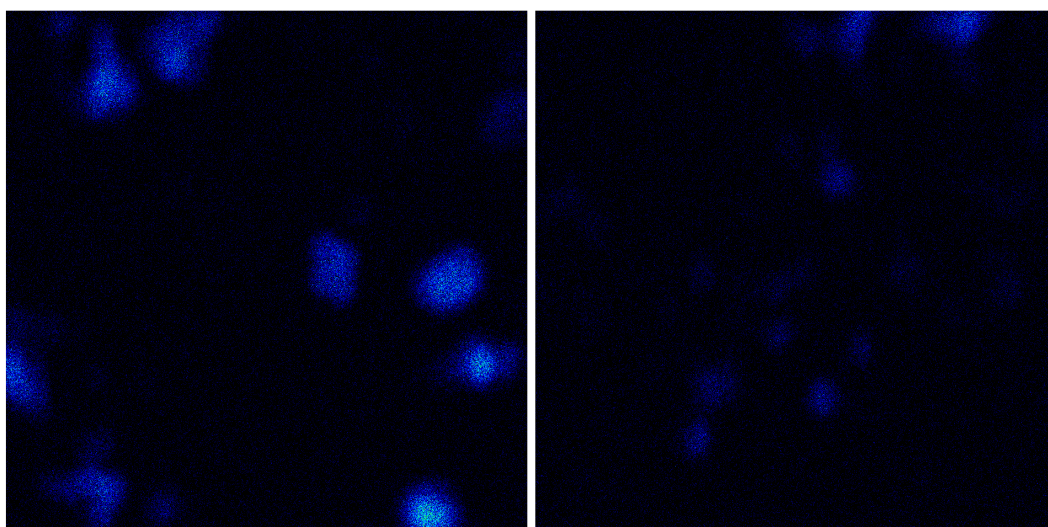
Figure 4.3-LIX: Sulphur elemental map of batches A-2a (left hand) and R-1a (right hand)

4.3.6. Interpretation of the microstructure and chemical composition

The results presented in the previous sections have been sorted in a specific order to permit an appropriate and effective line of argumentation for the interpretation. Firstly, the ρ-T-characteristics are discussed in relation to the microstructure, which has been presented in section 4.3.1 and 4.3.2. Secondly, the relation of the chemical variations that have been illustrated in sections 4.3.3, 4.3.4 and 4.3.5 to the change in PTCR-performance is argued. Finally, the consequences of the above mentioned results on the defect chemistry and the PTCR in donor- and acceptor-codoped (Ba,Ca)TiO$_3$ are debated in section 4.4.

Starting with the microstructural investigation it seems useful to correlate the obtained grain sizes (q.v. section 4.3.1) with the room temperature resistivity of the investigated batches. This correlation is illustrated in Figure 4.3-LX. The graph clearly demonstrates that the resistivity of the a-batches having an A/B-ratio of 0.998 or rather close to one strongly depends on the grain size, which shows values between 4µm and 5µm. For this reason, the differences in resistivity between anatase- and rutile-based materials in a-batches cannot only be attributed to microstructural variations but rather seem to result from the impurity content, which is displayed in Figure 4.3-LXI and Figure 4.3-LXII. On the contrary, for the b-batches having an A/B-ratio of 0.985 the correlation seems to work the other way around i.e. the material properties mainly depend on the microstructural changes, which is in agreement with the observations made by Amin et al. [Ami-83]. These researchers investigated the PTCR-performance of La-Mn-codoped BaTiO$_3$ prepared from commercial anatase and rutile TiO$_2$. The raw materials they used were comparable to the titania raw materials A-1, A-2 and R-1 used in this work. Their compositions contained a Ti-excess of 1.5mol-%, which is similar to the b-batches, but were prepared without silicon addition. Amin et al. [Ami-83] found that for similar sintering regimes the rutile batch showed coarse-grained microstructure whereas the anatase batch produced small-grained microstructures. This finding is contradictory to the results obtained in this work where the anatase compositions A-1b and A-2b resulted in coarse-grained microstructure compared to the rutile reference R-1b. This discrepancy can be attributed to the differences in sintering additives (segregative additives) added. In the case of Amin et al. [Ami-83], the secondary liquid phase is produced by Ti-excess, which results in the BaTiO$_3$-Ba$_6$Ti$_{17}$O$_{40}$ eutectic. On the contrary, in the compositions prepared in this work the secondary phase additionally contains silicon, which results in a lower melting liquid phase compared to the eutectic.

However, Amin et al. sintered the anatase batch to a similar microstructure and verified that the PTCR-performance for both materials is comparable in that case [Ami-83]. Referring to their results and the findings obtained from the b-batches prepared in this work it can be concluded that for compositions containing a high amount of Ti-excess, the variation in microstructure becomes the predominant parameter that determines the PTCR-properties of the material.
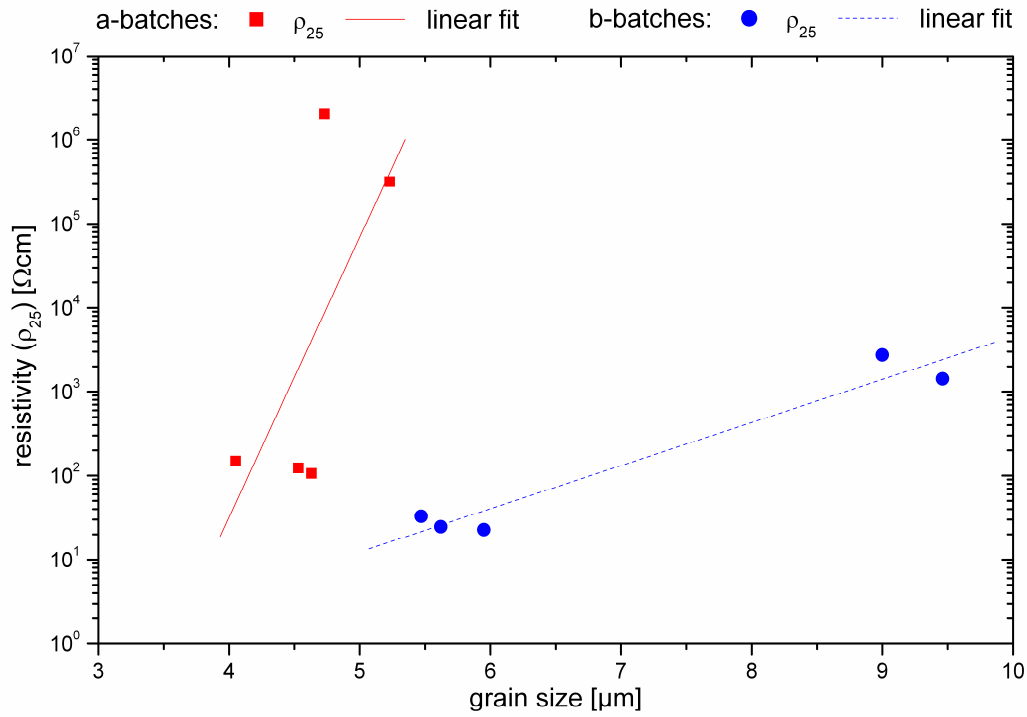
Figure 4.3-LX: Room temperature resistivity as a function of grain size
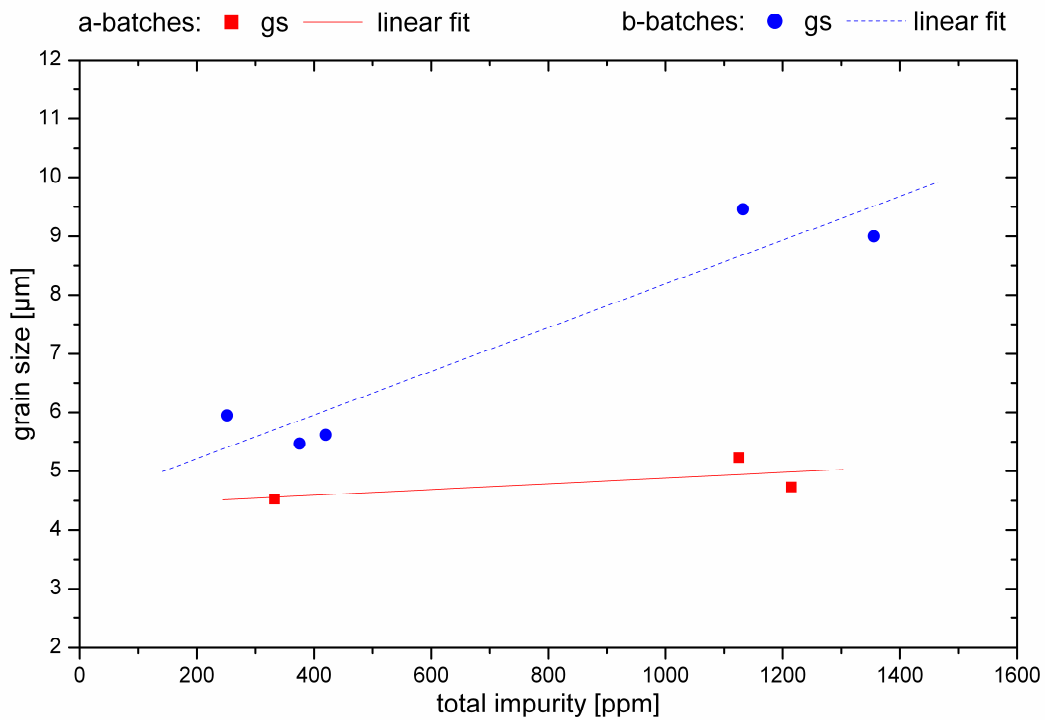

Figure 4.3-LXI: Average grain size as a function of the total impurity content. Total impurities contain Na, Mg, P, K, Cl, Fe, Zr, Nb (see Table 3.1-I)
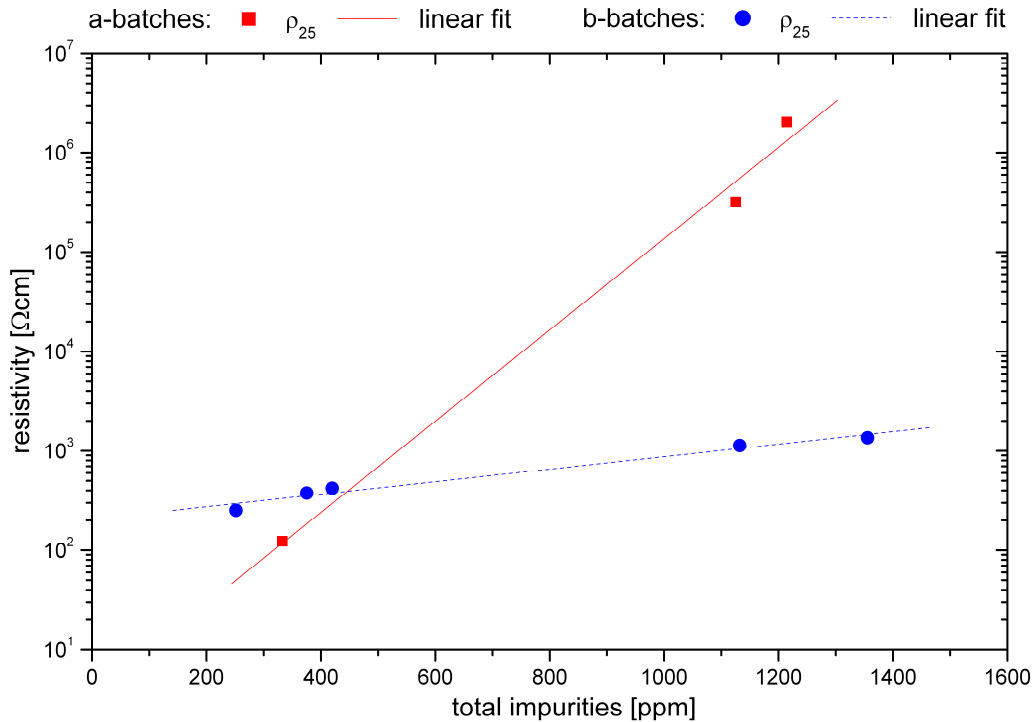
4. Results and discussion

Figure 4.3-LXII: Correlation of the total impurities with resistivity. Total impurities contain Na, Mg, P, K, Cl, Fe, Zr, Nb (see Table 3.1-I)

Experiments with varying donor content have been carried out for composition A-2b as described in section 3.2 (anatase experiments). The results of the ρ-T-characteristic and the characteristic values are presented in Figure 4.3-LXIII and Table 4.3-IV respectively. Comparing batches A-2b with A-2c (reduced donor content) and A-2d (increased donor content) clearly shows that increasing the donor dopant content about 0.1mol-% reduces the resistivity values at low temperatures about one decade from 2810Ωcm to 319Ωcm. On the contrary, reduced donor content resulted in highly resistive material with a value of 2.32*10^{10}Ωcm for the room temperature resistivity without any PTCR-characteristics. Additionally, the microstructures of the basic anatase compositions are depicted in Figure 4.3-LXIV to Figure 4.3-LXVII. The average grain sizes of these materials amount to 19.3µm for A-2c and 6.4µm for A-2d. In comparison to composition A-2b, which shows an average grain size of about 9.0µm, this is in complete agreement with the model proposed by Drofenik [Dro-87, Dro-90, Dro-93, Dro-99, Dro-02] and summarised in section 2.2.5. This model correlates the anomaly of grain size with the anomaly in conductivity. Regarding the Drofenik model, it is concluded for the b-batches that the variation in ρ-T-characteristic between anatase- and rutile-based materials mainly originates from the variation in microstructure as illustrated in section 4.3.1. Based on the Drofenik model the sintering behaviour can be described in the following manner. During sintering, the donor dopants are incorporated following Equation 2.2-X (section 2.2.5), which is widely accepted to represent the major defect compensation mechanism (electron compensation) in n-BaTiO$_3$ [Cha-84, Lew-86, Smy-23]. The mentioned incorporation mechanism is accompanied by an oxygen release, which is proportional to the incorporated donor dopant amount. The incorporated dopant then retards normal grain growth (NGG) and results in smaller grain size exhibiting higher conductivity. Consequently, it can be

4. Results and discussion

concluded for the compositions prepared in this work that an increased grain size arises from decreased donor dopant incorporation or rather an increased GBL width (q.v. Figure 2.2-IV). Accordingly, the varied grain growth inhibition results from differences in the effective donor dopant concentration dissolved in the $(Ba,Ca)TiO_3$ lattice. In this conext it is worth to note that different dopants inhibit grain growth to a varying extend [Ala-88, Pen-88, Xue-88/1, Xue-88/2, Gli-00, Qi-02, Fis-06].

Other studies provide another possibility to explain the observed shifts in PTCR-jump. For example Jayanthi [Jay-06] or Ho [Ho-94] found that additives such as Al_2O_3, B_2O_3, SiO_2, TiO_2 or BaO influence the activation of defect states due to intergranular secondary phases [Ho-94, Kut-98, Jay-06]. Following Jayanthi [Jay-06], who describes the influence of SiO_2-, B_2O_3- and Al_2O_3-addition on the PTCR characteristics of n-$BaTiO_3$, this effect will further be called the effect of segregative additives. Jayanthi [Jay-06] detected that B_2O_3 addition causes a steep rise in PTCR-jump whereas Al_2O_3 addition results in flattened resistivity jumps hence shifting ρ_{max} and T_{max} to higher values. Nevertheless, he also demonstrated that these shifts were clearly distinguishable from the T_C-modifications resulting from lead or strontium addition both causing much stronger shifts. Supposing that such an effect also occurs in the compositions prepared from commercial anatase in this study, the observed changes in slope and height of the PTCR-jump might be due to phosphorus containing secondary phase or liquid phase. With regard to the microstructure observations, which prove the existence of a phosphor containing minor phase (see sections 4.3.3 to 4.3.5) located at the grain interspaces, the assumption is made that phosphor acts as segregative additive hence creating another liquid phase. To verify this assumption, two compositions A-2e and A-2f with reduced silicon content have been prepared and analysed (see Figure 4.3-LXIII and Table 4.3-IV). For the reference composition A-2b, the silicon content amounts to 0.98mol-%. In batches A-2e and A-2f the silicon content is reduced to 0.86mol-% and 0.74mol-% respectively. It is obvious from Figure 4.3-LXIII that reducing the silicon content from 0.98mol-% to 0.86mol-% does not change ρ_{min} but strongly affects ρ_{max}, which results in increased PTCR-performance (q.v. Table 4.3-IV). Further reduction of the silicon content to 0.74mol-% (A-2f) again increases ρ_{max} but contrary to A-2e strongly increases ρ_{min} too. Consequently, this results in decreased PTCR-characteristic (Table 4.3-IV). The microstructures of composition A-2e and A-2f are depicted in Figure 4.3-LXVI and Figure 4.3-LXVII. The average grain sizes amount to 8.4µm for composition A-2e and 9.4µm for batch A-2f. Compared to composition A-2b with average grain size of about 9.0µm these results indicate that grain growth in A-2f is suppressed whereas grain growth in A-2e is accelerated. With respect to the Drofenik model [Dro-87, Dro-90, Dro-93, Dro-99, Dro-02], the mentioned results indicate that the donor dopant incorporation is affected due to the amount and chemical composition of the secondary phases (segregative additive effect).
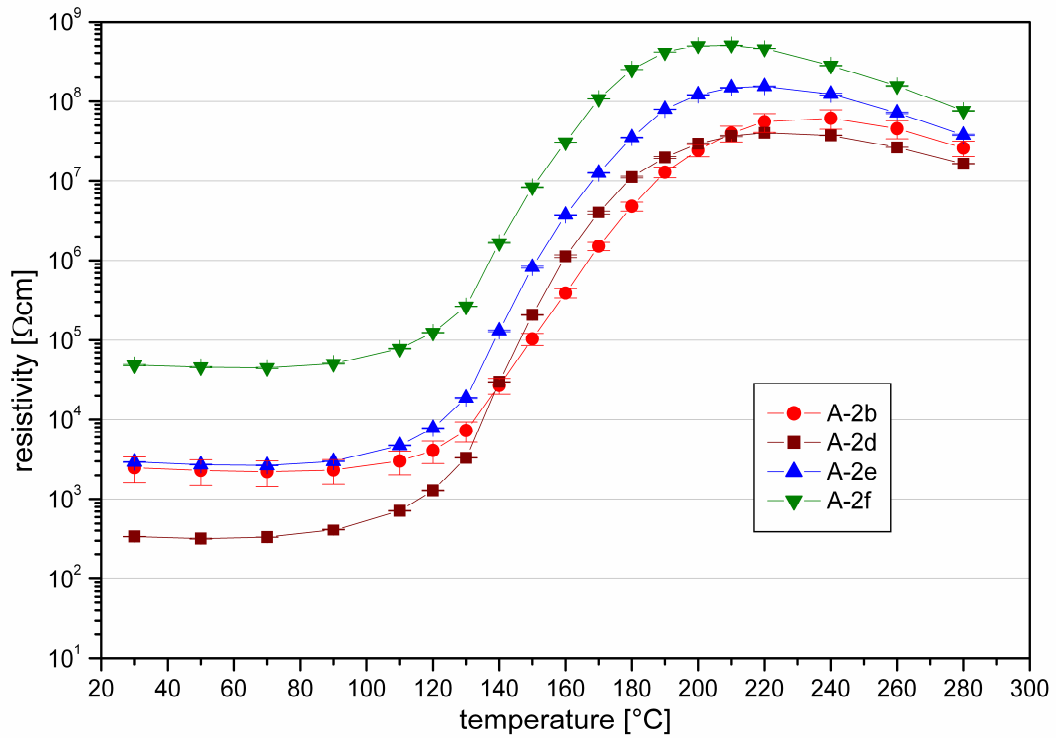
4. Results and discussion

Figure 4.3-LXIII: Resistivity as a function of temperature (ρ-T-characteristic) of the anatase-batches at a measurement voltage of 10V

Table 4.3-IV: Characteristic values of the ρ-T-graphs (measured at 10V)

Batch no.	ρ_{min} [Ωcm]	ρ_{max} [Ωcm]	T_{max} [°C]	$\alpha_{(130-180°C)}$ [%/°C]
A-2b	2.81E+03	7.41E+07	233	12.84
A-2c	2.32E+10	n.d.	n.d.	n.d.
A-2d	3.19E+02	4.02E+07	223	16.25
A-2e	2.67E+03	1.53E+08	214	15.08
A-2f	4.48E+04	5.08E+08	207	13.71
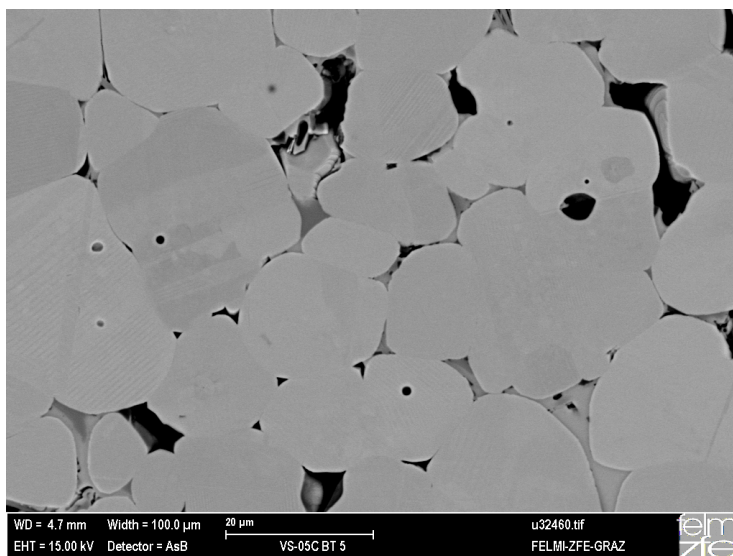
Figure 4.3-LXIV: A-2c SEM micrograph; picture width 100µm

4. Results and discussion
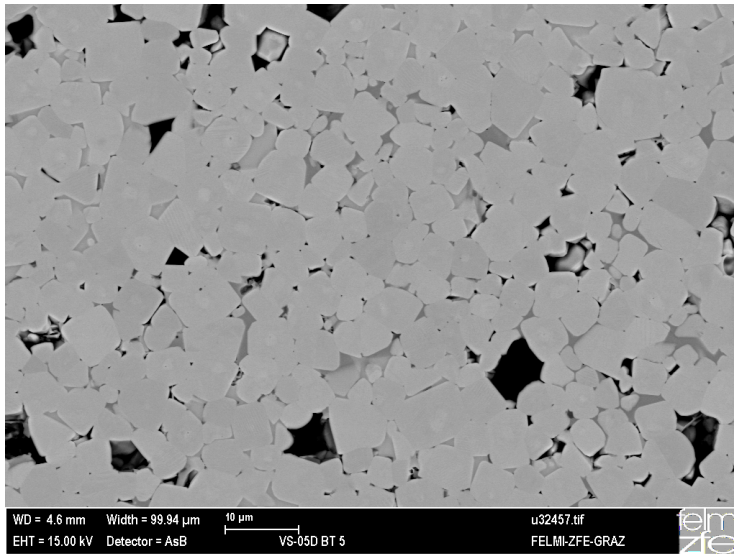
Figure 4.3-LXV: A-2d SEM micrograph; picture width 100µm
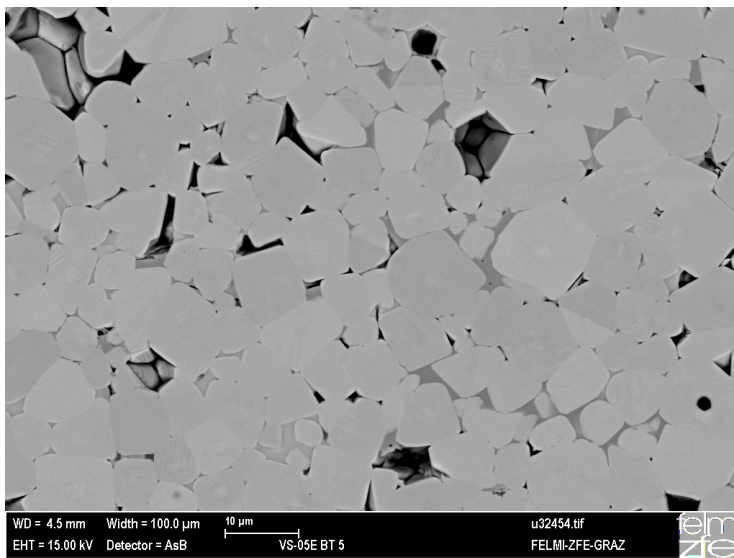
Figure 4.3-LXVI: A-2e SEM micrograph; picture width 100µm
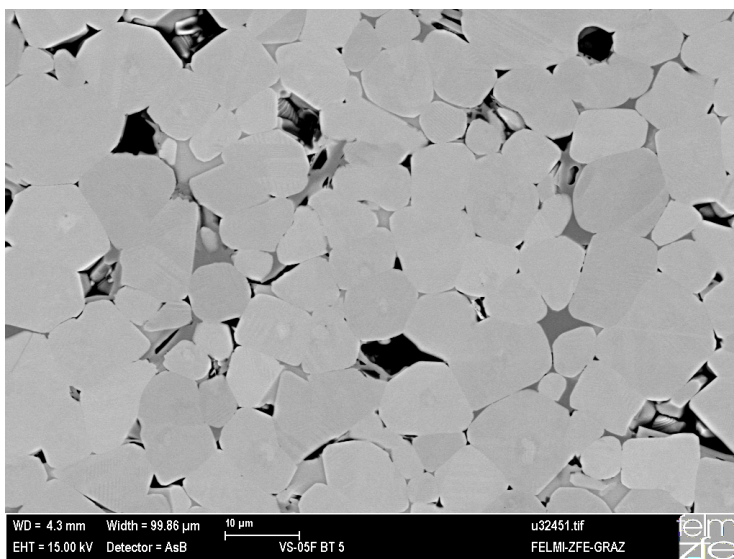
Figure 4.3-LXVII: A-2f SEM micrograph; picture width 100µm

4. Results and discussion

Furthermore, an assumption can be made about the influences of the main impurities phosphor and potassium on the PTCR-characteristics in n-(Ba,Ca)TiO$_3$. It is supposed that the addition of phosphor provokes liquid phase generation due to its ability to act as a glass network former [Sch-90, Vog-92] but alternatively it must be taken into account that the P^{5+} ion might be incorporated into the BaTiO$_3$ lattice substituting for Ti^{4+} hence acting as donor dopant ($P_{Ti}^{\bullet}$) [Cab-95, Wan-98]. Additionally, similar assumptions can be made in case of potassium, which might act as glass network modifier influencing the liquid phase properties [Sch-90, Vog-92] or substitute for Ba^{2+} thus acting as acceptor dopant (K_{Ba}'). The latter assumption especially is valid for impurity ions, which are able to substitute for barium or titanium by reason of the ionic radii, as is the case for phosphor and potassium. Finally, it is important to note that alkaline metals such as potassium tend to volatilize under temperature load (alkali volatility) especially at temperatures above 1000°C [Sch-90].

The results obtained by SEM-EDX, TEM and EPMA support the above made presumptions. On the one hand, potassium, with its ionic radius of 1.52Å ranging close to the barium ionic radius of 1.49Å, is partly incorporated into the grains (see Equation 4.3-I and Equation 4.3-II) thus acting as acceptor dopant. On the other hand, potassium is mainly detected in the phosphorus secondary phase and consequently acts as glass network modifier (q.v. section 4.3.4). On the contrary, phosphorus without exception is located at the grain interspaces hence acting as segregative additive. Referring to the microscopic investigations (sections 4.3.3, 4.3.4 and 4.3.5) one of the remaining questions concerns the role of the Y-containing CaTiO$_3$ minor phase. Due to the results obtained by XRD (Table 4.2-II and Table 4.2-III) it is concluded that this phase represents a residual CaTiO$_3$ phase, which was assumed to be completely dissolved in the BaTiO$_3$ lattice to form (Ba,Ca)TiO$_3$ solid solution as illustrated in Figure 2.2-XV and Figure 2.2-XIV [Dev-55, Kwe-59]. The mentioned extraordinary high yttrium content (see section 4.3.3 and 4.3.4) detected within the CaTiO$_3$ phase can be explained by taking into account the radii of the involved ions. The ionic radius of the Ba^{2+}-ion is 1.49Å whereas the Ca^{2+} ionic radius of 1.14Å is significantly smaller. Comparing these ionic radii with the donor ion radius of Y^{3+} (1.04Å) it is apparent why yttrium preferentially is incorporated into the CaTiO$_3$ lattice. Additionally, it is worth noting that during calcination the CaTiO$_3$ formation takes place at temperatures between 550 to 720°C whereas BaTiO$_3$ forms between 720 to 1050°C due to the lower decomposition temperatures of CaCO$_3$ compared to BaCO$_3$ (see section 4.2.2). Taking into account the earlier formation and the higher melting point of CaTiO$_3$ as well as the similarity of the ionic radii between calcium and yttrium, it becomes more reasonable why such a residual CaTiO$_3$ minor phase acts as a sink for donors.

The observed phase composition gives rise to the presumption that the effective donor concentration, which has to be taken into account when describing the electrical behavior of PTCR-materials, is much lower than it is expected from the nominal composition. Based on a study of the defect chemistry of n-conducting barium titanate at high temperatures (1100–1250°C), Preis and Sitte [Pre-06] estimated the concentrations of point defects for (Ba$_{0.85}$,Ca$_{0.15}$)TiO$_3$ doped with 0.5mol% yttrium and 0.1mol% manganese. The donor concentration was found to be approximately 0.22mol-%, which is significantly lower than the nominal value of 0.3mol-% obtained from the overall composition. This discrepancy cannot

4. Results and discussion

entirely be explained, leaving the open question whether the yttrium dopant is segregated at the grain boundaries or is partly incorporated into the titanium sublattice acting as acceptor ion (partially self compensation of $Y^{\bullet}_{Ba}$ by Y'_{Ti}). The latter assumption is less propable for the compositions investigated in this work. On the one hand, it is well known, that yttrium due to its ionic radius behaves as acceptor (Ti-site occupation) only in the presence of Ba-excess [Tak-90, Smy-00]. Consequently, in compositions A-1a and R-1a, in which Ti-excess has been detected by EPMA-measurements (see Equation 4.3-I and Equation 4.3-II), yttrium preferentially occupies the barium lattice site. On the other hand, no indication of yttrium segregation at the grain boundaries could be observed in compositions A-1a and R-1a investigated by TEM (see section 4.3.4).

Moreover, Blanchart et al. [Bla-92] investigated the grain and grain boundary resistivity in $BaTiO_3$ as a function of yttrium doping by means of impedance spectroscopy and microprobe analysis. They detected that the amount of yttrium incorporated into the $BaTiO_3$ grains is always lower than the overall concentration in the starting powder. Nevertheless, they detected yttrium rich areas inhomogeneously dispersed in the $Ba_6Ti_{17}O_{40}$ minor phase [Bla-92]. They did not find any additional intergranular minor phase that dissolves the residual yttrium as is the case in the $(Ba,Ca)TiO_3$ system studied in this work. Referring to these authors and taking into account the microscopic investigations an explanation is now available to resolve the discrepancy between the nominal value and the donor content obtained from defect chemical calculations based on conductivity measurements. It is concluded that the above-mentioned residual $CaTiO_3$ phase dissolves an additional amount of yttrium.

Furthermore it is expected that potassium, introduced by the anatase raw materials, acts as acceptor ion [K'_{Ba}] compensating the donor dopant [$Y^{\bullet}_{Ba}$]. From these considerations it can be concluded that the effective donor concentration ([$D^{\bullet}$]$_{eff}$) must be significant lower than 0.2mol-% thus increasing the potential barrier. Moreover, in accordance with Equation 2.2-VI a tremendous increase of the Schottky barrier height Φ_w is anticipated when the interfacial charge density (occupied acceptor state density N_s) is increased probably owing to segregation of acceptor co-dopants and/or impurities [Huy-95, Pre-04]. It can be deduced from these results that such a decrease of [$D^{\bullet}$]$_{eff}$ accompanied with an increase of N_s provokes the observed increase of the room temperature resistivity and ρ_{min}, respectively (Figure 4.1-II and Figure 4.1-III) by increasing the barrier height, which fits the results of the impedance analysis (see section 4.1.2).

The mentioned results indicate that modifications in defect chemistry at the grain boundaries e.g. the variation in effective donor concentration ([$D^{\bullet}$]$_{eff}$) or the additional incorporation of acceptor states (N_s), give rise to the higher resistivity of the anatase compositions A-1 and A-2. In the following section, a model is proposed that accounts for the observed variation in defect chemistry due to a modified sintering mechanism.

4.4. Consideration of the sintering mechanism with respect to the defect chemistry

Referring to the results presented in sections 4.1.1 and 4.1.2 two facts are known for sure. Firstly, the ρ-T-characteristics of the anatase-based materials A-1 and A-2 show much higher resistivity values compared to the rutile reference and the anatase-rutile mixture materials (q.v. Figure 4.1-II and Figure 4.1-III). Secondly, the impedance measurements clearly demonstrate that the variation in resistivity between anatase- and rutile-based materials is located at the grain boundaries (see Figure 4.1-XII and Figure 4.1-XIII).

The essential question now is which effect generates high resistivity without modifying the grain conductivity.

The answer can easily be given by considering the GBL width of the material. In Heywang's model, which has already been mentioned in section 2.2.3, the GBL width (Equation 2.2-V) is correlated with the potential barrier height (Equation 2.2-VI) and the resistivity of the material (Equation 2.2-VII). On the one hand, a dramatic increase of the Schottky barrier height Φ_w is provoked (Equation 2.2-VI) when the occupied acceptor state density N_s is increased due to the quadratic dependence of the barrier height on N_s. On the other hand, lowering the effective donor concentration also increases the potential barrier height by increasing the GBL width hence increasing the resistivity of the material. The latter minor effect can be induced by varying the donor dopant content [Dan-79, Pen-88, Huy-95] as described for the anatase batches A-2b, A-2c and A-2d in the previous section 4.3.6. On the contrary, an increase of the occupied acceptor states N_s can be achieved by variations in the chemistry and quantity of secondary phases or rather segregative additives. As the name implies, such additives affect the segregation behaviour of dopants and impurities thus affecting the density of occupied acceptor states [Huy-95, Pre-04, Pre-06, Jay-06] as illustrated above for compositions A-2b, A-2d and A-2e (section 4.3.6).

It is widely accepted that in donor- and acceptor-codoped $BaTiO_3$ the following defects occur accompanied by the mentioned major compensation mechanisms [Bus-01].

- A-site donor dopant compensated by electrons (Y)
- A-site acceptor dopant compensated by oxygen vacancies (K)
- B-site donor dopant compensated by electrons (Nb, P)
- B-site acceptor dopant compensated by oxygen vacancies (Mn, Al, Fe, possibly Ca)

For the materials investigated in this thesis, Equation 4.4-I and Equation 4.4-II illustrate the doping incorporation of the donor ion Y^{3+} and the acceptor ion Mn^{2+} respectively[Lew-86, Dro-86, Sas-99, Bus-01]. Moreover, Equation 4.4-III and Equation 4.4-IV denote the corresponding defect chemical equations of the impurity ions Nb^{5+} and Al^{3+}, the latter also being valid for Fe^{3+} [Lew-86, Dro-86, Sas-99, Bus-01]. Additionally the main impurities phosphorus and potassium, which have been detected in the anatase materials A-1 and A-2, may be incorporated as donor- and acceptor-ions following Equation 4.4-III and Equation 4.4-V respectively [Lew-86, Dro-86, Sas-99, Bus-01]. Finally, a direct compensation mechanism of the donor dopant ions by acceptor ions has to be

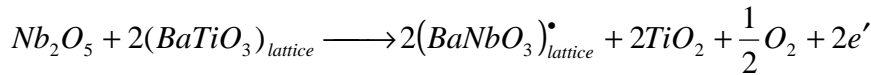## 4. Results and discussion

taken into account as illustrated in Equation 4.4-VI [Dro-86]. The mentioned impurity ions mainly result from the ore quality and the preparation route used in TiO_2 production (see section 2.1).
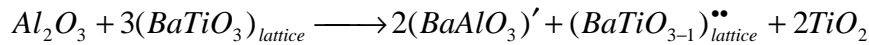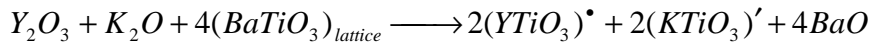
$$Y_2O_3 + 2(BaTiO_3)_{lattice} \longrightarrow 2(YTiO_3)^{\bullet}_{lattice} + 2BaO + \frac{1}{2}O_2 + 2e'$$

Equation 4.4-I

$$MnO + 2(BaTiO_3)_{lattice} \longrightarrow (BaMnO_3)''_{lattice} + (BaTiO_{3-1})^{\bullet\bullet}_{lattice}$$

Equation 4.4-II

$$Nb_2O_5 + 2(BaTiO_3)_{lattice} \longrightarrow 2(BaNbO_3)^{\bullet}_{lattice} + 2TiO_2 + \frac{1}{2}O_2 + 2e'$$

Equation 4.4-III

$$Al_2O_3 + 3(BaTiO_3)_{lattice} \longrightarrow 2(BaAlO_3)' + (BaTiO_{3-1})^{\bullet\bullet}_{lattice} + 2TiO_2$$

Equation 4.4-IV

$$K_2O + 3(BaTiO_3)_{lattice} \longrightarrow 2(KTiO_3)'_{lattice} + (BaTiO_{3-1})^{\bullet\bullet}_{lattice} + 2BaO$$

Equation 4.4-V

$$Y_2O_3 + K_2O + 4(BaTiO_3)_{lattice} \longrightarrow 2(YTiO_3)^{\bullet} + 2(KTiO_3)' + 4BaO$$
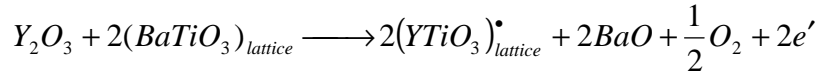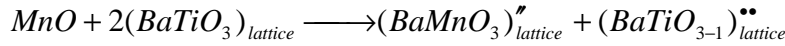
Equation 4.4-VI

Based on the results presented in this thesis a modified sintering mechanism of the anatase-based materials in comparison to the rutile reference is proposed that can be described in the following manner. The anatase-based calcined powders contain of $BaTiO_3$, $CaTiO_3$, a Ba-rich phosphorus phase and a Ba-rich silicon phase, both located at the grain surfaces, as well as of a Ti-rich secondary phase. These surface located secondary phases reduce the grain-grain surface contact area thus acting as barriers to volume diffusion during initial sintering stage [Sal-07]. Caballero et al. [Cab-95, Cab-98, Cab-00] and Wang et al. [Wan-98] firstly investigated this effect for phosphorus-doped $BaTiO_3$ as discussed in section 4.2.4. The formation of an additional Ba-rich phosphorus secondary phase shifts the A/B-ratio of the bulk towards lower values [Cab-95]. In compositions prepared with minor Ti-excess (a-batches), this shift results in significantly increased Ti-excess, which gives rise to exaggerated grain growth below 1200°C [Mau-87]. Furthermore Caballero et al. [Cab-95] as well as Wang et al. [Wan-98] figured out that below 1300°C phosphorus is incorporated into the $BaTiO_3$ lattice thus acting as donor dopant as illustrated in Equation 4.4-III for niobium. Again, the phosphorus behaviour produces an increase of the Ti-excess or rather keeps the Ti-excess at a constant level emerging from the consumption of BaO during phosphor incorporation [Cab-95]. Guha and Kolar [Guh-74] investigated the liquid phase formation in the ternary system $BaO-TiO_2-SiO_2$. Later Felgner et al. [Fel-01] adapted the findings of Guha et al. to the $BaTiO_3-SiO_2$ system. The latter found that the ternary eutectic at 1195°C also forms from $BaTiO_3$ in the presence of silicon-containing secondary phase generated during calcination or initial sintering as illustrated in Equation 4.4-VII and Equation 4.4-VIII [Fel-01]. Consequently, it can be concluded that the phosphor-induced increase of the

4. Results and discussion

limiting Ti-rich secondary phase $Ba_6Ti_{17}O_{40}$ strongly enhances liquid phase formation in the mentioned temperature range between 1200°C and 1300°C.

$$28BaTiO_3 + 22SiO_2 \xrightarrow{T<T_{eutectic}} 11Ba_2TiSi_2O_8 + Ba_6Ti_{17}O_{40}$$

Equation 4.4-VII

$$5BaTiO_3 + 2.5Ba_6Ti_{17}O_{40} + 6.5Ba_2TiSi_2O_8 \xrightarrow{T_{eutectic}=1195°C} (Ba_{33}Ti_{54}Si_{13}O_{167})_{liquid}$$
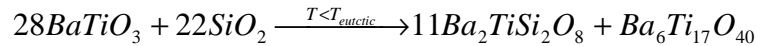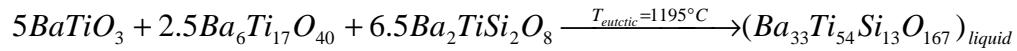
Equation 4.4-VIII

At temperatures above 1300°C, the phosphorus resegregates at the grain boundaries leaving behind titanium vacancies inside the $BaTiO_3$ grains [Cab-95, Wan-98]. To compensate the generated vacancies two mechanism can be assumed. Firstly, compensation is achieved by mass transport of titanium ions from secondary phases e.g. from the liquid phase formed around 1200°C. Secondly, the compensation mechanism takes place by the formation of oxygen vacancies. Due to the high temperatures (>1300°C) it is expected that both compensation mechanisms proceeed very fast and achieve equilibrium during further sintering. As a result, the Ti-depletion of the eutectic liquid gives rise to a change in the grain growth rate of the liquid phase due to variations in the liquid phase chemistry and the dissolution-precipitation characteristics [Fel-01]. Additionally the phosphorus resegregation at the grain boundaries induces an increase of the grain boundary resistance by increasing the acceptor state density N_s due to secondary phase formation (effect of segregative additives). The results of the impedance data are in accordance with this assumption (q.v. section 4.1.2). Simultaneously the potassium behaviour has to be taken into account. Fundamentally, potassium affects the properties of the silicon- and phosphorus-containing low melting secondary phases by reducing the melting points of the liquids due to its ability to act as glass network modifier [Rao-02]. As already mentioned, the anatase based batches contain of a high-melting Ba-rich phosphorus secondary phase ($Ba_3(PO_4)_2$) before sintering (q.v. section 4.2.4). Additionally, the secondary phases resulting from the silicon addition (see Equation 4.4-VII), likewise start melting at elevated temperatures (>1195°C). Consequently, potassium tends to be incorporated into the bulk with increasing temperature during initial sintering following Equation 4.4-V or Equation 4.4-VI. The simultaneous incorporation of potassium and yttrium provokes compensation of the donor dopant, entails an increased Ba-rich secondary phase formation (Equation 4.4-VI) and gives rise to a grain growth mechanism that is independent of the donor dopant content [Dro-86]. With further increasing temperature, particularly >1300°C when the phosphorus resegregation proceeds, the tendency of potassium to volatilise strongly increases. On this account a considerably amount of potassium expels from the bulk leaving behind an enhanced concentration of barium vacancies, which lead to an enlargement of the GBL-width by raising the occupied acceptor state density N_s thus increasing the grain boundary resistance. The reason why potassium at such high temperatures does not completely volatilise out of the material into the furnace atmosphere can be given by taking into account the phosphorus- and silicon-containing secondary phases, which are located at the grain interspaces and for this reason block the pathways of gaseous components. Finally, during cooling the potassium again dissolves in the liquid phases thus decreasing the viscosity of the melts, which

4. Results and discussion

results in an extended mass transport or rather grain growth due to the increased mobility [Sch-90].

In the end, it can be summarised that almost all mentioned changes in local chemical composition or defect chemistry affects the grain growth behaviour or rather the sintering of the PTCR-material. Thus, the predominant grain growth effect, wheather it is inhibiting or accelerating, finally determines the microstructure. For the compositions prepared in this work this means that in the case of a-batches with A/B-ratio of 0.998, the differences in grain growth process between anatase- and rutile-based materials is mainly independent of the titania raw material. This indicates that the inhibiting and accelerating effects compensate for each other and the microstructure gives no evidence of the PTCR-properties. In this case, the defect chemistry along the grain boundaries, which is mainly affected by segregative additives, accounts for the changes in PTCR-performance. On the contrary, in b-batches having A/B-ratios of 0.985 the microstructure between anatase- and rutile-based compositions is strongly affected by the titania raw material indicating that the predominant grain growth mechanism varies and finally gives rise to the differences in PTCR-characteristics.

5. Summary and Conclusion

The effect of commercially anatase TiO_2 raw materials containing the main impurities phosphor and potassium on the PTCR-characteristics of donor and acceptor codoped $(Ba,Ca)TiO_3$ ceramics has been investigated. It is illustrated that the purity of the titania raw material is responsible for the observed changes in shape and height of the PTCR-jump. Furthermore, it is demonstrated that, in the case of similar impurity levels of the titania materials, both rutile and anatase generate comparable PTCR-characteristics verifying that anatase in principle is applicable in PTCR-production.

The investigated compositions on the one hand have been prepared with a minor titanium excess (AB-ratio of about 0.998). On the other hand, the raw materials have been compared in compositions containg increased titanium excess (AB-ratio of about 0.985). The results have shown that both mechanism and magnitude of the impurity effect are strongly affected by the A/B-ratio of the material at least during sintering.

With help of process-control analyses as well as STA- and XRD-measurements, a modified solid-state synthesis process has been proposed for the anatase-based compositions. The modified formation mechanism includes the participation of the main impurities phosphorus and potassium, which in this combination act as glass network former and modifier respectively.

During the investigation of the a-compositions having minor titanium excess, microscopic techniques such as SEM-EDXS/WDXS, EBSD as well as impedance spectroscopy are applied. It is shown that in a-batches no significant changes in microstructure evolution concerning grain size and low Σ grain boundaries are detectable. Likewise, no significant differences in chemical composition regarding the expected main and minor phases are identified. These results indicate that in a-compositions other effects give rise to the huge differences in PTCR-characteristics. Contrary, the b-compositions containing an A/B-ratio of 0.985 have revealed pronounced differences in microstructure. Taking into account the lower magnitude of the impurity effect in the b-batches this suggests that the variations in microstructure mainly give rise to the differences in PTCR-performance.

According to the mentioned results, a modified sintering mechanism is proposed that includes the role of the main impurities phosphor and potassium. It is concluded that the variations in PTCR-jump, detected for the compositions prepared and investigated in this thesis, result from the combined effects of modified defect chemistry and segregative additives. This sintering mechanism is provoked by the main impurities present in commercial anatase materials. It is supposed that dependent on the type of impurity and the material composition the grain growth mechanism is inhibited or accelerated hence the PTCR properties are affected. Referring to the results obtained by impedance analysis and microprobe investigations (EPMA) it is inferred that on the one hand potassium is most probably incorporated into the barium sublattice. For this reason potassium acts as acceptor ion (K'_{Ba}), which compensates for the donor dopant ($Y^{\bullet}_{Ba}$). This decreases the effective donor concentration $[D^{\bullet}]_{eff}$ and consequently raises the

5. Summary and Conclusion

resistivity of the material. On the other hand, the phosphor impurity is found to be exclusively located in the grain interspaces hence acting as segregative additive.

6. Indexes

6.1. Tables

6.2. Figures

6. Indexes

6. Indexes

6. Indexes

6. Indexes

6.3. Glossary, abbreviations and symbols

(ε_0) Permittivity of vacuum; elemental constant: $\varepsilon_0 = 8.85 \cdot 10^{-12}\ As/Vm$

(ε_r) Relative permittivity; material dependent; designation in [As/Vm]

(A/B ratio) Kation relation between A- and B-side ions in the kation sub lattice e.g. in ABO_3

(BET) Specific Surface Area; designation in [m²/g]

(C) Capacitance of a material; designation in [F]

(CL) Cathode Luminescence

(Curie-Weiss law) Describes the permittivity (ε) evolution with temperature (T) above the Curie point (T_C) (phase transition temperature); C denotes a material constant

$$\varepsilon = \frac{C}{T - T_C}$$ Equation 6.3-I

(DSC) Differential Scanning Calorimetry

(EBSD) Electron Backscatter Diffraction

(EDXS) Energy Dispersive X-ray Spectrometry

(EELS) Electron Energy-Loss Spectrometry

(EFTEM) Energy-Filtering TEM

(EPMA) Electron Probe Micro Analysis (or analyser)

(EPR) Electron Paramagnetic Resonance

(FDM) Finite Difference Method; Numerical calculation method based on the principle to find approximate solutions of differential equations using finite difference equations such as $f(x+b) - f(x+a)$

(GBL) Grain Boundary Layer

6. Indexes

(GSD) Grain Size Distribution
(HAADF) High Angle Annular Dark Field
(ICP-OES) Inductive Coupled Plasma - Optical Emission Spectrometer
(ICSD) Inorganic Crystal Structure Database;
https://cds.dl.ac.uk/cds/datasets/crys/icsd/llicsd.html (page version: 22.02.2011)
(LIF) Lithium Fluoride
(LOI) Loss on Ignition
(NGG) Normal Grain Growth
(NTCR) Negative Temperature Coefficient of Resistivity
(PET) PolyEthylene-Therephtalat
(PTCR) Positive Temperature Coefficient of Resistivity
(RT) Room Temperature
(SEM) Scanning Electron Microscopy
(SMD) Surface-Mounted Device
(STA) Simultaneous Thermal Analysis
(STEM) Scanning Transmission Electron Microscopy
(TAP) Thallium Acid Pthalate
(T_b) Reference temperature; calculated by $2 \cdot T(\rho_{min})$
(T_C) Currie-temperature; temperature at which a phase transformation occurs
(TD) Theoretical Density calculated from XRD; designation in [g/cm³]
(TEM) Transmission Electron Microscopy
(TG) Thermal Gravimetry
(T_{max}) Temperature at which ρ_{max} occurs $T(\rho_{max})$
(T_{min}) Temperature at which ρ_{min} occurs $T(\rho_{min})$
(WDXRF) Wavelength Dispersive X-Ray Fluorescence
(WDXS) Wavelength Dispersive X-ray Spectrometry
(XRD) X-Ray Diffraction
(XRF) X-Ray Fluorescence analysis
(YSZ) Yttrium-Stabilized Zirconia
($\alpha_{(130\text{-}140°C)}$) Average ascending slope of the ρ-T-characteristic between 130°C and 140°C; also referred to as α_{max}
($\alpha_{(130\text{-}180°C)}$) Average ascending slope of the ρ-T-characteristic between 130°C and 180°C
($\alpha_{(\rho max\text{-}\rho min)}$) Averaged ascending slope of the ρ-T-characteristic between minimum and maximum specific resistance
(α_{max}) Maximum ascending slope of the ρ-T-characteristic
(ρ_{max}) Highest specific resistance value of the ρ-T-characteristic; designation in [Ωcm]
(ρ_{min}) Lowest specific resistance value of the ρ-T-characteristic; designation in [Ωcm]

(ρ-T-ratio) Characterising value of the ρ-T-curve; calculated by $\dfrac{\rho_{max}/\rho_{min}}{T_{max}-T_{min}}$

7. References

[Abi-91]   H.-P.Abicht, H.T.Langhammer, K.-H.Felgner. The influence of silicon on microstructure and electrical properties of La-doped BaTiO$_3$ ceramics. J Mater Sci 1991; **26**: 2337-2342

[Ala-88/2] H.M.Al-Allak, J.Illingsworth, A.W.Brinkman, G.J.Russel, J.Woods. The effect of donor dopant concentration on the grain boundary layer characteristics in n-doped BaTiO$_3$ ceramics. J Appl Phys 1988; **64**: 6477-6482

[Ala-88]   H.M.Al-Allak, H.W.Brinkman, G.J.Russel, A.W.Roberts, E.Woods. Effect of donor dopant concentration on the room temperature resistivity of BaTiO$_3$ with positive temperature coefficient of resistance. J Phys D: Appl Phys 1988; **21**: 1226-1233

[All-89]   A.B.Alles. V.R.W.Amarakoon, V.L.Burdick. Positive temperature coefficient of resistivity effect in undoped, atmosphericalle reduced barium titanate. J Am Ceram Soc 1989; **72**: 148-151

[Ami-83]   A.Amin, M.Spears, B.Kulwicki. Reaction of Anatase and Rutile with Barium Carbonate. J Am Ceram Soc 1983; **66**:733-738

[Amo-95]   J.M.G.Amores, V.S.Escribano, G.Busca. Anatase crystal growth and phase transformation to rutile in high-area Ti0$_2$, MoO$_3$-TiO$_2$ and other Ti0$_2$-supported oxide catalytic systems. J Mater Chem 1995; **5**: 1245-1249

[Ant-07]   S.M.Antao, I.Hassan. BaCO$_3$: High-temperature crystal structures and the Pmcn $\rightarrow$ R3m phase transition at 811°C. Phys Chem Minerals 2007; **34**: 573-580

[Aue-01]   G.Auer, P.Woditsch, A.Westerhaus, J.Kischkewitz, W.-D.Griebler, M.De Liedekerke. Pigments, inorganic, 2.White pigments. Ullmann's Encyclopedia of Industrial Chemistry 2001;

[Bar-04]   A.S.Barnard, P.Zapol. Effects of particle morphology on surface hydrogenation on the phase stability of TiO$_2$. Phys Rev B 2004; **70**: 235403

[Bar-05]   A.Barnard, L.Curtiss. Prediction of TiO$_2$ Nanoparticle Phase and Shape Transitions Controlled by Surface Chemistry. Nanoletters 2005; **5**:1261-1266

[Bar-49]   J.Barksdale. Titanium; Its occurrence, chemistry, and technology. New York: Ronald Press; 1949

[Bea-83/1] A.Beauger, J.C.Mutin, J.C.Niepce. Synthesis reaction of metatitanate BaTiO$_3$; Part 1: Effect of the gaseous atmosphere upon the thermal evolution of the system BaCO$_3$-TiO$_2$. J Mater Sci 1983; **18**:3041-3046

[Bea-83/2] A.Beauger, J.C.Mutin, J.C.Niepce. Synthesis reaction of metatitanate BaTiO$_3$; Part 2: Study of solid-solid reaction interfaces. J Mater Sci 1983; **18**: 3543-3550

[Bea-84]   A.Beauger, J.C.Mutin, J.C.Niepce. Role and behaviour of orthotitanate Ba$_2$TiO$_4$ during the processing of BaTiO$_3$ based ferroelectric ceramics. J Mater Sci 1984; **19**: 195-201

7. References

[Ber-01]   V.Berbenni, A.Marini, G.Bruni. Effect of mechanical milling on solid state formation of $BaTiO_3$ from $BaCO_3$-TiO_2 (rutile) mixtures. Thermochimica Acta 2001; **374**: 151-158

[Bla-92]   P.Blanchart, J.F.Baumard, P.Abelard. Effect of Yttrium Doping on the Grain and Grain-Boundary Resistivities of $BaTiO_3$ for Positive Temperature Coefficient Thermistors. J Am Ceram Soc 1992; **75**:1068-1072

[Bla-93/1]   J.M.Blamey, T.V.Parry. The effect of processing variables on the mechanical and electrical properties of barium-titanat positive-temperature-coefficient-of-resistance ceramics. Part I. Additives and processing prior to sintering. J Mater Sci 1993; **28**:4311-4316

[Bla-93/2]   J.M.Blamey, T.V.Parry. The effect of processing variables on the mechanical and electrical properties of barium-titanat positive-temperature-coefficient-of-resistance ceramics. Part II. Sintering atmospheres. J Mater Sci 1993; **28**:4317-4324

[Bom-05]   P.Bomlai, N.Sirikulrat, T.Tunkasiri. Effect of heating rate on the properties of Sb and Mn-doped barium strontium titanate PTCR ceramics. Mater Lett 2005; **59**: 118-122

[Bra-65]   D.G.Brandon. The structure of field-evaporated surfaces. Surface Science 1965; **3**:1-18

[Brz-00]   E.Brzozowski, M.S.Castro. Synthesis of barium titanate improved by modifications in the kinetics of the solid state reaction. J Eur Ceram Soc 2000; **20**: 2347-2351

[Brz-02]   E.Brzozowski, J.Sanchez, M.S.Castro. $BaCO_3$–TiO_2 Solid State Reaction: A Kinetic Study. J Mater Synth Process 2002; **10**:1-5

[Brz-03]   E.Brzozowski, M.S.Castro. Lowering the synthesis temperature of high-purity $BaTiO_3$ powders by modifications in the processing conditions. Thermochimica Acta 2003; 398: **123**-129

[Bus-01]   M.T.Buscaglia, V.Buscaglia, M.Viviani, P.Nanni. Atomistic simulation of dopant incorporation in barium titanate. J Am Ceram Soc 2001; **84**: 376-384

[Bus-05]   M.T.Buscaglia, M.Bassoli, V.Buscaglia. Solid-state synthesis of ultrafine $BaTiO_3$ powders from nanocrystalline $BaCO_3$ and TiO_2. J Am Ceram Soc 2005; **88**: 2374-2379

[Bus-08]   M.T.Buscaglia, M.Bassoli, V.Buscaglia. Solid-state synthesis of nanocrystalline $BaTiO_3$: Reaction kinetics and powder properties. J Am Ceram Soc 2008; **91**: 2862-2869

[Cab-00]   A.C.Caballero, J.F.Fernández, M.Villegas, C.Moure, P.Duran. Intermediate Phase Development in Phosphorus-Doped Barium Titanate. J Am Ceram Soc 2000; **83**:1499-1505

[Cab-95]   A.C.Caballero, J.F.Fernández, P.Duran, C.Moure. Phosphor-doped $BaTiO_3$: microstructure development and dielectric properties. J Mater Sci 1995; **30**: 3799-3804

[Cab-97]   A.C.Caballero, J.F.Fernández, C.Moure, P.Duran, J.L.G.Fierro. Dopant distribution and grain growth control in $BaTiO_3$ ceramics doped with ZnO-SiO_2-P_2O_5. J Eur Ceram Soc 1997; **17**: 1223-1230

[Cab-98]   A.C.Caballero, J.F.Fernandez, C.Moure, P.Duran. Phase Formation in phosphorus doped $BaTiO_3$. Mater lett 1998; **35**:72-77

[Car-61]   R.E.Carter. Kinetic model for solid-state reactions. Journal of Chemical Physics 1961; **34**: 2010-2015

7. References

[Cha-84]   N.-H.Chan, D.M.Smyth. Defect chemistry of donor-doped $BaTiO_3$. J Am Ceram Soc 1984; **67**: 285-288

[Cha-86]   H.M.Chan, M.P.Harmer, D.M.Smyth. Compensating defects in highly donor-doped $BaTiO_3$. J Am Ceram Soc 1986; **69**: 507-510

[Che-01]   M.C.Cheung, H.L.W.Chan, C.L.Choy. Study on barium titanate prepared by various methods. J Mater Sci 2001; **36**: 381-387

[Cou-79/1]   M.Cournil, M.Soustelle, G.Thomas. Solid-solid reactions, I: Experimental study of barium metatitanate synthesis. Oxidation of metals 1979; **13**: 77-88

[Cou-79/2]   M.Cournil, M.Soustelle, G.Thomas. Solid-solid reactions, II: Mechanism of barium metatitanate synthesis. Oxidation of metals 1979; **13**: 89-104

[Cri-83]   J.Criado, C.Real. Mechanism of the inhibiting effect of phosphate on the anatase-rutile transformation induced by thermal and mechanical treatment. J Chem Soc, Faraday Trans 1 1983; **79**: 2765-2771

[Cza-57]   A.W.Czanderna, A.F.Clifford, J.M.Honig. Preparation of highly purified TiO_2 (Anatase). J Am Chem Soc 1957; **79**:5407–5409

[Cza-58]   A.W.Czanderna, C.N.R.Rao, J.M.Honig. The Anatase-Rutile transition, part 1: Kinetics of the transformation of pure anatase. Trans Faraday Soc 1958; **54**: 1069-1073

[Dan-76/2]   J.Daniels. Doped barium titanate ceramics, Part II: Defect equilibria in acceptor-doped barium titanate. Philips Res Repts 1976; **31**:505-515

[Dan-76/3]   J.Daniels, R.Wernicke. Doped barium titanate ceramics, Part V: New Aspects of an improved PTC model. Philips Res Repts 1976; **31**:544-559

[Dan-76]   J.Daniels, K.Härdtl. Doped barium titanate ceramics, Part I: Electrical conductivity at high temperatures of donor-doped barium titanate ceramics. Philips Res Repts 1976; **31**:489-504

[Dan-79]   J.Daniels, K.H.Härdtl, R.Wernicke. Der PTC-Effekt von $BaTiO_3$. Philips techn Rdsch 1979; **38**: 1-11

[Dev-55]   R.C.DeVries, R.Roy. Phase equilibria in the system $BaTiO_3$-$CaTiO_3$. J Am Ceram Soc 1955; **38**: 142-146

[Din-08/1]   R.E.Dinnebier, S.J.L.Billinge. Powder Diffraction: Theory and Practice. Cambridge (UK): RSC Publishing, 2008

[Din-08/2]   S.W.Ding, G.Jia, J.Wang, Z.Y.He. Electrical properties of Y- and Mn-doped BaTiO3-based PTC ceramics. Ceramics International 2008; **34**: 2007-2010

[Dro-02]   M.Drofenik, D.Makovec, I.Zajc, H.T.Langhammer. Anomalous Grain Growth in Donor-Doped Barium Titanate with Excess Barium Oxide. J Am Ceram Soc 2002; **85**:653-660

[Dro-82]   M.Drofenik, A.Popovič, L.Irmančnik, D.Kolar, V.Kraševec. Release of oxygen during the sintering of donor-doped $BaTiO_3$ ceramics. J Am Ceram Soc 1982; **65**: C203-C204

[Dro-84]   M.Drofenik, A.Popovič, D.Kolar. Grain growth and related effects in doped $BaTiO_3$. Ceram Bull 1984; **63**: 702-704

[Dro-86]   M.Drofenik. Grain Growth During Sintering of donor-doped Barium Titanate. J Am Ceram Soc 1986; **69**:C8-C9

7. References

[Dro-87]   M.Drofenik. Oxigen Partial Pressure and Grain Growth in Donor-Doped BaTiO$_3$. J Am Ceram Soc 1987; **70**:311-314

[Dro-90]   M.Drofenik. Initial Specific Surface Area and Grain Growth in Donor-Doped Barium Titanate. J Am Ceram Soc 1990; **73**: 1587-1592

[Dro-93]   M.Drofenik. Origin of the Grain Growth Anomaly in Donor-Doped Barium Titanate. J Am Ceram Soc 1993; **76**:123-128

[Dro-99]   M.Drofenik. Grain size and conductivity anomaly in donor-doped barium titanate. Acta Chim Slov 1999; **46**: 355-364

[EIP-07/1]   Author unknown. Reference Document on Best Available Techniques for the Manufacture of Large Volume Inorganic Chemicals - Solids and Others industry. European Commission Directorate-General JRC Joint Research Centre 2007. ftp://ftp.jrc.es/pub/eippcb/doc/lvic-s_bref_0907.pdf (page version February 2011)

[EIP-07/2]   Author unknown. Reference Document on Best Available Techniques in the Ceramic Manufacturing Industry. European Commission Directorate-General JRC Joint Research Centre 2007. http://eippcb.jrc.ec.europa.eu/reference/brefdownload/download_CER.cfm (page version February 2011)

[EIP-07/3]   Author unknown. Reference Document on Best Available Techniques for the Production of Speciality Inorganic Chemicals. European Commission Directorate-General JRC Joint Research Centre 2007. http://eippcb.jrc.ec.europa.eu/reference/brefdownload/download_SIC.cfm (page version February 2011)

[EPC-08]   Author unknown. PTC Thermistors (Data Book 2009). EPCOS AG, A group company of TDK-EPC Corporation. Edition 10/2008. Munich (Germany), 2008

[Erk-06]   H.Erkalfa, B.Yuksel, T.O.Ozkan. The effect of TiCl$_3$ on the microstructure of donor-doped boron-added Ti-excess BaTiO$_3$. J Eur Ceram Soc 2006; **26**: 2909-2913

[Fel-01]   K.-H.Felgner, T.Müller, H.T.Langhammer, H.-P.Abicht. Investigations on the liquid phase in barium titanate ceramics with silica additives. J Eur Ceram Soc 2001; **21**: 1657-1660

[Fel-04]   K.-H.Felgner, T.Müller, H.T.Langhammer, H.-P.Abicht. On the formation of BaTiO$_3$ from BaCO$_3$ and TiO$_2$ by microwave and conventional heating. Materials Letters 2004; **58**: 1943-1947

[Fer-91/1]   J.F.Fernandez, P.Duran, C.Moure. Dielectric and microstructural properties of sintered BaTiO$_3$ ceramics prepared from different TiO$_2$ raw materials. J Mater Sci 1991; **26**:3257-3263

[Fer-91/2]   J.F.Fernandez, P.Duran, C.Moure. Reaction kinetics in the BaTiO$_3$ synthesis: Influence of the TiO$_2$ crystalline structure and morphology. Ceramics Today - Tomorrow's Ceramics; Proc. 7th Int. Meeting on Modern Ceramics Technologies (7th CIMTEC-World Ceramics Congress Montecatini Terme, June 1990). p.1973-1982; Materials Science Monographs, 66C (Elsevier Science Publishing Co.Inc.)

[Feu-82]   O.Feustel, W.Schmidt. Sensorhalbleiter und Schutzelemente. Würzburg: Vogel Verlag; 1982

7. References

[Fis-06] J.G.Fisher, S.-Y.Choi, S.-J.L.Kang. Abnormal grain growth in barium titanate doped with alumina. J Am Ceram Soc 2006; 89: 2206-2212

[Fuk-79] T.Fukami, H.Tsuchiya. Dependence of Resistivity on Donor Dopant Content in Barium Titanate Ceramics. Jpn J Appl Phys 1979; **18**:735-738

[Ger-01] V.Y.Gertsman. Coincide site lattice theory of multicrystalline ensembles. Acta Cryst A 2001; **57**:649-655

[Ges-01] U.Gesenhues. Review: Calcination of metatitanic acid to titanium dioxide white pigments. Chem Eng Technol 2001; 24: 685-693

[Ges-97] U.Gesenhue. Doping of TiO_2 pigments by Al^{3+}. Solid State Ionics 1997; **101-103**: 1171-1180

[Gli-00] M.Glinchuk, I.P.Bykov, S.M.Kornienko, V.V.Laguta, A.M.Slipenyuk, A.G.Bilous, et al. Influence of impurities on the properties of rare-earth-doped barium titanate ceramics. J Mater Chem 2000; **10**:941-947

[Gom-00] C.Gomez-Yañez, C.Benitez, H.Balmori-Ramirez. Mechanical activation of the synthesis reaction of $BaTiO_3$ from a mixture of $BaCO_3$ and TiO_2 powders. Ceramics International 2000; **26**: 271-277

[Gra-05] A.Graff, S.Senz, D.Völtzke, H.-P.Abicht, D.Hesse. Microstructure evolution during $BaTiO_3$ formation by solid-state reactions on rutile single crystal surfaces. J Eur Ceram Soc 2005; **25**: 2201-2206

[Gre-05] V.A.Greenhut, R.A.Haber. Ceramics, Ceramic – Metal Systems. In Ullmann´s Encyclopedia of Industrial Chemistry. Weinheim: Wiley VCH Verlag; 2005

[Grz-04] B.Grzmil, B.Kic, M.Rabe. Inhibition of the anatase-rutile phase transformation with addition of K_2O, P_2O_5 and Li_2O. Chem Pap 2004; 58: 410-414

[Grz-07] B.Grzmil, M.Rabe, B. Kic, K.Lubkowski. Influence of Phosphate, Potassium, Lithium, and Aluminium on the Anatase-Rutile Phase Transformation. Ind Eng Chem Res 2007; **46**: 1018-1024

[Guh-74] J.P.Guha, D.Kolar. Phase equilibria, sintering characteristics and dielectric properties in the $BaTiO_3$-rich portion of the system BaO–TiO2–SiO2. 5th Conference on Ceramics for Electronics, Liblice, 1974, pp. 1–9

[Had-89] K.I.Hadjivanov, D.G.Klissurski, A.A.Davydov. Study of phosphate-modified TiO_2-anatase. J Catal 1989; **116**:498-505

[Han-87] Y.H.Han, J.B.Applby, D.M.Smyth. Calcium as an acceptor impurity in $BaTiO_3$. J Am Ceram Soc 1987; **70**: 96-100

[Hay-96] K.Hayashi, T.Yamamoto, T.Sakuma. Grain Orientation Dependence of the PTCR Effect in Nb-doped Barium Titanate. J Am Ceram Soc 1996; **79**:1669-1972

[Hea-72] E.F.Heald, C.W.Weiss. Kinetics and mechanism of the anatase/rutile transformation as catalyzed by ferric oxide and reducing. American Mineralogist 1972; **57**: 10-23

[Hen-01/1] D.F.K.Hennings, B.S.Schreinemacher, H.Schreinemacher. Solid-state preparation of $BaTiO_3$-based dielectrics, using ultrafine raw materials. J Am Ceram Soc 2001; **84**: 2777-2782

7. References

[Hen-01/2]   D.F.K.Hennings. Dielectric materials for sintering in reducing atmospheres. J Eur Ceram Soc 2001; **21**: 1637-1642

[Hen-76]   D.Hennings. Doped barium titanate ceramics, Part III: Thermogravimetric investigations. Philips Res Repts 1976; **31**:516-525

[Her-88]   W.Hertl. Kinetics of barium titanate synthesis. J Am Ceram Soc 1988; **71**: 879-883

[Heu-06]   M.Heuschmann. Einfluss der Stöchiometrie auf die elektrischen Eigenschaften ausgewählter PTC Massen. Diploma thesis. Nürnberg: Georg-Simon-Ohm University of Applied Science Nürnberg (faculty of material science); 2006

[Hey-61]   W.Heywang. Bariumtitanat als Sperrschichthalbleiter. Solid-State Electron 1961; **3**: 51-58

[Hey-65]   W.Heywang, H.Brauer. Zum Aufbau der Sperrschichten in kaltleitendem Bariumtitanat. Solid-State Electron 1965; **8**:129-135

[Hey-71]   W.Heywang. Semiconducting Barium Titanate. J Mater Sci 1971; **6**:1214-1226

[Ho-94]   I.-C.Ho. Semiconducting Barium Titanate Ceramics prepared by Boron-containing liquid-phase sintering. J Am Ceram Soc 1994; **77**: 829-832

[Hur-98]   S.H.Hur, J.K.Lee, K.-S.Hong, S.J.Park. Incorporation phenomena of donor dopant in $BaTiO_3$ systems. Solid State Ionics 1998; **108**: 81-84

[Huy-95]   B.Huybrechts, K.Ishizaki, M.Takata. Review: The positive temperature coefficient of resistivity in barium titanate. J Mater Sci 1995; **30**:2463-2474

[Iga-81]   H.Igarashi, S.Hayakawa, K.Okazaki. PTC behavior of semiconductive ceramics under reduced atmosphere. Jpn J Appl Phys 1981; **20** (suppl. 20-4): 135-138

[Ihr-81]   H.Ihrig. PTC Effect in $BaTiO_3$ as a Function of Doping with 3d Elements. J Am Ceram Soc 1981; **64**:617-620

[Ill-90]   J.Illingsworth, H.M.Al-Allak, A.W.Brinkman. Dependence of the grain boundary potential barrier height of $BaTiO_3$ ceramics on donor dopant concentration. J Phys D: Appl Phys 1990; **23**: 971-975

[Ish-87]   T.Ishii. Surface reactivity of powders in barium carbonate-titanium dioxid reaction systems by emanation thermal analysis. Reactivity of Solids 1987; **3**: 85-100

[Jay-04]   S.Jayanthi, T.R.N.Kutty. Extended phase homogeneity and electrical properties of barium calcium titanate prepared by the wet chemical methods. Mater Sci Eng B 2004; **110**: 202-212

[Jay-06]   S.Jayanthi, T.R.N.Kutty. Effect of segregative additives on the positive temperature coefficient in resistance characteristics of n-$BaTiO_3$ ceramics. J Mater Sci: Mater Electron 2006; **17**:883-897

[Jia-02]   Q.Jianquan, G.Zhilun, W.Yajing, L.Longtu. Influence of manganese on PTCR effect in $BaTiO_3$-based ceramics doped with Bi_2O_3 vapor. Mater Chem Phys 2002; **73**: 97-100

[Jid-96]   S.Jida, T.Miki. Electron paramagnetic resonance of Nb-doped $BaTiO_3$ ceramics with positive temperature coefficient of resistivity. J Appl Phys 1996; **80**: 5234-5239

7. References

[Jo-09]	S.K.Jo, Y.H.Han. Effects of Sr and Ca addition on the microstructure and the PTCR properties of Ho-doped (Ba,Sr)TiO$_3$. J Kor Phys Soc 2009; **55**: 765-769
[Jon-64]	G.H.Jonker. Some aspects of semiconducting barium titanate. Solid State Ionics 1964; **7**: 895-903
[Jon-67]	G.H.Jonker. Halogen treatment of barium titanate semiconductors. Mat Res Bull 1967; **2**: 401-407
[Kim-92]	H.-S.Kim, G.Y.Sung, C.H.Kim. Determination of Inversion Temperature of Sb$_2$O$_3$-Doped BaTiO$_3$ Positive Temperature Coefficient of Resistivity (PTCR) Ceramics by the Finite Difference Method. J Am Ceram Soc 1992; **75**: 587-591
[Kir-91]	K.W.Kirby, B.A.Wechsel. Phase relations in the barium titanate-titanium oxide system. J Am Ceram Soc 1991; **74**: 1841-1847
[Kna-79]	U.Knauer. Distribution of iron dopant in barium titanate ceramic, determined by scanning transmission electron microscope. Phys Stat Sol (A) 1979; **53**: 207-210
[Kob-08]	K.Kobayashi, T.Suzuki, Y.Mizuno. Microstructure analysis of solid-state reaction in synthesis of BaTiO$_3$ powder using transmission electron microscopy. Applied Physics Express 2008; **1**: 041602
[Kon-02]	L.B.Kong, J.M.Huang, R.F.Zhang, W.X.Que. Barium titanate derived from mechanically activated powders. Journal of Alloys and compounds 2002; **337**: 226-230
[Kos-85]	G.Koschek, E.Kubalek. Grain-boundary characteristics and their influence on the electrical resistance of barium titanate ceramics. J Am Ceram Soc 1985; **68**: 582-586
[Kos-89]	G.Koschek. Ein Beitrag zur Mikroanalyse der Akzeptorzustände an den Korngrenzen in Bariumtitanatkeramik. Cfi/Ber DKG 1989; **66**: 13-17
[Krö-56]	F.A.Kröger, H.J.Vink. Relations between the concentrations of imperfections in crystalline solids. Solid State Physics 1956; **3**: 307-435
[Kub-67]	T.Kubo, M.Kato, T.Fujita. Festphasenreaktion zwischen Titanoxid und Bariumcarbonat. J Chem Soc Jpn 1967; **70**:847-853
[Kul-81]	B.M.Kulwicki. PTC materials technology, 1955-1980. In: L.M.Levinson, D.C.Hill, editors. Advances in Ceramics Vol.1. Grain boundary phenomena in electronic ceramics. Columbus, OH: Am. Ceram. Soc.; 1981, p.138-154
[Kut-85]	T.R.N.Kutty, P.Murugaraj, N.S.Gajbhiye. EPR evidence for activation of trap centers in PTCR BaTiO$_3$ ceramics. Mat Res Bull 1985; **20**: 565-574
[Kut-86]	T.R.N.Kutty, L.Gomathi Devi, P.Murugaraj. The change in oxidation state of Mn ions in semiconducting BaTiO$_3$ and SrTiO$_3$ around the phase transition temperatures. Mat Res Bull 1986; **21**: 1093-1102
[Kut-98]	T.R.N.Kutty, N.S.Hari. Effect of charge redistribution through secondary phase formation on PTCR characteristics of n-BaTiO$_3$ ceramics. Mater lett 1998; **34**:43-49

7. References

[Kuw-83]   M.Kuwabara, K.Kumamoto. PTCR Characteristics in Barium Titanate Ceramics with Curie Points between 60° and 360°C. J Am Ceram Soc 1983; **66**:C214-C215

[Kuw-84]   M.Kuwabara. Determination of the potential barrier height in barium titanate ceramics. Solid-state electron 198; **27**: 929-935

[Kuw-96]   M.Kuwabara, K.Morimo, T.Matsunaga. Single-Grain Boundaries in PTC Resistors, J Am Ceram Soc 1996; **79**:997-1001

[Kwe-59]   W.Kwestroo, H.A.M.Paping. The system $BaO-SrO-TiO_2$, $BaO-CaO-TiO_2$ and $SrO-CaO-TiO_2$. J Am Ceram Soc 1959; **42**: 292-299

[Lac-95]   B.C.LaCourse, V.R.W.Amarakoon. Characterization of the firing schedule for positive temperature coefficient of resistance $BaTiO_3$. J Am Ceram Soc 1995; **78**: 3352-3356

[Lan-49]   J.J.Lander. Polymorphism and Anion Rotational Disorder in the Alkaline Earth Carbonates. J Chem Phys 1949; **17**: 892-901

[Lee-07/1] S.Lee, Z.-K.Liu, M.-H.Kim, C.A.Randall. Influence of nonstoichiometry on ferroelectric phase transition in $BaTiO_3$. J Appl Phys 2007; **101**: 054119

[Lee-07/2] S.Lee, C.A.Randall, Z.-K.Liu. Modified phase diagram for the barium oxide-titanium dioxide system for the ferroelectric barium titanate. J Am Ceram Soc 2007; **90**: 2589-2594

[Lee-09]   S.Lee, C.A.Randall, Z.-K.Liu. Factors Limiting Equilibrium in Fabricating a Simple Ferroelectric Oxide: $BaTiO_3$. J Am Ceram Soc 2009; **92**:222-228

[Lew-85]   G.V.Lewis, C.R.A.Catlow. R.E.W.Casselton. PTCR effect in $BaTiO_3$. J Am Ceram Soc 1985; **68**: 555-558

[Lew-86]   G.V.Lewis, C.R.A.Catlow. Defect studies of doped and undoped barium titanate using computer simulation techniques. J Phy Chem Solids 1986; **47**: 89-97

[Lin-90]   T.-F.Lin, C.-T.Hu, I.-N.Lin. Influence of Stoichiometry on the Microstructure and Positive Temperature Coefficient of Resistivity of Semiconducting Barium Titanate Ceramics. J Am Ceram Soc 1990; **73**: 531-536

[Lin-91]   T.-F.Lin, C.-T.Hu, I.-N-Lin. Influence of Stoichiometry on the Microstructure and Positive Temperature Coefficient of Resistivity of Semiconducting Barium Titanate Ceramics. J Am Ceram Soc 1990; **73**: 531-536

[Liu-04]   H.Liu, L.Guo, L.Zou, M.Cao, J.Zhou, S.Ouyang. Theoretical and experimental study on solid chemical reaction between $BaCO_3$ and TiO_2 in microwave field. Mater Sci Eng B 2004; **113**: 161-165

[Mak-00]   D.Makovec, M.Drofenik. Microstructural changes during reduction/reoxidation process in donor-doped $BaTiO_3$ ceramics. J Am Ceram Soc 2000; **83**: 2593-2599

[Mau-87]   A.K.Maurice, R.C.Buchanan. Preparation and stoichiometry effects on microstructure and properties of high purity $BaTiO_3$. Ferroelectrics 1987; **74**: 61-75

[McC-68]   R.A.McCauley, F.A.Hummel. Phase Relationships in a. Portion of the System $BaO-P_2O_5$. Trans Br Ceram Soc 1968; **67**: 619-628

[Mik-98]   T.Miki, A.Fujimoto, S.Jida. An evidence of trap activation for positive temperature coefficient of resistivity in $BaTiO_3$ ceramics

7. References

             with substitutional Nb and Mn as impurities. J Appl Phys 1998; **83**: 1592-1603

[Mor-01]   F.D.Morrison, D.C.Sinclair, A.R.West. Characterization of Lanthanum-Doped Barium Titanate Ceramics Using Impedance Spectroscopy. J Am Ceram Soc 2001; **84**: 531-538

[Mou-03]   A. J. Moulson and J. M. Herbert.Electroceramics: Materials, Properties, Applications. 2nd Edition. Chichester: John Wiley & Sons, Ltd; 2003

[Mur-87]   J.L.Murray, H.A.Wriedt. (A) T-X diagram; (B) P-T diagram for anatase transformation; (C) P-T diagram for brookite transformation. Bull. Alloy Phase Diagrams 1987; **8**: 148-165

[Mut-84]   J.C.Mutin, J.C.Niepce. About stoichiometry of polycrystalline BaTiO3 synthesized by solid-solid reaction. J Mater Sci Lett 1984; **3**: 591-592

[Nak-63]   T.Nakayama, T.Sasaki. The diffusion of barium in a rutile single crystal. Bull Chem Soc Jpn 1963; **36**: 569-574

[Neg-74]   T.Negas, R.S.Roth, H.S.Parker, D.Minor. Subsolidus phase relations in trhe $BaTiO_3$-TiO_2 system. J Solid State Chem 1974; **9**: 297-307

[Nem-80]   H.Nemoto und I. Oda. Direct Examination of PTC action of single grains. J Am Ceram Soc 1980; **63**:398-401

[Nie-90]   J.C.Niepce. About the mechanism of the solid-state synthesis of barium metatitanate. Industrial consequences. Solid State Ionics 1990; **43**: 69-76

[Nii-07]   H.Niimi, K.Mihara, Y.Sakabe. Influence of Ba/Ti Ratio on the Positive Temperature Coefficient of Resistivity Characteristics of Ca-Doped Semiconducting $BaTiO_3$ Fired in Reducing Atmosphere and Reoxidized in Air. J Am Ceram Soc 2007; **90**:1817-1821

[Nom-78]   T.Nomura, T.Yamaguchi. Evaluation of TiO_2 powders and effects of calcination in the sintering of $BaTiO_3$ ceramics. Yogyo-Kyokai-Shi 1978; **86**: 13-19

[Obr-74]   H.M.O`Bryan Jr., J.Thomas Jr.. Phase equilibria in the TiO_2-rich region of the system BaO-TiO_2. J Am Ceram Soc 1974; **57**: 522-526

[Oga-95]   H.Ogawa, M.Demura, T.Yamamoto, T.Sakuma. Estimation of PTCR effect in single grain boundary of Nb-doped BaTiO3. J Mater Sci Lett 1995; **14**:537-538

[Oli-93]   G.Oliveri, G.Ramis, G.Busca, V.S.Escribano. Thermal stability of vanadia-titania catalysts. J Mater Chem 1993; **3**: 1239-1249

[Par-09]   K.-J.Park, C.-H.Kim, Y.J.Yoon, S.M.Song, Y.-T.Kim, K.-H.Hur. Doping behaviors of dysprosium, yttrium and holmium in $BaTiO_3$ ceramics. J Eur Ceram Soc 2009; **29**: 1735-1741

[Pav-08]   V.P.Pavlovic, B.D.Stojanovic, V.B.Pavlovic, Z.Marinkovic-Stojanovic, Lj.Živković, M.M.Ristic. Synthesis of $BaTiO_3$ from a mechanically activated $BaCO_3$-TiO_2 system. Science of Sintering 2008; **40**: 21-26

[Pen-88]   C.-J.Peng, H.-Y.Lu. Compensation Effect in Semiconducting Barium Titanate. J Am Ceram Soc 1988; **71**:C44-C46

7. References

[Phe-05]   G.W.Phelps, J.B.Wachtman Jr. Ceramics, General Survey. In Ullmann´s Encyclopedia of Industrial Chemistry. Weinheim: Wiley VCH Verlag; 2005

[Pit-05]   C.Pithan, D.Hennings, R.Waser. Progress in the synthesis of nanocrystalline $BaTiO_3$ powders for MLCC. Int J Appl Ceram Technol 2005; 2: 1-14

[Pre-04]   W.Preis, A.Bürgermeister, W.Sitte, P.Supancic. Bulk and grain boundary resistivities of donor-doped barium titanate ceramics. Solid State Ionics 2004; **173**:69-75

[Pre-06]   W.Preis, W.Sitte. Electronic conductivity and chemical diffusion in n-conducting barium titanate at high temperatures. Solid State Ionics 2006; **177**:3093-3098

[Pre-90]   W.Preis, W.Sitte. Modelling of grain boundary resistivities of n-conducting $BaTiO_3$ ceramics. Solid State Ionics 2006; **177**: 2549-2553

[Qi-02]   J.Qi, Z.Gui, Y.Wang, Q.Zhu, Y.Wu, L.Li. The PTCR effect in $BaTiO_3$ ceramics modified by donor dopant. Ceramics International 2002; **28**: 141-143

[Ran-05]   V.Randle, Y.Hu. The role of vicinal $\Sigma3$ boundaries and $\Sigma9$ boundaries in grain boundary engineering. J Mater Sci 2005; **40**:3243-3246

[Rao-02]   K.J.Rao. Structural chemistry of glasses. 1st edition. Kidlington, Oxford: Elsevier Science Ltd.; 2002

[Rao-60]   C.N.R.Rao, M.P.Lewis. Impurity effects on the anatase-rutile transformation. Current Science 1960; **29**: 52

[Rao-61]   C.N.R.Rao. Kinetics and thermodynamics of the crystal structure transformation of spectroscopically pure anatase to rutile. Can J Chem 1961; **39**: 498-500

[Rao-79]   C.R.M.Rao, P.N.Mehrotra. DTA studies on the effect of impurities on the phase transformations of barium carbonate. J Therm Anal Calorim 1979; **17**: 539-542

[Ras-55]   D.E.Rase, R.Roy. Phase equilibria in the system BaO-TiO_2. J m Ceram Soc 1955; **38**: 102-113

[Rav-92]   V.Ravi, T.R.N.Kutty. A novel method for the uniform incorporation of grain-boundary layer modifiers in positive temperature coefficient of resistivity barium titanate. J Am Ceram Soc 1992; **75**: 203-205

[Ryu-07]   S.-S.Ryu, D.-H.Yoon. Solid-state synthesis of nano-sized $BaTiO_3$ powder with high tetragonality. J Mater Sci 2007; **42**:7093-7099

[Sak-04]   Y.Sakabe, Development of Dielectric Ceramics for Nickel Electrode Multilayer Capacitors. J Jpn Soc Powder Powder Metallurgy 2004; **51**: 274-284

[Sal-07]   H.Salmang, H.Scholze, R.Telle (Ed.). Keramik. 7th edition. Berlin-Heidelberg: Springer; 2007

[Sas-99/2]   K.Sasaki, J.Maier. Low-temperature defect chemistry of oxides. II. Analytical relations. J Appl Phys 1999; **86**: 5434-5443

[Sas-99]   K.Sasaki, J.Maier. Low-temperature defect chemistry of oxides. I. General aspects and numerical calculations. J Appl Phys 1999; **86**: 5422-5433

7. References

[Sau-60] H.A.Sauer, J.R.Fischer. Processing of Possitive Temperature Coefficient Thermistors. J Am Ceram Soc 1960; **43**:297-301

[Sch-90] H.Scholze. Glass: Nature, Structure and Properties. 3rd edition. Berlin: Springer; 1990

[Sea-05] J.Seaton, C.Leach. Evolution of low sigma grain boundaries in PTC thermistors during sintering. J Eur Ceram Soc 2005; **25**:3055-3058

[Sha-65] R.D.Shannon, J.A.Pask. Kinetics of the anatase-rutile transformation. J Am Ceram Soc 1965; **48**: 391-398

[Sim-07] L.Simon-Seveyrat, A.Hajjaji, Y.Emziane, B.Guiffard, D.Guyomar. Re-investigation of synthesis of BaTiO3 by conventional solid-state reaction and oxalate coprecipitation route for piezoelectric applications. Ceramics International 2007; **33**: 35–40

[Smy-00] D.M.Smyth. The defect chemistry of metal oxides. 1st edition. New York: Oxford University Press; 2000

[Smy-23] F.H.Smyth, L.H.Adams. The system, calcium oxide-carbon dioxide. J Am Chem Soc 1923; **45**: 1167-1184

[Spi-61] G.Spieß. Über die Bildung von Bariummetatitanat. Ber DKG 1961; **38**:495-528

[Sui-01] K. Suito, J.Namba, T.Horikawa, Y.Taniguchi, N.Sakurai, M.Kobayashi, A.Onodera, O.Shimomura, T.Kikegawa. Phase relations of $CaCO_3$ at high pressure and high temperature. Am Mineral 2001; 86: 997–1002

[Suy-75/1] Y.Suyama, A.Kato. Reactivity of ultrafine-TiO_2 (anatase) powders with $BaCO_3$. Ceramurgia Interational 1975; **1**:5-9

[Suy-75/2] Y.Suyama, A.Kato. A comment on the chemical equilibrium in the $BaCO_3$-TiO_2 system. Ceramurgia Interational 1975; **1**:123-126

[Suy-77] Y.Suyama, A.Kato. Solid-State Reactions between CVD-TiO_2 and $BaCO_3$. Bull Chem Soc Jpn 1977; **50**:1361-1366

[Suz-62] A.Suzuki, Y.Kotera. The Kinetics of the Transition of Titanium Dioxide. Bull Chem Soc Jpn 1962; **35**:1353-1357

[Suz-69] A.Suzuki, R.Tukuda. Kinetics of the Transition of Titanium Dioxide Prepared by Sulfate Process and Chloride Process. Bull Chem Soc Jpn 1969; **42**:1853-1857

[Tak-90] T.Takahashi, Y.Nakano, N.Ichinose. Influence of reoxidation on PTC effect of porous $BaTiO_3$. J Ceram Soc Jpn (Int Edition) 1990; **98**: 146-151

[Tie-62] T.-Y.Tien, F.A.Hummel. The system SiO_2-P_2O_5. J Am Ceram Soc 1962; **45**: 422-424

[Tin-90] C.-J.Ting, C.-J.Peng, H.-Y.Lu, S.-T.Wu. Lanthanum- Magnesium and Lanthanum- Manganese Donor-Acceptor-Codoped Semiconducting Barium Titanate. J Am Ceram Soc 1990; **73**:329-334

[Tse-90] T.Y.Tseng, S.H.Wang. AC electrical properties of high-Curie-point barium-lead titanate PTCR ceramics. Mater lett 1990; **9**:164-168

[Tsu-00] S.Tsunekawa, S.Ito, T.Mori, K.Ishikawa, Z.-Q.Li, Y.Kawazoe. Critical size and anomalous lattice expansion in nanocrystalline $BaTiO_3$ particles. Phys Rev B 2000; **62**: 3065-3070

[Tsu-01] S.Tsutai, T.Hayashi, S.Hayashi, Z-Nakagawa. Reaction Mechanism of $BaTiO_3$ from Powder Compacts, $BaCO_3$ and TiO_2 and

7. References

	Expansion Phenomenon during Formation Process. J Chem Soc Jpn 2001; **109**:1028-1034
[Ueo-74/1]	H.Ueoka, M.Yodogawa. Ceramic Manufacturing Technology fort the High Performance PTC Thermistor. IEEE T Manuf Tech 1974; **2**:77-82
[Ueo-74/2]	H.Ueoka. The Doping Effects of Transition Elements on the PTC Anomaly of Semiconductive Ferroelectric Ceramics. Feroelectrics 1974; **7**:351-353
[Ure-00]	S.Urek, M.Drofenik, D.Makovec. Sintering and properties of highly donor-doped barium titanate ceramics. J Mater Sci 2000; **35**: 895-901
[Ure-99]	S.Urek, M.Drofenik. PTCR behaviour of highly donor-doped BaTiO$_3$. J Eur Ceram Soc 1999; **19**: 913-916
[UWi-01]	Author unknown. German Notes on BAT for the production of Large Volume Solid Inorganic Chemicals: Titandioxid. Final report. Umweltbundesamt, University of Witten/Herdecke gGmbH (Institut für Umwelttechnik und Management). Witten: 2001. http://www.umweltdaten.de/publikationen/fpdf-l/3225.pdf (page version August 2011)
[Val-96/1]	F.Valdivieso, M.Pijolat, C.Magnier, M.Soustelle. Kinetic study and modelling of coarsening in BaTiO$_3$ powder at 850°C. Solid State Ionics 1996; **83**: 283-292
[Val-96/2]	F.Valedivieso, M.Pijolat, M.Soustelle. Kinetic study of a way of solid state synthesis of barium titanate. Chem Eng Sci 1996; **51**: 2535-2540
[Vog-92]	W.Vogel. Glaschemie. 3rd edition. Berlin: Springer; 1992
[Wan-90]	D.Y.Wang, K.Umeya. Electrical properties of PTCR barium titanate. J Am Ceram Soc 1990; **73**: 669-677
[Wan-98]	X.-H.Wang, Z.-L.Gui, L.-T.Li. Effect of phosphor doping on the microstructure and dielectric properties of barium titanate ceramics. Mater Chem Phys 1998; **55**: 193-196
[Was-94]	R.Waser. Lineare und nicht-lineareWiderstände. In: H. Schaumburg, editor. Werkstoffe und Bauelemente der Elektrotechnik, Bd.5. Stuttgart: Teubner; 1994, p.129-218
[Wer-76]	R.Wernicke. Doped barium titanate ceramics, Part IV: The kinetics of equilibrium restoration in barium titanate ceramics. Philips Res Repts 1976; **31**:526-543
[Xia-08]	Characterization of manganese-doped BaTiO3-(Bi1/2Na1/2)TiO3 positive temperature coefficient of resistivity ceramics using impedance spectroscopy. J Appl Phys 2008; **103**: 064102
[Xue-88/1]	L.A.Xue, Y.Chen, R.J.Brook. The effect of lanthanide contraction on grain growth in lanthanide-doped BaTiO$_3$. J Mater Sci Lett 1988; **7**: 1163-1165
[Xue-88/2]	L.A.Xue, Y.Chen. R.J.Brook. The influence of ionic radii on the incorporation of trivalent dopants into BaTiO$_3$. Mater Sci Eng B 1988; **1**: 193-201
[Yam-76]	T.Yamaguchi, S.H.Cho, M.Hakomori, H.Kuno. Effects of raw materials and mixing methods on the solid state reactions involved in fabrication of electronic ceramics. Ceramurgia International 1976; **2**: 76-80

7. References

[Yog-62]   S.R.Yoganarasimhan, C.N.R.Rao. Mechanism of Crystal Structure Transformations, Part 3.-Factors affecting the Anatase-Rutile Transformation. Trans Faraday Soc1962; **58**:1579-1589

[Yoo-00]   S.H.Yoon, K.H.Lee, H.Kim. Effect of Acceptors on the Segregation of Donors in Niobium-Doped Barium Titanate Positive Temperature Coefficient Resistors. J Am Ceram Soc 2000; **83**:2463-2472

[Yoo-03]   S.-H.Yoon, J.-H.Lee, D.-Y.Kim, N.M.Hwang. Effect of Liquid-Phase Characteristic on the Microstructure and Dielectric Properties of Donor- (Niobium) and Acceptor- (Magnesium) doped Barium Titanate. J Am Ceram Soc 2003; **86**:88-92

[Yoo-97]   Y.-S.Yoo, H.Kim, D.-Y.Kim. Effect of SiO_2 and TiO_2 Addition on the Exaggerated Grain Growth of $BaTiO_3$. J Eur Ceram Soc 1997; **17**:805-811

[Zhu-10]   N.Zhu, A.R.West. Formation and stability of ferroelectric BaTi2O5. J Am Ceram Soc 2010; **93**: 295-300

[Zub-08/1] M.A.Zubair, C.Leach. The influence of cooling rate and SiO2 addition on the grain boundary structure of Mn-doped PTC thermistors. J Eur Ceram Soc 2008; **28**: 1845-1855

[Zub-08/2] M.A.Zubair, C.Leach. Modeling the effect of SiO_2 additions and cooling rate on the electrical behaviour of donor-acceptor codoped positive temperature coefficient thermistors. J Appl Phys 2008; **103**: 123713

8. Appendix

8.1. Appendix figures
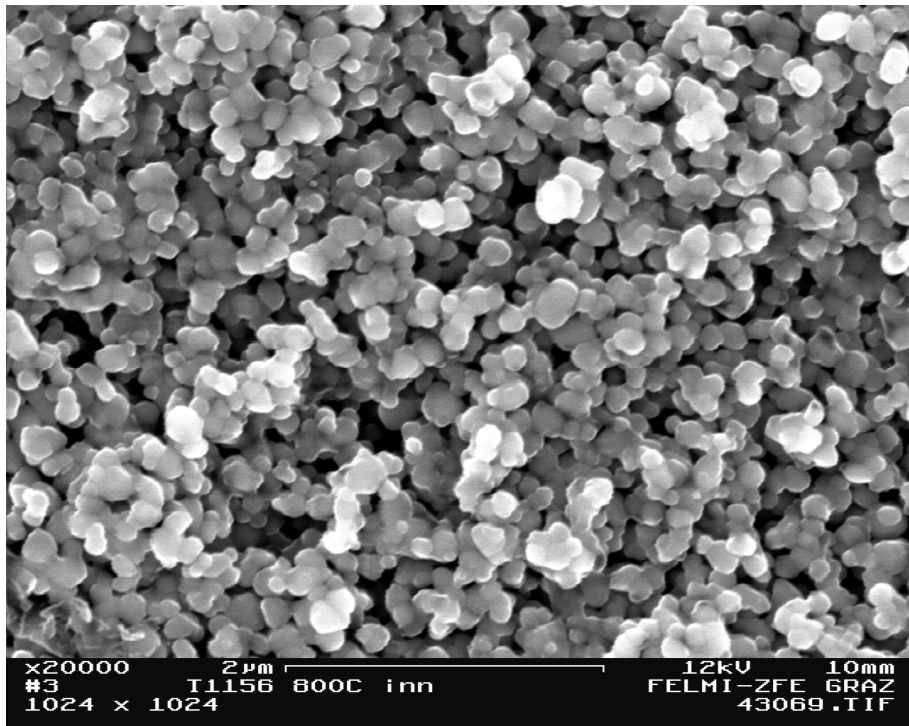
Figure 8.1-I: Compacted sample of A-1 TiO$_2$ sintered in air at 800°C; scale bar 2µm
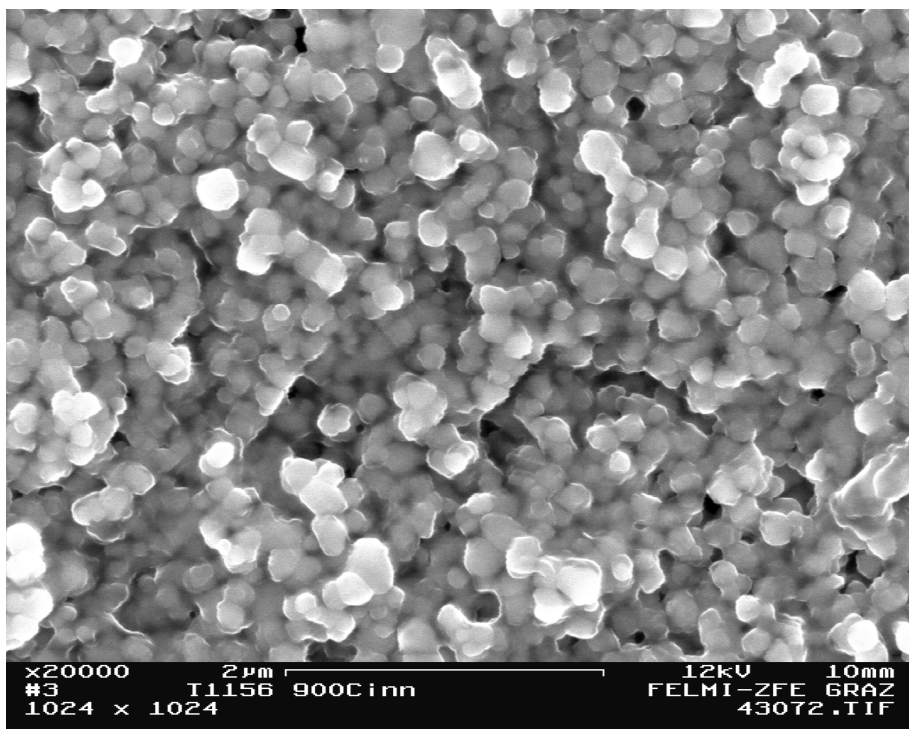
Figure 8.1-II: Compacted sample of A-1 TiO$_2$ sintered at 900°C; scale bar 2µm
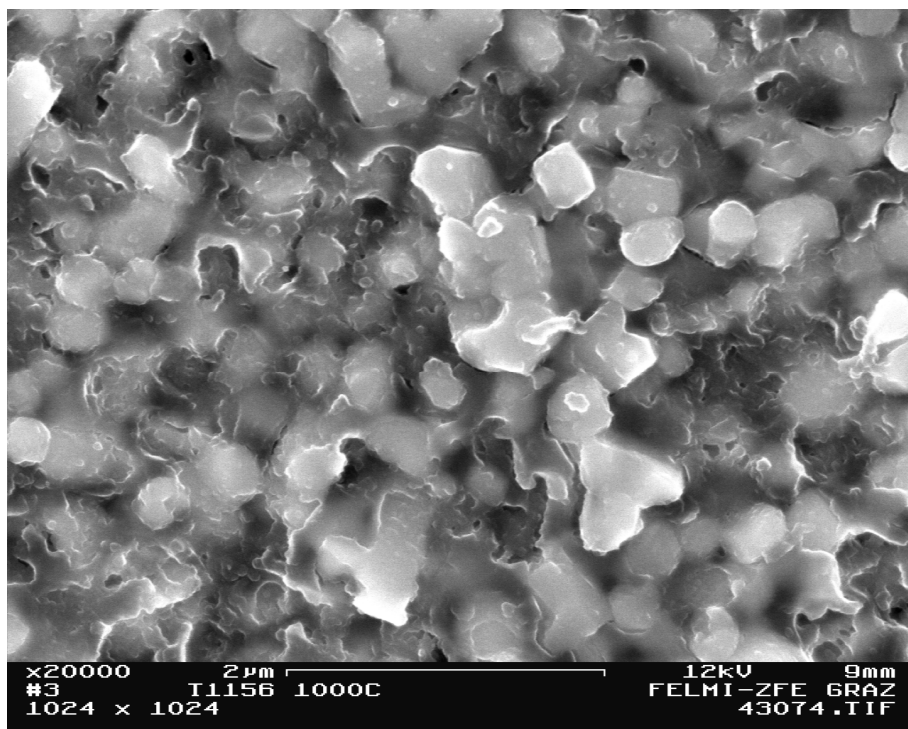
Figure 8.1-III: Compacted sample of A-1 TiO$_2$ sintered at 1000°C; scale bar 2µm
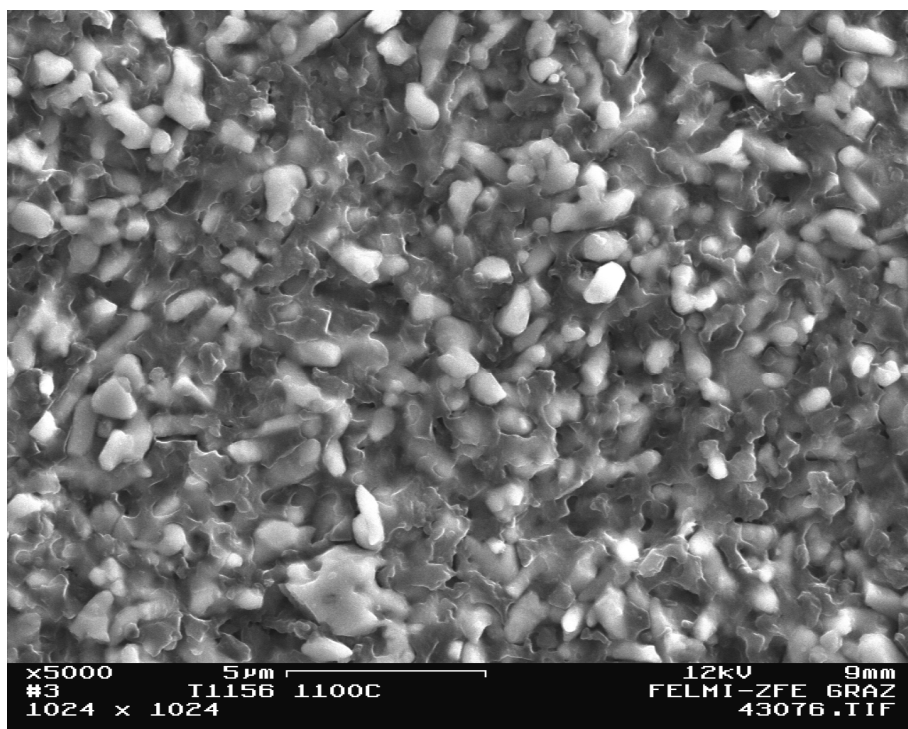
Figure 8.1-IV: Compacted sample of A-1 TiO$_2$ sintered at 1100°C; scale bar 5µm
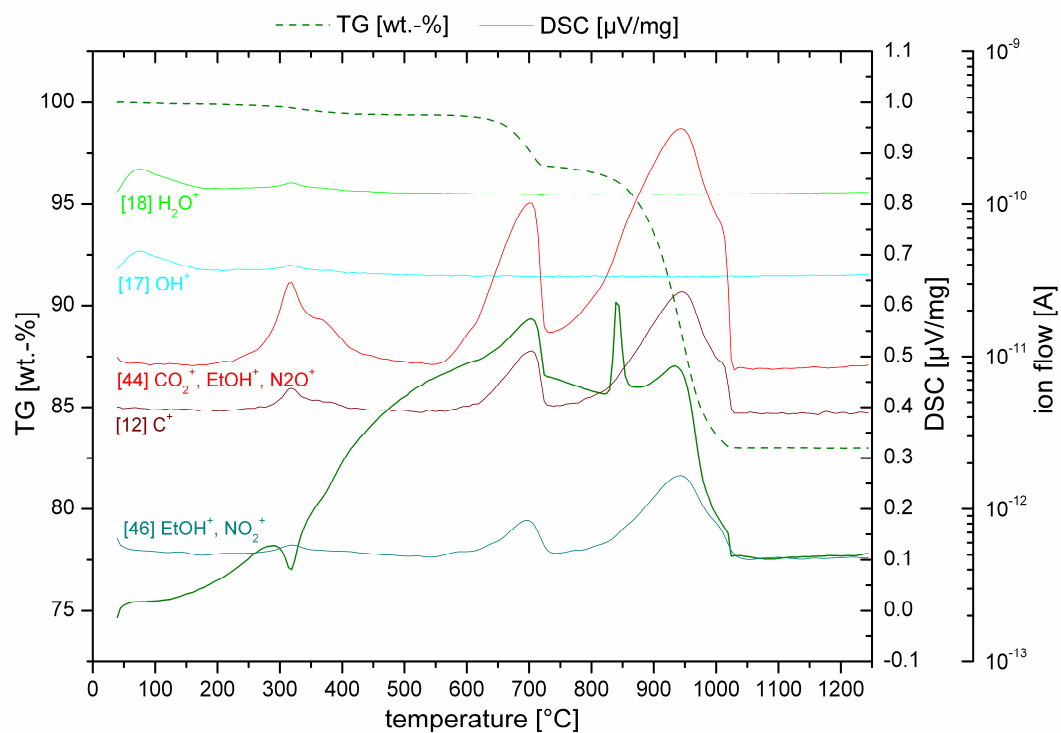
Figure 8.1-V: STA-MS of composition R-1a
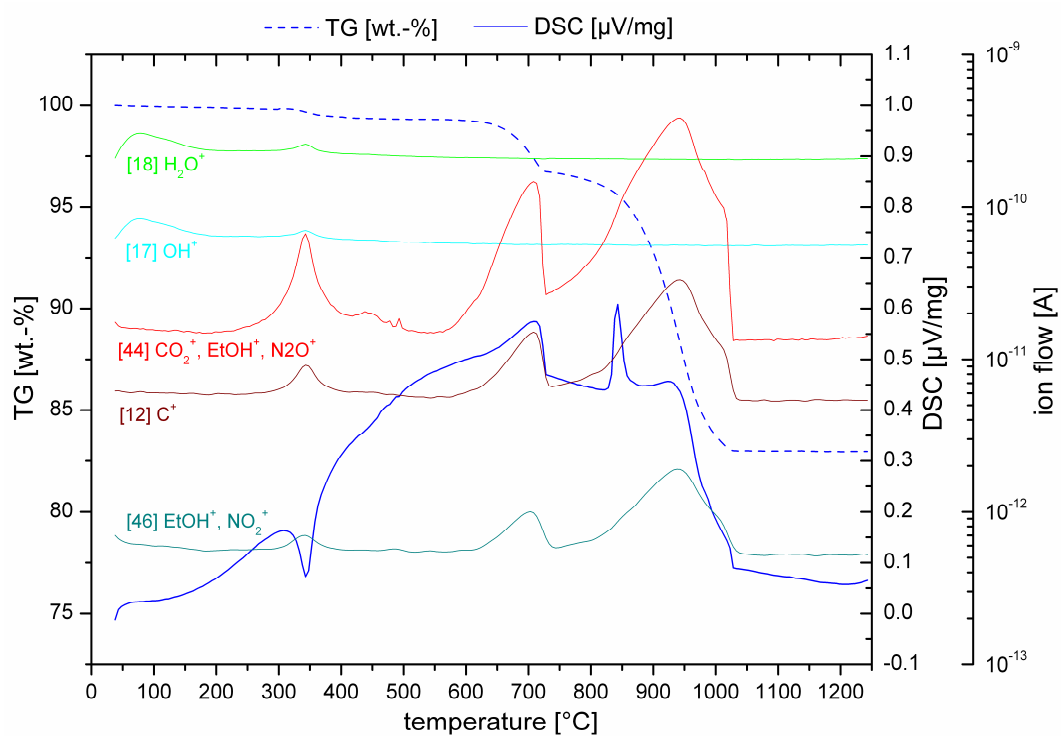
Figure 8.1-VI: STA-MS of composition A-1a
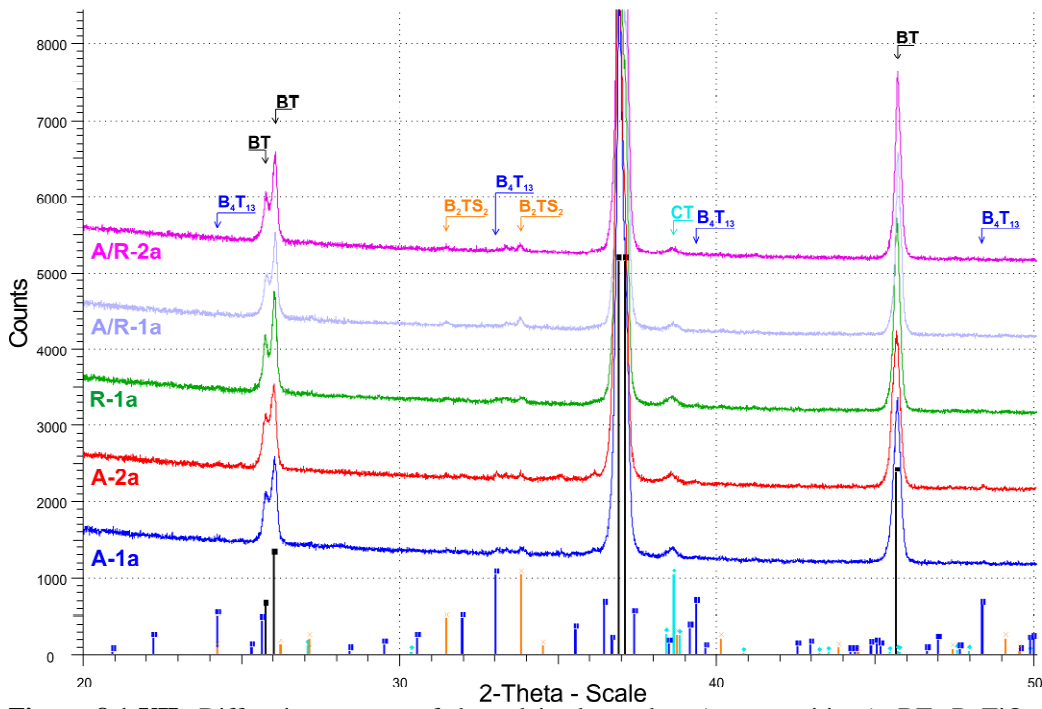
Figure 8.1-VII: Diffraction spectra of the calcined powders (a-compositions); BT: $BaTiO_3$ or rather $(Ba_{0.95},Ca_{0.05})TiO_3$, CT: $CaTiO_3$, B_2TS_2: $Ba_2TiSi_2O_8$ (Fresnoite), B_4T_{13}: $Ba_4Ti_{13}O_{30}$
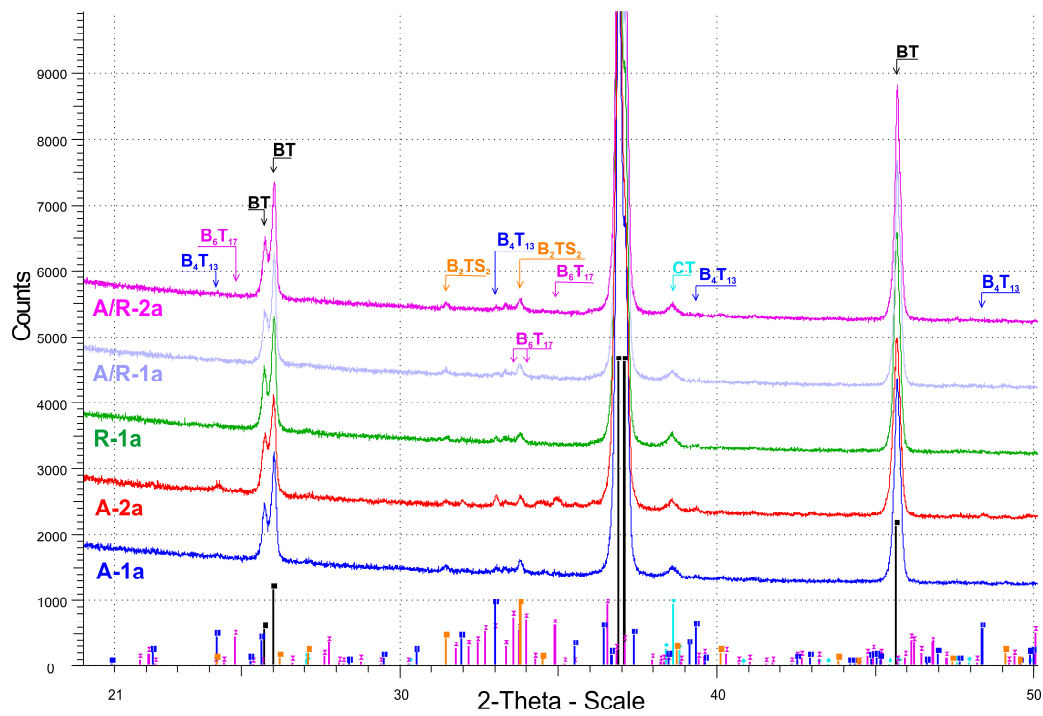
Figure 8.1-VIII: Diffraction spectra of the calcined powders (b-compositions); BT: $BaTiO_3$ or rather $(Ba_{0.95},Ca_{0.05})TiO_3$, CT: $CaTiO_3$, B_2TS_2: $Ba_2TiSi_2O_8$ (Fresnoite), B_4T_{13}: $Ba_4Ti_{13}O_{30}$

8. Appendix
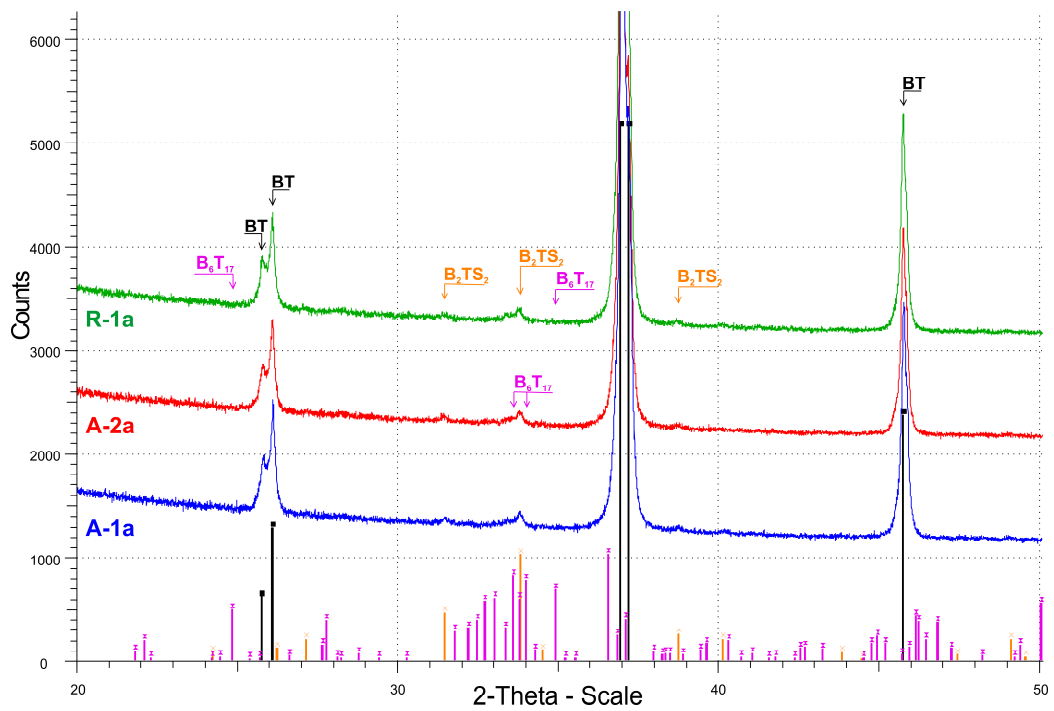
Figure 8.1-IX: Diffraction spectra of the sintered parts (a-compositions); BT: $BaTiO_3$ or rather $(Ba_{0.9},Ca_{0.1})TiO_3$, CT: $CaTiO_3$, B_2TS_2: $Ba_2TiSi_2O_8$ (Fresnoite), B_6T_{17}: $Ba_6Ti_{17}O_{40}$
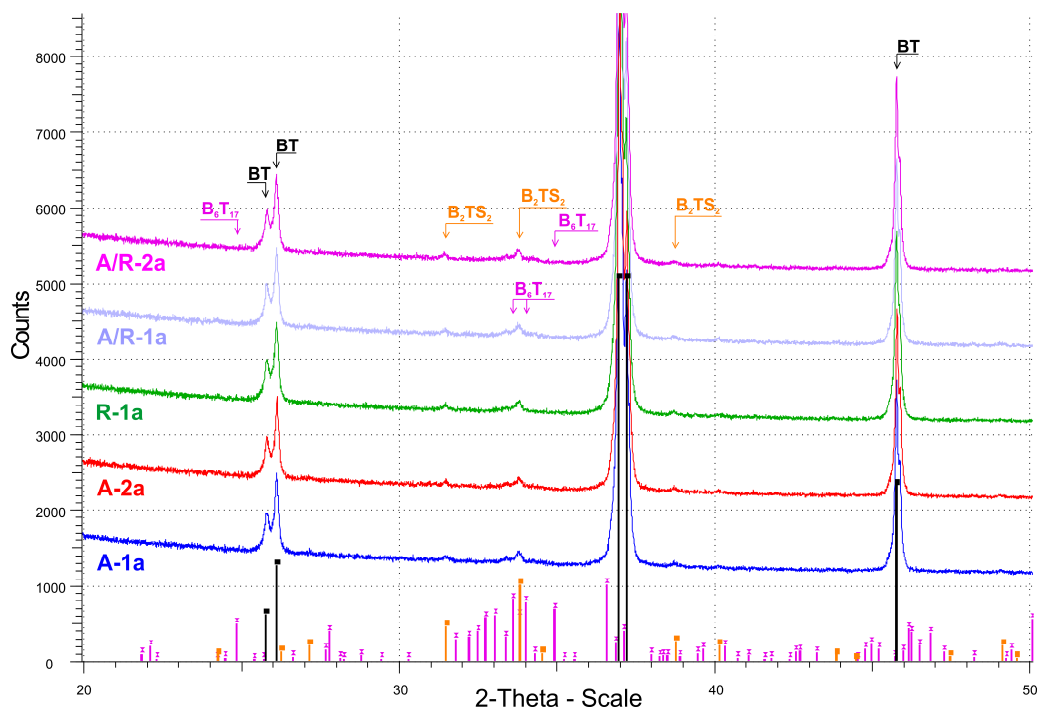
Figure 8.1-X: Diffraction spectra of the sintered parts (b-compositions); BT: $BaTiO_3$ or rather $(Ba_{0.9},Ca_{0.1})TiO_3$, CT: $CaTiO_3$, B_2TS_2: $Ba_2TiSi_2O_8$ (Fresnoite), B_6T_{17}: $Ba_6Ti_{17}O_{40}$

8. Appendix

8. Appendix

8.2. Appendix tables

Table 8.2-I: Summary of literature regarding the effect of impurities on the anatase-rutile phase transition

Ref. no.	Preparation process	Impurities	Additives	Specific surface and/or grain size	Anatase-rutile transformation temperature	Activation energy (kcal/mol)	Effect of additive or impuritiy
Cza-58	Ti-oxidation	n.d.	none	40m²/g (~0.04µm)	>610°C, fast above 730°C	110±10; 90±10	Pure anatase
Rao-61	Ti-oxidation	n.d.	none	40m²/g (~0.04µm)	> 630°C	80±10	Pure anatase
Rao-60	Ti-oxidation	n.d.	5at.-% of Zn^{2+},Al^{3+}, Cl^-, SO_4^{2-}, PO_4^{3-}	40m²/g (~0.04µm)	>640°C pure; >740°C Zn; >920°C Al; >780°C Cl; >940°C SO_4^{2-}; >1005°C PO_4^{3-}	n.d.	impurities increase transformation start temperature
Suz-62	Sulphate process from $TiCl_4$	Si	1% LiCl	0.09-1µm (~17.1-1.5m²/g)	750-800 °C	110; 116	LiCl accelerates phase transition
Yog-62	Sulphate process from $TiCl_4$	SO_4^{2-}	0.1/1.0/5.0 at.-% SO_4^{2-}	54m²/g (~0.03µm)	> 695°C, fast above 780°C	90/100/120±10	No transformation <695°C (see [16]); SO_4^{2-} decelerating effect; lower GSD accelerates transition
Suz-69	Sulphate (S) and chlorine (Cl) process	n.d.	none	S: 0.2-0.3µm (16m²/g); Cl: 0.05-0.3µm (34m²/g)	> 880 °C	105 and 107	Sulphate-anatase transforms slowly compared to chlorine-anatase (constant temperature)
Hea-72	Commercial	H_2O-soluble salts, As, Fe, Pb, Zn	0.1% Fe_2O_3; CO_2/H_2-atmosphere	0.05-0.14µm (~30.8–11.0m²/g)	900-1000°C	124±16	Fe_2O_3, CuO accelerate transformation in CO_2/H_2- atmosphere
Cri-83	Commercial chlorine	n.d.	KH_2PO_4	54 m²/g	>800°C	n.d.	Phosphate inhibits transformation due to surface adsorption
Oli-93	8 different anatase materials	Sulphate from preparation	K_2SO_4; K_2CO_3; SiO_2; MoO_3; V_2O_5	7 to 122m²/g (~0.22–0.01µm)	700 to >1000°C for pure anatase	n.d.	SiO_2, WO_3 and sulphate constrain transition and sintering; MoO_3, V_2O_5 accelerate; K_2CO_3, K_2SO_4 strongly stabilize anatase

8. Appendix

Amo-95	Commercial and precipitation	Brookit	MoO_3; Co_3O_4; CuO; V_2O_5; WO_3; SiO_2	122 (~0.01µm) and 177 m²/g (~0.009µm)	607-627°C crystal growth; 707-717°C transformation	n.d.	Cu and V accelerate transition and grain growth; Mo and Co inhibit both; WO_3 and SiO_2 inhibit both
Grz-07	Commercial sulphate	Rutile seeds, SO_4^{2-}	NH_4-phosphate; K-, Li-, Al-sulphate	n.d.	>850°C	n.d.	Li and P increases transition temperature; K and P lower temperature; intermediate behaviour of Al and P

8. Appendix

Table 8.2-II: Summary of PDF files used for phase identification and quantification of the diffraction data

Phase	Short name	Molecular formular	Crystal system	Space group	ICSD-no.	PDF-no.
Rutile	R	TiO_2	tetragonal	P42/mnm	63710	021-1276
Anatase	A	TiO_2	tetragonal	I41/amd	63711	021-1272
Witherite	B	$BaCO_3$	orthorhombic	Pnma	26718	045-1471
Calcite	C	$CaCO_3$	orthorhombic	Pmcn	170255	041-1475
Barium titanate	BT	$BaTiO_3$	tetragonal	P4mm	86286	005-0626
Barium calcium titanate	BCT	$(Ba,Ca)TiO_3$	tetragonal	P4mm	71368	081-1288
Calcium titanate	CT	$CaTiO_3$	orthorhombic	Pnma	153172	042-0423
Hexa-barium titanate	B_6T_{17}	$Ba_6Ti_{17}O_{40}$	monoclinic	A2/a	49576	035-0817
Tetra-barium titanate	B_4T_{13}	$Ba_4Ti_{13}O_{30}$	orthorhombic	Abma	30032	035-0750
Fresnoite	B_2TS_2	$Ba_2TiSi_2O_8$	tetragonal	P4bm	201845	022-0513
Di-barium titanate (m)	B_2T	Ba_2TiO_4	monoclinic	P21/n	2625	070-1377
Di-barium titanate (o)	B_2T	Ba_2TiO_4	orthorhombic	Pnam	29389	038-1481
Barium di-titanate	BT_2	$BaTi_2O_5$	monoclinic	A12/m1	2326	070-1188
Barium tetra-titanate	BT_4	$BaTi_4O_9$	orthorhombic	Pnmm	49575	034-0070

8. Appendix

8. Appendix

Table 8.2-III: Measurements during preparation process

Batch no.		A-1a	A-2a	R-1a	A/R-1a	A/R-2a	A-1b	A-2b	R-1b	A/R-1b	A/R-2b
TiO$_2$ labelling		T1156	K3000	TR-HP-2	HT130R	HT1311	T1156	K3000	TR-HP-2	HT130R	HT1311
Moisture after drying [%]		0.16	0.18	0.11	n.d.	n.d.	0.09	0.11	0.06	0.12	0.11
LOI [wt.-%]		17.03	17.25	17.10	17.17	17.15	17.04	17.03	17.03	16.99	16.99
Calcined powder density [g/cm³]		5.63	5.60	5.65	5.70	5.71	5.63	5.53	5.64	5.68	5.68
BET calcined powder [m²/g]		1.18	1.15	0.92	0.71	0.86	0.84	1.06	0.76	0.77	0.83
A/B-ratio calcine (calculated)		0.998	0.998	0.998	0.998	0.998	0.985	0.985	0.985	0.985	0.985
A/B-ratio calcine (measured)		1.005	1.006	0.997	1.001	0.997	0.988	0.994	0.986	0.988	0.986
A/B-ratio difference		0.007	0.008	-0.001	0.003	-0.001	0.003	0.009	0.001	0.003	0.001
(B,C)T c/a-ratio (calculated from XRD)		1.010	1.010	1.011	1.011	1.011	1.011	1.010	1.011	1.011	1.011
GSD post refining d50 [µm]		2.65	2.63	2.65	2.54	2.63	2.60	2.70	2.60	2.66	2.61
GSD spray drying granules d$_{50}$ [µm]		43.9	43.4	42.8	38.5	45.7	40.4	44.1	40.7	41.9	41.1
Bulk density of granules [g/cm³]		1.02	1.00	1.11	1.17	1.14	1.16	1.04	1.20	1.21	1.16
Density of granules [g/cm³]		3.20	3.21	3.21	3.28	3.27	3.21	3.22	3.20	3.21	3.20
Angle of repose [deg]		49	47	52	34	38	44	36	38	40	43
Green density of compacts [g/cm³]		3.17	3.16	3.18	3.17	3.17	3.15	3.16	3.17	3.17	3.17
Sintering density of compacts [g/cm³]		5.27	5.28	5.40	5.42	5.42	5.23	5.24	5.26	5.29	5.28

8. Appendix

Table 8.2-IV: Summary of the STA characteristic values

Temperature range [°C]	Method	Batch							
		A-1a	A-2a	R-1a	A-1b	A-2b	R-1b	A/R-1b	A/R-2b
50-550	Weight loss [wt.-%]	0.7	0.7	0.6	0.7	0.8	0.7	1.4	1.6
550-720		2.6	2.5	2.5	2.6	2.6	2.5	2.6	2.5
720-1050		13.8	13.8	13.9	13.8	14.0	13.9	13.1	13.5
50-1050	Total weight loss [wt.-%]	17.0	17.0	17.0	17.1	17.4	17.1	17.0	17.7
313-345	Temperature at peak maximum (DSC) [°C]	344	345	318	334	342	318	330	313
695-711		711	705	705	699	698	699	696	695
836-841		842	841	841	838	837	839	836	837
906-934		924	926	934	929	927	928	906	916
312-1028	Peak area [µVs/mg]	1468	1461	1463	1065	1301	1148	901	1095
Additional information	ρ [Ωcm]	3.19E+05	2.04E+06	1.23E+02	1.42E+03	2.75E+03	3.28E+01	2.46E+01	2.27E+01
	BET calcined powder [m²/g]	1.18	1.15	0.92	0.84	1.06	0.76	0.77	0.83
	Relative BET calcined powder [%[*]]	11.5	12.3	15.2	8.2	11.3	12.6	5.4	8.2
	BET TiO_2 [m²/g]	10.277	9.38	6.06	10.277	9.38	6.06	14.25	10.17

---

[*] Calculated in relation to the BET of the titania raw material

8. Appendix

Table 8.2-V: Overview of the characteristic-values of the compositions

Batch no.	ρ_{min}[†]	ρ_{max}[*]	T_{min}[‡]	T_{max}[†]	T_b[§]	T_c[†]	$\alpha_{(130-140℃)}$	$\alpha_{(130-180℃)}$	$\alpha_{(\rho max-\rho min)}$	ρ-T-ratio	Y	Mn
	[Ωcm]	[Ωcm]	[℃]	[℃]	[℃]	[℃]	[%/℃]	[%/℃]	[%/℃]	[1/℃]	[mol-%]	[mol-%]
A-1a	5.69E+04	2.92E+08	54	200	108	145	17.0	11.7	5.7	35.1	0.25	0.05
A-2a	1.57E+05	4.38E+08	68	209	136	147	15.0	10.5	5.7	19.9	0.25	0.05
R-1a	5.31E+01	2.13E+07	69	247	138	148	18.5	15.2	7.6	2255.5	0.25	0.05
A/R-1a	8.56E+01	6.64E+07	56	224	112	n.d.	23.0	17.2	8.0	4619.6	0.25	0.05
A/R-2a	1.27E+02	9.81E+07	52	223	104	n.d.	21.5	17.2	8.0	4505.4	0.25	0.05
A-1b	1.10E+03	8.22E+07	71	240	142	137	15.1	14.6	6.6	443.0	0.25	0.05
A-2b	2.81E+03	7.41E+07	68	233	136	143	12.7	12.8	6.0	159.8	0.25	0.05
R-1b	2.95E+01	1.00E+07	70	252	140	148	17.9	15.5	6.7	1866.6	0.25	0.05
A/R-1b	2.35E+01	1.01E+07	72	257	144	155	16.6	15.1	6.8	2325.4	0.25	0.05
A/R-2b	2.03E+01	5.77E+06	75	253	150	155	17.0	14.6	6.0	1598.4	0.25	0.05
A-2c	2.32E+10	n.d.	n.d.	n.d.	n.d.	n.d.	n.d.	n.d.	n.d.	n.d.	0.15	0.05
A-2d	3.13E+02	3.96E+07	54	223	108	n.d.	21.9	16.2	6.9	747.5	0.34	0.05
A-2e	2.66E+03	1.54E+08	65	214	130	n.d.	19.4	15.0	7.3	387.1	0.25	0.05
A-2f	4.41E+04	5.12E+08	64	207	128	n.d.	18.3	13.7	6.7	81.2	0.25	0.05

[†] Measured value
[‡] Graphically received value
[§] Calculated value

8. Appendix

Table 8.2-VI: Theoretical composition of the material investigated

Composition theoretical [at.-%]					
Ba	Ca	Ti	Si	Y	Mn
41.79	7.43	49.49	0.99	0.25	0.05
Composition theoretical [wt.-%]					
67.85	3.52	28.01	0.33	0.26	0.04

Table 8.2-VII: Bulk compositions detected by EPMA; results of the line scans

Normalised composition detected by EPMA											
Formula		Si	Ca	K	Ba	P	Ti	Y	Mn	Total	O
R-1a bulk	mean	0.0006	0.1485	0.0001	0.8435	0.0000	0.9995	0.0043	0.0014	1.9980	3.0000
	std dev	0.0004	0.0049	0.0001	0.0089	0.0001	0.0041	0.0006	0.0003	0.0041	0
A-2a bulk	mean	0.0007	0.1508	0.0009	0.8378	0.0000	1.0008	0.0044	0.0014	1.9968	3.0000
	std dev	0.0004	0.0041	0.0004	0.0084	0.0001	0.0036	0.0004	0.0004	0.0038	0
Composition detected by EPMA [mol-%]											
Mole		Si	Ca	K	Ba	P	Ti	Y	Mn	Total	
R-1a bulk	mean	0.0297	7.4427	0.0021	42.2576	0.0005	50.0880	0.1081	0.0712	100.0000	
	std dev	0.0181	0.2470	0.0031	0.3835	0.0013	0.3046	0.0146	0.0160	0.0000	
A-2a bulk	mean	0.0373	7.5671	0.0230	42.0046	0.0011	50.1872	0.1097	0.0700	100.0000	
	std dev	0.0196	0.2058	0.0111	0.3602	0.0026	0.2739	0.0105	0.0182	0.0000	
Composition detected by EPMA [wt.-%]											
Mass		SiO_2	CaO	K_2O	BaO	P_2O_5	TiO_2	Y_2O_3	MnO	Total	
R-1a bulk	mean	0.0164	3.8335	0.0018	59.5126	0.0007	36.7565	0.2241	0.0464	100.3920	
	std dev	0.0099	0.1298	0.0027	0.6632	0.0017	0.3622	0.0302	0.0106	0.7603	
A-2a bulk	mean	0.0206	3.9006	0.0199	59.2031	0.0015	36.8594	0.2278	0.0456	100.2785	
	std dev	0.0109	0.1065	0.0095	0.4770	0.0034	0.3637	0.0219	0.0118	0.5248	

Acknowledgement

CURRICULUM VITAE

KATHLEEN KIRSTEIN

PERSONAL DETAILS

address	Herbersdorf 11/8
	8510 Stainz; Austria
e-mail	kathleen.kirstein@inode.at
date of birth	31.08.1980
place of birth	Leipzig (Germany)

PROFESSIONAL EXPERIENCE

05.11 – present   EPCOS OHG   Deutschlandsberg (Austria)
Product Development Engineer for PTC Thermistors

04.08 – 04.11.   Technical University Graz   Graz (Austria)
Research assistant

Performed a PhD project in cooperation with EPCOS OHG. Investigated the effect of titanium dioxide raw materials on the solid-state synthesis and the electrical characteristic of $(Ba,Ca)TiO_3$-based ceramics with PTCR effect.

12.07 – 03.08   EPCOS OHG   Deutschlandsberg (Austria)
Employee

Continued my diploma thesis project. Successfully upgraded the dip coating equipment. Transferred the finished project to EPCOS Ltd. Zhuhai (China).

04.07 – 11.07   EPCOS OHG   Deutschlandsberg (Austria)
Diploma thesis

"Entwicklung einer Glasursuspension und eines Auftragsverfahrens zur Tauchbeschichtung von Zinkoxid- Energievaristoren mit einem passivierenden Glas"

(design and development of a glaze suspension and a dip coating process for the passivation of zinkoxide energy varistors)

10.05 – 02.06   Bundesanstalt für Materialforschung und –prüfung (Federal Institute of Materials Research and Testing)   Berlin

5th semester trainee (practical training)

Evaluated new equipment for measuring the green density of ceramic tapes.

07.05 – 09.05   Horn & Co group of companies   MMW Weitefeld

- Student assistant at quality assurance laboratory

07.04 – 02.05   Lafarge Refractories GmbH   Hangelar

- Student assistant quality assurance laboratory

01.03 – 02.04   Lafarge Refractories GmbH   Scheuerfeld

- Employee at quality assurance laboratory

Operated the newly implemented computer-assisted quality assurance management system. Developed and performed quality control plans.

07.02 – 09.02   Lafarge Refractories GmbH   Scheuerfeld

- Student assistant quality assurance laboratory

EDUCATION

04.08 – 04.11.   Technical University Graz   Graz (Austria)

PhD student

03.04 – 11.07   University of Applied Science Koblenz   Höhr-Grenzhausen

Subject "materials science glass and ceramics"

Awarded academic degree "Diplom-Ingenieur (FH)" - equivalent to M.Sc.

Completed studies with top grade.

03.01 – 02.03   University of Applied Science Koblenz   Höhr-Grenzhausen

- Subject "materials science glass and ceramics"

09.97 – 06.00 Privates Gymnasium Abtei Marienstatt   Marienstatt

Passed "Allgemeine Hochschulreife" - equivalent to A-levels in GB